Technische Universität München
Institut für Energietechnik

Lehrstuhl für Thermodynamik

Influence of Enhanced Heat Transfer in Pulsating Flow on the Damping Characteristics of Resonator Rings

Alejandro Cárdenas Miranda

Vollständiger Abdruck der von der Fakultät für Maschinenwesen der Technischen Universität München zur Erlangung des akademischen Grades eines

Doktor – Ingenieurs

genehmigten Dissertation.

Vorsitzender:
Univ.-Prof. Dr.-Ing. Nikolaus A. Adams
Prüfer der Dissertation:
1. Univ.-Prof. Wolfgang Polifke, Ph.D
2. Univ.-Prof. Dr. Michael Oschwald
RWTH Aachen

Die Dissertation wurde am 12.06.2014 bei der Technischen Universität München eingereicht und durch die Fakultät für Maschinenwesen am 29.09.2014 angenommen.

Vorwort

Die vorliegende Arbeit entstand am Lehrstuhl für Thermodynamik der Technischen Universität München während meiner Tätigkeit als wissenschaftlicher Mitarbeiter. Diese wurde durch die Deutsche Forschungsgemeinschaft (DFG) im Rahmen des Sonderforschungsbereichs Transregio 40 gefördert.

Mein erster und aufrichtiger Dank gilt meinen Doktorvater, Prof. Wolfgang Polifke, PhD., für seine fachliche Orientierung und für seine stets konstruktiven Anregungen. Vor allem danke ich Ihm dafür, dass er mir wissenschaftlichen Freiraum gab, mich aber gleichzeitig durch seine menschliche Art motivierte und Vertrauen schenkte. Prof. Dr. Michael Oschwald danke ich für die freundliche Übernahme des Koreferats sowie Prof. Dr.-Ing. Nikolaus A. Adams für die Übernahme des Vorsitzes bei meiner mündlichen Prüfung.

Für die hilfsbereite Athmosphäre am Lehrstuhl will ich mich bei allen Kolleginnen und Kollegen bedanken. Es ist keine Selbstverständlichkeit so viel Öffenheit und Freundschaft in ein Kollegium zu finden. Dazu gehört mein langjähriger Bürokollege Dr. Christoph Hirsch, mit dem ich das Glück hatte, schon als Student das Büro teilen zu dürfen. Während dieser ganzen Zeit stand er mir mit wertvollem Rat zur Seite, wofür ich Ihm herzlich danke.

Mehrere Kollegen trugen mit wertvollen fachlichen Diskussionen und Unterstützung zur Besserung dieser Arbeit bei. Besonders will ich hier Kilian Förner danken, der das Forschungsprojekt für die zweite Phase mit Interesse übernahm und diese Arbeit akkurat Korrektur las. Frédérik Collonval danke ich für seine Hilfe bei der Programmierung in openFoam und Tobias Holzinger für die gründlichen Diskussionen zu akustischen Wellen. Die Raketen-Gruppe am Lehrstuhl, vor allem Daniel Morgenweck und Moritz Schulze danke ich für die gute Zusammenarbeit.

Für die sehr gute Zusammenarbeit während meiner Zeit in der Systemadministration des Lehrstuhls danke ich dem IT-Team, insbesondere meinem Admin-Kollegen Christoph Jörg.

Zu Dank verpflichtet bin ich auch dem Sekretariat-Team, das mir bei organisatorischen und vor allem finanziellen Projekt-Angelegenheiten half.

Die Studenten, die im Rahmen von Studienarbeiten oder Hiwi-Tätigkeiten diese Arbeit unterstützten verdienen auch meine Anerkennung. Besonders der Einsatz von Thomas Emmert und Christoph Kunzer will ich hier hervorheben.

Ganz besonders will ich auch meiner Gastfamilie in Deutschland, Familie v. Kruedener, für all die Fürsorge während meines Studiums und die vielen Jahren die ich schon in Deutschland lebe, danken.

Diese Arbeit steht als Abschluss eines langen Ausbildungsweges. Mein innigster Dank gilt meiner Familie in Mexiko, vor allem meinen Eltern, die mir diesen Weg erst ermöglichten. El mayor mérito de éste trabajo les pertenece a mis padres. Es imposible plasmar en unas cuantas palabras todo el apoyo, orientación y cariño que he recibido de parte de ellos. Les agradesco de corazón a mis padres Fernando y Bety, y a mis hermanos Gabi y Fer su apoyo incondicional.

Vom Herzen will ich meiner Freundin Nelli Born für all Ihr Verständnis und Ihre Hilfe danken. Insbesondere danke ich Ihr dafür, dass Sie mir selbst in den schwierigen Phasen so einer Arbeit die Ruhe und die Freude im Leben schenkt. Ohne Ihre Hilfe hätte ich diese Arbeit nicht in dieser Form zum Abschluss gebracht.

München, im Juni 2014 Alejandro Cárdenas Miranda

Teile dieser Dissertation wurden vom Autor bereits vorab als Konferenz- und Zeitschriftenbeiträge veröffentlicht [12–18, 32, 35]. Alle Vorveröffentlichungen sind entsprechend der gültigen Promotionsordnung ordnungsgemäß gemeldet. Sie sind deshalb nicht zwangsläufig im Detail einzeln referenziert. Vielmehr wurde bei der Referenzierung eigener Vorveröffentlichungen Wert auf Verständlichkeit und inhaltlichen Bezug gelegt.

Parts of this Ph.D. thesis were published by the author beforehand in conference proceedings and journal papers [12–18, 32, 35]. All of these prior printed publications are registered according to the valid doctoral regulations. For this reason, they are not quoted explicitly at all places. Whether these personal prior printed publications were referenced, depended on maintaining comprehensibility and providing all necessary context.

Abstract

Rocket thrust chambers are prone to thermoacoustic instabilities. Apart of the structural loads induced by pressure fluctuations, considerably enhanced heat transfer has been repeatedly observed under pulsating flow driven by unstable combustion. To increase stability and extend the operation margin of the engine, the application of resonator rings is common practice. This thesis aims at providing a more fundamental understanding of the functionality of resonator rings and their sensitivity to gas temperature inhomogeneities possibly caused by the aforementioned enhanced heat transfer. To truly evaluate the functionality of the resonators and provide a complete picture of their stabilizing influence, a linear thermoacoustic stability prediction method is presented. This low-order acoustic network approach is capable not only of handling three-dimensional acoustic modes, but also of accounting for the essential driving and damping mechanisms, giving special attention to the resonator ring, and allowing parametric studies. It is shown that the inhomogeneity in the gas temperature can indeed reduce the performance of the resonators and might lead to the destabilization of the engine. Furthermore, the mechanisms that lead to enhanced heat transfer in pulsating flow induced by acoustic waves are also investigated through a series of configurations of increasing complexity. Firstly, a low-order analytical model for the convective heat flux through a wall of finite thickness is given, that accounts for heat transfer coefficient and bulk flow temperature imposed pulsations. In subsequent steps, computational fluid dynamic approaches are employed to study the response of the laminar and turbulent boundary layers, and resulting heat transfer, to bulk flow velocity pulsations. An acoustically compact LES approach is followed, allowing for management of the turbulent case with an incompressible solver under admissible computational costs. The method is extended into a weakly-compressible formalism to account for temperature-dependent properties and imposed acoustic pressure fluctuations. These investigations give a qualitative order of the magnitude of the enhancement for a wide range of pulsation parameters.

Kurzfassung

Raketentriebwerke sind anfällig für thermoakustische Instabilitäten. Bei instabiler Verbrennung mit pulsierender Strömung wird, neben der durch die Druckschwankungen induzierten Strukturlasten, auch von einer deutlich erhöhten Wärmeübertragung in der Literatur berichtet. Die Anwendung von Resonator-Ringen ist dabei gängige Praxis, um die Stabilität bzw. den Betriebsbereich des Motors zu vergrößern. Diese Arbeit zielt darauf ab, ein tieferes Verständnis der Wirksamkeit von Resonator-Ringen zu schaffen, sowie deren Empfindlichkeit gegenüber Gastemperatur-Inhomogenitäten abzuschätzen. Letzteres wird als Konsequenz von der oben erwähnten erhöhten Wärmeübertragung angenommen. Eine Methode zur thermoakustischen Stabilitätsanalyse wird vorgestellt, um ein vollständiges Bild der stabilisierenden Wirkung von Resonatoren zu bekommen. Dieser niedrig-dimensionale, akustische Netzwerkansatz berücksichtigt nicht nur die wesentlichen antreibenden und dämpfenden Mechanismen, sondern auch drei-dimensionale Moden. Besonderes Augenmerk wird hierbei auf den Resonator-Ring gelegt. Außerdem ermöglicht die Methode Parameterstudien. Es wird gezeigt, dass eine Inhomogenität der Gastemperatur tatsächlich die Wirksamkeit der Resonatoren reduziert, was zur einer Destabilisierung des Motors führt. Darüber hinaus werden die Mechanismen in einer durch Schallwellen induzierten pulsierenden Strömung, die zur erhöhten Wärmeübertragung führen, durch eine Reihe von Konfigurationen von zunehmender Komplexität untersucht. Als Erstes wird ein analytisches niedrig-dimensionales Modell für den konvektiven Wärmefluss durch eine Wand endlicher Dicke vorgestellt. Anströmtemperatur und Wärmeübergangskoeffizient werden dabei pulsierend vorgegeben. Anschließend wird die Antwort der Wärmeübertragung auf pulsierende Strömung für laminare und turbulente Fälle mittels numerischer Strömungssimulation untersucht. Ein akustisch kompakter LES-Ansatz erlaubt die Behandlung der turbulenten Fälle mit einem inkompressiblen Solver unter vertretbaren Rechenaufwand. Die Methode wird auf einem schwach-kompressiblen Formalismus erweitert, um temperaturabhängige Stoffeigenschaften und vorgegebene akustische Druckpulsationen zu berücksichtigen. Diese Untersuchungen geben eine qualitative Abschätzung der Erhöhung des Wärmeübergangs für eine breite Parameterauswahl.

Contents

Nomenclature

Latin Characters

$\mathbf{A}$	Acoustic network system matrix	[-]
a	Thermal diffusivity	$[\mathrm{m^2\,s^{-1}}]$
a_{uc}	Axial velocity center-line amplitude	$[\mathrm{m\,s^{-1}}]$
c	Speed of sound	$[\mathrm{m\,s^{-1}}]$
c_p	Specific heat at constant pressure	$[\mathrm{J\,kg^{-1}\,K^{-1}}]$
C_s	Sutherland constant	[-]
$c_s,\ c_k,\ c_\epsilon$	Smagorinsky, kinetic energy and dissipation subgrid model constants	[-]
c_v	Specific heat at constant volume	$[\mathrm{J\,kg^{-1}\,K^{-1}}]$
d	Resonator cavity mouth diameter	[m]
D_{ji}	Shear strain tensor	$[\mathrm{s^{-1}}]$
$\mathbf{E}$	Identity matrix	[-]
e	Specific internal energy	$[\mathrm{J\,kg^{-1}}]$
EHT	Ratio of heat transfer enhancement	[-]
$\hat{F}_{mn},\ \hat{G}_{mn}$	Down- and upstream traveling wave amplitudes	$[\mathrm{m\,s^{-1}}]$
$f_{mn},\ g_{mn}$	Down- and upstream traveling waves	$[\mathrm{m\,s^{-1}}]$
h	Specific enthalpy	$[\mathrm{J\,kg^{-1}}]$
i	Imaginary unit $\sqrt{-1}$	[-]
J_m	Bessel function of the first kind of order m	[-]
$k_{mn}^{\pm}$	Axial wave numbers of order m and n	$[\mathrm{m^{-1}}]$
k_{sgs}	Subgrid turbulent kinetic energy	$[\mathrm{m^2\,s^{-2}}]$
$l_a,\ l_e,\ l_r$	Geometrical, effective and equivalent mass length of quarter wave cavity	[m]
L_c	Thrust chamber effective length	[m]
l_s^+	Stokes' length in wall units	[-]
M	Molar mass	$[\mathrm{kg\,mol^{-1}}]$
m	Tangential wave number	$[\mathrm{rad^{-1}}]$
n_r	Number of cavities in a resonator ring	[-]
p	Pressure	[Pa]
$\dot{Q}$	Volumetric heat release rate	$[\mathrm{W\,m^{-3}}]$
$\dot{q}$	Specific heat flux	$[\mathrm{W\,m^{-2}}]$
$\dot{q}_w$	Specific wall heat flux	$[\mathrm{W\,m^{-2}}]$
R	Universal gas constant	$[\mathrm{J\,mol^{-1}\,K^{-1}}]$
r	Reflection coefficient	[-]
R_c	Thrust chamber radius	[m]
R_s	Specific ideal gas constant	$[\mathrm{J\,kg^{-1}\,K^{-1}}]$

$r,\ \varphi,\ x$	Cylindrical coordinate system	[m, rad, m]
$\mathbf{S}$	Scattering matrix	[-]
$\mathbf{T}$	Transfer matrix	[-]
T	Temperature	[K]
t	Time	[s]
T_τ	Friction temperature	[K]
$u,\ v,\ w$	Three dimensional components of velocity	$[\mathrm{m\,s^{-1}}]$
U_b	Bulk flow velocity	$[\mathrm{m\,s^{-1}}]$
u_τ	Friction velocity	$[\mathrm{m\,s^{-1}}]$
$x,\ y,\ z$	Cartesian coordinate system	[m]
Y_m	Bessel function of the second kind of order m	[-]
Z	Acoustic impedance	$[\mathrm{N\,s\,m^{-3}}]$

Greek Characters

α	Heat transfer coefficient (in the context of heat transfer)	$[\mathrm{W\,m^{-2}\,K^{-1}}]$
α	Absorption coefficient (in the context of acoustics)	[-]
$\alpha^{\pm}_{mn}$	Radial wave numbers	$[\mathrm{m^{-1}}]$
Γ	Cycle increment	[-]
γ	Ratio of heat capacities	[-]
Γ_{vt}	Visco-thermal propagation constant	$[\mathrm{m^{-1}}]$
δ	Boundary layer thickness	[m]
δ_{ij}	Kronecker symbol	[-]
δ_s	Stokes' length	[m]
ε	Small quantity	[-]
ϵ_{nl}	Non-linear resistance factor	[-]
η_{mn}	Roots of the derivative of the Bessel function of first kind	[-]
κ_{K}	Von Karman constant	[-]
λ	Thermal conductivity	$[\mathrm{W\,m^{-1}\,K^{-1}}]$
μ	Dynamic Viscosity	$[\mathrm{kg\,m^{-1}\,s^{-1}}]$
ν	Kinematic viscosity	$[\mathrm{m^2\,s^{-1}}]$
ν_{sgs}	Subgrid viscosity	$[\mathrm{m^2\,s^{-1}}]$
Ξ	Excess temperature	[-]
ξ	Ratio of specific impedance	[-]
ρ	Density	$[\mathrm{kg\,m^{-3}}]$
σ_{ji}	Stress tensor	$[\mathrm{N\,m^{-2}}]$
τ	Combustion time lag	[s]
τ_{ji}	Shear stress tensor	$[\mathrm{N\,m^{-2}}]$
τ_w	Skin friction	$[\mathrm{N\,m^{-2}}]$
Θ	Resistance	$[\mathrm{N\,s\,m^{-3}}]$
ϕ_{diss}	Viscous dissipation	$[\mathrm{N\,m^{-2}\,s}]$
χ	Temperature inhomogeneity ratio	[-]
Ψ	Reactance	$[\mathrm{N\,s\,m^{-3}}]$
$\Omega = \omega + i\vartheta$	Complex valued frequency	$[\mathrm{rad\,s^{-1}}]$
ω^c_{mn}	Cut-on frequency	$[\mathrm{rad\,s^{-1}}]$
$\triangle$	Grid size	[m]

$\blacktriangle$	Test filter size	[m]

Subscripts

$(.)_C$	Cold state
$(.)_{eig}$	Resonance
$(.)_H$	Hot state
$(.)_{mnl}$	Tangential, radial and longitudinal mode order
$(.)_o$	Reference state

Superscripts

$\vec{(.)}$	Vector
$(.)^*$	Non-dimensionalized quantity
$\hat{(.)}$	Complex valued amplitude of harmonic oscillation
$(.)^+$	Wall units
$(.)'$	Acoustic fluctuation
$\bar{(.)}$	Mean value
$(.)`$	Turbulent fluctuation
$\widehat{(.)}$	Resolved or grid scale
(.)’	Unresolved or subgrid scale

Operators

$\langle \ldots \rangle$	Temporal and spatial averaging
$\langle \ldots \rangle_p$	Ensemble and spatial averaging
$\det\{\ldots\}$	Determinant
$\mathrm{Re}\{\ldots\}$	Real part
$\mathrm{Im}\{\ldots\}$	Imaginary part
Δ	Change
$\vec{\nabla}$	Spatial differentiation
$\vec{\nabla}^2$	Laplace operator
$\frac{D}{Dt} = \frac{\partial}{\partial t} + \vec{u} \cdot \vec{\nabla}$	Total derivative

Dimensionless Numbers

Bi	Biot number
Fo	Fourier number
He	Helmholtz number
M	Mach number
Nu	Nusselt number
Pr	Prandtl number
Re	Reynolds number
Re_τ	Turbulent Reynolds number

Abbreviations

BC	Boundary Condition
CFD	Computational Fluid Dynamics
DNS	Direct Numerical Simulation
EHT	Enhanced Heat Transfer
LES	Large Eddy Simulation
OLTF	Open Loop Transfer Function
PISO	Pressure Implicit with Splitting of Operators
RANS	Reynolds Averaged Navier-Stokes Simulation
SPL	Sound Pressure Level
TKE	Turbulent Kinetic Energy

1 Introduction

1.1 Motivation

Space transportation systems have become indispensable for the global society of our days. The applications that directly benefit from the access to space are wide, including telecommunication, earth observation, weather forecast and navigation, to name some of them. Furthermore, the opportunities that the access to space offers to the basic research areas like astronomy, natural sciences and medicine have considerably contributed to fundamental advances. These space systems demand key technological expertise, which drives innovation and translates indirectly into enormous benefits for the society when transferred to other more common areas.

To assure the access to space, efficient and reliable rocket propulsion systems are required, which in the civil sector are predominately feed by liquid propellants. Liquid propellants offer the best trade-off between performance, costs and efficiency for the present and near future propulsion systems. Modern rocket engines exhibit a noticeably complexity due to the extreme conditions they are operated under. A look at some key performance parameters of the Ariane 5 launcher and its primary engine, the Vulcain 2, gives a representative example. The core of the primary engine is the thrust chamber. In this relatively small device of approximately 900 kg weight, fuel and oxidizer are pumped through the injector plate at a rate of more than 300 kg/s and subsequently burned releasing about 3 GW power. Acceleration and expansion of the exhaust gases through the nozzle deliver the desired thrust of 1400 kN [1]. There is no other machine with a higher energy conversion density.

Despite the impressive achievements in rocket propulsion performance during the last space programs, further improvement is still needed. One of the more critical issues present in these propulsion devices is the emergence of thermoacoustic instabilities, which may occur due to a feedback between the unsteady combustion heat release and the acoustic field of the chamber. This phenomenon is not exclusive of rocket chambers, also modern, lean premixed gas turbines [63] or even heating units [90] are prone to this kind of instabilities.

Figure 1.1 gives a simplified diagram of the mechanisms leading to self sustained thermoacoustic oscillations. A perturbation in the combustion zone generates some heat release fluctuations $\dot{Q}'$. These heat release fluctuations, added to the inherently thermal expansion, locally induce pressure fluctuations p' and act thus as a source of sound. These pressure perturbations propagate as acoustic waves through the chamber. Due to reflection at boundaries or discontinuities, a feedback mechanism can be induced such that these waves reach the combustion region again. Rayleigh has explained the sources for this phenomenon in 1878 by giving a necessary condition [111]: *"For instability to*

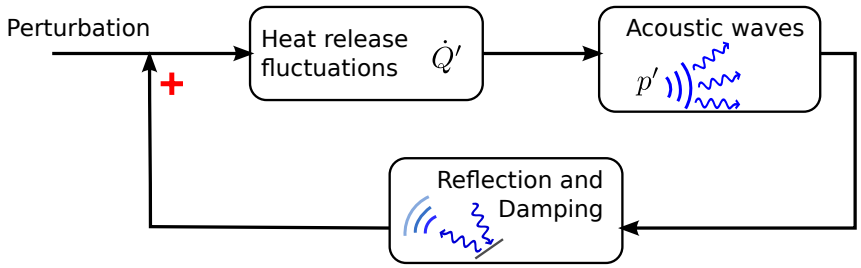

Figure 1.1: Schematic description of coupling between heat release and acoustic perturbations leading to self sustained oscillations.

occur, heat must be released at the moment of greatest compression". Mathematically, this Rayleigh criterion can be written as:

$$\int_0^{1/f} \dot{Q}' p' \, dt \; > \; 0 \quad , \tag{1.1}$$

where f denotes the oscillating frequency, $\dot{Q}'$ and p' the heat release and pressure fluctuations, respectively, and the time integration covers one period of oscillation. This condition is necessary for thermoacoustic driving, but not sufficient for the occurrence of instabilities. In addition to the acoustic driving, also damping is present in the chambers. So, even if the previous condition is fulfilled, the damping can suppress the oscillations.

Most rocket engine development programs have been suffering of thermoacoustic instability issues. The pressure oscillations lead to vibrations that might damage the sensible payload or even interfere with navigation instruments [49]. Because energy density in rocket thrust chambers is extremely high, unstable oscillations can even destroy the engine within a few seconds. Apart of these structural loads, several investigations report considerably enhanced convective heat transfer coefficients at walls of devices with thermoacoustic instabilities [29, 49, 99]. Under certain conditions, which are not totally clarified yet, the high frequency pressure and the corresponding velocity fluctuations seem to stimulate the momentum and energy transfer. This increases the thermal and mechanical loads on the chamber walls even further and compromises the proper operation of the engine. Often, a considerably number of design changes and subsequent tests have been required to find a stable configuration. E.g. for the F-1 engine of the Apollo program, circa 2000 full-scale tests and several subsequent design modifications were necessary to stabilize it in order to comply with the safety requirements [25]. The lost of the Ariane 4 mission in 1990 is an other striking example. An instability in the upper stage engine, which was not detected in the design phase, lead to the destruction of the rocket [48].

Concerning the heat transfer in pulsating flows, a variety of experimental, numerical and theoretical investigations exist. Section 5.1 gives an extensive literature review on the topic. All the investigations reporting striking heat transfer enhancement are of experimental nature. Unfortunately, the magnitude of these higher heat transfer rates has not been reproduced by any of the numerical or theoretical approaches. Thus, while serious experimental evidence on its occurrence exists, a satisfactory explanation

of the responsible mechanisms has not yet been given. Fundamental research in this area is still necessary.

According to the feedback analysis, the balance between the driving and damping mechanisms present in the chamber determine whether the oscillations are stable or not. In rocket thrust chambers, the main components relevant for this balance are the injector plate, the nozzle, the chamber volume, and the combustion front. To increase stability and extend the operation margin of the engine, the application of small passive acoustic cavities, so-called *resonators*, has been demonstrated repeatedly [93]. Other possibilities to stabilize the chamber are an adapted injector design and baffles, which both have the drawback that they can affect the performance of the thrust chamber. Two mechanisms are believed to be responsible for the stabilizing influence of resonators: First, the attached cavities shift the eigenfrequencies of the overall system, thus disturbing the feedback mechanism between heat release and acoustic field. Second, dissipation of acoustic energy through viscous and turbulent losses at the cavities mouth. This dissipation is maximum within small frequency ranges around the eigenfrequency of the cavities. Thus, resonators have to be tuned according to the oscillations modes of the overall system. However, the optimal cavity design that leads to maximum stabilization is still challenging. Since the resonators themselves influence those eigenmodes significantly, this is not a simple task. The eigenfrequency of a cavity depends primarily on its geometrical dimensions and on the speed of sound of the gas inside it.

Under operation, the superimposed acoustic velocity perturbations may also flush hot exhaust gases into the cavity. Furthermore, the possibly enhanced heat transfer both in axial as well as in wall normal direction in acoustic pulsating flows can compromise under certain conditions the thermal integrity of the cavities and the chamber walls. These two mechanisms might change the temperature distribution inside the cavities. Due to the temperature dependency of the speed of sound, the propagation of the acoustic waves would also change, bringing the resonators out of their design point. For instance, the cavities might fail in stabilizing the engine.

Due to the aggressive conditions at operation with temperatures of up to 3600 K and pressure of about 100 bar, measurements and experimental verification of functionality are difficult and expensive. Theoretical and numerical approaches are thus desirable in all phases of the design process. An accurate prediction of the stabilizing influence of resonators under real operation conditions taking the previous effects into account would be of great interest for the development of more reliable space transportation systems.

1.2 Scope of the Work

The work presented in this thesis is funded by the German Research Foundation (DFG) in the framework of the "Sonderforschungsbereich SFB-TRR40" [3], which focuses on the technological foundations for the design of thermally and mechanically highly loaded components of future space transportations systems. Several German institutions are involved in a long-term cooperation initiative planed to last approximately 12 years. It is divided into three subsequent phases that should gradually evolve from fundamental research towards development of new technologies and demonstration of applicability.

This work belongs to the project A3 and covers the investigations of the first fundamental phase.

The long-term objective of this project is the development of reliable engineering tools to characterize the damping behavior of resonator rings in rocket thrust chambers under real operation conditions. Hereby, the influence of enhanced heat transfer presumably driven by the acoustic fluctuations should be considered in the analysis. The overall intention of the project is to clarify the following questions:

1. Is enhanced heat transfer present in resonators or in the vicinity of the cavity mouths?
2. Does this enhanced heat transfer have any consequences on the stabilizing influence of resonators?

Two top level topics and the interaction between them are covered by the foregoing questions, namely: heat transfer in pulsating flow and damping characteristics of resonator rings.

The long-term objective is indeed quite ambitious. In order to provide satisfactory answers to the two mentioned questions, firstly, a variety of preliminary issues have to be solved. As mentioned in the motivation of this thesis, yet, the mechanisms leading to enhanced heat transfer in pulsating flows are not totally clarified. This is indicated by the lack of models that are able to reproduce the large heat transfer rates observed in some experiments and the partially contradictory results that can be found in the literature. Furthermore, the initial investigations during the course of this project showed that the mere description of the damping characteristics of resonators does not necessarily provide a complete picture of their stabilizing influence. The balance between the driving and damping mechanisms present in the thrust chamber decides whether its operation is stable or not. Thus, extended models that are able to incorporate the influence of enhanced heat transfer on the damping characteristics of resonator rings are not sufficient. Additionally, in order to truly estimate the consequences of enhanced heat transfer, a method that is able to evaluate the stability of a representative thrust chamber coupled to the extended resonator ring model is necessary.

1.3 Strategy and Thesis Outline

Both the enhanced heat transfer in pulsating flows driven by acoustic fields and the stabilizing influence of resonators are not totally clarified yet. Wide ranges of time and length scales are present in both problems, as will be explained in Sec. 2.1.3. Thus, a coupled analysis considering all these scales would not be efficient or even possible at this stage. Instead, a decoupled analysis of these two main topics, stabilizing influence of resonators on the one hand and heat transfer in pulsating flows on the other, appears as an appropriate strategy to bring more fundamental understanding. For this purpose, adequate simulation approaches have to be defined and extended.

Following this strategy, the first task is the development of resonator ring models that are able to account for some influence of enhanced heat transfer. As a first attempt, it

will be assumed that, if present, enhanced heat transfer will primarily modify the gas temperature profile inside the cavities. A milestone is the estimation of the sensitivity of the resonator rings to an imposed inhomogeneous temperature profile. Furthermore, an appropriate method for the stability analysis of rocket thrust chambers that incorporates the extended resonator ring model has to be developed. Using this method, the stabilizing influence of the resonator rings should be investigated for various operation conditions. Thus, the method should be able to reproduce the essential driving and damping mechanisms present in the chamber, give especial attention to the resonator ring, and afford parametric studies.

In the second part of this thesis, the mechanisms leading to enhanced heat transfer in pulsating flows are studied. These investigations should clarify whether an enhancement of energy transfer is expected to occur under periodic transient conditions. Rather than a quantitative estimate, it should give a qualitative order of magnitude and highlight the key parameters controlling the presumably heat transfer enhancement. The first task involves the identification and definition of the periodic transient conditions present in the rocket thrust chamber. A divide and conquer strategy is followed, that studies problems of increasing complexity. Each of this problems aim to estimate the influence of some precise transients on the heat transfer. In this way, mechanisms leading to enhanced heat transfer in rocket chambers can be identified.

The thesis is organized as follows: Chapter 2 presents the necessary theoretical background on fluid mechanics and thermodynamics. Based on a first estimation of length and time scales, simulation approaches that focus on certain scales are introduced. Chapter 3 presents relevant models describing the acoustic damping of resonator rings and an extension of these models to account for inhomogeneous temperature profiles is derived. A preliminary investigation of the cavities' sensitivity to temperature inhomogeneities is also given in this chapter. In Ch. 4, a methodology for the stability analysis of representative rocket thrust chambers is proposed. The method is validated and the stabilizing influence of resonator rings in rocket trust chambers is discussed. The results of a sensitivity analysis for a representative thrust chamber configuration over a range of operation conditions and resonator ring geometries concludes this chapter. Chapter 5 introduces the heat transfer in pulsating flows, defines the environment to be studied and presents an appropriate strategy. A preliminary investigation using a low order model of conjugate heat transfer and a laminar pulsating flow past a flat plate is presented in the same chapter. The third and most challenging configuration studies the heat transfer in turbulent pulsating channel and is given in Ch. 6. An extended CFD simulation technique that accounts for the influence of acoustic fields on turbulent heat transfer is presented. After validation, the results of an extensive simulation campaign are presented, that estimate the heat transfer enhancement for a variety of pulsation parameters. Finally, Ch. 7 summarizes this thesis and gives the conclusions of the investigations.

2 Theoretical Background and Simulation Approaches

2.1 Conservation Equations

In the context of continuum mechanics, gases and liquids can be treated as a fluid composed of infinitesimal elements assumed to be small compared to all length scales of the problem, but large compared to the molecular scales. The conservation equations of mass, momentum and energy provide a framework for the mathematical description of fluid dynamics. These conservation laws are derived in an integral sense over a control volume using the density ρ, pressure p, velocity vector $\vec{u}$ and internal energy e as primitive variables. Application of Gauß' integral theorem allows to express them in differential form, too. Several textbooks devote detailed chapters to the derivation and formulation of these laws [8, 97]. This section presents only the essential information necessary in the appreciation of the topics handled in this thesis.

The convective or total derivative operator

$$\frac{D}{Dt} = \frac{\partial}{\partial t} + u_i \frac{\partial}{\partial x_i} \quad , \tag{2.1}$$

accounts for the total change of a property. Using this operator, three dimensional Cartesian coordinates and Einsteins index notation, the conservation equations can be written as [8]:

$$\frac{D\rho}{Dt} = -\rho \frac{\partial u_i}{\partial x_i} + \mathbb{k}_m \quad , \tag{2.2}$$

$$\rho \frac{Du_j}{Dt} = \frac{\partial \sigma_{ji}}{\partial x_i} + \mathbb{k}_{f,j} \quad , \tag{2.3}$$

$$\rho \frac{De}{Dt} = -\frac{\partial \dot{q}_i}{\partial x_i} + \sigma_{ji} \frac{\partial u_i}{\partial x_j} + \mathbb{k}_e \quad . \tag{2.4}$$

Equation (2.2) represents the continuity equation considering mass sources $\mathbb{k}_m$. The momentum conservation is expressed by Eq. (2.3) and states that the change in overall momentum can be induced by surface forces given by the stress tensor σ_{ji} and body forces given by the source term $\mathbb{k}_{f,j}$. Finally, based on the first law of thermodynamics, the conservation of energy Eq. (2.4) relates the total change in internal energy e to surface heat fluxes $\dot{q}_i$, mechanical power $\sigma_{ji}(\partial u_i/\partial x_j)$ and energy sources $\mathbb{k}_e$. These equations are valid for any single species fluid. In cases with several fluid species, diffusion fluxes have to be additionally considered [103]. All quantities different than the primitive variables present in this conservation equations depend on the specific fluid and problem properties.

2.1.1 Constitutive Laws

Constitutive laws are necessary to express the fluid properties in the just given set of equations as functions of the primitive variables.

The stress tensor is commonly decomposed into the shear or viscous stress tensor τ_{ji} and the normal stress tensor $-\delta_{ji}p$:

$$\sigma_{ji} = \tau_{ji} - \delta_{ji}p + \zeta\frac{\partial u_k}{\partial x_k}\delta_{ji} \quad . \tag{2.5}$$

The third term in this expression accounts for a possible non-equilibrium between normal stresses and thermodynamic pressure. The proportionality factor, the so-called volume viscosity ζ, is very small for most fluids and is only relevant for very fast deformations. All problems studied in this thesis are assumed to obey thermodynamic equilibrium at all instants and the volume viscosity is neglected. It is mentioned here for completeness.

Concerning the shear stresses and contrary to solids, it is the rate of shear deformation and not the deformation itself that matters. The rate of shear deformation is given by the shear strain tensor:

$$D_{ji} = \frac{1}{2}\left[\left(\frac{\partial u_j}{\partial x_i} + \frac{\partial u_i}{\partial x_j}\right) - \frac{2}{3}\delta_{ji}\frac{\partial u_k}{\partial x_k}\right] \quad . \tag{2.6}$$

In general, the shear stress tensor is a function of the shear strain tensor $\tau_{ji} = f(D_{ji})$. For Newtonian fluids, the relation between shear stresses and shear strain is assumed as linear $\tau_{ji} = 2\mu D_{ji}$, with the dynamic viscosity μ as proportionality factor [8]:

$$\tau_{ji} = \mu\left[\left(\frac{\partial u_j}{\partial x_i} + \frac{\partial u_i}{\partial x_j}\right) - \frac{2}{3}\delta_{ji}\frac{\partial u_k}{\partial x_k}\right] \quad . \tag{2.7}$$

In the energy equation, the mechanical power can be expressed as:

$$\sigma_{ji}\frac{\partial u_i}{\partial x_j} = -p\frac{\partial u_i}{\partial x_i} + \tau_{ji}\frac{\partial u_i}{\partial x_j} \quad . \tag{2.8}$$

The second term on the right-hand side accounts for the mechanical dissipation through viscous forces.

In addition to the stress tensor, a relation for the heat fluxes is also necessary. Fourier's law correlates the heat flux as a function of the temperature gradient:

$$\dot{q}_i = -\lambda\frac{\partial T}{\partial x_i} \quad , \tag{2.9}$$

with the fluid thermal conductivity λ as proportionality factor.

Still, the number of unknowns (p, ρ, u_i, T and e) is larger than the number of equations (1×continuity, 3×momentum and 1×energy) and two additional laws are necessary to close the problem.

For moderate pressures and temperatures, the ideal gas law relates the density, pressure and temperature of a fluid through the following equation of state:

$$\frac{p}{\rho} = R_s T \quad , \tag{2.10}$$

where the specific ideal gas constant R_s is a property of the fluid and can be expressed using the universal gas constant R and the molecular weight of the fluid M as:

$$R_s = \frac{\mathrm{R}}{\mathrm{M}} \quad . \tag{2.11}$$

Often, the ideal gas law written in differential form is useful:

$$\frac{d\rho}{\rho} = \frac{dp}{p} - \frac{dT}{T} \quad . \tag{2.12}$$

A variety of state equations derived from the basic laws of thermodynamics exist that express the internal energy as a function of other two primitive variables, e.g. density and temperature. Combination with the ideal gas law gives:

$$e = \int c_v \, dT = h - \frac{p}{\rho} = \int c_p \, dT - \frac{p}{\rho} \quad , \tag{2.13}$$

where c_v denotes the heat capacity at constant specific volume, h the specific enthalpy and c_p the heat capacity at constant pressure. For ideal gases, the following relations hold:

$$R_s = c_p - c_v = c_v(\gamma - 1) \quad , \tag{2.14}$$

$$c^2 = \left.\frac{\partial p}{\partial \rho}\right|_s = \gamma R_s T \quad , \tag{2.15}$$

where $\gamma = c_p/c_v$ denotes the ratio of heat capacities. For perfect gases, the heat capacities are assumed to be constant and the specific internal energy can be given by:

$$e = c_v T + e_{\mathrm{ref}} = c_p T - \frac{p}{\rho} + h_{\mathrm{ref}} \quad . \tag{2.16}$$

The proportionality factors for the viscous μ and thermal diffusion λ are also functions of the thermodynamic state, principally from temperature if ideal gas behavior is assumed. A well known approximate expression for the dynamic viscosity is given by the Sutherland law [131]:

$$\mu(T) = \mu_{ref} \left(\frac{T_{ref} + C_s}{T + C_s}\right) \left(\frac{T}{T_{ref}}\right)^{3/2} \quad , \tag{2.17}$$

with reference Temperature T_{ref} and viscosity μ_{ref}, and Sutherland constant C_s, respectively. Similar expressions exist for the thermal conductivity. Another possibility is to express it in terms of the Prandtl number, which gives the ratio of momentum to thermal diffusivity:

$$\mathrm{Pr} = \frac{\nu}{a} = \frac{\mu c_p}{\lambda} \quad , \tag{2.18}$$

and can be approximately taken as constant for most fluids. For perfect gases the thermal conductivity can be expressed as:

$$\lambda(T) = \frac{\mu(T)c_p}{\mathrm{Pr}} \quad . \tag{2.19}$$

The constitutive equations presented in this section are valid for moderate pressures lower than the critical pressure and temperature higher than the critical temperature. These expressions provide a good approximation for single species mixtures. Under more critical conditions, so-called real gas expressions should be used [109]. Another possibility is the use of polynomial expressions fitted from very accurate tabulated values [73, 128].

2.1.2 Navier-Stokes Equations

Assuming Newtonian fluids, neglecting the volume viscosity and dropping the source terms, the general conservation Eqs. (2.2) to (2.4) can be expressed as:

$$\frac{D\rho}{Dt} = -\rho\frac{\partial u_i}{\partial x_i} \tag{2.20}$$

$$\rho\frac{Du_j}{Dt} = -\frac{\partial p}{\partial x_i} + \frac{\partial}{\partial x_i}\mu\left[\left(\frac{\partial u_j}{\partial x_i} + \frac{\partial u_i}{\partial x_j}\right) - \frac{2}{3}\delta_{ji}\frac{\partial u_k}{\partial x_k}\right] \tag{2.21}$$

$$\rho\frac{De}{Dt} = -\frac{\partial \dot{q}_i}{\partial x_i} - p\frac{\partial u_i}{\partial x_i} + \phi_{diss} \quad , \tag{2.22}$$

where the viscous dissipation is denoted by $\phi_{diss} = \tau_{ji}\frac{\partial u_j}{\partial x_i}$. This set of equations will be denoted from now on as Navier-Stokes equations (NS-equations), even though strictly speaking this term refers solely to the momentum equation.

For some problems, it is more convenient to express the energy equation as a function of a different primitive variable. The enthalpy form is given by:

$$\rho\frac{Dh}{Dt} = -\frac{\partial \dot{q}_i}{\partial x_i} + \frac{Dp}{Dt} + \phi_{diss} \quad . \tag{2.23}$$

Another practical form for perfect gases uses the temperature as independent variable:

$$\rho c_p\frac{DT}{Dt} = \frac{\partial}{\partial x_i}\left(\lambda\frac{\partial T}{\partial x_i}\right) + \frac{Dp}{Dt} + \phi_{diss} \quad . \tag{2.24}$$

These set of equations provide a complete framework for the mathematical description of fluid dynamical problems. All problems treated in this thesis can be described by these set of equations. However, closed form solutions are only known for cases allowing considerable simplifications.

2.1.3 Numerical Challenges Arising from Compressibility

Any attempt to solve the full set of compressible Navier-Stokes equations in problems in which only some scales dominate would be very complicated and inefficient. This is

especially true for fluid problems accounting only small *compressibility*, that is to say only small density changes due to changes in pressure. Note that changes in density may also be caused by changes in temperature or fluid mixture, which in this study will be denoted as *stratification*. The main criterion for the compressibility of a flow is the Mach number:

$$M = \frac{u_{\text{ref}}}{c} \quad , \tag{2.25}$$

defined as the ratio of the fluid characteristic velocity to the speed of sound in the medium. In the context of compressibility, the speed of sound is not only a measure of the wave propagation velocity, but also an indication of the density changes in the flow, as stated by Panton [97]. The kinetic energy of the flow gives an estimate for the pressure changes present in the flow $\Delta p \approx \rho_{\text{ref}} u_{\text{ref}}^2/2$ or $u_{\text{ref}}^2 \approx 2\Delta p/\rho_{\text{ref}}$. Using this estimate in the definition of the Mach number and Eq. (2.15) gives:

$$M^2 = \frac{u_{\text{ref}}^2}{c^2} \approx \frac{2\Delta p}{\rho_{\text{ref}}} \left.\frac{\Delta\rho}{\Delta p}\right|_s \sim \frac{\Delta\rho}{\rho_{\text{ref}}} \quad . \tag{2.26}$$

For low Mach number flows $M^2 \ll 1$, the fluid dynamics display two types of motions of considerably different magnitude and time scale. Acoustic motions of small magnitude travel much faster than the hydrodynamic motions. This makes the consideration of both acoustic and hydrodynamic flow fields in a single analysis extremely difficult, especially in numerical solution approaches. To overcome this issue, the two fluid motions can be handled separately, as will be presented in the following sections.

2.2 Linearized Analysis for Acoustics

In acoustics, sound is defined as a small pressure perturbation p' that moves as a wave through a medium at the speed of sound c. This pressure perturbation induces also small velocity u' and density ρ' perturbations. As shown by Rienstra and Hirshberg [115], in free space, these perturbations are almost insensitive to viscous and thermal dissipation. Thus, the small perturbations can be treated as isentropic such that:

$$c^2 = \frac{p'}{\rho'} \quad . \tag{2.27}$$

Since the perturbations are small, the fluid motion can be described by a linearized analysis in which the variables are decomposed into a mean quantity denoted by an over-bar and a small perturbation denoted by a prime:

$$p = \bar{p} + p' \quad , \tag{2.28}$$

$$\rho = \bar{\rho} + \rho' \quad , \tag{2.29}$$

$$\vec{u} = \bar{\vec{u}} + \vec{u}' \quad . \tag{2.30}$$

Substitution into the conservation equations for perfect, inviscid and non heat conducting fluids leads to a set of linearized perturbation equations. Depending on the spatial dependency of the mean quantities, the resulting linearized perturbation equations can still be to complex for an analytical treatment. Numerical solvers have emerged that are able to treat also complex geometries [42, 86, 103].

If the mean field allows the introduction of some spatial simplifications, a *wave equation* for the pressure p' might be deduced from the perturbation equations. In this thesis, two cases are considered for which this condition holds. For completeness, their derivation is shown in App. A.1.

- Homogeneous mean flow with constant properties and no sources:

$$\left(\frac{\partial}{\partial t} + \vec{\bar{u}} \cdot \vec{\nabla}\right)^2 p' - \bar{c}^2 \vec{\nabla}^2 p' = 0 \quad . \tag{2.31}$$

- Stagnant fluid with non-uniform properties:

$$\frac{\partial^2 p'}{\partial t^2} - \vec{\nabla}\left(\bar{c}^2 \vec{\nabla} p'\right) = 0 \quad . \tag{2.32}$$

Due to linearity of the wave equation, the general solution can also be determined in the frequency domain assuming harmonic dependency:

$$p' \sim \mathrm{Re}\{\hat{p}\, e^{i\Omega t}\} \quad , \tag{2.33}$$

where the amplitude of the perturbation $\hat{p}$ and the angular frequency Ω are complex valued. The complex notation brings several advantages in the mathematical treatment. Of course, only the real part is physical. Substitution of this approach in the wave equation leads to the *Helmholtz equation*. For several geometries, analytical solutions are possible that express the solution of the Helmholtz equation in a very descriptive manner in terms of up- and downstream traveling waves [33, 104].

2.2.1 Propagation of Acoustic Waves in Cylindrical Ducts with Mean Flow

Throughout this thesis, the propagation of acoustic waves in cylindrical geometries will be widely studied, because rocket thrust chambers can be effectively simplified as cylindrical ducts. In the presence of a uniform mean flow $\vec{\bar{u}} = [U, 0, 0]^T$ in axial direction x and homogeneous speed of sound $\bar{c}$, Eq. (2.31) can be written as [115]:

$$\frac{1}{\bar{c}^2}\left(\frac{\partial}{\partial t} + U\frac{\partial}{\partial x}\right)^2 p' = \vec{\nabla}^2 p' \quad . \tag{2.34}$$

Using cylindrical coordinates (x, r and θ) and Mach number $M = U/\bar{c}$ gives:

$$\frac{1}{\bar{c}^2}\frac{\partial^2 p'}{\partial t^2} + \frac{2M}{\bar{c}}\frac{\partial^2 p'}{\partial t \partial x} + M^2\frac{\partial^2 p'}{\partial x^2} = \frac{\partial^2 p'}{\partial r^2} + \frac{1}{r}\frac{\partial p'}{\partial r} + \frac{1}{r^2}\frac{\partial^2 p'}{\partial \theta^2} + \frac{\partial^2 p'}{\partial x^2} \quad . \tag{2.35}$$

Following the method of separation of variables, substitution of an harmonic approach for the pressure fluctuations $p' = \mathsf{R}(r)\exp(i\Omega t - ikx + im\theta)$ leads after some rearrangement to:

$$r^2\frac{d^2\mathsf{R}}{dr^2} + r\frac{d\mathsf{R}}{dr} + \left[r^2\left((\Omega/\bar{c} - Mk)^2 - k^2\right) - m^2\right]\mathsf{R} = 0 \quad . \tag{2.36}$$

Please note that throughout this thesis, the acoustic notation $e^{+i\Omega t}$ is used for the time dependency. The motivation for this decision and the resulting implications are given in App. A.2. Introducing the dispersion relation

$$\alpha^2 = (\Omega/\bar{c} - Mk)^2 - k^2 \tag{2.37}$$

and using the substitution $\tilde{r} = \alpha r$, the wave equation can be written as:

$$\tilde{r}^2 \frac{d^2\mathsf{R}}{d\tilde{r}^2} + \tilde{r}\frac{d\mathsf{R}}{d\tilde{r}} + \left[\tilde{r}^2 - m^2\right]\mathsf{R} = 0 \quad , \tag{2.38}$$

which is a Bessel differential equation of order m. The general solution for such an equation is [80]:

$$\mathsf{R} = CJ_m(\tilde{r}) + DY_m(\tilde{r}) \quad , \tag{2.39}$$

where J_m and Y_m are Bessel functions of the first and second type, respectively. Y_m is divergent at $\tilde{r} = 0$ and thus, the coefficient D has to be zero to keep the pressure p' physical in the absence of sources at this position. Back transformation into the r-space and substitution in the harmonic approach gives:

$$p' = CJ_m(\alpha r)\exp(i\Omega t - ikx + im\theta) \qquad , \quad m \in \mathbb{Z} \tag{2.40}$$

where C is a constant defining the magnitude of the pressure amplitude, α, m and k are the radial, tangential and axial wave numbers, respectively, that describe the spatial dependency. To close the problem, radial and tangential boundary conditions are needed to determine these wave numbers. For cylindrical ducts, axial symmetry enforces periodicity in the tangential direction such that $e^{im\theta} = e^{im(\theta+2\pi)}$. Thus the tangential wave numbers can only take integer values $m \in \mathbb{Z}$. Furthermore, the radial and axial wave numbers are related to each other trough the dispersion relation Eq. (2.37).

Due to its quadratic dependency, the dispersion relation has two solutions, one for the positive root (α^+) and another for the negative one (α^-). The general solution of the linearized convective wave equation Eq. (2.34) is thus a superposition of four linearly independent terms. In the most general case, they represent helical waves with positive and negative sense of rotation ($\sim \exp(\pm im\theta)$) that travel the duct in up- and downstream direction ($\sim \exp(-ik_{mn}^{\pm}x)$) [104]. Depending on the magnitude of the amplitudes of the helical waves relative to each other, so-called *spinning* tangential modes are physically possible [33]. However, this thesis is restricted to the case where the helical waves have equal amplitudes, leading to standing tangential modes $\sim \cos(m\theta)$ with positive tangential wave number $m \in \mathbb{N}_0$.

Table 2.1: Roots η_{mn} of the derivative of the Bessel function satisfying $J'_m(\eta_{mn}) = 0$.

	n						
m	0	1	2	3	4	5	6
0	0	3.832	7.016	10.173	13.324	16.471	19.616
1	1.841	5.331	8.536	11.706	14.863	18.016	21.164

The radial boundary condition at the cylinder shell $r = R$ provides a relation to determine the radial wave numbers $\alpha^{\pm}$. For the hard-wall case, the radial velocity at the cylinder shell vanishes $v'(R) = 0$. Substitution in the radial component of the linearized momentum equation

$$\rho\left(i\frac{\Omega}{\bar{c}} + M\frac{\partial}{\partial x}\right)v' + \frac{1}{\bar{\rho}\bar{c}}\frac{\partial p'}{\partial r} = 0 \quad , \tag{2.41}$$

leads to:

$$\frac{d}{dr} J_m(\alpha r)\bigg|_{r=R} = 0 \quad . \tag{2.42}$$

For each tangential order m, the solutions of this transcendental equation are given by $\alpha_{mn} R = \pm \eta_{mn}$, where η_{mn} corresponds to the n'th root of the Bessel function derivative. Some roots of the Bessel function derivative are given in Tab. (2.1). They are purely real valued and frequency independent. Furthermore, the up- and downstream traveling waves have equal mode shape even in the presence of mean flow:

$$\alpha_{mn}^{+} = \alpha_{mn}^{-} = \frac{\eta_{mn}}{R} = const. \qquad \in \mathbb{R} \quad . \tag{2.43}$$

The radial and tangential wave numbers determine the transverse mode shape of the traveling waves $(f, g) \sim J_m(\alpha_{mn}^{+} r)\cos(m\theta)$. Figure 2.1 give some examples of them. In the same figure, a widely used notation by the acoustic community is also indicated. The radial n and tangential m order is used in combination with the abbreviations T and R, respectively.

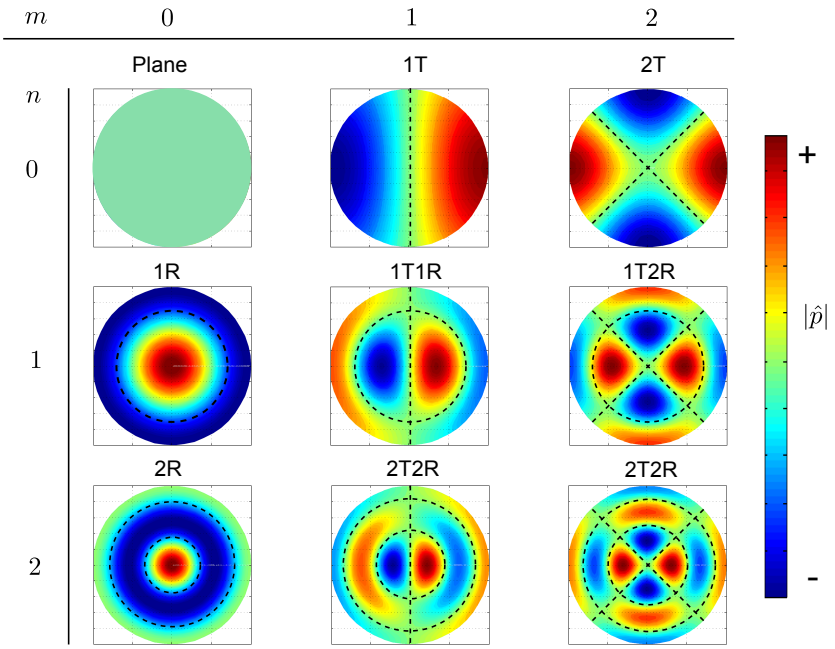

Figure 2.1: Transverse acoustic mode shapes for a hard walled cylinder. Dashed lines denote the location of the pressure nodal lines.

Substitution of the radial wave numbers in the dispersion relation Eq. (2.37) gives, after some rearrangement, a relation for the axial wave numbers:

$$k_{mn} = \frac{-M\Omega/c \pm \sqrt{(\Omega/c)^2 - (\eta_{mn}/R)^2(1-M^2)}}{1-M^2} \quad . \tag{2.44}$$

This frequency dependent and complex valued function $k_{mn} = \mathrm{Re}\{k_{mn}\} + i\ \mathrm{Im}\{k_{mn}\}$ has two branches corresponding to the positive $k_{mn}^{\oplus}$ and negative $k_{mn}^{\ominus}$ square root, respectively. The association of these branches to the corresponding up- and downstream traveling waves is not a trivial task. Figure 2.2 shows these branches in the complex plane for the first tangential order and real valued frequencies $\Omega = \omega$. For increasing

frequencies, the imaginary part of the branches decreases until it vanishes. At this frequency, both branches exhibit the same value and the curves display a singularity. This frequency is known as *cut-on* frequency and can be determined by the following relation:

$$\omega_{mn}^{\mathrm{c}} = \bar{c}\frac{\eta_{mn}}{R}\sqrt{1-M^2} \quad , \tag{2.45}$$

for each transfer mode shape.

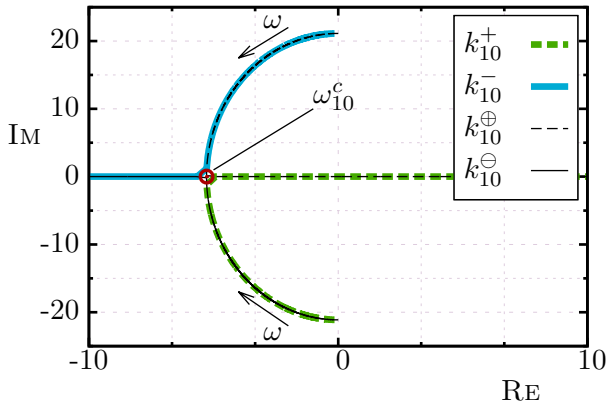

Figure 2.2: Two branches of solution of dispersion relation for the hard-wall case, dashed lines. Limiting case of soft-wall with complex-valued radial wave number.

Morfey [84] explains the physical meaning of this cut-on frequency through an analogy using plane waves. In this analogy, the propagation of each of the transverse modes in the duct's axial direction can be approximated by the propagation of plane waves traveling with certain inclination. The angle of inclination of the plane waves in the analogy is fixed by the radial and axial wave numbers of the true transverse wave. The plane waves get reflected at the boundaries of the duct such that in total, a net axial propagation occurs. Morfey has shown that this analogy is only possible for certain combinations of radial η_{mn} and axial k_{mn} wave numbers. This condition can be expressed in terms of the cut-on frequency as follows:

$$\omega \geq \omega_{mn}^{\mathrm{c}} \quad . \tag{2.46}$$

Provided that this condition holds, the angle of propagation leads to an optimal constructive interaction of the plane waves. In contrast, for frequencies below cut-on, the plane waves interfere destructively with each other. The longer the plane waves travel, the stronger the interference. Thus, in total, the amplitude of the waves decays in axial direction.

When transferred to the propagation of the true transverse modes, Eq. (2.46) is referred to as *cut-on condition*. It states that a transverse mode propagates with constant amplitude only at frequencies above cut-on. For frequencies below cut-on, the amplitude of the transverse mode decreases exponentially in axial direction and the mode is denoted as *cut-off* or *evanescent*.

The association of the different branches in Eq. (2.44) to the corresponding up- and downstream traveling waves can be achieved with the help of the cut-on condition. For

the chosen acoustic notation $e^{+i\omega t}$, for real valued frequencies, an alternation of the two branches is necessary to satisfy the cut-on condition:

$$k_{mn}^{+} = \begin{cases} k_{mn}^{\ominus} & \text{if } \omega < \omega^{\mathrm{c}} \ , \\ k_{mn}^{\oplus} & \text{if } \omega \geq \omega^{\mathrm{c}} \ . \end{cases} \qquad \text{and} \qquad k_{mn}^{-} = \begin{cases} k_{mn}^{\oplus} & \text{if } \omega < \omega^{\mathrm{c}} \ , \\ k_{mn}^{\ominus} & \text{if } \omega \geq \omega^{\mathrm{c}} \ . \end{cases} \tag{2.47}$$

Mathematically, this alternation can be expressed in a single formula as:

$$k_{mn}^{\pm} = \frac{-M\omega/\bar{c} \pm \operatorname{sign}(\omega - \omega_{mn}^{\mathrm{c}})\sqrt{(\omega/\bar{c})^2 - (\eta_{mn}/R)^2(1-M^2)}}{1-M^2} \ . \tag{2.48}$$

Note that the alternation is only necessary for hard walled ducts in the limiting case of real valued frequencies. For a detailed explanation and validation of this necessity please refer to App. A.2. Figure 2.2 shows the axial wave numbers associated to the corresponding up- and downstream direction of propagation using the previously introduced notation k_{mn}^{-} and k_{mn}^{+}, respectively.

After determination of all wave numbers, the general solution in cylindrical coordinates can finally be written as:

$$\frac{p'}{\bar{c}\bar{\rho}} = \sum_{m,n} \left[J_m(\alpha_{mn}^{+} r)\hat{F}_{mn} e^{-ik_{mn}^{+}x} + J_m(\alpha_{mn}^{-} r)\hat{G}_{mn} e^{-ik_{mn}^{-}x} \right] \cos(m\theta) e^{i\Omega t} = \sum_{m,n} (f_{mn} + g_{mn}) \ , \tag{2.49}$$

which can be interpreted as three dimensional waves or "modes" of tangential and radial order m and n traveling in the down- "f" and upstream "g" direction, respectively. The amplitudes $\hat{F}_{mn}$ and $\hat{G}_{mn}$ give information about the relative local sound pressure level.

Due to the linearity of the linearized momentum equation, the same holds for the velocity fluctuations. Introducing the abbreviations

$$\kappa_{mn}^{\pm} = \frac{k_{mn}^{\pm}}{\Omega/\bar{c} - Mk_{mn}^{\pm}} \ , \qquad \text{and} \qquad \beta_{mn}^{\pm} = \frac{1}{\Omega/\bar{c} - Mk_{mn}^{\pm}} \ , \tag{2.50}$$

these fluctuations can be written in terms of the characteristic amplitudes f_{mn} and g_{mn} as:

$$u' = \sum_{m,n} \left(\kappa_{mn}^{+} f_{mn} + \kappa_{mn}^{-} g_{mn} \right) \ , \tag{2.51}$$

$$v' = i \sum_{m,n} \left(\beta_{mn}^{+} \frac{\partial f_{mn}}{\partial r} + \beta_{mn}^{-} \frac{\partial g_{mn}}{\partial r} \right) \ , \tag{2.52}$$

$$w' = -\frac{m}{r} \sum_{m,n} \left(\beta_{mn}^{+} f_{mn} + \beta_{mn}^{-} g_{mn} \right) \ . \tag{2.53}$$

2.2.2 Plane Wave Approximation

For systems in which the frequency range of interest lies well below the cut-on frequency of the first transverse mode, a plane wave approximation is applicable. This is based

on the assumption that any transverse mode will rapidly decay in axial direction. The general solution given by Eqs. (2.49) and (2.51) to (2.53) simplifies considerably for plane waves ($m = n = 0$):

$$\frac{p'}{\bar{\rho}\bar{c}} = \left[\hat{F}e^{-ik^+x} + \hat{G}e^{-ik^-x}\right] e^{i\Omega t} \quad , \tag{2.54}$$

$$u' = \left[\hat{F}e^{-ik^+x} - \hat{G}e^{-ik^-x}\right] e^{i\Omega t} \quad , \tag{2.55}$$

$$v' = w' = 0 \quad , \tag{2.56}$$

where the solution is expressed solely as a superposition of one up- and one downstream traveling wave of amplitude $\hat{F}$ and $\hat{G}$, respectively. For simplicity, the mode order $_{00}$ is omitted in this representation. The axial wave numbers simplify to:

$$k^{\pm} = \frac{\pm\Omega/\bar{c}}{1 \pm M} \quad . \tag{2.57}$$

It is also useful to express the characteristics acoustic amplitudes in terms of the primitives variables:

$$f = \hat{F}e^{-ik^+x}e^{i\Omega t} = \frac{p'}{\bar{\rho}\bar{c}} + u' \quad , \tag{2.58}$$

$$g = \hat{G}e^{-ik^-x}e^{i\Omega t} = \frac{p'}{\bar{\rho}\bar{c}} - u' \quad . \tag{2.59}$$

For vanishing Mach number, the axial wave numbers simplify further into $k^+ = -k^- = k = \Omega/\bar{c}$ and the general solution can be written as:

$$\frac{p'}{\bar{\rho}\bar{c}} = \left[\hat{F}e^{-ikx} + \hat{G}e^{ikx}\right] e^{i\Omega t} \quad , \tag{2.60}$$

$$u' = \left[\hat{F}e^{-ikx} - \hat{G}e^{ikx}\right] e^{i\Omega t} \quad . \tag{2.61}$$

The relative magnitude of the amplitudes $\hat{F}$ and $\hat{G}$ to each other depends on the boundary conditions. General expressions suitable for the description of such boundary conditions are given in the next sections.

2.2.2.1 Acoustic Impedance

The *acoustic impedance* is defined on a surface as the Fourier transform of the ratio of acoustic pressure perturbation to acoustic velocity perturbation and is in general complex valued. Only the surface normal velocity component is considered for this ratio. Thus, for plane waves it can simply be expressed as:

$$Z(\Omega) = \frac{p'}{u'} = \Theta + i\ \Psi \quad . \tag{2.62}$$

The real part Θ is named *resistance*, while the imaginary part Ψ *reactance*. The specific impedance of a fluid is given by $\bar{\rho}\bar{c}$. This factor is commonly used as a reference to non-dimensionalize the acoustic impedance:

$$z = \frac{Z}{\bar{\rho}\bar{c}} = \theta + i\ \psi \quad . \tag{2.63}$$

As explained by Rienstra and Hirschberg [115], the acoustic impedance can be used to describe the coupling between two adjacent regions in an acoustic system. Any kind of boundary condition can be expressed as an effective impedance. Furthermore, the acoustic impedance allows to use well established electric network rules to calculate the equivalent impedance of a system [88].

2.2.2.2 Reflection Coefficient

A more descriptive quantity considering the influence of a boundary on traveling waves is the *reflection coefficient*. It is defined as the ratio of reflected to incident wave amplitude:

$$r = \frac{\hat{G}}{\hat{F}} = \frac{p'/(\bar{\rho}\bar{c}) - u'}{p'/(\bar{\rho}\bar{c}) + u'} = \frac{z-1}{z+1} \quad . \tag{2.64}$$

Alternatively, the specific impedance can be given in terms of the reflection coefficient by:

$$z = \frac{1+r}{1-r} \quad . \tag{2.65}$$

Table 2.2 gives an overview of idealized boundary conditions with their corresponding impedance and reflection factors.

Table 2.2: Relation between specific impedance and reflection coefficient for ideal boundary conditions.

	closed end $u'=0$	open end $p'=0$	non-reflective	partially reflective	reactive	general
z	∞	0	1	θ	ψi	$\theta + i\ \psi$
r	1	-1	0	$\frac{\theta-1}{\theta+1}$	$\frac{1-\psi^2}{1+\psi^2} - i\frac{2\psi}{1+\psi^2}$	$\frac{(\theta^2+1+\psi^2)+2\psi\ i}{(\theta+1)^2+\psi^2}$

2.2.2.3 Standing Acoustic Waves

Depending on the boundary conditions, traveling waves can form standing waves. This is the case for the majority of self sustained oscillations, as encountered in rocket chambers. This thesis focuses on this kind of acoustic waves.

As an example, consider the acoustic field in a channel of length L and uniform flow with two acoustically closed ends, i.e. $u'(x=0) = u'(x=L) = 0$. Substitution in the general solution, Eqs. (2.54) and (2.55) delivers the conditions $\hat{F} = \hat{G}$ and $\hat{F}(e^{-ik^+L} - e^{-ik^-L}) = 0$. For finite amplitudes, the relation $e^{-ik^+L} - e^{-ik^-L} = 0$ has to be fulfilled. With some mathematical manipulation, this relation can be recast into:

$$e^{-i(k^+-k^-)L} - 1 = e^{\frac{2\Omega/\bar{c}L}{1-M^2}i} - 1 = 0 \quad . \tag{2.66}$$

The roots of Eq. (2.66) correspond to the eigenfrequencies of the acoustic system and are given by the following expression:

$$\omega_l = l\pi\frac{\bar{c}(1-M^2)}{L} \quad , \qquad l = 1, 2, 3, ... \quad . \tag{2.67}$$

For this simplified system, they are all real valued, $\omega_l \in \mathbb{R}$. The interpretation of a complex valued eigenfrequency will be given in Sec. 2.2.4.

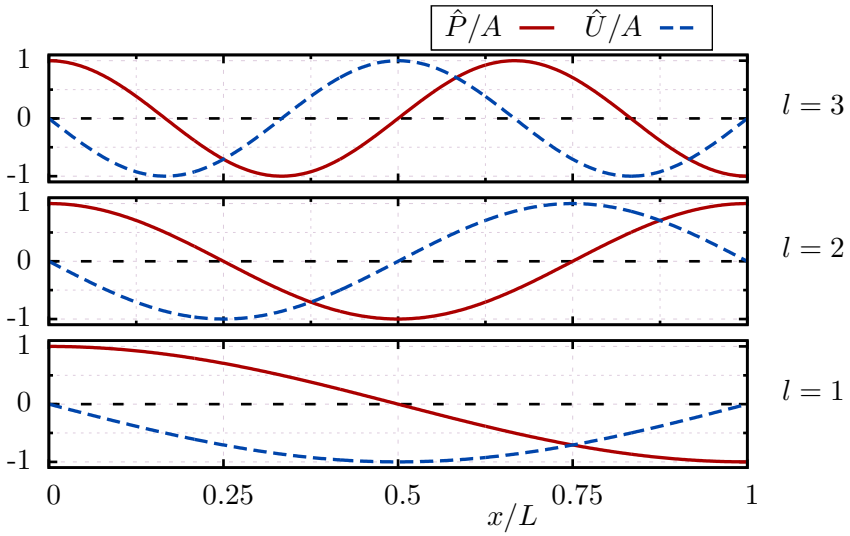

Figure 2.3: Normalized pressure and velocity amplitudes in a channel with two open ends for various mode shapes. Bottom, $l = 1$; middle, $l = 2$; top, $l = 3$.

The same acoustic field can be achieved by forcing the system at both ends with traveling waves of same amplitude $\hat{F} = \hat{G} = A/2$ at one of the eigenfrequencies ω_l. Substitution in Eqs. (2.54) and (2.55) gives, after some mathematical simplification, the resonant acoustic field in the following form:

$$\frac{p'}{\bar{\rho}\bar{c}} = A\cos\left(l\pi x/L\right) e^{i\phi_p(x)} e^{i\omega_l t} = \hat{P}_l(x) e^{i\phi_p(x)} e^{i\omega_l t} \quad , \tag{2.68}$$

$$u' = -A\sin\left(l\pi x/L\right) e^{i\phi_u(x)} e^{i(\omega_l t - \pi/2)} = \hat{U}_l(x) e^{i\phi_u(x)} e^{i(\omega_l t - \pi/2)} \quad , \tag{2.69}$$

with axial phase dependencies $\phi_p = \phi_u = -l\pi Mx/L$. This axial phase lag occurs only when mean flow is present and is usually neglected for small Mach numbers. In contrast, a constant temporal phase lag of $-\pi/2$ is always present for the velocity. Figure 2.3 shows schematically the normalized amplitudes $\hat{P}_l(x)/A$ and $\hat{U}_l(x)/A$ of the velocity and pressure standing waves along the channel for the three first longitudinal modes. They have all harmonic dependency along the channel axis, but a phase shift between pressure and velocity fluctuations. This means that pressure and velocity *nodes*, e.g. locations at which either pressure or velocity fluctuations vanish, alternate in intervals of $L/(2l)$.

2.2.3 Networks of Low Oder Acoustic Elements

For relatively simple geometries, the acoustic field can be determined analytically and the solution decomposed into linear acoustic modes. If the wave numbers $k^{\pm}_{mn}$ and $\alpha^{\pm}_{mn}$ are known, the characteristic amplitudes $\hat{F}_{mn}$ and $\hat{G}_{mn}$ are sufficient to reconstruct the acoustic field. It is thus feasible to divide a complex acoustic system into more simpler, mathematically solvable sections and link only the characteristic amplitudes at the connecting planes. Such a network of low order, quasi one-dimensional discrete

elements allows to study acoustic systems in a very flexible and descriptive manner [88, 103, 104]. Each element in the network is mathematically described by expressions linking the characteristic amplitudes of the downstream and upstream traveling waves at the connecting planes, in the following referred to as *ports*. This method has been extensively applied to estimate the response of acoustic systems especially at frequencies below the cut-on, where only plane-waves propagate [7, 59, 66, 67, 90]. In this case, the connecting ports in the network have only two *pins*, one for the plane f_{00} and one for the plane g_{00} wave. Networks treating higher order modes are also possible [33, 107, 120], but their application is not common. Especially the handling of the connecting planes becomes in this case challenging, where additional assumptions are necessary. This section gives only an introduction to conventional plane wave acoustic networks. Because of this, the mode indices $_{mn}$ are omitted in the rest of this section to improve readability. The necessary extensions and considerations for network above cut-on will be given in Sec. 4.3.

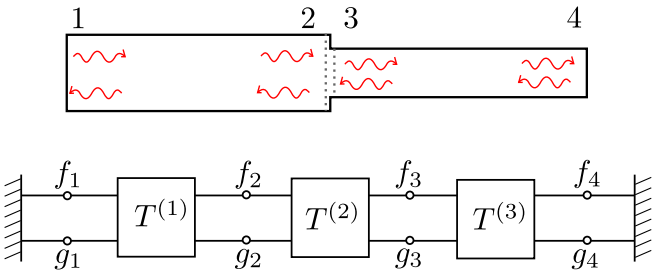

Figure 2.4: Acoustic system consisting of three elements bounded by proper terminations.

Figure 2.4 schematically shows the network representation of a simple acoustic system with connecting ports of each two pins for the plane up- and downstream traveling waves. This example consists of two ducts of different cross-sectional areas connected with each other and bounded by two acoustically hard boundaries. Three basic types of elements can be observed in this network:

(i) one port boundary conditions,
(ii) two-port *continuous* or homogeneous elements (duct segments),
(iii) and two-port *compact* or discontinuity elements (area change).

Additional element types exist, like three-port junctions or even multi-port elements, see [59].

The boundary elements simply relate the amplitudes of the up- and downstream waves to each other, i.e. via a reflection coefficient r:

$$\hat{F}_1 = r_l \hat{G}_1 \qquad \text{or} \qquad \hat{G}_2 = r_r \hat{F}_2 \quad , \tag{2.70}$$

where the indices $_l$ and $_r$ denote the left left and right side of the network, respectively. The typical reflection coefficients given in Tab. 2.2 can be employed.

For the continuous duct segments, two relations based on Eqs. (2.58) and (2.59) can be used:

$$\hat{F}_2 = e^{-ik^+ l_{12}}\ \hat{F}_1 \quad , \qquad \hat{G}_1 = e^{-ik^- l_{12}}\ \hat{G}_2 \quad , \tag{2.71}$$

and

$$\hat{F}_4 = e^{-ik^+ l_{34}}\ \hat{F}_3 \quad , \qquad \hat{G}_3 = e^{-ik^- l_{34}}\ \hat{G}_4 \quad . \tag{2.72}$$

Finally, the compact element relates the amplitudes of the up- and downstream traveling waves across the sudden area change. Actually, any discontinuity in an acoustic system like area changes, jumps in fluid properties induced for example by flames, sudden changes in shell boundary conditions and so on, can be modeled in the network as compact elements. The derivation of the relations for compact elements strongly depends on the type of discontinuity. Often, the relations are derived based on conservation equations in the limiting case of a domain of zero thickness enclosing the discontinuity plane. In a pure plane wave approximation, some simplified formulations exist, that can be expressed in form of transmission and reflection coefficients. However, it is important to remark that in the general case, such a discontinuity can also induce scattering into higher order modes, even for frequencies below cut-on. This behavior in usually referred to as *mode coupling* and plays an important role in the derivation of low order acoustic elements for resonator rings. The derivation and the necessary considerations for the discontinuity types treated in this study will be given in detail in Sec. 4.3.2.

The basic example shown in Fig. 2.4 should serve only as a reference to explain the formalism of acoustic low order networks. Of course, the number of possible elements is large, see for example [59, 88]. The relations for the elements used in this thesis are given in Sec. 4.5.1.

In a pure plane wave simplification, the two relations between the characteristic amplitudes of the acoustic waves at the connecting ports left and right from an element (continuous or compact) can be arranged in matrix form as:

$$\begin{pmatrix} \hat{F}_r \\ \hat{G}_r \end{pmatrix} = \begin{bmatrix} T_{11} & T_{12} \\ T_{21} & T_{22} \end{bmatrix} \begin{pmatrix} \hat{F}_l \\ \hat{G}_l \end{pmatrix} \quad . \tag{2.73}$$

One advantage of this so-called transfer matrix notation is that the relation between non-adjacent ports can be simply determined by matrix multiplication. E.g., a transfer matrix between ports 1 and 3 can be expressed as matrix multiplication using the transfer matrices between the adjacent ports: $\mathbf{T}^{(3)} = \mathbf{T}^{(1)}\mathbf{T}^{(2)}$.

Physically, the scattering matrix notation offers a more descriptive representation of the elements that preserves causality. In this case, the relations are arranged such that the resulting matrix relates the amplitudes of the outgoing to the incoming waves:

$$\begin{pmatrix} \hat{F}_r \\ \hat{G}_l \end{pmatrix} = \begin{bmatrix} S_{11} & S_{12} \\ S_{21} & S_{22} \end{bmatrix} \begin{pmatrix} \hat{F}_l \\ \hat{G}_r \end{pmatrix} \quad . \tag{2.74}$$

The diagonal entries of the scattering matrix represent transmission and the off-diagonal entries reflection coefficients for the up- and downstream traveling waves.

Combined with proper boundary conditions at the terminations the whole network can be described by a system of linear equations:

$$\mathbf{A}\vec{x} = \vec{b} \quad , \tag{2.75}$$

with system matrix $\mathbf{A}$, state vector $\vec{x}$ containing the characteristic amplitudes of all pins at the connecting ports and, depending on the boundary conditions or the presence of sources within the system, excitation vector $\vec{b}$.

The state vector can be easily built from the local port vectors, e.g. $\vec{x} = [\hat{F}_1, \hat{G}_1, \hat{F}_2, \hat{G}_2, \hat{F}_3, \hat{G}_3, \hat{F}_4, \hat{G}_4]^T$ for the network sketched in Fig. 2.4. Several methodologies have been proposed concerning the building of the system matrix $\mathbf{A}$ from the single element transfer matrices [59, 88]. In this thesis, a software package developed at the chair of Thermodynamics called *taX* [72] is used. It owns a database with several well established elements, a graphical user interface for the building of the system matrix using blocks and connectors, and a numerical eigenvalue solver among other functions. Without going into the details of the used automation algorithm, the system matrix and state vector of the system shown in Fig. 2.4 can be given as:

$$\begin{bmatrix} 1 & -r_l & 0 & 0 & 0 & 0 & 0 & 0 \\ T_{11}^{(1)} & 0 & -1 & 0 & 0 & 0 & 0 & 0 \\ 0 & T_{22}^{(1)} & 0 & -1 & 0 & 0 & 0 & 0 \\ 0 & 0 & T_{11}^{(2)} & T_{12}^{(2)} & -1 & 0 & 0 & 0 \\ 0 & 0 & T_{21}^{(2)} & T_{22}^{(2)} & 0 & -1 & 0 & 0 \\ 0 & 0 & 0 & 0 & T_{11}^{(3)} & 0 & -1 & 0 \\ 0 & 0 & 0 & 0 & 0 & T_{22}^{(3)} & 0 & -1 \\ 0 & 0 & 0 & 0 & 0 & 0 & r_r & -1 \end{bmatrix} \begin{pmatrix} \hat{F}_1 \\ \hat{G}_1 \\ \hat{F}_2 \\ \hat{G}_2 \\ \hat{F}_3 \\ \hat{G}_3 \\ \hat{F}_4 \\ \hat{G}_4 \end{pmatrix} = \begin{pmatrix} b_l \\ 0 \\ 0 \\ 0 \\ 0 \\ 0 \\ 0 \\ b_r \end{pmatrix} . \tag{2.76}$$

2.2.4 Linear Stability Analysis

This thesis studies the stability of systems against self sustained oscillations without external excitation. The excitation vector $\vec{b}$ is thus zero and the homogeneous system is described entirely by the matrix $\mathbf{A}(\Omega)$, which is of course a function of frequency. The determinant of this matrix provides a characteristic equation for the frequency:

$$\det\{\mathbf{A}(\Omega)\} = 0 \quad . \tag{2.77}$$

The roots of this equation correspond to the eigenfrequencies Ω_{eig} of the acoustic system. For each of the eigenfrequencies Ω_{eig}, the corresponding system matrices are denoted by $\mathbf{A}_{eig} = \mathbf{A}(\Omega_{eig})$. Evaluated at these eigenfrequencies, the homogeneous system of equations $\mathbf{A}_{eig}\vec{x} = \vec{0}$ is also satisfied by state vectors others than the trivial solution $\vec{x} = \vec{0}$. These non trivial solutions of the homogeneous system can be determined from the eigenvalue problem:

$$\mathbf{A}_{eig}\vec{x}_{\lambda_n} = \lambda_n \vec{x}_{\lambda_n} \quad , \tag{2.78}$$

where λ_n stands for the eigenvalues of the matrix $\mathbf{A}_{eig}$. The eigenvector $\vec{x}_{\lambda_n=0}$ assigned to the eigenvalue $\lambda_n = 0$ corresponds to the non trivial solution $\mathbf{A}_{eig}\vec{x}_{\lambda_n=0} = \vec{0}$. This state vector gives the relative amplitudes to each other at the network ports and is usually referred to as *mode shape* or *eigenmode* of the system. Thus, there is a mode shape assigned to each of the eigenfrequencies of the acoustic system.

Note that the index $_{eig}$ denotes all eigenfrequencies of the system. As will be explained in Sec. 4.3.3, higher order acoustic modes can also be determined from quasi one-dimensional low order networks. Depending on the shape of the corresponding eigenmodes, the previously introduced index notation $_{mnl}$, that distinguishes between

tangential, radial and longitudinal order, respectively, can be also employed. In this thesis, the latter notation will be used, when a specific eigenfrequency of a given geometrical problem is meant. Instead, the former notation is used when all eigenfrequencies of a general undefined problem are meant.

With the time dependency convention $\sim e^{i\Omega t} = e^{i\omega t}e^{-\vartheta t}$, the imaginary part ϑ_{eig} of the eigenfrequencies Ω_{eig} decides whether the system is stable or not. An eigenmode is linearly stable if $\vartheta_{eig} > 0$, metastable if $\vartheta_{eig} = 0$ and unstable otherwise. A more convenient quantity for the stability behavior is the *cycle increment* [66]

$$\Gamma_{eig} = e^{-2\pi\frac{\vartheta_{eig}}{\omega_{eig}}} - 1 \quad , \tag{2.79}$$

that represents the percentage by which the amplitude of a perturbation grows or decays during one cycle.

2.2.5 Generalized Nyquist Criterion

The stability of an acoustic system can be determined by finding the roots of the determinant, e.g. characteristic equation, of the homogeneous system (2.75). In some cases, especially when the transfer matrix of an element is not given in closed form, as it will the case in this study for the resonator ring element, graphical methods derived from control theory are more convenient to estimate the eigenfrequencies and stability of the system. The generalized Nyquist criterion proposed by Polifke et al. [106] that establishes an analogy of thermoacoustic network models to control systems is applied in this study. First, an introductory description of this method is given for systems considering only plane waves [66, 67]. Considerations for higher mode orders and mode coupling will be given at the end of this section.

By inserting a *diagnostic dummy* element, sketched in Fig. (2.5), into the network, a closed system is cut to enable an equivalent open loop transfer function. One of the channels is "short-cut" $g_u = g_d$. The second channel is cut and one of the variables, f_u in this case, is left unspecified, while f_d is set to a constant amplitude value of unity. The *open loop transfer* function is defined at the position of the cut as

$$OLTF(\Omega) = -\frac{f_u}{f_d} \quad , \tag{2.80}$$

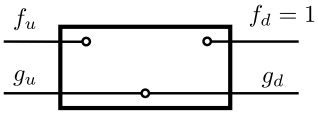

Figure 2.5: Two port "diagnostic dummy" element, adapted from [66].

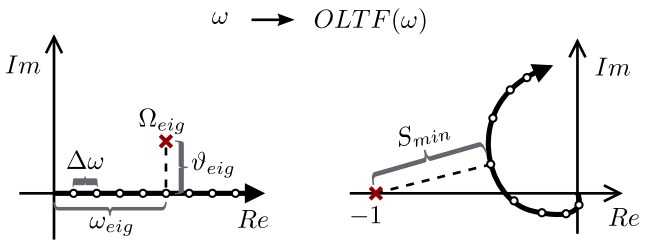

Figure 2.6: Conformal mapping of ω into $OLTF(\omega)$.

which may be interpreted as the response of the system to a constant amplitude forcing. Thus, the system is changed into an inhomogeneous one:

$$\mathbf{A}_{\mathrm{Nyq}}\vec{x}_{\mathrm{Nyq}} = \vec{b}_{\mathrm{Nyq}} = [0, \ldots, 1, \ldots, 0]^T \quad . \tag{2.81}$$

Hereby, the index $_{\mathrm{Nyq}}$ refers to the extended acoustic network with the Nyquist dummy. The solution of the now inhomogeneous forced system will coincide with the unperturbed homogeneous one only at the eigenfrequencies Ω_{eig}, where $f_u/f_d = 1$. Thus the $OLTF$ can be interpreted as a conformal mapping $\Omega \rightarrow OLTF(\Omega)$ that maps all the eigenfrequencies of the unforced system Ω_{eig} to the critical point $-1 + 0i$ in the image space.

Applying the generalized Nyquist criterion and keeping in mind that some elements are eventually only available for real frequencies, the $OLTF$ is evaluated for real valued frequencies only. The Nyquist curve represents thus the mapping of the positive real axis into the image plane, see Fig. (2.6). The $OLTF(\omega)$ curve will orbit the origin without necessary crossing the critical point. Following the curve towards higher frequencies, its position with respect to the critical point $-1 + 0i$ determines stability. For stable eigenmodes with $\vartheta_{eig} > 0$ the critical point will be on the left side of the curve, as sketched in Fig. (2.6).

As shown in [118], exploiting the properties of conformal mappings that locally preserve orientation or handedness, the frequencies at which the $OLTF$ curve passes the critical point with minimal distance identify the real part of the eigenfrequencies. At these locations denoted by $OLTF(\omega_\perp)$, the connecting line to the critical point will be perpendicular to the $OLTF$ curve. The imaginary part of the eigenfrequencies can be estimated from the minimal distance using a proper scaling factor. The factor by which the critical distance $S_{\min}$ in the image plane has to be scaled $\vartheta_{eig} = S_{\min}/\sigma$ can be determined from geometrical considerations as:

$$\sigma = \lim_{\Delta\omega \to 0} \left| \frac{OLTF(\omega_\perp + \Delta\omega) - OLTF(\omega_\perp - \Delta\omega)}{\Delta\omega} \right| \quad . \tag{2.82}$$

For a discrete $OLTF$, Sattelmayer and Polifke [118] proposed a polynomial fit of the $OLTF$ curve to increase the accuracy when only low frequency resolution is feasible. As shown by Kopitz et al. [66], for small frequency increments, the linear approximation of the scaling factor provides adequate accuracy. The imaginary part of the eigenfrequencies can then be estimated as:

$$\Omega_n \approx \omega_\perp + sign(RHR)i \, \frac{2|S_{min}|\Delta\omega}{|OLTF(\omega_\perp + \Delta\omega) - OLTF(\omega_\perp - \Delta\omega)|} \quad , \tag{2.83}$$

where the sign of the imaginary part is determined through the right-hand rule (RHR). With the eigenfrequencies estimated in this way, the cycle increment can be deduced from the Nyquist plot using Eq. (2.79). The method is well tested and validated for systems of frequency range below the first cut-on frequency incorporating only plane waves. Advantages and disadvantages are also mentioned in the literature [59, 66].

2.3 Low Mach Number Approximations

To overcome the compressibility issues discussed in Sec. 2.1.3, a series of simplifications can be applied to the fully compressible governing equations. The derivation is based on the dimensional analysis presented by Panton [97] and assuming ideal gas behavior.

2.3.1 Dimensional Analysis

To estimate the order of magnitude of the different terms present in the fully compressible NS-equations, a proper non-dimensionalization is necessary. Most of the variables can be non-dimensionalized in a straightforward manner by the boundary conditions of the problem:

$$x_i^* = \frac{x_i}{L} \quad , \quad t^* = \frac{t u_o}{L} \quad , \quad u_i^* = \frac{u_i}{u_o} \quad , \quad \rho^* = \frac{\rho}{\rho_o} \quad , \quad \lambda^* = \frac{\lambda}{\lambda_o} \quad ,$$
$$p^* = \frac{p}{\rho_o u_o^2} \quad , \quad T^* = \frac{T - T_C}{T_H - T_C} \quad , \tag{2.84}$$

where L is the characteristic length of the geometry, the temperature field is bounded by the limits T_H and T_C, and the index $_o$ denotes a reference state at the cold temperature, respectively. Substitution in the ideal gas law in differential form (Eq. (2.12)) gives after some thermodynamic development:

$$\frac{D\rho^*}{Dt^*} = \gamma M^2 \frac{Dp^*}{Dt^*} - \frac{\Delta T}{T_C} \left[\frac{\rho^*}{T^* \frac{\Delta T}{T_C} + 1} \right] \frac{DT^*}{Dt^*} \quad , \tag{2.85}$$

where $\Delta T = T_H - T_C$ stands for the maximum temperature difference. Put in this form, the ideal gas law states that the total change in density depends on two parameters: γM^2 and the relative temperature difference $\Delta T / T_c$. Similarly, substitution in the fully compressible NS-equations gives:

$$\frac{1}{\rho^*} \frac{D\rho^*}{Dt^*} = -\frac{\partial u_i^*}{\partial x_i^*} \quad , \tag{2.86}$$

$$\rho^* \frac{Du_i^*}{Dt^*} = -\frac{\partial p^*}{\partial x_i^*} + \frac{1}{\mathrm{Re}} \frac{\partial}{\partial x_i^*} \left[\mu^* \left(\frac{\partial u_i^*}{\partial x_j} + \frac{\partial u_j^*}{\partial x_i} - \frac{2}{3} \frac{\partial u_j^*}{\partial x_j} \right) \right] \quad , \tag{2.87}$$

$$\rho^* \frac{DT^*}{Dt^*} = \frac{1}{\mathrm{Re}\,\mathrm{Pr}} \frac{\partial}{\partial x_i^*} \left(\lambda^* \frac{\partial T^*}{\partial x_i^*} \right) + M^2 (\gamma - 1) \frac{T_c}{\Delta T} \left[\frac{Dp^*}{Dt^*} + \phi^* \right] \quad . \tag{2.88}$$

2.3.1.1 Weakly Compressible Flows

For low Mach flows $\gamma M^2 \to 0$ and neglecting dissipation $\phi^*_{diss} \ll 1$, the set of equations can be simplified into the so-called weakly compressible form:

$$\frac{D\rho^*}{Dt^*} = -\frac{\Delta T}{T_C}\left[\frac{\rho^*}{T^*\frac{\Delta T}{T_C}+1}\right]\frac{DT^*}{Dt^*} \quad , \tag{2.89}$$

$$\frac{1}{\rho^*}\frac{D\rho^*}{Dt^*} = -\frac{\partial u_i^*}{\partial x_i^*} \quad , \tag{2.90}$$

$$\rho^*\frac{Du_i^*}{Dt^*} = -\frac{\partial p^*}{\partial x_i^*} + \frac{1}{\mathrm{Re}}\frac{\partial}{\partial x_i^*}\left[\mu^*\left(\frac{\partial u_i^*}{\partial x_j} + \frac{\partial u_j^*}{\partial x_i} - \frac{2}{3}\frac{\partial u_j^*}{\partial x_j}\right)\right] \quad , \tag{2.91}$$

$$\rho^*\frac{DT^*}{Dt^*} = \frac{1}{\mathrm{Re}\,\mathrm{Pr}}\frac{\partial}{\partial x_i^*}\left(\lambda^*\frac{\partial T^*}{\partial x_i^*}\right) \quad . \tag{2.92}$$

From the ideal gas law, the density is solely a function of temperature uncoupled from the pressure perturbations. The same holds for the transport coefficients μ and λ. A more rigorous approach expanding the primitive variables as a power series in $\epsilon = \gamma M^2$ can also be applied [92]. The resulting first order approximation with constant reference atmospheric pressure is equivalent to the approach presented above.

2.3.1.2 Fully Incompressible Flows

In the double limiting case of low Mach number $\gamma M^2 \to 0$ and negligible temperature differences $\Delta T/T_C \to 0$, the Navier-Stokes equations simplify into their fully incompressible form. From the differential ideal gas law, the total change of density vanishes. Furthermore, it can be easily shown that the transport properties become constant:

$$\mu = \mu_o \quad , \quad \lambda = \lambda_o \quad . \tag{2.93}$$

The non-dimensionalized equations of motion simplify to:

$$\frac{\partial u_i^*}{\partial x_i^*} = 0 \quad , \tag{2.94}$$

$$\frac{Du_i^*}{Dt^*} = -\frac{\partial p^*}{\partial x_i^*} + \frac{1}{\mathrm{Re}}\frac{\partial^2 u_i^*}{\partial x_j^{*2}} \quad , \tag{2.95}$$

$$\frac{DT^*}{Dt^*} = \frac{1}{\mathrm{Re}\,\mathrm{Pr}}\frac{\partial^2 T^*}{\partial x_i^{*2}} \quad . \tag{2.96}$$

Again, the viscous dissipation is neglected. In this case, the momentum equation uncouples from the energy equation. The momentum transfer is solely characterized by the Reynolds number and the energy equation takes the form of a transport equation for a passive scalar.

Even in the fully incompressible case, an analytical solution of the Navier-Stokes equations is only possible for strongly simplified configurations. Especially the non-linear term on the momentum equation impedes the solution of the system.

2.3.2 Simplified Characterization of Turbulence

Based on the non-dimensional representation of the governing equations, the magnitude of the individual terms can be estimated. Concerning the momentum equation, the most important parameter is the well known non-dimensional Reynolds number:

$$\mathrm{Re} = \frac{u_o L}{\nu} \sim \frac{\rho u_o^2 / L}{\mu u_o / L^2} \quad . \tag{2.97}$$

It can be interpreted as the ratio of inertial ($\sim \rho u_o^2/L$) to viscous forces ($\sim \mu u_o/L^2$) in the flow. For low Reynolds numbers, a perturbation will decay fast because the fluid particles can be stabilized by the viscous forces. The fluid particles follow well defined stream lines in this so-called *laminar* regime. For large Reynolds numbers, the inertia of the fluid is too high to be stabilized by the small viscous forces. The flow field becomes *turbulent* displaying transient, three-dimensional and chaotic velocity perturbations.

A useful manner to characterize turbulence is via the Reynolds decomposition. All primitive variables in the flow are split into a mean and a turbulent fluctuating quantity:

$$f = \overline{f} + f` \quad , \tag{2.98}$$

where the mean component $\overline{f}$ corresponds to a time average over a sufficiently large period of time. By definition, the time average of the chaotic fluctuations vanishes $\overline{f`} = 0$.

The spectrum of turbulent scales present in a turbulent flow is large. The size of the largest structures is constrained by the domain geometry. Furthermore, these large eddies behave anisotropic being affected by the boundary conditions of the flow. Within the concept of energy cascade presented by Richardson and demonstrated by Kolmogorov [108], the large eddies are unstable and transfer their kinetic energy by inviscid processes to smaller and smaller eddies when breaking up. This energy transfer ends when the turbulent motions are small enough, such that the viscous forces can stabilize the eddies. This size of eddies is denoted by the *Kolmogorov length scale* η_k. The kinetic energy is dissipated trough viscous effects and converted to heat. In contrast to the larger scales, the small eddies can be statistically treated as isotropic.

The turbulent kinetic energy associated to each eddy size r can be also described in spectral space. The well known Kolmogorov decay law is derived from the assumption that the rate of production and dissipation of turbulent kinetic energy are in balance [108]:

$$E(k_{\mathrm{turb}}) \sim k_{\mathrm{turb}}^{-5/3} \epsilon_{\mathrm{turb}}^{2/3} \quad , \tag{2.99}$$

where $k_{\mathrm{turb}} = \pi / r$ is the wave number and ϵ_{turb} the dissipation rate.

2.3.3 Turbulent Boundary Layer: Law of the Wall

For fully developed turbulent flows, the region close to a wall or turbulent boundary layer exhibits a universal behavior. Using the Reynolds decomposition, the wall normal momentum transfer is characterized by the shear stresses:

$$\frac{\bar{\tau}_{xy}}{\rho} = \nu \frac{\partial \bar{u}}{\partial y} - \overline{u` v`} \quad . \tag{2.100}$$

At the location of the wall, the wall normal velocity fluctuations vanish and the wall shear stresses or *skin friction* $\bar{\tau}_{xy}(0) = \tau_w$ is simply given by the gradient of the mean velocity component. Based on this quantity, a so-called *friction velocity*

$$u_\tau = \sqrt{\frac{\tau_w}{\rho}} \tag{2.101}$$

is defined. Together with the dynamic viscosity, non-dimensional wall units can be introduced:

$$u^+ = \frac{u}{u_\tau} \qquad \text{and} \qquad y^+ = y\frac{u_\tau}{\nu} \quad . \tag{2.102}$$

The Prandtl mixing-length theory provides an estimation for the shear stress distribution $\overline{u'v'}$ at various wall normal locations given in non-dimensional wall units as [62]:

$$1 = \frac{d\bar{u}^+}{dy^+} + \kappa_\mathrm{v}^2 y^{+2} \left(\frac{d\bar{u}^+}{dy^+}\right)^2 \quad , \tag{2.103}$$

with the v. Karman constant κ_v. Building the limit of this equation for regions close $y^+ \to 0$ and far away from the wall $y^+ \to 0$ allows an asymptotic solution denoted as law of the wall:

$$u^+ = \begin{cases} y^+ & \text{in the viscous sublayer} \quad y^+ \lesssim 5, \\ \\ \frac{1}{\kappa_\mathrm{v}} \ln(y^+) + C & \text{in the logarithmic region } y^+ \gtrsim 60. \end{cases} \tag{2.104}$$

For fully turbulent flows, this law of the wall reflects the universal behavior of the flow. The transition between the two regions occurs smoothly within the region $5 \gtrsim y^+ \lesssim 60$. The constants $\kappa_\mathrm{v} \approx 0.4$ and $C \approx 5.5$ [62] are determined experimentally.

A similar analysis is also possible for the fully developed turbulent thermal boundary layer. In an analogy to the friction velocity, a so-called friction temperature T_τ derived from the wall heat flux $\dot{q}_w$ is used to characterize the heat transfer problem:

$$T_\tau = \frac{\dot{q}_w}{\rho c_p u_\tau} = \frac{\nu}{\mathrm{Pr}\, u_\tau} \left.\frac{\partial T}{\partial y}\right|_{y=0} \quad . \tag{2.105}$$

Within the thermal boundary layer, this quantity is also used to non-dimensionalize the temperature:

$$T^+ = \frac{T - T_w}{T_\tau} \quad , \tag{2.106}$$

where the wall surface temperature is denoted by T_w. Expressed in non-dimensional form, the temperature profile can also be divided into a diffusion layer close to the wall and a logarithmic bulk region. Based on the Reynolds analogy, the temperature profile can be expressed as:

$$T^+ = \begin{cases} \mathrm{Pr}\, y^+ & \text{in the diffusion sublayer } y^+ \lesssim 5, \\ \\ \frac{1}{\alpha} \ln(y^+) + \beta(\mathrm{Pr}) & \text{in the logarithmic region } y^+ \gtrsim 40. \end{cases} \tag{2.107}$$

where the coefficients α and β are functions of the Prandtl number. Kays and Crowford [62] give the following expression for the logarithmic thermal layer:

$$T^+ = \frac{\mathrm{Pr}_t}{\kappa_\mathrm{v}} \ln(y^+) + 13.2\,\mathrm{Pr} - \frac{\mathrm{Pr}_t}{\kappa_\mathrm{v}} \ln(13.2) \quad , \tag{2.108}$$

where the turbulent Prandtl number can be approximately taken as constant $\mathrm{Pr}_t \approx 0.9$. Kader [58] proposed a closed form expression that matches both asymptotic solutions of the thermal law of the wall.

2.4 Computational Fluid Dynamics

The increasing growth of computational resources makes the numerical treatment of fluid dynamic problems a promising strategy. While several discretization approaches exist for the numerical solution of differential equations, within Computational Fluid Dynamics (CFD) the finite volume discretization dominates [34].

2.4.1 Simulation Approaches

Despite the tremendous advances concerning computational power, the simulation of turbulent flows is still challenging. Over the years, three main simulation approaches for the treatment of turbulent flows have emerged, that differ from each other in the level of resolution of the flow structures.

The *Direct Numerical Simulation* approach (DNS) resolves the whole turbulence spectrum by solving the full Navier-Stokes equations. This brings considerable requirements on the grid and time step to be used. Furthermore, accurate numerical schemes are necessary. Consequently, this approach is restricted to academic cases of small Reynolds numbers and simple geometries. The advantage of this approach is that no turbulence models are needed, providing a high level of validity.

The opposite level of resolution is achieved by the *Reynolds Averaged Navier-Stokes* (RANS) approach. It uses the Reynolds decomposition and solves the equations only for the time averaged quantities. Due to the non-linearities in the set of equations, additional terms have to be modeled to account for the contributions of the turbulent fluctuations. Coarser grids designed to resolve only the global fluid motions in the geometry afford the simulation of engineering problems.

The *Large Eddy Simulation* approach (LES) lies between the two just mentioned approaches concerning the resolution of the flow motions. The approach is intended to resolve the large energy containing turbulent scales, which are difficult to model, since they depend on the specific domain. Models to account for the influence of unresolved small turbulent scales have a universal validity assuming isotropy. As will be explained in Ch. 6, the LES approach has proven to be very suitable for the numerical simulation of turbulent pulsating flows.

2.4.2 Large Eddy Simulation Approach

In the context of the LES approach, only the large scales of the flow have to be resolved by the grid. The grid acts as a low pass filter for the primitive variables. This spatial filtering operation can be expressed by the convolution of the primitive variable f with a grid dependent filter function $G(\vec{x})$:

$$\widehat{f} = \int_{-\infty}^{+\infty} G(\vec{x} - \vec{x}')f(\vec{x})\ d\vec{x}' \quad . \tag{2.109}$$

Several filter or kernel functions G in both spectral or physical space exist [103], that depend on the local grid size $\triangle$. Using this filter, the primitive variables are decomposed into a resolved or *grid scale*, and an unresolved or *subgrid scale*:

$$f = \widehat{f} + f' \quad . \tag{2.110}$$

The governing equations for the LES approach are obtained by filtering the instantaneous balance equations for mass, momentum and energy. For the fully incompressible case, the filtered set of equations can be written as:

$$\frac{\partial \widehat{u}_i}{\partial x_i} = 0 \quad , \tag{2.111}$$

$$\frac{\partial \widehat{u}_i}{\partial t} + \frac{\partial}{\partial x_j}(\widehat{u_i u_j}) = -\frac{1}{\rho}\frac{\partial \widehat{p}}{\partial x_i} + \frac{\partial}{\partial x_j}\left(\nu \frac{\partial \widehat{u}_i}{\partial x_j}\right) \quad , \tag{2.112}$$

$$\frac{\partial \widehat{T}}{\partial t} + \frac{\partial}{\partial x_i}(\widehat{T u_i}) = -\frac{\partial}{\partial x_i}\left(\frac{\nu}{\mathrm{Pr}}\frac{\partial \widehat{T}}{\partial x_i}\right) \quad , \tag{2.113}$$

for which the commutability of derivative and filtering operations is assumed [103]. Neglecting the Leonard and Cross terms [53], the non-linearities in the NS-equations can be written as:

$$\widehat{u_i u_j} = \widehat{u}_i \widehat{u}_j + \widehat{u'_i u'_j} \quad , \tag{2.114}$$

$$\widehat{T u_i} = \widehat{T}\widehat{u}_i + \widehat{T' u'_i} \quad , \tag{2.115}$$

where the contributions of the subgrid components have to be modeled in terms of filtered variables to close the problem. Several so-called subgrid scale models exist, see e.g. [37, 103], to model the unresolved Reynolds stresses and heat fluxes.

2.4.2.1 Subgrid Scale Models Based on Eddy Viscosity

In the incompressible case, subgrid scale models of the eddy viscosity type assume that the unresolved Reynolds stresses are locally aligned with the resolved strain tensor [37]:

$$\widehat{u'_i u'_j} = \frac{\partial}{\partial x_j}\left(\nu_{\mathrm{sgs}} \widehat{D}_{ij}\right) \quad , \tag{2.116}$$

and

$$\widehat{D}_{ij} = \frac{1}{2}\left(\frac{\partial \widehat{u}_i}{\partial x_j} + \frac{\partial \widehat{u}_j}{\partial x_i}\right) \quad . \tag{2.117}$$

The physical interpretation is that the effects of the unresolved scales can be correlated to the resolved strain tensor by means of a *subgrid viscosity* ν_{sgs}. This fictive viscosity depends on the kinetic energy of the unresolved scales k_{sgs} [37]:

$$\nu_{\text{sgs}} = c_k \triangle \sqrt{k_{\text{sgs}}} \quad . \tag{2.118}$$

Based on statistical theory, estimates for the subgrid kinetic energy can be used to give a closed form expression for the subgrid viscosity. The subgrid kinetic energy is modeled primarily as a function of the grid size $\triangle$, resolved strain $\widehat{D}_{ij}$ and eventually some model constants, see e.g. Eq. (2.121). A more general approach proposed by Yoshizawa and Horiuti [53] starts from a conservation equation for k_{sgs}:

$$\frac{\partial k_{\text{sgs}}}{\partial t} = -\widehat{u}_i \frac{\partial k_{\text{sgs}}}{\partial x_i} + \frac{1}{2}\nu_{\text{sgs}}|\widehat{D}_{ij}|^2 + \frac{\partial}{\partial x_i}\left[(\nu + \nu_{\text{sgs}})\frac{\partial k_{\text{sgs}}}{\partial x_i}\right] - \frac{c_\epsilon}{\triangle} k_{\text{sgs}}^{3/2} \quad . \tag{2.119}$$

The terms on the right-hand side of Eq. (2.119) represent convection, production, diffusion and dissipation, respectively. The production term is correlated to the magnitude of the resolved strain $|\widehat{D}_{ij}| = (2\widehat{D}_{ij}\widehat{D}_{ij})^{1/2}$. The diffusion term accounts for the contribution of both molecular and subgrid viscosity. Finally, the dissipation term depends on the cut-off grid scale and a model constant. The model constants take approximately the values $c_k = 0.05$ and $c_\epsilon = 1$ [37].

As showed by Horiuti [53], the most commonly and popular SGS model developed by Smagorinsky [123] can be derived from Eq. (2.119) assuming equilibrium between energy production and dissipation:

$$\frac{1}{2}\nu_{\text{sgs}}|\widehat{D}_{ij}|^2 = \frac{c_\epsilon}{\triangle} k_{\text{sgs}}^{3/2} \quad . \tag{2.120}$$

Substitution of Eq. (2.118) gives after some rearrangement

$$\nu_{\text{sgs}} = \frac{c_k^{3/2}}{\sqrt{2c_\epsilon}} \triangle^2 \, |\widehat{D}_{ij}|^2 = (c_s \triangle)^2 |\widehat{D}_{ij}|^2 \quad , \tag{2.121}$$

that clearly displays the Smagorinsky formalism. The value $c_s = 0.09$ lies close to the well established optimal value of $c_s \approx 0.1$.

Concerning the unresolved heat fluxes, a gradient approach also based on SGS eddy diffusivity proposed by Moin et al. [83] is well established:

$$\widehat{T'u'}_j = -\frac{\partial}{\partial x_j}\left(\frac{\nu_{\text{sgs}}}{\text{Pr}_{\text{sgs}}}\frac{\partial \widehat{T}}{\partial x_j}\right) \quad . \tag{2.122}$$

The subgrid scale viscosity models depend on the proper choice of several model parameters. As argued by Germano et al. [41], it is not possible to effectively model all kinds of turbulent flows treating these parameters as global constants. Several investigations have shown that the optimal values for the parameters depend on the boundary conditions, local flow regime and local grid resolution. To overcome this deficiencies, Germano et al. [41] proposed a dynamic procedure to estimate the model coefficients as part of the simulation. The approach samples information from the resolved scales via a coarser *test filter* of size ▲ and assumes similarity between the test-grid and subgrid scales. This leads to a tensor relation for the model coefficients, which depends

solely on the resolved variables. Lilly extended the method by expressing the Germano identity as a least square optimization problem [76].

To increase numerical stability, two additional actions suggested by Fureby [36] can be applied: firstly, the amount of backscatter denoted by negative values of the sub-grid transport coefficients, is limited by the entropy conditions $\mu + \mu_{sgs} \geq 0$ and $a + a_{sgs} \geq 0$ and secondly, in the least squares optimization, the local cell values are computed as the average over the neighboring cells.

2.4.3 Simulation Tool

In this thesis, the open-source package *openFOAM* is used for the numerical investigation of heat transfer in pulsating flows. *OpenFOAM* (Open Field Operation and Manipulation) is an open-source simulation package for the solution of continuum mechanics problems, including computational fluid dynamics. It consists of a large number of libraries written in C++ and build up using common object-orientation techniques like encapsulation, inheritance and polymorphism. The code has been initially developed by Jasak [57] and formally presented by Weller et al. [130]. The intention of the package is to provide a general code that uses a top-level syntax very close to conventional mathematical notation for tensors and partial differential equations in order to facilitate the programming and extension of solvers [130]. Currently, the software package is a registered trademark owned by the ESI Group, but is distributed by the OpenFoam Foundation [2] under the General Public License and provides a variety of solvers and utilities applicable to a wide range of problems. Furthermore, a growing community of developers all over the world contribute, permanently extending and improving its functionality.

The package has been chosen because of its flexibility to create or modify solvers and post-processing utilities. Through the course of this thesis, several solvers and utilities have been extended.

Detailed information concerning the numerical schemes used in *openFoam* can be taken from the official documentation [2] or the extensive literature on the topic, e.g. [34]. In the framework of this thesis, some properties of the principal schemes have been described and evaluated by Kunzer [69]. Based on this study, the optimal combination of numerical schemes used in most simulations presented in this work was chosen.

2.4.3.1 Iterative Solution of the NS-Equations

There exist several algorithms for the numerical solution of the resulting system of discretized Navier-Stokes equations within the finite volume approach. The PISO (Pressure Implicit with Splitting of Operators) algorithm is an iterative approach proposed by Issa [56] that has become very popular in the majority of commercial CFD codes because of its robustness and numerical efficiency. The basic principle of the method is to solve the linear system approximately in a series of steps, in which the pressure and velocity are uncoupled. The approximate solutions are subsequently improved iteratively.

The steps in this methodology will be presented in this section in its most essential form. Details can be found in [34, 56, 102]. To keep a general formalism independent of the discretization scheme, a matrix notation will be employed. The momentum equation can be written in its discretized form using the vectors of cell values $\vec{u}$ and $\vec{p}$ as:

$$\mathbf{A}\vec{u}^{*} + \mathbf{H}'\vec{u}^{*} = \vec{r} - \nabla\vec{p}^{n} \quad , \tag{2.123}$$

where the matrix $\mathbf{A}$ accounts the diagonal and $\mathbf{H}'$ the off diagonal entries of the discretization matrix. The vector $\vec{r}$ accounts all explicit terms: either values from the previous time iteration, imposed values at boundaries or source terms. This equation can be solved for the velocity using the previous values for the pressure $\vec{p}^{n}$ in the so-called predictor step denoted by a *. The resulting velocity field does not satisfy mass conservation and has to be corrected.

In a subsequent step, Eq. (2.123) is recast using the predicted velocity values for the cell fluxes $\mathbf{H}'\vec{u}^{*}$, a new set of corrected values $\vec{u}^{**}$ and $\vec{p}^{*}$, and matrix inversion:

$$\vec{u}^{**} = \mathbf{A}^{-1}\left[\vec{r} - \mathbf{H}'\vec{u}^{*}\right] - \mathbf{A}^{-1}\nabla\vec{p}^{*} \quad . \tag{2.124}$$

The unknown corrected velocity can be substituted from the mass conservation $\nabla(\rho\vec{u}^{**}) = -\frac{\partial\rho}{\partial t}$ by application of the divergence operator to Eq. (2.124):

$$-\frac{\partial\rho}{\partial t} = \nabla\left(\rho\mathbf{A}^{-1}\left[\vec{r} - \mathbf{H}'\vec{u}^{*}\right]\right) - \nabla\left(\rho\mathbf{A}^{-1}\nabla\vec{p}^{*}\right) \quad . \tag{2.125}$$

This pressure equation is uncoupled from the velocity, because the density can be computed from the constitutive laws. For constant density flows, the transient term vanishes. For compressible or weakly compressible flows, the energy equation has to be incorporated in the analysis to estimate the temperature and the density via ideal gas law. A similar predictor-corrector scheme can be derived in this case, see [56]. Solution of Eq. (2.125) gives the corrected values for the pressure $\vec{p}^{*}$. Using Eq. (2.124), the corrected velocity $\vec{u}^{**}$ can also be computed. In this manner, a series of corrector steps can be performed until the solution converges. For constant density flows, Issa [56] has shown that two corrector steps in the PISO-loop are sufficient when using second order numerical schemes. Compressible flows need additional corrections due to the coupling with the energy equation.

2.5 Pulsating Flows

A variety of both engineering and natural flows are accompanied by an inherent periodic unsteadiness. Examples belonging to the latter group are ocean flows or blood flow in large arteries. The former group comprises for example flows in the exhaust of reciprocating engines, turbo-machinery or, as is the case concerning the present study, combustor chambers suffering from thermoacoustic instabilities. The characteristic feature of all mentioned flows is that they are composed of a temporal mean and a time oscillating component. The terms used in the literature to describe such kind of flows are sometimes misleading. This study uses the definition adopted in [19], in which a *pulsating flow* denotes the more general case of a steady state component superimposed with a time oscillating component. If the mean part vanishes, the flow is denoted as *oscillating flow* and is strictly speaking a sub-branch of pulsating flow.

Pulsating flows have been studied for many years. An extensive review of the literature and state of the art can be found in [19, 45, 46, 125]. This introduction gives only a brief description of the most relevant characteristics. The so-called *triple decomposition* can be written in the following form:

$$\vec{u}(\vec{x},t) = \bar{\vec{u}}(\vec{x}) + \vec{u}^{\wr}(\vec{x},t) + \vec{u}^{\backprime}(\vec{x},t) \quad , \tag{2.126}$$

where $\bar{\vec{u}}$ represents the time averaged or mean component, $\vec{u}^{\wr}$ is the periodic fluctuating part with evident frequency ω and $\vec{u}^{\backprime}$ the turbulent part with chaotic random fluctuations. An example axial velocity decomposition is shown schematically in Fig. 2.7. Note however, that all three terms in Eq. 2.126 are actually three dimensional vectors. Thus, a variety of combinations concerning the pulsation direction are possible.

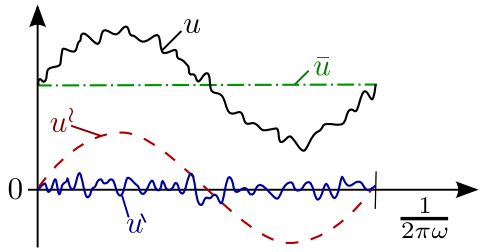

Figure 2.7: Decomposition of pulsating flows into mean $\bar{u}$, periodic $u^{\wr}$ and turbulent part $u^{\backprime}$

The turbulent pulsating case, which is inherently three dimensional, will be treated in detail in Sec. 6. This introduction focuses on laminar cases.

2.5.1 Oscillating flow

An infinite flat plate that oscillates harmonically in its plane along the x direction in a stagnant fluid is a very simple example that elucidates some of the important characteristics of pulsating flows. This problem was solved analytically by Stokes, and it is often referred to in literature as Stokes' second problem. Due to the symmetry of the problem no quantities vary with x and the momentum equation reduces to:

$$\frac{\partial u}{\partial t} = \nu \frac{\partial^2 u}{\partial y^2} \quad , \tag{2.127}$$

with the boundary conditions for the problem:

$$\begin{aligned} u &\to 0 && \text{as} && y \to \infty \quad , \\ u &= a_u \cos(\omega t) && \text{for} && y = 0 \quad , \end{aligned} \tag{2.128}$$

where a_u is the constant velocity amplitude of the plate. As shown in App. B.1, the general solution of this problem reads [125]:

$$u = a_u \ \cos(\omega t + y/\delta_s)\ e^{-y/\delta_s} \quad . \tag{2.129}$$

The flow motion induced by the plate oscillations dies out exponentially when moving away from the wall. The amplitude decay rate in the y direction is a typical length scale of the problem and is called *Stokes' length*:

$$\delta_s = \sqrt{\frac{2\nu}{\omega}} \quad . \tag{2.130}$$

It depends solely on the oscillating frequency and the fluid viscosity. Furthermore, the oscillations experience an increasing phase lag proportional to the wall distance and the Stokes' length.

The extensive number of studies concerning oscillating flows have lead to a quite good understanding of the problem [45]. The relevant parameter for their characterization is a Reynolds number based on the Stokes' length, oscillating velocity amplitude and fluid viscosity [121]:

$$\mathrm{Re}_{os} = \frac{u^{\wr}\delta_s}{\nu} \quad . \tag{2.131}$$

Depending on this parameter, oscillating flows can display laminar, transitional or turbulent behavior. Critical values for a variety of geometries like plate, channel, pipe and so on can be found in the literature, see [19].

2.5.2 Pulsating Flow

Lighthill studied the response of the hydrodynamic boundary layer to fluctuations of small amplitude in the external flow about a mean value [75]. In the streamwise direction he expresses the pulsating external flow (capital letters) with harmonic perturbations as follows:

$$U(t) = \bar{U}\left(1 + \epsilon e^{i\omega t}\right) \quad , \tag{2.132}$$

where the oscillating component is of small order $\epsilon \ll 1$. He further assumes that the axial boundary layer velocity (small letters) will perform small harmonic oscillations about a steady mean, too:

$$u(x, y, t) = \bar{u}(x, y) + \hat{u}(x, y)e^{i\omega t} \quad , \tag{2.133}$$

however with a possible phase lag with respect to the far field velocity oscillations. Thus, the amplitude of the velocity in the boundary layer $\hat{u}$ can be a complex valued quantity. Of course, only the real parts of the expressions represent the physical velocities. Figure 2.8 illustrates this behavior in a polar diagram. The complex vector oscillates with the same angular frequency as the external flow, but might have a phase lag.

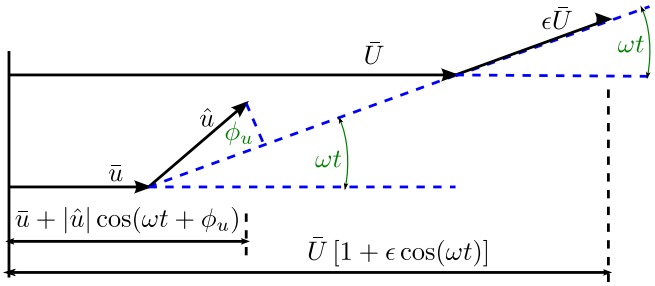

Figure 2.8: Polar diagram of boundary layer and far field velocities, displaying a possible phase lag ϕ_u [125].

Lighthill solved this problem for two limiting cases. His solution procedure is summarized in App. B.2. The high frequency approximation is valid for flows with boundary

layer thickness much larger than the Stokes' length, $\delta \gg \delta_s$. In this case, the general solution for the oscillating velocity component in the boundary layer reads:

$$\hat{u} = \epsilon \bar{U} \left[1 - e^{-y/\delta_s} e^{-iy/\delta_s} \right] \quad . \tag{2.134}$$

The stationary component $\bar{u}$ can be determined from a Karman-Pohlhausen treatment [44], see App. B.2. From Eq. (2.134), the wall normal dependency of the phase lag ϕ_u can be expressed as:

$$\tan(\phi_u) = \frac{\sin(y)}{e^{\delta_s^2}/\delta_s - \cos(y)} \quad . \tag{2.135}$$

At distances far away from the wall, $y \to \infty$, the phase lag vanishes $\phi_u \to 0$ and the velocity amplitude tends to the far field value $\hat{u} \to \bar{U}$. Towards the wall, $y \to 0$, the phase lag tends to the limit $\phi_u \to \pi/4$ and the velocity amplitude vanishes $\hat{u} \to 0$. This means that the velocity fluctuations in the boundary layer advance always the fluctuations of the external flow. This is a very important feature of pulsating flows. Due to the viscous forces in the boundary layer, the magnitude of the velocity is smaller. Thus, the inertia of the fluid in this region is lower and it can respond faster to external perturbations.

The small frequency approximation given by Lighthill is valid for flows with boundary layer thickness much smaller than the Stokes' length $\delta \ll \delta_s$. The details of his derivation and the solution for this case are given in App. B.2.

3 Characterization of Resonator Rings

3.1 Application of Acoustic Cavities in Rocket Chambers

As mentioned in the introduction, the use of passive acoustic devices has proven to be an effective way to suppress combustion instabilities and to increase the stability margin of rocket engines. One of the first generation of passive acoustic devices in thrust chambers were so-called linings: a backing volume divided from the main chamber by a perforated wall. They covered the majority of the cylindrical section in the chamber, as shown in Fig. 3.1. As the performance of the propulsion systems increased, the combustion temperature and chamber pressure raised, too. Linings had to be protected from the aggressive environment in the chamber. Even though it is possible to cool the lined walls, the required efforts should not be underestimated. Additional experience in this field revealed that the lining section close to the injector plate brings the major contribution to the overall damping. More effective designs with only partial linings or even single slots attached to the injector plate emerged, which are considerable easier to cool. See e.g. Fig. 3.2. More recent designs introduced the concept of resonators, or more precisely, *resonator rings*. They consist of an array of acoustic cavities placed in parallel as a ring.

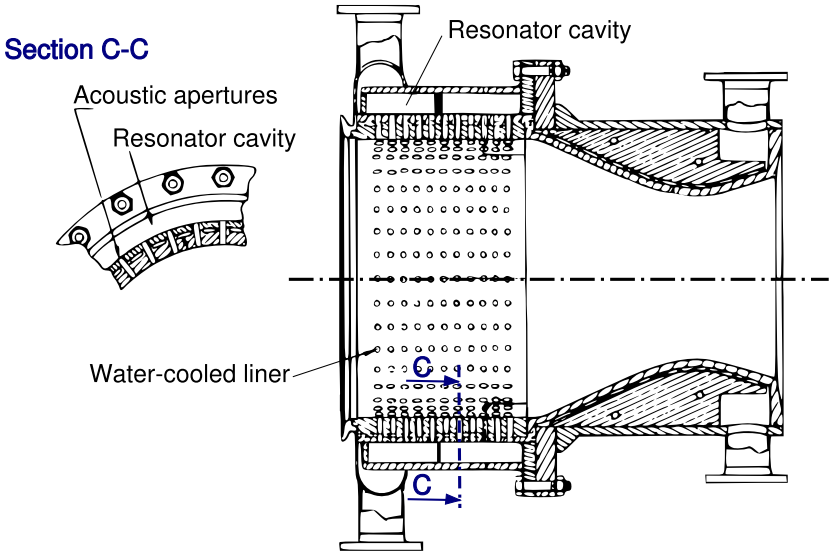

Figure 3.1: Sketch of a typical lining configuration in rocket thrust chambers, reproduced from [49].

While in some modern combustion systems like gas turbines or aero-engines bias flow is used to cool the cavities [30], resonators in rocket chambers are usually not cooled convectively.

The effectiveness of a resonator in suppressing thermoacoustic instabilities relies mainly on two mechanisms. The most prevalent one is damping induced by the gas motions in the cavities. This occurs through linear viscous dissipation at the cavity walls, and more predominately, through flow separation at edges. In this case, the jets emerging in the vicinity of the cavities' mouth break up into vortices and lead to additional non-linear dissipation. Furthermore, acoustic cavities might change the eigenfrequency of the combustion chamber disturbing the coupling between acoustics and heat release fluctuations. This second mechanism acts indirectly against the driving force of the instability.

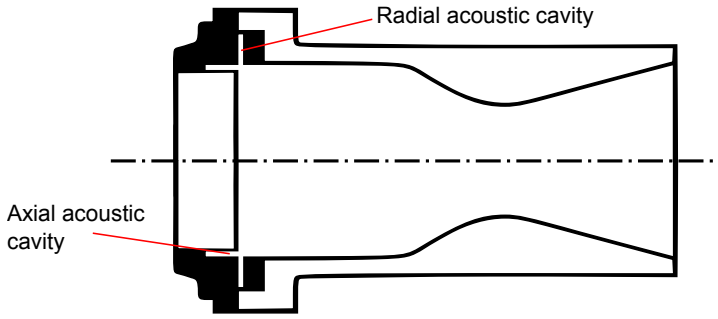

Figure 3.2: Sketch of a typical resonator ring or slot configuration in rocket thrust chambers, reproduced from [94].

The response of a resonator to acoustic perturbations can be characterized through its acoustic impedance Z at the cavity mouth. Two main types of acoustic cavities or resonators can basically be classified: *Helmholtz resonators* and *quarter waves tubes*. These two types, for which appropriate models exist, will be described in the following sections. Due to geometrical constrains in rocket chambers, unconventional cavities are also used, that exhibit characteristics of both main types.

3.2 State of the Art Impedance Models for Single Cavities

3.2.1 Helmholtz Resonators

This resonator type consists of a small volume connected to the main chamber through a short channel or neck, as depicted in Fig. 3.3. If the resonator is acoustically compact, which means that its dimensions are small compared to the wave length of the oscillations, the acoustic behavior can be described by an oscillating mass-spring-dashpot system. The cavity volume with its compressibility acts as the spring, while the gas in the channel corresponds to the oscillating mass, damped by linear visco-thermal losses at the channel walls. For high velocity amplitudes, flow separation at edges occurs forming jets outside the neck, which leads to additional non-linear losses. According to Ingard [55], the radiation losses of a circular opening can be neglected for typical resonators.

Keller and Zauner [64] developed a thorough approach based on the conservation of mass and momentum, which considers the linear losses and, up to a certain extent, the non-linear losses, too. However, empirical discharge coefficients are needed to estimate

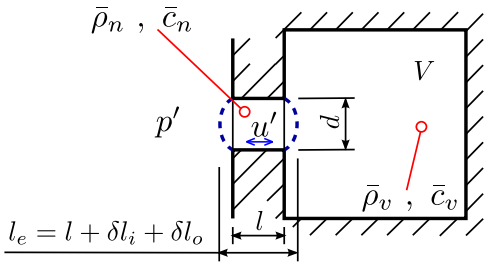

Figure 3.3: Sketch of a resonator cavity of the Helmholtz type.

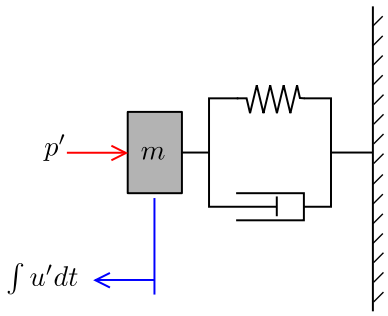

Figure 3.4: Analogy of Helmholtz resonator as mass-spring-dashpot system.

these non-linear losses. They derived the following equation of motion for the gas inside the neck assuming compactness:

$$(1+s) l_e \bar{\rho}_n \frac{d^2 u'}{dt^2} - \left[s\bar{\rho}_n (l + l_f)\omega + \zeta \bar{\rho}_n |u'| \right] \frac{du'}{dt} + \frac{A_n \bar{\rho}_v \bar{c}_v^2}{V} u' = \frac{dp'}{dt} \quad , \tag{3.1}$$

where u' represents the axial acoustic velocity in the neck, p' the acoustic pressure acting on the left side of the neck, $A_n = \pi d^2/4$ denotes the neck transverse area, and the indices $_n$ and $_v$ stand for average values at the neck and backing volume locations, respectively (see Fig. 3.3). A so-called boundary layer parameter s accounts for the thermal and viscous dissipation. For cylindrical ducts and small Stokes' numbers $d/\delta_s \gg 1$, it can be given by the following expression [64, 117]:

$$s = \frac{1}{d}\left(1 + \frac{\gamma - 1}{\sqrt{\mathrm{Pr}}}\right)\delta_s \quad . \tag{3.2}$$

Equation (3.1) corresponds to the time derivative of a mass-spring-dashpot differential equation, as sketched in Fig. 3.4. The first term on the left-hand side corresponds to the inertia of the gaseous mass in the neck with some correction due to boundary layer effects. An *effective length* l_e accounting the mass of gas surrounding the neck that takes part in the oscillation is also applied:

$$l_e = l + \delta l_i + \delta l_o \quad . \tag{3.3}$$

For the outside correction δl_o on the chamber side the well known model of a piston radiating into half space can be used [88]:

$$\delta l_o \approx \frac{4}{3\pi} d \quad . \tag{3.4}$$

Ingard [55] proposed to model the inside correction δl_i on the backing volume side as a piston radiating into a volume of equivalent diameter $D_e \approx \sqrt[3]{V}$:

$$\delta l_i = \frac{4}{3\pi} d \left(1 - 1.24 \frac{d}{D_e}\right) \qquad \text{for} \qquad \frac{d}{D_e} < 0.4 \quad . \tag{3.5}$$

For high aspect ratios $d/D_e \ll 1$, Eq. (3.5) converges to Eq. (3.4) and the effective length can be approximated as

$$l_e \approx l + 2\delta_o \quad . \tag{3.6}$$

More accurate approaches exist, that take also the frequency dependency into account, see [52].

The second term on the left-hand side of Eq. (3.1) corresponds to the damping due to linear and non-linear losses. The first term in the brackets corresponds to the linear losses in the channel with a correction l_f to account for additional damping at the face plate. According to Ingard [55], it can be approximated as $l_f \approx d$ based on measured data. The second term in the brackets corresponds to non-linear losses expressed in form of discharge coefficients. The third term can be interpreted as the force induced by a fictive spring with stiffness proportional to the compressibility of the backing volume. Finally, the term on the right-hand side accounts for the forcing of the system by the oscillating chamber pressure p'. For linear forcing $p' = \hat{p}e^{i\omega t}$, the system can be transferred into the frequency domain assuming a linear response $u' = \hat{u}e^{i\omega t}$, too:

$$(1+s)l_e\bar{\rho}_n\omega i\hat{u} - \left[s\bar{\rho}_n(l+d)\omega + \zeta\bar{\rho}_n\hat{u}\right]\hat{u} - \frac{A_n\bar{\rho}_v\bar{c}_v^2}{V\omega}i\hat{u} = \hat{p} \quad . \tag{3.7}$$

At resonance, the system becomes neutrally stable and the forcing is entirely compensated by the damping. Hence, a relation for the eigenfrequency can be written in this case as:

$$f_{\mathrm{eig}} = \frac{\bar{c}_v}{2\pi}\sqrt{\frac{A_n}{V(1+s)l_e}\frac{\bar{\rho}_v}{\bar{\rho}_n}} \quad . \tag{3.8}$$

In order to get an expression for the acoustic impedance at the cavity mouth from this motion equation, the non-linear term $\zeta\bar{\rho}_n\hat{u}^2$ has to be approximated. One practical possibility is to linearize it upon a certain sound pressure level and express it in a similar form as the visco-thermal losses:

$$\zeta\bar{\rho}_n\hat{u}^2 \approx \epsilon_{nl}s\bar{\rho}_n d\omega\hat{u} \quad , \tag{3.9}$$

where the *non-linear resistance factor* $\epsilon_{nl}(\hat{u})$ depends on the amplitude of the oscillations and has to be determined empirically. Substitution of s from Eq. (3.2) gives after some rearrangement an expression for the acoustic impedance $Z = \hat{p}/\hat{u}$:

$$Z_{\mathrm{H}} = \left(1 + \frac{\gamma-1}{\sqrt{\mathrm{Pr}}}\right)\left(1 + \epsilon_{nl} + \frac{l}{d}\right)\sqrt{2\bar{\rho}_n\mu_n\omega} \; + \; i\left[l_e\bar{\rho}_n\omega(1+s) - \frac{A\bar{\rho}_v\bar{c}_v^2}{V\omega}\right] \quad . \tag{3.10}$$

The imaginary part or reactance consists of the neck inertance and cavity compliance in series [88]. Furthermore, for high frequencies and small Stokes' lengths the boundary layer effects can be neglected leading to the well established relation:

$$\Psi_{\mathrm{H}} = l_e\bar{\rho}_n\omega - \frac{A_n\bar{\rho}_v\bar{c}_v^2}{V\omega} \quad . \tag{3.11}$$

In order to evaluate the resistance, an estimation of the non-linear factor is needed. A correlation proposed by Garrisson et al. [40] and based on measurements is:

$$\epsilon_{nl} \approx 1.62 \; SPL^{0.93} \quad , \tag{3.12}$$

where SPL stands for the sound pressure level of the incoming waves in decibel.

Some measurements for the non-linear factor can also be found in [40, 55]. Figure 3.5 shows a set of three measurements of the resistance factor ϵ_{nl} for a single cavity and moderate SPLs. The strong difference in the predicted values reveals a high uncertainty concerning this parameter. Typical SPLs in rocket chambers at stable conditions can reach up to 5% of the average chamber pressure.

Strictly speaking, due to its non-linearity, the value of this factor will depend on the SPL present in the chamber, which might range from moderate values at normal operation to very high values at resonance or unstable conditions. Thus, an assumed constant non-linear factor over all frequencies and SPLs might not reproduce accurately the dynamic behavior of the cavities at non resonant frequencies. This issue in the formulation of Eq. (3.10) has already been pointed out by Ingard [55]. However, this study is mainly interested in the response of these devices at resonant conditions, where high SPLs are expected. Thus, as a first approximation, this factor is assumed to be constant and to take relatively large values.

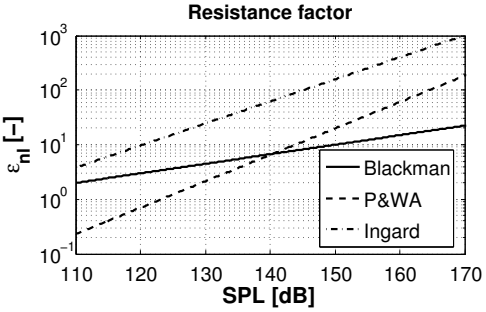

Figure 3.5: Correlated measurements of the non-linear resistance factor as a function of the sound pressure level, reproduced from [40].

3.2.2 Quarter-Wave Tubes

Quarter-wave resonators are small pipes connected at one end to the chamber and closed at the other as shown in Fig. 3.6. Due to the small cavity to chamber volume ratio, the end connected to the chamber can be approximated as an open end. Since the transverse dimensions are much smaller than the axial ones, the acoustic field inside the cavities can be effectively described by the one dimensional wave equation. The boundary conditions $p' = 0$ for the open end and $u' = 0$ for the closed end are used to close the problem. To account for the mass of gas surrounding the cavity mouth taking part in the oscillation, the already introduced outer end correction δl_o given by Eq. (3.4) is added to the geometrical length $l_e = l + \delta l_o$.

In the homogeneous case without mean flow, the solution for the acoustic pressure and velocity field is given by expressions Eqs. (2.60) and (2.61) and the proper BC from Tab. 2.2:

$$\frac{p'}{\bar{\rho}_v \bar{c}_v} = C \cos(kx) e^{i\Omega t} \quad , \tag{3.13}$$

$$u' = -iC \sin(kx) e^{i\Omega t} \quad , \tag{3.14}$$

where the constant C gives the sound pressure level. However, for the ratio of pressure to velocity fluctuations at the cavity mouth $x = l_e$, this constant cancels out. And,

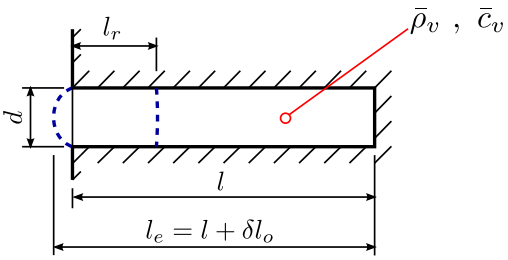

Figure 3.6: Sketch of a quarter wave type resonator.

since all losses have been neglected in the wave equation, this ratio corresponds only to the reactance of the cavity:

$$\Psi_{\mathrm{Q}} = -\bar{\rho}_v \bar{c}_v \cot\left(\frac{\omega l_e}{\bar{c}_v}\right) \quad . \tag{3.15}$$

The minus sign comes from the choice of the coordinate system pointing into the cavity volume. The reactance vanishes at resonance and thus, the eigenfrequencies of a half-closed pipe with homogeneous properties can be determined by the following relation:

$$f_{\mathrm{eig}} = \frac{(2n+1)\bar{c}_v}{4l_e} \qquad \text{for} \qquad n = 0, 1, 2, 3, \ldots \quad . \tag{3.16}$$

The first harmonic has a wavelength four times the tube length. This is the reason for the name of the resonator type.

As for the case of Helmholtz resonators two main types of losses exist: linear dissipation through viscous and thermal effects, and non-linear dissipation through jet separation. An overview of models describing the dissipation of acoustic waves through ducts taking thermal and viscous dissipation into account is given by Tijdemann [127]. All the approaches share the idea to express the visco-thermal effects in terms of a *propagation constant* Γ_{vt}, such that:

$$p' \sim e^{\pm i(k+\Gamma_{vt})x} e^{i\omega t} \quad . \tag{3.17}$$

The simplifications used in the derivation of Eq. (3.2) are not applicable here because for quarter-wave tubes the Helmholtz number is not small and thus, they are not acoustically compact. However, for most of the models, this propagation parameter is proportional to

$$\Gamma_{vt} \sim \frac{\sqrt{2\omega\nu}}{\bar{c}d} \ll 1 \quad , \tag{3.18}$$

which is very small for common geometries and properties of rocket chambers. Thus, it is also a good approximation to assume that the main contribution to the dissipation comes from the jet separation at the cavity mouth. In addition to the lack of accurate analytical models, measurements and corresponding correlations for quarter wave tubes are rare compared to those for Helmholtz resonators. A possibility proposed by Laudien et al. [70] is to use the correlations available from Helmholtz resonators and adapt them to estimate the resistance of quarter wave cavities using a representative neck length l_r.

This fictive neck length can be determined from a geometrical analogy with the Helmholtz cavity. Because quarter wave tubes have only one flanged end, the effective length of the oscillating mass in the Helmholtz analogy is simply $l_e^H = l_r + \delta l_o$.

Furthermore, the whole tube volume is assumed to act as the backing volume or gas spring in the analogy $V^H \approx \pi d^2 l/4$. Assuming equal eigenfrequencies for both the geometrical analogy (Helmholtz cavity) and the quarter wave tube leads to the following relation:

$$\frac{\bar{c}}{2\pi}\sqrt{\frac{\pi d^2/4}{V^H(l_r+\delta l_o)}} = \frac{\bar{c}}{4(l+\delta l_o)} \quad , \tag{3.19}$$

where the boundary layer parameter s has been neglected. Solving for the fictive neck length yields after some rearrangement:

$$\frac{l_r}{d} = \frac{4}{\pi^2}\frac{l}{d} - \left(1-\frac{8}{\pi^2}\right)\frac{\delta l_o}{d} + \frac{4(\delta l_o/d)^2}{\pi^2(l/d)} \quad . \tag{3.20}$$

For quarter wave resonators, the length to diameter ratio is usually large $l/d \gg 1$, and the last term in the previous expression can be neglected. Substitution of Eq. (3.4) for the outer correction length δl_o gives finally:

$$\frac{l_r}{d} \approx 0.405\frac{l}{d} - 0.08 \quad . \tag{3.21}$$

Using this fictive length instead of the neck length in the real part of Eq. (3.10) gives the expression for the resistance of a quarter wave tube:

$$\Theta_{\mathrm{Q}} = 2\left(1+\epsilon_{nl}+\frac{l_r}{d}\right)\sqrt{2\bar{\rho}_n\bar{\mu}_n\omega} \quad . \tag{3.22}$$

The values at the cavity mouth are used for the fluid properties $\bar{\rho}_n$ and $\bar{\mu}_n$. Finally, the impedance expression for a quarter wave type resonator can be given as:

$$Z_{\mathrm{Q}} = 2\left(1+\epsilon_{nl}+\frac{l_r}{d}\right)\sqrt{2\bar{\rho}_n\bar{\mu}_n\omega} - i\bar{\rho}_v\bar{c}_v\cot\left(\frac{\omega l_e}{\bar{c}_v}\right) \quad . \tag{3.23}$$

3.2.3 Cavities of Mixed Type

Often, cavities that exhibit characteristics of both Helmholtz and quarter-wave tubes are used. This is e.g. the case, when the backing volume is not acoustically compact as shown in Fig. 3.7. The expressions for the resistance are still valid if the orifice is compact, thus the real part of Eq. (3.10) can directly be used. For the reactance, higher harmonics have to be taken into account. Such an analysis is given by Paton and Miller [98] and also by Keller and Zauner [64].

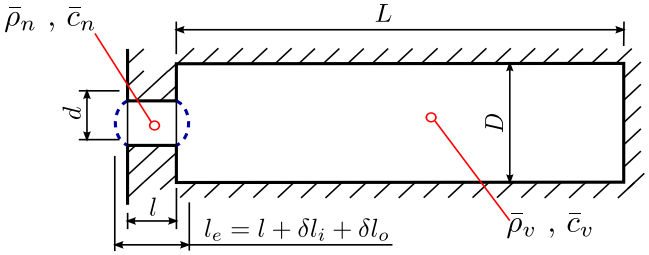

Figure 3.7: Sketch of resonator of mixed type.

The problem can be solved using the one-dimensional wave equation, but with different boundary condition for the end connected to the channel. Instead of an open end, a neck inertance of the gaseous mass in the channel is used. Thus, the reactance can be modeled as a neck inertance in series with a quarter wave tube:

$$\Psi_{\mathrm{M}} = l_e \bar{\rho}_n \omega - \bar{\rho}_v \bar{c}_v \cot\left(\frac{L\omega}{\bar{c}_v}\right) \quad . \tag{3.24}$$

The effective length of the neck can be determined using Eq. (3.5) for the inner and Eq. (3.4) for the outer length correction.

The eigenfrequencies at which the reactance vanishes are given by the transcendental equation:

$$l_e \frac{\bar{\rho}_n}{\bar{\rho}_v} \frac{\omega}{\bar{c}_v} = \cot\left(\frac{L\omega}{\bar{c}_v}\right) \quad . \tag{3.25}$$

A closed form solution is not possible. However, Panton and Miller [98] showed that an approach with series expansion of the right-hand side at $L = 0$:

$$\cot\left(\frac{L\omega}{\bar{c}_v}\right) = \frac{\bar{c}_v}{\omega L} - \frac{1}{3}\frac{L\omega}{\bar{c}_v} - \frac{1}{45}\left(\frac{L\omega}{\bar{c}_v}\right)^3 + \mathcal{O}\left(\left(\frac{L\omega}{\bar{c}_v}\right)^5\right) \tag{3.26}$$

can give a good approximation. The classical formula for Helmholtz cavities given by Eq. (3.8) can be obtained by retaining only the first term in the series expansion.

In fact, Eq. (3.24) is a general model for the reactance of resonators. The two main types are limiting cases of the mixed type resonator.

3.3 Equivalent Shell Impedance of a Resonator Ring

The expressions given in Sec. 3.2 describe the behavior of a single cavity in form of its cavity mouth impedance. In modern thrust chambers, the parallel arrangement of several cavities into resonator rings is a common practice. Thus, a model that accounts for interaction effects is needed.

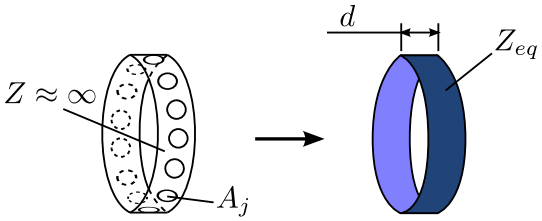

Figure 3.8: Equivalent specific impedance of a resonator ring homogenized over a portion of the cylinder shell.

Knowing the specific impedance of the base elements of an acoustic system, the equivalent impedance of the circuit can be calculated following the well established electric network rules [88]. For an array of n_R resonators placed in parallel into a ring, the equivalent specific impedance $Z_{eq,R}$ weighted by the homogeneous area is readily obtained as [70]:

$$\frac{Z_{eq,R}}{A_{ref}} = \left(\sum_j \frac{A_j}{Z_j}\right)^{-1} \quad , \tag{3.27}$$

where the equivalent impedance is weighted by the total area $A_{ref} = \sum A_j = 2\pi R_c d$ and the individual local impedances Z_j by their local reaction area A_j. The portion of the shell with hard boundaries has an infinite impedance, because the wall-normal velocity fluctuations have to be zero there. Thus, their effect is taken inherently into account by the weighting area since $A_{ref} = \sum A_j$ in Eq. (3.27). This procedure corresponds to averaging the impedance over the cylinder shell area as illustrated in Fig. 3.8. In rocket chambers, resonator rings with cavities of different size are sometimes employed to provide damping over a broader range of frequencies. In principle, a ring with a set of cavities of different type or geometry can be modeled through this approach, too. However, the different sets of cavities should have a minimum number of cavities and be homogeneously distributed in the azimuthal direction to assure symmetry and justify the homogenization.

In this study, the resonator ring has identical cavities of reaction area $A_n = \pi d^2/4$ and acoustic impedance Z_R. Equation (3.27) can be then simplified to:

$$Z_{eq,R} = \frac{8R_c}{n_R d} Z_R \quad . \tag{3.28}$$

This model is denoted, from now on, as *soft-wall* shell. Here the cavities are placed perpendicularly to the chamber wall where a three dimensional acoustic field is present. The impedance expression for the cavity mouth takes only the surface normal velocity component into account. In this case, this corresponds to the radial component of the velocity fluctuations:

$$Z = \frac{p'}{\vec{n} \cdot \vec{u}'} = \frac{\hat{p}}{\hat{v}} \quad . \tag{3.29}$$

3.4 Absorption Coefficient as an Evaluation Parameter

In general terms, the efficiency of a resonator can be evaluated by its *absorption coefficient* α. It is defined as the ratio of the power absorbed by a surface to the power of the incident traveling acoustic waves. The absorbed power per unit area is the product of acoustic velocity at the surface times the force needed for this motion. In acoustics, this force is in general the component of the pressure fluctuation p' in phase with the velocity fluctuation at the cavity mouth. However, the acoustic pressure and velocity fluctuations depend on the reflection factor r of the corresponding surface. Assuming negligible chamber flow effects (no mean flow and bias flow), the reflection factor can be expressed via Eq. (2.65) as a function of the surface impedance. For incident plane waves normal to the boundary, the absorption coefficient can be written after some rearrangement as [87]:

$$\alpha = 1 - |r|^2 = \frac{4\theta}{(\theta + 1)^2 + \psi^2} \quad , \tag{3.30}$$

where $|r|$ stands for the modulus of the reflection factor. Figure 3.9 shows this dependency for a series of parameters.

By definition, the optimum value of the absorption coefficient is unity, which means that 100% of the incident wave energy is absorbed. At resonance, the reactance of the

cavities vanishes and the resistance becomes then the controlling factor. As shown by the curve of this limiting case $\psi = 0$ in Fig. 3.9, the absorption coefficient decreases for resistance values larger than $\theta > 1$. The physical interpretation of this behavior is that with increasing resistance values the surface behaves more and more like a hard wall boundary. The system is over-damped and the incident waves get predominately reflected. Thus, a simple maximization of the resistance does not necessarily maximizes damping. In addition to this, it is important to note that if the resonators are not operated at their resonant frequency, the reactance of the cavities might play an important role, as shown by the various curves in Fig. 3.9.

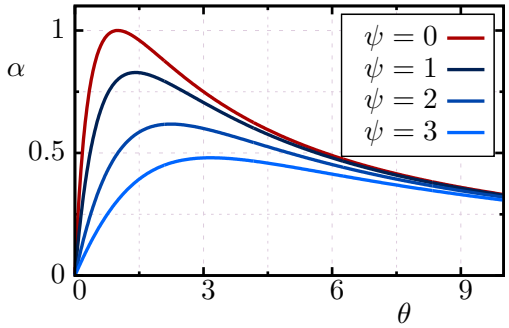

Figure 3.9: Absorption coefficient α dependency on specific resistance θ for various reactance values ψ.

3.4.1 Simplified Comparison Between Cavity Types

This section intends to give a simple, but still illustrative comparison between the different cavity types. As a simplification, the gas properties are assumed to be equal and homogeneous $\bar{\rho}_n = \bar{\rho}_v = \bar{\rho}$. The geometrical lengths are chosen such that all cavities have the same eigenfrequency f_{eig} for the first harmonic. Furthermore, it is assumed that all cavities operate at high amplitude ratios where the non-linear losses dominate the resistance. Thus, the resistance for all three types is assumed to be equal taking the following form:

$$\Theta \approx 2\epsilon_{nl}\sqrt{2\bar{\rho}\bar{\mu}\omega} \quad . \tag{3.31}$$

Figure 3.10 shows the frequency dependency of the reactance for the three cavity types using Eqs. (3.11), (3.15) and (3.24), respectively. As expected, the zero cross point is the same in all three cases. While the quarter wave and mixed type cavities behave similarly, the cavity of Helmholtz type differs strongly at frequencies far beyond the design point.

As explained in Sec. 3.4, the absorption coefficient is a more descriptive quantity for the comparison. Its frequency dependency for the three cavity types is shown in Fig. 3.11. Again, the cavities of the quarter wave and mixed type behave very similar with a definite maximum at their eigenfrequency. In contrast, the Helmholtz type cavity has a considerably stepper growth at low frequencies and an almost constant value at frequencies beyond the eigenfrequency. However, the validity of this behavior has to be mistrusted, since the model given by Eq. (3.11) is only valid for low Helmholtz numbers.

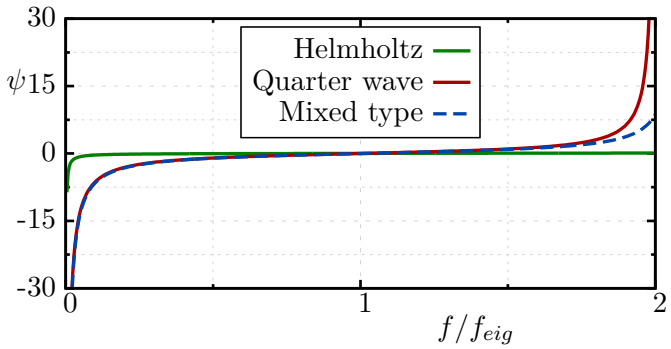

Figure 3.10: Simplified comparison of the reactance ψ for the three different cavity types.

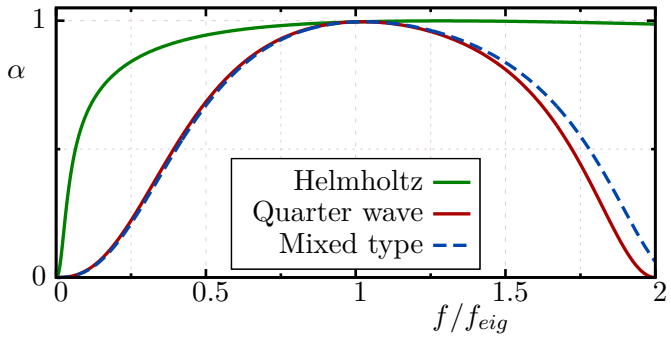

Figure 3.11: Simplified comparison of the absorption factor α for the three different cavity types.

3.5 Accounting for Gas Temperature Inhomogeneity

The previously presented impedance models for the cavities rest on the assumption of homogeneous properties inside the cavities. For cases with small temperature differences, the consideration of an average value is certainly a reasonable approximation. However, under unstable conditions, the temperature in the vicinity of the cavities might rise to considerable higher values.

Essentially, temperature inhomogeneities lead to changes in the medium properties. For the impedance, expressions given in Sec. 3.2, the relevant properties are the speed of sound $\bar{c}$, the density $\bar{\rho}$, and the dynamic viscosity $\bar{\mu}$. Assuming ideal gas behavior, the temperature dependency of these properties has been already presented in this thesis: the dynamic viscosity via Sutherland law (Eq. (2.17)), density via ideal gas law (Eq. (2.10)) and the speed of sound via the constitutive relation (Eq. (2.15)).

The following two sections give additional models to account for the influence of these property changes on the resistance and reactance of resonators. This thesis focuses on the influence of gas temperature inhomogeneity in quarter-wave cavities on their damping behavior. The treatment of all kinds of resonator cavities that are used in rocket thrust chambers would exceed the time frame of this project. Furthermore, some promising approaches accounting for the sensitivity of Helmholtz resonators to gas temperature inhomogeneity exist. For example, Ćosić et al. [22] studied the acoustic response of a Helmholtz resonator to hot-gas penetration. As will be explained in Ch. 4,

the inclusion of additional cavity impedance models in the methodology presented in this thesis is straightforward.

3.5.1 Resistance

The major contribution to the resistance comes from a small portion of the cavity close to the mouth. Thus, a cavity mouth temperature T_m can be used to estimate the gas properties in this region. Using Eqs. (2.17) to (2.15), the expression for the cavity resistance given by Eq. (3.22) can be evaluated for various temperature ratios.

The non-linear factor ϵ_{nl} inherits again a high degree of uncertainty. Physically, it is comprehensible to expect also a temperature dependency of it, simply because the Reynolds and Strouhal numbers change with temperature, leading to perhaps completely different flow regimes. The jet separation responsible for the non-linear dissipation will thus be influenced by the rise in temperature. However, due to the lack of an accurate analytical model, a constant non-linear factor is assumed in this work.

3.5.2 Reactance

The response of the reactance to temperature inhomogeneities demands a more detailed analysis. In contrast to the resistance, the reactance of a backing cavity is not necessarily acoustically compact.

In this thesis, a quarter-wave resonator impedance is derived from a general approach presented by Kumar & Sujith [68]. They give closed form expressions for one-dimensional sound propagation in ducts with axial temperature profiles of polynomial form:

$$\tilde{T}(x) = \int_0^{2\pi} \int_0^{d/2} T(x, r, \varphi)\ dr\ d\varphi \equiv (a_\mathrm{p} x + b_\mathrm{p})^{n_\mathrm{p}} \quad , \tag{3.32}$$

where at each axial location the transverse averaged value is used. The one dimensional wave equation (Eq. (2.32)) for a quiescent fluid with an axial temperature gradient, but negligible thermal and viscous dissipation, is the starting point of their derivation. For a perfect gas and using $\bar{c}^2 = \gamma R_s T$, the wave equation can be written as:

$$\frac{\partial^2 p'}{\partial x^2} + \frac{1}{\tilde{T}} \frac{d\tilde{T}}{dx} \frac{\partial p'}{\partial x} - \frac{1}{\gamma R_s \tilde{T}} \frac{\partial^2 p'}{\partial t^2} = 0 \quad . \tag{3.33}$$

In the linear case, a solution of the form $p' = \hat{p} e^{i\omega t}$ can be assumed. Substitution gives a Helmholtz equation

$$\frac{d^2 \hat{p}}{dx^2} + \frac{1}{\tilde{T}} \frac{d\tilde{T}}{dx} \frac{d\hat{p}}{dx} + \frac{\omega^2}{\gamma R_s \tilde{T}} \hat{p} = 0 \quad , \tag{3.34}$$

which Kumar and Sujith were able to solve using a special transformation, see [68]. They determined the following solution for the pressure field

$$\hat{p} = \tilde{T}^{\alpha_\mathrm{p}} \left[c_1 J_{\nu_\mathrm{p}}(\beta_\mathrm{p} \tilde{T}^{\sigma_\mathrm{p}}) + c_2 J_{-\nu_\mathrm{p}}(\beta_\mathrm{p} \tilde{T}^{\sigma_\mathrm{p}}) \right] \quad , \tag{3.35}$$

where

$$\alpha_\mathrm{p} = \frac{1}{2}\left(\frac{1}{n_\mathrm{p}} - 1\right) \quad , \quad \beta_\mathrm{p} = \frac{\omega}{a n_\mathrm{p} \sqrt{\gamma R_s} \sigma_\mathrm{p}} \quad , \quad \sigma_\mathrm{p} = \left(\frac{1}{n_\mathrm{p}} - \frac{1}{2}\right) \quad , \quad \nu_\mathrm{p} = \frac{1 - n_\mathrm{p}}{2 - n_\mathrm{p}} \quad , \tag{3.36}$$

and J_{ν_p} are Bessel functions of order ν_p. The solution presented here is only valid for non integer valued ν_p and $n_\mathrm{p} \neq 2$. For integer valued ν_p Neumann functions have to be taken additionally into account, see [68]. Using the linearized momentum equation, the acoustic velocity can be expressed as:

$$\hat{u} = -\frac{a_\mathrm{p} n_\mathrm{p} \tilde{T}^{\alpha_\mathrm{p}-1/n_\mathrm{p}}}{i\omega\bar{\rho}} \Bigg[\alpha_\mathrm{p}\{c_1 J_{\nu_\mathrm{p}}(\beta_\mathrm{p}\tilde{T}^{\sigma_\mathrm{p}}) + c_2 J_{-\nu_\mathrm{p}}(\beta_\mathrm{p}\tilde{T}^{\sigma_\mathrm{p}})\} \quad + \\ \frac{\beta_\mathrm{p}\sigma\tilde{T}^{\sigma_\mathrm{p}}}{2}\Big[c_1\{J_{\nu_\mathrm{p}-1}(\beta_\mathrm{p}\tilde{T}^{\sigma_\mathrm{p}}) - J_{\nu_\mathrm{p}+1}(\beta_\mathrm{p}\tilde{T}^{\sigma_\mathrm{p}})\} + \; c_2\{J_{-\nu_\mathrm{p}-1}(\beta_\mathrm{p}\tilde{T}^{\sigma_\mathrm{p}}) - J_{-\nu_\mathrm{p}+1}(\beta_\mathrm{p}\tilde{T}^{\sigma_\mathrm{p}})\}\Big]\Bigg] \tag{3.37}$$

The constants c_1 and c_2 can be determined from the boundary conditions at the left and right duct ends. Using the general solution, the primitive variables on the left, (index "l"), and on the right side of the duct, (index "r"), can be expressed in matrix form as:

$$\begin{pmatrix} \frac{\hat{p}}{\bar{\rho}\bar{c}} \\ \hat{u} \end{pmatrix}_l = \begin{bmatrix} A_{11} & A_{12} \\ A_{21} & A_{22} \end{bmatrix} \begin{pmatrix} c_1 \\ c_2 \end{pmatrix} \quad , \qquad \begin{pmatrix} \frac{\hat{p}}{\bar{\rho}\bar{c}} \\ \hat{u} \end{pmatrix}_r = \begin{bmatrix} B_{11} & B_{12} \\ B_{21} & B_{22} \end{bmatrix} \begin{pmatrix} c_1 \\ c_2 \end{pmatrix} \quad , \tag{3.38}$$

where the pressure has been weighted by $\bar{\rho}\bar{c}$ for dimensional consistency and the matrix coefficients A_{ij} and B_{ij} are functions of $f(\alpha_\mathrm{p}, \sigma_\mathrm{p}, \beta_\mathrm{p}, \nu_\mathrm{p}, n_\mathrm{p})$. By substituting the vector of constants in the previous expressions, the acoustic quantities on the right-hand side are related to the ones on the left-hand side by:

$$\begin{pmatrix} \hat{p}/(\bar{\rho}\bar{c}) \\ \hat{u} \end{pmatrix}_r = \begin{bmatrix} B_{11} & B_{12} \\ B_{21} & B_{22} \end{bmatrix} \begin{bmatrix} A_{11} & A_{12} \\ A_{21} & A_{22} \end{bmatrix}^{-1} \begin{pmatrix} \hat{p}/(\bar{\rho}\bar{c}) \\ \hat{u} \end{pmatrix}_l \quad . \tag{3.39}$$

As an analogy to Eq. (2.73), the matrix $\mathbf{T} = \mathbf{B}\mathbf{A}^{-1}$ is sometimes regarded as a transfer matrix, too. The linear system can be rearranged into:

$$\begin{pmatrix} \hat{p}_l/(\bar{\rho}\bar{c}) \\ \hat{u}_r \end{pmatrix} = \mathbf{S} \begin{pmatrix} \hat{p}_r/(\bar{\rho}\bar{c}) \\ \hat{u}_l \end{pmatrix} \quad . \tag{3.40}$$

For quarter wave cavities the boundaries can be assumed as ideal, with $\hat{p}_r = 0$ at the left opened end and $\hat{u}_l = 0$ at the right closed end. In this case, the system given by Eq. (3.40) becomes homogeneous:

$$\mathbf{S} \begin{pmatrix} \hat{p}_r/(\bar{\rho}\bar{c}) \\ \hat{u}_l \end{pmatrix} = \vec{0} \quad . \tag{3.41}$$

To allow also non-trivial solutions, the determinant of such systems has to be zero. This condition $\det\{\mathbf{S}\} = 0$ is given in closed form as:

$$J_{\nu_\mathrm{p}}(\beta_\mathrm{p}\tilde{T}_2^{\sigma_\mathrm{p}}) \left[\alpha_\mathrm{p} J_{-\nu_\mathrm{p}}(\beta_\mathrm{p}\tilde{T}_1^{\sigma_\mathrm{p}}) + \frac{\sigma_\mathrm{p}\beta_\mathrm{p}\tilde{T}_1^{\sigma_\mathrm{p}}}{2}\{J_{-\nu_\mathrm{p}-1}(\beta_\mathrm{p}\tilde{T}_1^{\sigma_\mathrm{p}}) - J_{-\nu_\mathrm{p}+1}(\beta_\mathrm{p}\tilde{T}_1^{\sigma_\mathrm{p}})\}\right] \\ - \; J_{-\nu_\mathrm{p}}(\beta_\mathrm{p}\tilde{T}_2^{\sigma_\mathrm{p}}) \left[\alpha_\mathrm{p} J_{\nu_\mathrm{p}}(\beta_\mathrm{p}\tilde{T}_1^{\sigma_\mathrm{p}}) + \frac{\sigma_\mathrm{p}\beta_\mathrm{p}\tilde{T}_1^{\sigma_\mathrm{p}}}{2}\{J_{\nu_\mathrm{p}-1}(\beta_\mathrm{p}\tilde{T}_1^{\sigma_\mathrm{p}}) - J_{\nu_\mathrm{p}+1}(\beta_\mathrm{p}\tilde{T}_1^{\sigma_\mathrm{p}})\}\right] = 0 \tag{3.42}$$

For given temperature profile and fluid properties, the determinant is only a function of the frequency ω (via the parameter β_p). The roots of this transcendental equation

can be determined numerically and correspond to the eigenfrequencies of the cavity $\det\{\mathbf{S}(\omega_{eig})\} = 0$.

The acoustic impedance at the cavity mouth is used for the characterization of the cavities with polynomial temperature inhomogeneity. Applying the matrix notation given in Eq. (3.39), the ratio between pressure and velocity perturbations can be written as:

$$\frac{1}{\overline{\rho c}}\frac{\hat{p}_r}{\hat{u}_r} = \frac{T_{11}\hat{p}_l + T_{12}\hat{u}_l}{T_{21}\hat{p}_l + T_{22}\hat{u}_l} \quad . \tag{3.43}$$

This ratio corresponds to the reactance of the cavity. It is purely complex-valued, because the underlying wave equation does not account for any dissipation effects. Because the velocity fluctuation has to be zero at the closed left end, the expression for the reactance at the resonator mouth is given as:

$$\begin{aligned}
\Psi_{\mathrm{Q}^*} \;=\; & \bar{\rho}\bar{c}\,\frac{T_{11}}{T_{21}} \;= \\
& -\Big[(i\bar{\rho}\omega((\alpha_\mathrm{p}+\nu_\mathrm{p}\sigma_\mathrm{p})J_{-\nu_\mathrm{p}}(\beta_\mathrm{p}\tilde{T}_1^{\sigma_\mathrm{p}})J_{\nu_\mathrm{p}}(\beta_\mathrm{p}\tilde{T}_2^{\sigma_\mathrm{p}}) + \beta_\mathrm{p}\sigma_\mathrm{p}J_{-1-\nu_\mathrm{p}}(\beta_\mathrm{p}\tilde{T}_1^{\sigma_\mathrm{p}})J_{\nu_\mathrm{p}}(\beta_\mathrm{p}\tilde{T}_2^{\sigma_\mathrm{p}})\tilde{T}_1^{\sigma_\mathrm{p}} \\
& \quad -J_{-\nu_\mathrm{p}}(\beta_\mathrm{p}\tilde{T}_2^{\sigma_\mathrm{p}})\Big((\alpha_\mathrm{p}-\nu_\mathrm{p}\sigma_\mathrm{p})J_{\nu_\mathrm{p}}(\beta_\mathrm{p}\tilde{T}_1^{\sigma_\mathrm{p}}) + \beta_\mathrm{p}\sigma_\mathrm{p}J_{-1+\nu_\mathrm{p}}(\beta_\mathrm{p}\tilde{T}_1^{\sigma_\mathrm{p}})\tilde{T}_1^{\sigma_\mathrm{p}}\Big))\tilde{T}_2^{1/n_\mathrm{p}}\Big]\Big/ \\
& \Big[a_\mathrm{p}n_\mathrm{p}\Big(\quad \Big((\alpha_\mathrm{p}-\nu_\mathrm{p}\sigma_\mathrm{p})\; J_{\nu_\mathrm{p}}(\beta_\mathrm{p}\tilde{T}_1^{\sigma_\mathrm{p}}) \;+\beta_\mathrm{p}\sigma_\mathrm{p}J_{-1+\nu_\mathrm{p}}(\beta_\mathrm{p}\tilde{T}_1^{\sigma_\mathrm{p}})\tilde{T}_1^{\sigma_\mathrm{p}}\Big) \\
& \qquad\quad \Big((\alpha_\mathrm{p}+\nu_\mathrm{p}\sigma_\mathrm{p})J_{-\nu_\mathrm{p}}(\beta_\mathrm{p}\tilde{T}_2^{\sigma_\mathrm{p}}) + \beta_\mathrm{p}\sigma_\mathrm{p}J_{-1-\nu_\mathrm{p}}(\beta_\mathrm{p}\tilde{T}_2^{\sigma_\mathrm{p}})\tilde{T}_2^{\sigma_\mathrm{p}}\Big) \\
& \qquad - \quad \Big((\alpha_\mathrm{p}+\nu_\mathrm{p}\sigma_\mathrm{p})J_{-\nu_\mathrm{p}}(\beta_\mathrm{p}\tilde{T}_1^{\sigma_\mathrm{p}}) + \beta_\mathrm{p}\sigma_\mathrm{p}J_{-1-\nu_\mathrm{p}}(\beta_\mathrm{p}\tilde{T}_1^{\sigma_\mathrm{p}})\tilde{T}_1^{\sigma_\mathrm{p}})\Big) \\
& \qquad\qquad \Big((\alpha_\mathrm{p}-\nu_\mathrm{p}\sigma_\mathrm{p})\; J_{\nu_\mathrm{p}}(\beta_\mathrm{p}\tilde{T}_2^{\sigma_\mathrm{p}}) + \beta_\mathrm{p}\sigma_\mathrm{p}J_{-1+\nu_\mathrm{p}}(\beta_\mathrm{p}\tilde{T}_2^{\sigma_\mathrm{p}})\tilde{T}_2^{\sigma_\mathrm{p}})\Big) \quad \Big)\Big] \quad .
\end{aligned} \tag{3.44}$$

For given temperature profile and fluid properties, it is again only a function of frequency ω.

3.6 Decoupled Analysis

In a general sense, the behavior of a given system depends on its own system dynamics subjected to certain boundary conditions. However, from a practical point of view, a study restricted to the boundary conditions can also provide valuable preliminary conclusions. Thus, as a starting point, the stabilizing influence of resonators might be assessed by a decoupled analysis that considers only the impedance expressions by which they are described. In the same way, the sensitivity of the cavities to changes in their local environment can be estimated as a first approximation, too. Note that this is a preliminary study that should serve as a reference. In the next Ch. 4, the stabilizing influence of the cavities attached to a rocket thrust chamber will be studied. It will be shown that a fully coupled analysis provides a much more accurate description of the damping behavior of resonators.

3.6.1 Preliminary Estimation of Sensitivity to Temperature Inhomogeneity

As stated by Acker and Mitchell [4], the gas filling the resonator cavities can locally exhibit strong temperature differences because the cavities are placed on cooled chamber walls. From the few documented cases in the literature, a sudden rise in the wall surface temperature of the chamber can be expected upon the occurrence of combustion instability. This will in turn lead to an increase in the cavity mouth temperature increasing the temperature inhomogeneity ratio in the cavities. Indeed, such strong temperature spatial variations have been measured by Oberg [93] during full-scale test programs.

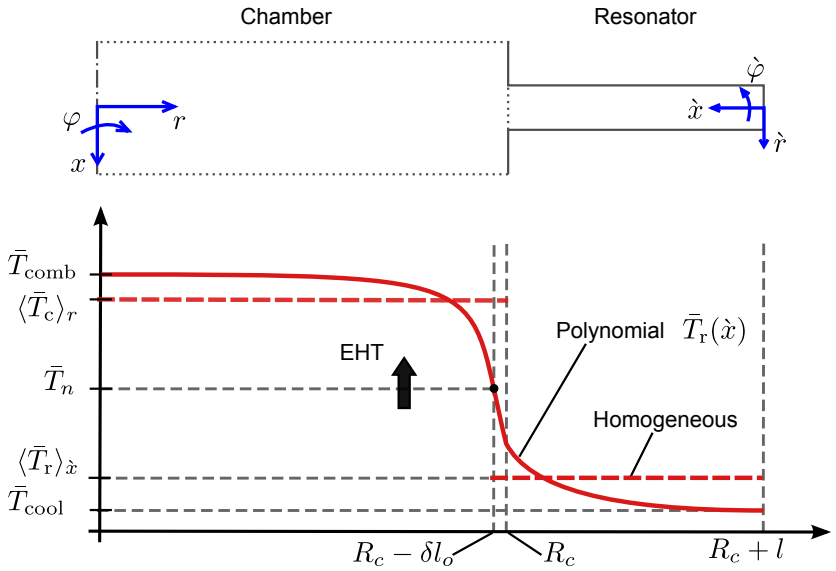

Figure 3.12: Temperature levels present in the rocket thrust chamber

Without going into the detailed mechanisms leading to this rise in temperature or heat load, this first approximated analysis simply assumes a higher neck temperature. The situation is sketched in Fig. 3.12, where the radial temperature dependency in the chamber and cavities is given at the axial location where the resonator ring is placed. The chamber radius is denoted by R_c. The temperature range is bounded by the cooling temperature T_{cool} and the combustion temperature T_{comb}, which are assumed to be constant even in the case of an instability. At the radial position $r = R_c - \delta l_o$ the cavity neck temperature T_n is measured. Due to the mean flow in the chamber section, the thermal boundary layer on this side is small and a steep temperature gradient is expected. On the cavity side, no mean flow is present and the cavity temperature decreases smoother towards the cooling temperature. If enhanced heat transfer appears due to an instability, the neck temperature T_n will rise, leading also to a change in the cavity temperature distribution. For simplicity, a second reference coordinate system $\grave{x}, \grave{r}$ and $\grave{\varphi}$ is defined with origin at the cavity's closed end. As a first approximation, the gas temperature in the cavity $\bar{T}_r$ is assumed to be homogeneous in the transverse plane but to vary along the cavity axial direction. This cavity temperature distribution can be given by Eq. (3.32) in form of a polynomial function. Introducing the inhomogeneity ratio

$$\chi = \frac{\bar{T}_n}{\bar{T}_{\mathrm{cool}}} \quad , \tag{3.45}$$

and imposing the previously described boundary conditions to Eq. 3.32, the non-dimensional temperature profile can be written as:

$$\frac{\bar{T}_\mathrm{r}(\grave{x})}{\bar{T}_\mathrm{cool}} = \left[\left(\chi^{1/n_\mathrm{p}} - 1\right)\frac{\grave{x}}{l_e} + 1\right]^{n_\mathrm{p}} \quad . \tag{3.46}$$

Figure 3.13 shows three exemplary profiles with increasing temperature inhomogeneity. A polynomial of the order $n_\mathrm{p} = 8$ is used. The corresponding average values can be determined from the axial integration of Eq. (3.46):

$$\frac{\langle\bar{T}_\mathrm{r}\rangle_{\grave{x}}}{\bar{T}_\mathrm{cool}} = \frac{1}{l_e\bar{T}_\mathrm{cool}}\int_0^{l_e}\bar{T}_\mathrm{r}\,d\grave{x} = \frac{\chi^{\frac{n_\mathrm{p}+1}{n_\mathrm{p}}} - 1}{(n_\mathrm{p}+1)\left(\chi^{1/n_\mathrm{p}} - 1\right)} \quad . \tag{3.47}$$

These homogeneous profiles are also shown in Fig. 3.13 by dashed lines.

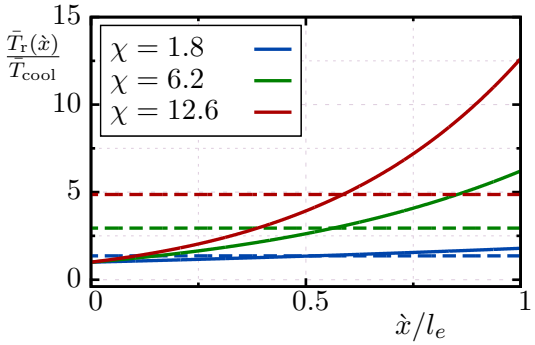

Figure 3.13: Assumed temperature profiles along the cavities for three different inhomogeneity ratios. Dashed lines denote the corresponding average value.

The first goal of this section is to estimate the influence of the inhomogeneity by comparing the two previously described approaches: state of the art with average homogeneous temperature versus the extended approach taking the inhomogeneity into account. For this purpose, a resonator ring configuration described by Tab. 3.1 is used.

Table 3.1: Geometrical and thermodynamical parameters of resonator ring for the decoupled analysis.

l/R_c	d/R_c	n_r	ϵ_{nl}	n_p	γ	$P_c/(\rho_{cool}\gamma R_s T_{cool})$
0.089	0.467	22	50	8	1.8	32.6

Figure 3.14 shows the absorption coefficient against frequency for the three different inhomogeneity ratios. The eigenfrequency of a cavity kept at a homogeneous cooling temperature $\omega_o = 2\pi\sqrt{\gamma R_s\bar{T}_\mathrm{cool}}/(4l_e)$ is used to normalize the frequency. Due to the increment in average temperature, for increasing inhomogeneity ratio the eigenfrequencies of the cavities and thus the absorption maxima are shifted towards higher frequencies. Furthermore, the higher viscosity at the cavity mouth increases the resistance. The chosen configuration is underdamped, and thus, this increment of resistance has a positive impact, because the absorption approaches its optimum value of unity. However, for overdamped systems, this would cause exactly the opposite effect. Finally, this figure clearly shows that the bandwidth of operation predicted by the approach

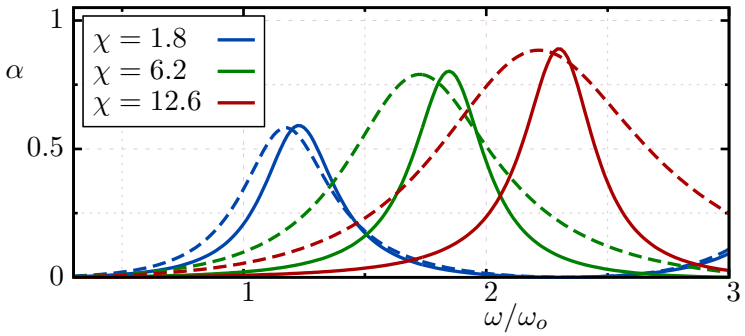

Figure 3.14: Absorption coefficient α as a function of the normalized frequency for the three assumed temperature profiles. Continuous lines give the real dependency taking the inhomogeneity into account, dashed lines denote the approximated approach using the homogeneous average value.

accounting the inhomogeneity is considerably thinner than the one predicted by the homogeneous approach. In contrast to the other two just mentioned effects (shift of eigenfrequencies to higher values and increased resistance), the third effect (narrowing of the high absorption frequency range) was rather unexpected.

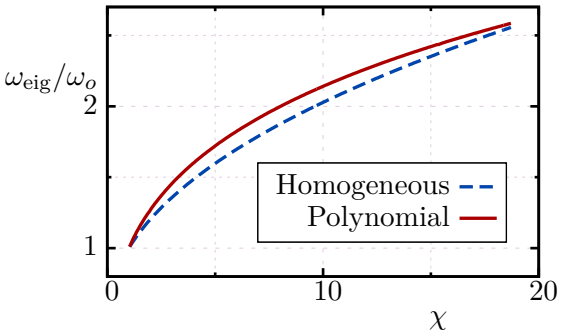

Figure 3.15: Dependency of the first eigenfrequency on the inhomogeneity ratio χ.

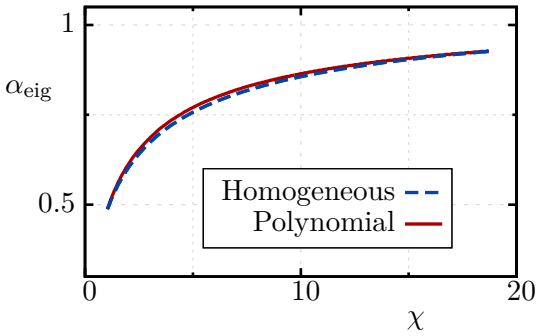

Figure 3.16: Absorption coefficient α_{eig} at resonance versus the inhomogeneity ratio χ.

At resonance, predictions of eigenfrequencies with both approaches differ only slightly from each other. This can be seen in Fig. 3.15 where the first eigenfrequency of the cavity is plotted against the inhomogeneity ratio for both impedance models. Similarly, the maxima in absorption for the different temperature inhomogeneity ratios predicted by the two approaches is very similar, as can be seen in Fig. 3.16. Thus, considering only this optimal design point given by the eigenfrequency of the cavities, the accuracy of the lumped temperature approach is very good.

However, the higher the inhomogeneity ratio, the stronger the differences between the two approaches at off-design frequencies. This can be seen in Fig. 3.17, where the absorption coefficient is plotted against the inhomogeneity ratio at an off-design frequency $\omega_{\text{off}} = 1.1\omega_{\text{eig}}$. While the homogeneous approach predicts a continuously growing absorption coefficient within the investigated temperature ranges, the polynomial approach predicts a maximum in absorption at approximately $\chi \approx 6.5$. For higher inhomogeneity ratios the absorption decreases towards values lower than 50%. This

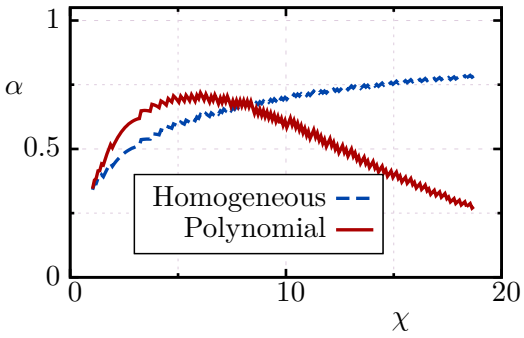

Figure 3.17: Absorption coefficient α for an off-design frequency $\omega_{\text{off}} = 1.1\omega_{\text{eig}}$ versus the inhomogeneity ratio χ.

difference is quite strong, considering that a relatively small frequency mismatch of 10% is investigated. Thus, a quarter wave cavity with strong temperature inhomogeneity is more sensitive to changes in operation conditions.

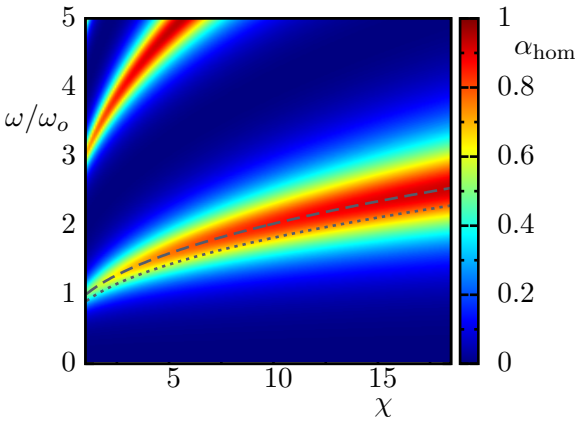

Figure 3.18: Dependency of the absorption coefficient on the temperature ratio and frequency using the homogeneous approach.

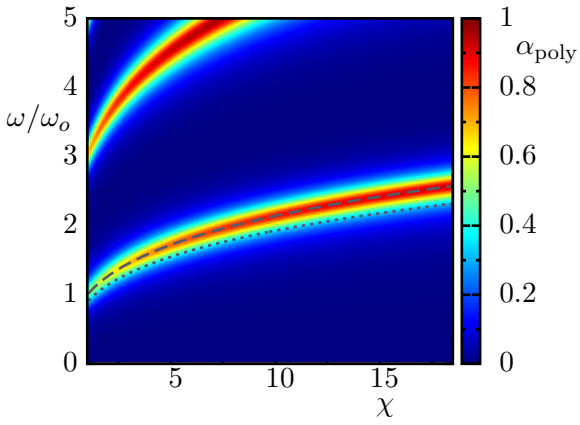

Figure 3.19: Dependency of the absorption coefficient on the temperature ratio and frequency using the polynomial approach.

To gain a more striking picture of this reduction in bandwidth of operation, Figs. 3.18 and 3.19 compare the absorption coefficients predicted by the two approaches for the whole range of frequencies and temperature ratios investigated in this preliminary study. The dashed lines correspond to the eigenfrequency of the cavities, while the dotted lines indicate a 10% offset from that optimal frequency. They are shown here to serve as a reference, since their paths are plotted in Figs. 3.15 and 3.17. It can clearly be seen that the peaks predicted by the polynomial approach are considerably narrower than the ones predicted by the homogeneous approach.

As a conclusion of this preliminary decoupled analysis, a strong temperature inhomogeneity in the gas filling the cavities has three major consequences:

(i) A slight shift of cavity eigenfrequency.

(ii) Since the inhomogeneity is accompanied by a higher neck temperature, the viscosity at the cavity mouth increases. This leads to a larger resistance that might bring the resonator ring in the over-damped region.
(iii) The strongest impact is a reduction of the frequency bandwidth of cavity operation.

The more surprising effect is certainly the third one. Thus, in order to accurately predict the stabilizing influence of acoustic cavities with strong temperature inhomogeneity, the approach proposed in Sec. 3.5 should be used.

3.6.2 Uncertainty Analysis Concerning the Non-Linear Resistance Factor

The non-linear resistance factor ϵ_{nl} that appears in the expressions for cavity impedance, i.e. Eq. (3.22), has to be modeled empirically. The measurements reported in the literature and plotted in Fig. 3.5 span almost two orders of magnitudes for comparable SPL's. To account for the impact of this factor on the efficiency of resonator rings, the absorption coefficient for the resonator ring described by Tab. 3.1 is computed within a range of frequencies and non-linear factors. A moderate inhomogeneity ratio of $\chi = 6$ is imposed inside the cavities. The results using both the homogeneous and the polynomial approach are given in Figs. 3.20 and 3.21, respectively. The different harmonics of the cavities are clearly displayed at the absorption local maxima in the frequency axis. Furthermore, for a non-linear resistance value of approximately $\epsilon_{nl} \approx 150$ the absorption has its overall maximum. For larger values the resonator ring is overdamped and the absorption starts to decrease again. In accordance to the results of the inhomogeneity sensitivity, the polynomial approach suggests considerable thinner frequency bandwidths of efficient absorption, even for the moderate inhomogeneity ratio imposed.

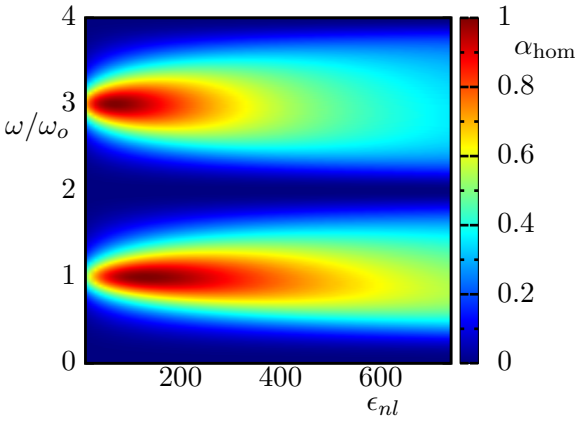

Figure 3.20: Dependency of the absorption coefficient on the non-linear resistance factor for an inhomogeneity ratio $\chi = 6$ using the homogeneous approach.

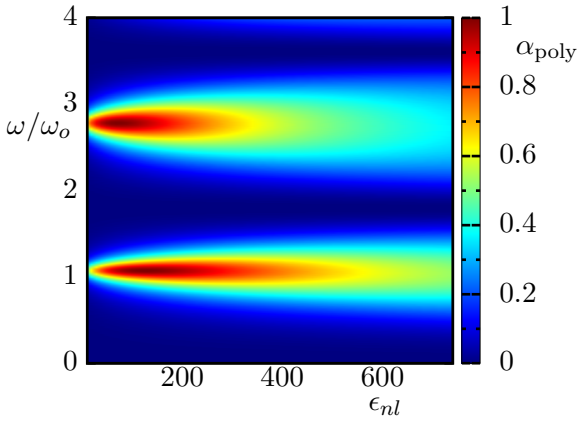

Figure 3.21: Dependency of the absorption coefficient on the non-linear resistance factor for an inhomogeneity ratio $\chi = 6$ using the polynomial approach.

4 Method to Account for The Stabilizing Influence of Resonator Rings on Rocket Thrust Chambers

The previous chapter presented some models for the characterization of resonators that are able to account for gas temperature inhomogeneity inside the cavities. It has been assumed that this temperature inhomogeneity has been caused by the occurrence of enhanced heat transfer. However, as pointed out in Sec. 1.2, the functionality (performance) of resonator rings should be evaluated through a stability analysis that takes the main driving and damping mechanisms present in the chamber into account.

This chapter starts with an overview of available thermoacoustic stability prediction tools commonly used in the design of rocket thrust chambers. Based on this review, a method to evaluate the performance of resonator rings under representative operation conditions will be presented, that offers some advantages for the present application. The method requires some extensions to existing models and considerations for its application in rocket thrust chambers. This is especially the case for the integration of the resonator ring in the analysis. After a thorough validation of the method, the stabilizing influence of a resonator ring, that is to say its impact on the growth rates of the coupled system, is predicted and the mechanisms leading to the stabilization are discussed. This leads to a better understanding of the effectiveness of resonator rings. Furthermore, this chapter presents the results of some sensitivity analysis concerning key geometrical parameters of resonator rings. Finally, the consequences of a gas temperature inhomogeneity inside the cavities presumably caused by enhanced heat transfer are evaluated.

This method has been published by the author in a preliminary formulation in [13]. The present formulation given in this thesis accounts some extensions and improvements, and has been published also by the author in [17, 18]. Part of the results presented in this section can be found in these publications, too.

4.1 Overview of Available Thermoacoustic Stability Prediction Methods

The range of time and length scales involved in a rocket thrust chamber is wide and not all of them can be considered in the same extent in a global stability analysis. Thus, approximate methods are indispensable. The majority of the approximate approaches for stability prediction available in the literature are based on the so-called perturbation equations. By expressing all variables involved as the sum of time average and fluctuating parts, the complete set of Navier-Stokes equations can be approximated up

to certain order. An overview of the derivation of these methods has been given by Culick [24]. In recent years, advances in computational resources have made the numerical solution of these equations by means of FDM feasible, see for example [86, 101]. Even if detailed geometries can be studied in this way, important issues like computational cost, code stability and application of boundary conditions are not totally solved yet.

As stated by Culick [24], the primary source of information concerning combustion instabilities is given by the oscillations of pressure p'. Thus, in the approximate methods proposed by Culick and co-workers, an inhomogeneous wave equation for the fluctuating pressure p' is derived from the perturbation equations, see Sec. 2.2 and App. A.1. Using a transformation into a velocity potential, an alternative wave equation is used in a similar way by Zinn et al. [132]. The wave equation is inhomogeneous due to mean flow and various source terms present in the perturbation equations. A modified Galerkin approach based on the application of the method of weighted residuals proposed by Zinn and Powell [133] can be used to solve the inhomogeneous wave equation for simplified cylindrical geometries and various boundary conditions. The essence of this semi-analytical approach is to express the unsteady pressure field as a superposition of the basic acoustic modes with time varying modal amplitudes. These basic acoustic modes correspond to solutions of the homogeneous wave equation with hard boundaries and form an orthogonal basis. Multiplication of the wave equation by a series of test functions - normalized basic acoustic modes - and integration over the chamber domain leads to a system of equations for the amplitudes of the perturbed solution, which can be solved by means of least residuals. In its general form, the method is capable of handling non-linear behavior with mode coupling [24]. Culick also proposed a linear stability analysis transforming the previously described approach from the time into the frequency domain [24]. Assuming linearity, all variables involved can be expressed with harmonic time dependence. One advantage of treating the problem in the frequency domain is that non-trivial acoustic boundary conditions are quite easy to apply. Non-trivial acoustic boundary conditions include frequency dependent impedance expressions, as is for example the case for the models describing the behavior of resonator cavities and given in Ch. 3. The transformation of such an expression into the time domain via inverse Fourier transformation requires the evaluation of a convolution integral [100]. This cumbersome procedure is avoided in a complete frequency domain formulation of the problem. Substitution of the linear harmonic approach into the system of equations for the amplitudes delivers a set of expressions for the eigenfrequencies of the system, from which stability can be deduced.

A similar linear approach has been developed by Mitchell and co-workers [4, 82]. He transformed the linearized inhomogeneous Helmholtz equation (frequency domain) into a surface integral following the Green's function approach and integrating over the chamber surface. The resulting frequency dependent integral equation holds only at the eigenfrequencies of the system. Thus, for given parameters, the solutions of this equation delivers the eigenfrequencies of the system, from which the linear stability can be deduced. Mitchell solved the integral equation iteratively expressing the Green's function also as a superposition of the classical acoustic modes with hard boundaries. Up to second order, the methods of Culick and Mitchell are equivalent [24].

The solution of the Helmholtz equation can also be achieved numerically using three dimensional Helmholtz tools. This has the advantage that several additional effects like

stratification, complex geometries, source terms, etc. can be considered in the linearized Helmholtz equation. The resulting Helmholtz equation can be solved by techniques based on the FEM [43, 91, 103].

Despite the simplistic assumptions of linearity, uniform flow, constant properties and so on, the semi-analytical approaches based on modes give insight in global trends and help in the fundamental understanding of the problem [113]. Furthermore, they are fast and thus afford parameter studies for optimization at early design stages. On the other hand, the resulting complex-valued equations for the eigenfrequencies have several solutions. In addition to the numerical complexity of solving them, it is not always simple to assure that all possible solutions in the parameter range of interest have actually been found. Furthermore, the expressions describing the different boundary conditions present in the system have to be known also for complex-valued frequencies, simply because a non-zero growth rate of an eigenmode implies a non-zero imaginary part of the corresponding eigenfrequency. If the expressions are given in closed form this is not a serious issue, while for expressions based on tabulated values from semi-analytical approaches – as it will be the case for the resonator rings in the present study – it brings considerably more computational effort. For data based on forced experiments, this might not be possible because only real frequencies can be excited. Another issue present in the two previously described methods is that, since the acoustic field is expressed as superposition of classical acoustic modes with hard boundaries, the solutions do not accurately reproduce the field near reactive and dissipative boundaries. Culick acknowledged this issue [24] and argued that the errors are small if the perturbation order is also small.

4.2 Proposed Method Based on Network Models and Nyquist Plot

As stated by Mitchell [82], in order to accurately predict the stabilizing influence of resonators in rocket thrust chambers, the main driving and damping mechanisms have to be taken into account. Attached to the shell of the thrust chamber, the resonators will interact with a three-dimensional acoustic pressure field. This acoustic field in turn is influenced by the mean flow, the combustion flame front, the injector plate and the choked nozzle. Thus, the resonator ring interacts through the acoustic field indirectly with the just mentioned effects. Thus, an appropriate method that accounts for the linear stability of the coupled system, chamber and resonator ring, is necessary to evaluate the performance of resonator rings. The method should fulfill some requirements: firstly, account for the just mentioned main driving and damping mechanisms present in the chamber, secondly, allow the incorporation of the resonator models presented in Ch. 3, and thirdly, afford parametric studies on critical resonator features.

The three-dimensional computational tools that solve linearized perturbation equations either in time or frequency domain can certainly reproduce the main driving and damping mechanisms present in the thrust chamber, as shown by [42, 86, 101]. They also allow the incorporation of resonator ring models as boundary conditions, although this is accompanied by some non-trivial difficulties concerning the code stability. Furthermore, the necessary computational efforts are not be underestimated, making the

parametric studies intended in this thesis not really feasible. Note that this decision concerns only the studies intended in the present investigation, where the focus lies on the resonator rings. Actually, such codes provide quite promising capabilities for the stability prediction of rocket thrust chambers. This is the scope of a parallel project within the SFB-TRR40 (project C3).

The linear stability analysis of Culick [24] and Mitchel et al. [82] fulfill the three requirements mentioned at the beginning of this section. However, their numerical implementation is not trivial, because the whole method is encapsulated into a single integral equation over the chamber boundaries and the solution procedure is iterative. Thus, convergence might play an important role. Furthermore, three issues related to such methods have been mentioned in Sec. 4.1: (i) complex root finding, (ii) necessity of boundary expressions over the whole complex-valued frequency range and (iii) inaccurate pressure field close to reactive and dissipative boundaries. The third issue is of minor importance, since the errors are small provided that the perturbation order is also small. In contrast, the former two can indeed lead to serious difficulties.

In this thesis, a different method for linear stability analysis of rocket thrust chambers is proposed, that fulfills the necessary requirements and overcomes the three issues mentioned above. Instead of solving the Helmholtz equation iteratively over the whole chamber domain, the acoustic field is constructed piecewise using cylindrical segments following the acoustic network approach introduced in Sec. 2.2.3. The acoustic field in the segments is described analytically in terms of up- and downstream traveling waves, i.e. Eq. (2.49) for a simple duct segment with hard shell. Exact solutions for additional segments or boundary types necessary for the description of rocket thrust chambers, like resonator rings, flame, nozzle and so on, will be presented later on in this chapter. Decisive is that the expressions describing the segments are exact solutions of the Helmholtz equation that fully satisfy the corresponding boundary conditions, thus resolving issue (iii). At connecting planes between two different segments, the compact elements introduced also in Sec. 2.2.3 are employed. As will be shown in Sec. 4.3.2, mode matching techniques based on the Galerkin approach can be applied for this purpose. They are similar to those used in ducts with discontinuous shell impedances widely studied in the field of aero engines with regard to suppression of noise. Finally, the linear stability of the acoustic network can be determined with the Nyquist-plot method introduced in Sec. 2.2.5 if some considerations for its application above cut-on are taken. The number and location of the eigenfrequencies present in the frequency range of interest are inferred graphically from the Nyquist-plot. The complex root finding procedure is avoided in this way, overcoming issue (i). Furthermore, since only transfer matrix coefficients at purely real valued frequencies are needed for the stability prediction, tabulated data used either by boundary conditions or semi-analytical solutions of the different segments reduces considerably. Thus, the application of the Nyquist-plot method overcomes issue (ii), too.

In addition to the advantages just mentioned, the acoustic network approach allows a strong flexibility, because the different mechanisms can be separated into elements that can be handled more easily. In this way, the network representation of the thrust chamber can be easily adapted, extended or improved by simply changing some of the elements without changing the solution procedure. Even elements derived from empirical approaches based on tabulated data can be incorporated via the Nyquist-plot technique. In the present case, the focus lies on the element representing the

resonator ring. For the elements representing the rest of the chamber, well established models are used. Finally, the "Fachgebiet für Thermodynamik" hosting this project owns a large expertise in the application of acoustic networks [72].

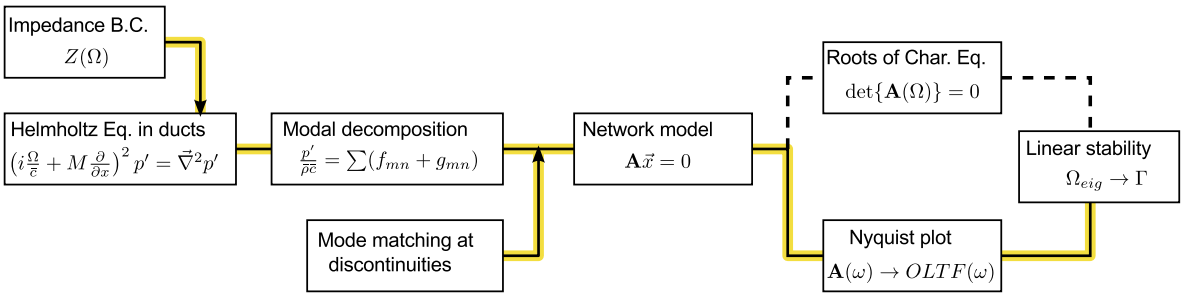

Figure 4.1: Block diagram for the proposed method to predict stability of rocket thrust chambers.

Figure 4.1 gives a block diagram of the proposed method. The three-dimensional Helmholtz equation is solved for simple duct segments with uniform mean flow, constant fluid properties and shell impedance boundary condition. The solutions on each segment are readily found and can be decomposed into linearly independent up- and downstream traveling waves. At discontinuities, where duct segments of different properties join, proper mode matching conditions based on the conservation of mass and momentum are applied. The characteristic amplitudes of the traveling waves at the connecting ports between the different duct segments are used to build a network model of the thrust chamber. With proper terminations as impedance models for the injector plate and nozzle, the network system can be characterized by the system matrix $\mathbf{A}$ and the vector of characteristic amplitudes $\vec{x}$, see Sec. 2.2.3. Instead of solving the characteristic equation to find the complex eigenfrequencies and thus the stability of the system (path with the dashed lines), the Nyquist-plot method described in Sec. 2.2.5 is used to estimate the eigenfrequencies.

4.3 Considerations and Necessary Extensions for Proposed Method

The application of the method sketched in Fig. 4.1 to systems in which also transverse acoustic waves propagate, as it is the case in rocket thrust chambers, is novel. The proposed method requires some considerations and extensions compared to the state of the art network approaches described in Sec. 2.2.3. In this section, these considerations will be reviewed.

4.3.1 Propagation of Acoustic Waves in Cylindrical Ducts with Arbitrarily Shell B.C.

To study the influence of resonator rings on the propagation of three-dimensional transverse waves along the generic thrust chamber, the propagation of acoustic waves in cylindrical ducts with locally reactive and dissipative shell is needed. For the solution of the three-dimensional Helmholtz equation semi-analytical approaches are well

established [65, 88]. The approach followed in this thesis is reviewed here due to its importance in the interpretation of the results.

The general solution given by Eq. (2.40) holds also for this case. However, a different radial boundary condition is needed to close the problem. In the presence of an homogeneous axial mean flow, the radial impedance boundary condition for a surface with frequency dependent impedance $Z(\Omega)$ and normal vector perpendicular to the mean flow is given by Myers [89] as:

$$\hat{v} = \left(1 - i\frac{U}{\Omega}\frac{\partial}{\partial x}\right)\left(\frac{\hat{p}}{Z}\right) \quad . \tag{4.1}$$

Combination of Eq. (4.1) with the radial component of the linearized momentum equation:

$$\bar{\rho}\left(i\frac{\Omega}{\bar{c}} + M\frac{\partial}{\partial x}\right)\vec{\hat{v}} + \vec{\nabla}\frac{\hat{p}}{\bar{\rho}\bar{c}} = \vec{0} \quad , \tag{4.2}$$

allows to cancel the radial velocity fluctuation [65]:

$$-\frac{i\Omega}{\bar{\rho}}\frac{\partial\hat{p}}{\partial r} = \left(i\Omega + U\frac{\partial}{\partial x}\right)^2 \frac{\hat{p}}{Z(\Omega)} \quad . \tag{4.3}$$

Substitution of $\hat{p}$ from Eq. (2.40) into the previous relation gives an eigenvalue equation for the frequency Ω. For the hard-wall case with $\hat{v} = 0|_{r=R_c}$ and thus $Z \to \infty$, Eq. (4.3) simplifies to Eq. (2.42). In the more general case of finite impedance $Z(\Omega)$, Eq. (4.3) can be written after some rearrangement as:

$$-i\Omega Z\frac{\frac{\partial}{\partial r}\left(J_m(\alpha r)\right)_{r=R_c}}{J_m(\alpha R_c)} + \bar{\rho}(\Omega - Uk)^2 = 0 \quad . \tag{4.4}$$

The essential difference to the hard wall case is that this equation for the boundary condition is complex-valued and frequency dependent. Thus, the radial wave numbers are complex-valued, frequency dependent, and generally not identical for the up- and downstream traveling waves:

$$\alpha^+_{mn} \neq \alpha^-_{mn} = f(\Omega) \qquad \in \mathbb{C} \quad . \tag{4.5}$$

Elimination of the radial wave numbers by substituting the dispersion relation Eq. (2.37) into Eq. (4.4) would give two expressions defining the axial wave numbers k_{mn}. However, the first term on the left-hand side is a meromorphic function in αr, i.e. its solution does not depend on the choice of branch $\alpha = \pm\sqrt{(\Omega/\bar{c} - Mk)^2 - k^2}$ [113]. Thus, only one transcendental equation per tangential order m has to be analyzed. Using an identity for the integer order Bessel function derivative [11]:

$$\frac{d}{dx}J_m(x) = J_{m-1}(x) - \frac{m}{x}J_m(x) \quad , \tag{4.6}$$

and evaluating it at the cylinder shell, the dispersion relation derived from the boundary condition is given by:

$$-i\Omega Z\left[\sqrt{(\Omega/\bar{c} - Mk)^2 - k^2}\frac{J_{m-1}(\sqrt{(\Omega/\bar{c} - Mk)^2 - k^2}R_c)}{J_m(\sqrt{(\Omega/\bar{c} - Mk)^2 - k^2}R_c)} - \frac{m}{R_c}\right] + \bar{\rho}(\Omega - Uk)^2 = 0 \quad . \tag{4.7}$$

There exist several algorithms capable of solving this complex equation. Here, the expression given by Eq. (4.7) is split into a system of two real equations, one for the real and an other for the complex part, respectively. The non-linear system is then solved numerically with the Newton method in the frequency range of interest. For each tangential order m and frequency Ω, Eq. (4.7) has an infinite number of roots distributed over the whole complex plane. The various roots correspond to the various radial orders of the upstream and downstream traveling waves. For systems with multiple solutions, the initial guess decides which root will be found by the Newton method. At low frequencies, the axial wave numbers of the hard wall duct can be used as initial guess for the Newton method and at the same time to identify the upstream and downstream axial wave numbers. Following an iterative marching approach [5, 65] the frequency dependency of each tangential m and radial order n is then computed. Using the previous solution as initial guess, Eq. (4.7) is solved subsequently for a slightly higher frequency. With this algorithm, a table of discrete values for the wave numbers can be calculated within the chosen frequency range of interest.

Depending on the impedance expression in Eq. (4.7), additional transverse duct modes may appear, that are not present in a hard walled duct. These additional modes are usually referred to as *surface waves*, because the pressure fluctuations within their transverse mode shape are confined into a very small region close to the reactive cylinder shell. The physical interpretation of these additional modes is a difficult task. They are sometimes recognized as an hydrodynamic instability. A thorough analysis of such modes is given by Rienstra [113].

As an example, the wave numbers of the first tangential mode for a soft-wall duct modeling the resonator ring of the generic thrust chamber are shown in Figs. (4.2) and (4.3) for real frequencies ω. The impedance boundary condition given by Eq. (3.23) is used. As a reference, the hard wall wave numbers are shown, too. For the hard wall case in Fig. (4.2), the cut-on frequency is clearly displayed at the point where the imaginary part of the axial wave numbers vanishes. In the soft-wall cases, the modes are damped because the imaginary part approaches only asymptotically the value zero. As expected, for higher resistance factors ϵ_{nl} the system becomes overdamped and the curves converge towards the hard-wall case. A physical justification for the usage of such high non-linear resistance factors can be vortex shedding in the region of the cavity mouth, as mentioned by Ingard [55]. Near the eigenfrequency of the resonators, the curves perform a loop, which increases the imaginary part and suggests additional damping. For the radial wave numbers shown in Fig. (4.3), the curves of the soft-wall cases converge also towards the hard-wall constant value of $\eta_{10} = 1.8412$ for increasing resistance. Furthermore, due to the mean flow, the upstream α_{1n}^{-} and downstream α_{1n}^{+} radial wave numbers differ slightly from each other.

4.3.2 Integral Mode Matching at Discontinuities

The expressions presented in Sec. 2.2.1 and 4.3.1 describe the propagation of acoustic waves in duct segments with homogeneous properties and boundary conditions. Due to linearity, the general solution may be represented as a sum over orthogonal modes, which can be treated independently from each other. At a discontinuity, caused for example by connecting two duct segments of different properties, the traveling waves get

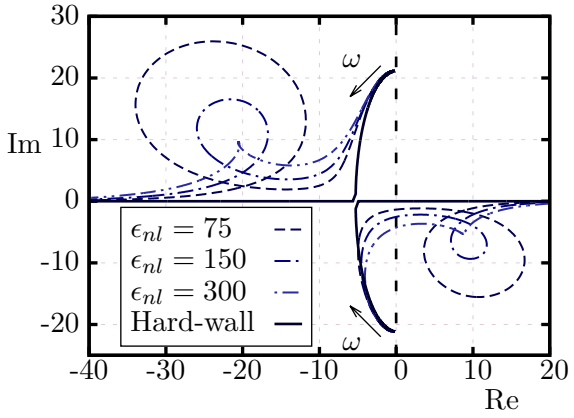

Figure 4.2: Axial wave numbers of the first tangential mode for various resistance factors. Upper branches give k_{10}^{+} while lower branches give k_{10}^{-}.

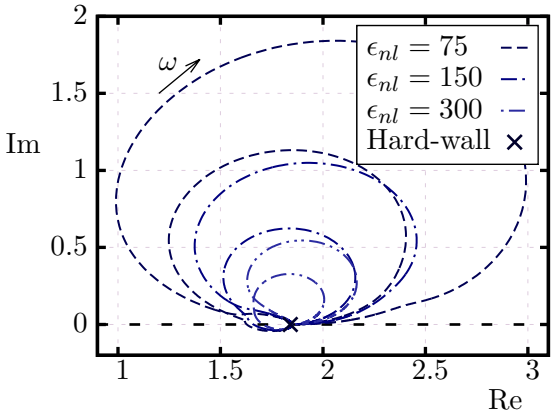

Figure 4.3: Radial wave numbers of the first tangential mode for various resistance factors. Upper branches give α_{10}^{+} while lower branches give α_{10}^{-}.

partially reflected and partially transmitted. In Sec. 2.2.3, compact network elements of vanishing thickness have been introduced, that can be used to model such kind of discontinuities. However, if the radial wave numbers across the jump differ from each other, proper matching conditions have to be applied to satisfy the acoustic field. As will be shown in this section, the modes cannot be treated independently any more, at least in the vicinity of the discontinuity. This behavior was referred to as mode coupling in Sec. 2.2.3.

In this study, two types of discontinuities arise in the network representation of the sample thrust chamber. The first one is a jump in temperature at the position of the compact flame. The second type corresponds to the jumps in cylinder shell impedance at the connecting planes of the resonator ring: from $Z_{shell} = \infty$ to $Z_{shell} = Z_{eq,R}$ and vice versa.

For the jumps in temperature, the radial wave numbers across the discontinuity are equal and only the axial numbers differ. The traveling waves will be reflected and transmitted in the same mode order and no mode coupling will occur. Thus, mode matching is not needed in this case. The scattering in the same mode order can be determined by the Rankine-Hugoniot relations as shown later in Sec. 4.5.1.

Whereas a discontinuity caused by connecting two duct segments of different shell impedance, the radial wave numbers, and thus the mode shapes, may differ particularly close to the eigenfrequencies of the cavities. For the application of resonator rings in rocket thrust chambers, the interest lies on the scattering at a plane connecting a hard- to a soft-wall duct segment and vice versa. However, the method presented here can be applied to a connecting plane of arbitrary impedance, e.g. two resonator rings equipped with different cavities.

Consider a cylindrical duct of radius R_c with a discontinuity in the wall impedance at axial position $x = 0$ as shown in Fig. 4.4. The left part of the duct, $x < 0$, has a hard wall where the radial acoustic velocity at the wall vanishes, i.e. $v'(r = R_c) = 0$. The shell of the right part of the duct, $x > 0$, is characterized by a frequency dependent

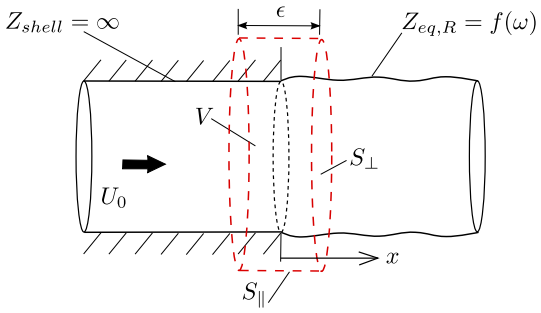

Figure 4.4: Control volume enclosing a shell impedance discontinuity.

impedance $Z_{eq,R} = f(\omega)$ and the radial velocity does not necessarily have to be zero there. Mode shapes and axial propagation are determined in each segment by the method described in Sec. 4.3.1.

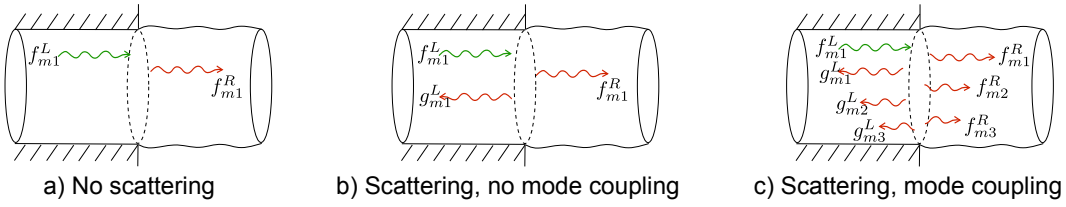

Figure 4.5: Sketch of three different approaches for the description of a jump in wall impedance.

To close the problem, the characteristic amplitudes $F^{R/L}_{mn}$ and $G^{R/L}_{mn}$ of the corresponding waves on the left and on the right of the discontinuity at position $x = 0$ have to be related to each other. This procedure is usually called "mode-matching". Figure 4.5 shows three approaches of increasing complexity. In the simplest one, a), all scattering is neglected and an incoming wave is just transmitted. For cases in which the radial wave numbers differ only slightly between the two connected regions, this is a reasonable first approximation. Approach b) allows some scattering, i.e. transmission and reflection, but only in the mode order of the incoming wave. In the general case, approach c), mode coupling, i.e. scattering into different mode orders, may occur.

In the literature, several mode matching approaches and discussion of the validity of them can be found, especially in cases where mean flow is present. A classical approach is to match pressure and axial velocity at the discontinuity [71, 81]. However, this is a valid approximation only for cases without mean flow. A more general mode matching approach based on the weak conservation of mass and axial momentum is given by Gabard [38].

More accurate approaches exist, which are capable of handling the discontinuity at the leading edge of the connecting plane. This is important for configurations where surface waves appear on the soft-wall section, see [113]. It is not trivial to determine the direction of propagation of these modes. This is because they may appear as an hydrodynamic instability at the connecting plane. In this case, a more accurate approach based on the Wiener-Hopf technique is proposed by Rienstra [114]. However, these are rather complicated and cumbersome. As pointed out by Rienstra [114], if the

acoustic impedance at the shell is high enough, surface waves do not usually appear and mode matching techniques are well suited. The majority of the engineering applications exhibit a rather large shell impedance. Actually, surface waves predominately appear due to the assumption of an homogeneous mean velocity profile [112]. In reality, the boundary layer considerable reduces the magnitude of the hydrodynamic singularity.

In this study, the approach proposed by Gabard [38] is used, whose basic idea was to derive an expression that preserves mass and momentum in an integral sense across the connecting plane. Their method is reviewed here to ease the interpretation of the results. A control volume enclosing the discontinuity is defined, see Fig. 4.4. The conservation equations for mass and momentum in integral form for inviscid flow are the starting point for the derivation:

$$\iiint\limits_V \frac{\partial \rho}{\partial t}\, dV + \sum \iint\limits_{S_i} \rho \vec{v} \cdot d\vec{S}_i = 0 \quad , \tag{4.8}$$

$$\iiint\limits_V \frac{\partial}{\partial t}(\rho \vec{v})\, dV + \sum \iint\limits_{S_i} \rho \vec{v} \otimes \vec{v} \cdot d\vec{S}_i = -\sum \iint\limits_{S_i} p\, d\vec{S}_i \quad , \tag{4.9}$$

where the surface integrals correspond to the cylinder shell and the two inflow and outflow planes. Linearization upon the mean flow state, homogeneous axial mean flow $\vec{v} = [U, 0, 0]^T + [u', v', w']^T$ and using the isentropic relation $\rho' = p'/c_0^2$ gives the first order approximation of mass conservation:

$$\int_0^{2\pi}\int_0^{R_c}\int_{-\epsilon/2}^{+\epsilon/2} i\omega \frac{p'}{\bar{c}^2} r\, dr\, dx\, d\theta + \left[\int_0^{2\pi}\int_0^{R_c} \left(\bar{\rho}u' + U\frac{p'}{\bar{c}^2}\right) r\, dr\, d\theta\right]_L^R + \int_0^{2\pi}\int_{-\epsilon/2}^{+\epsilon/2} \bar{\rho}v' R_c\, dx\, d\theta = 0 \quad , \tag{4.10}$$

where brackets represent difference of the borders $[a]_L^R \equiv a^R - a^L$ at the left "L" and right "R" sides of the jump. In the limiting case of vanishing control volume length $\epsilon \to 0$, the volume integral can be neglected. For the evaluation of the surface integral in the cylinder shell, in the presence of uniform mean flow, the impedance boundary condition given by Myers Eq. (4.1) has to be used to evaluate the surface integral on the cylinder shell:

$$\int_0^{2\pi}\int_0^{R_c}\int_{-\epsilon/2}^{+\epsilon/2} i\omega \frac{p'}{\bar{c}^2} r\, dr\, dx\, d\theta + \left[\int_0^{2\pi}\int_0^{R_c} \left(\bar{\rho}u' + U\frac{p'}{\bar{c}^2}\right) r\, dr\, d\theta\right]_L^R + \int_0^{2\pi}\int_{-\epsilon/2}^{+\epsilon/2} \bar{\rho} R_c \frac{p'}{Z}\, dx - i\frac{\bar{\rho}U}{\omega}\int_0^{2\pi}\int_L^R d\left(\frac{p'}{Z}\right)\, d\theta = 0 \; . \tag{4.11}$$

The last term in the previous equation can readily be evaluated as $[-i\bar{\rho}U \int p'/(\omega Z) d\theta]_L^R$. Following the compact approach of Gabard and Astley [39], the limit of Eq. (4.11) as $\epsilon \to 0$ is then considered. The first and third terms vanish and, as pointed out in [39], additional terms appear at interfaces with finite impedance $Z \neq \infty$.

Applying the same series of principles, linearization and limit to $\epsilon \to 0$, to the conservation of momentum yields after some rearrangement to:

$$\left[\int_0^{2\pi}\int_0^{R_c} \Psi \left(M u' \vec{e}_x + M \vec{v}' + (M^2+1)\frac{p'}{\bar{\rho}\bar{c}}\vec{e}_x \right) r \; dr \; d\theta \; - \; i\Psi \frac{M^2 \bar{c} R_c}{\omega} \int_0^{2\pi} \frac{p'}{Z} \; d\theta \; \vec{e}_x \right]_L^R \; = \; 0 \quad . \tag{4.12}$$

Again, additional terms at interfaces with finite impedance arise. However, these can be replaced by substitution of the mass conservation Eq. (4.11) into Eq. (4.12):

Due to the different mode shapes across the jump, a discontinuity in the $r\theta$-plane occurs and the conservation equations can only be weakly fulfilled. Following the Galerkin approach, the rearranged integral equations are weighted by a continuous function $\Psi(r, \theta)$:

$$\left[\int_0^{2\pi}\int_0^{R_c} \Psi \left(u' + M\frac{p'}{\bar{\rho}\bar{c}} \right) r \; dr \; d\theta - \; i \; \Psi \frac{M \bar{c} R_c}{\Omega} \int_0^{2\pi} \frac{p'}{Z} \; d\theta \right]_L^R \; = \; 0 \quad , \tag{4.13}$$

$$\left[\int_0^{2\pi}\int_0^{R_c} \Psi \left(M \vec{v}' + \frac{p'}{\bar{\rho}\bar{c}}\vec{e}_x \right) r \; dr \; d\theta \right]_L^R \; = \; 0 \quad , \tag{4.14}$$

where pure mean quantities vanish since they are continuous across the jump. For the general case with mean flow and constraining the system only by the conservation of mass and momentum, the problem is overdetermined. To overcome this issue only the axial component of the momentum conservation is considered. The resulting set of equations correspond to those given by Gabard and Astley [39]. In the absence of mean flow, the conservation equations for the jump reduce to the classical matching of pressure and velocity.

Substitution of the general solution Eq. (2.40) in the chosen set of equations delivers relations between the characteristic amplitudes on both sides of the jump. Since all quantities obey the same harmonic time dependency, the term $e^{i\Omega t}$ cancels out. Through the course of this study, all geometries to be treated are axisymmetric and thus no discontinuities in the θ coordinate are considered. Due to linearity, the tangential modes can be treated independently. This means that no scattering into different tangential mode orders occurs. Furthermore, without loss of generality, the axial position $x = 0$ is used. In practice, only a finite number of n_r radial modes can be taken into account. The problem has thus $2 \times n_r$ unknowns: the characteristic amplitudes on both sides of the discontinuity. The Galerkin approach with an orthogonal set of weighting functions $\Psi_{m\nu}$ with $\nu = 0, 1, \ldots, n_r$ is used to close the problem. Note that the radial and axial wave numbers have different values on the left and on the right side of the connecting plane. To distinguish them, the soft-wall case will be denoted by a * superscript. The radial mode shapes of the hard-wall case build an orthogonal set and are used as

weighting functions $\Psi_{m\nu} = J_m(\eta_{m\nu} r/R_c)$. This leads to the following linear system of equations:

$$\sum_{n=0}^{n_r} \zeta_{\nu n} \left[(\kappa_{mn}^{+} M + 1) F_{mn} + (\kappa_{mn}^{-} M + 1) G_{mn} \right] = \sum_{n=0}^{n_r} \left[\zeta_{\nu n}^{*+} (\kappa_{mn}^{*+} M + 1) F_{mn}^{*} + \zeta_{\nu n}^{*-} (\kappa_{mn}^{*-} M + 1) G_{mn}^{*} \right] - i \frac{M c_0 R_c}{\Omega} \frac{J_m(\eta_{m\nu})}{Z} \sum_{n=0}^{n_r} \left[J_m(\alpha_{mn}^{*+} R_c) F_{mn}^{*} + J_m(\alpha_{mn}^{*-} R_c) G_{mn}^{*} \right] \quad (4.15)$$

$$\sum_{n=0}^{n_r} \zeta_{\nu n} \left[(\kappa_{mn}^{+} + M) F_{mn} + (\kappa_{mn}^{-} + M) G_{mn} \right] = \sum_{n=0}^{n_r} \zeta_{\nu n}^{*+} (\kappa_{mn}^{*+} + M) F_{mn}^{*} + \sum_{n=0}^{n_r} \zeta_{\nu n}^{*-} (\kappa_{mn}^{*-} + M) G_{mn}^{*} \quad (4.16)$$

with integral terms that can be evaluated analytically [81]:

$$\zeta_{\nu n} = \int_0^{R_c} J_m \left(\frac{\eta_{m\nu} r}{R_c} \right) J_m \left(\frac{\eta_{mn} r}{R_c} \right) r \, dr = \begin{cases} \frac{R_c^2}{2} \left[1 - \left(\frac{m}{\eta_{mn}} \right)^2 \right] J_m^2(\eta_{mn}) & \text{if } \nu = n; \\ 0 & \text{if } \nu \neq n. \end{cases} \quad (4.17)$$

$$\zeta_{\nu n}^{*\pm} = \int_0^{R_c} J_m \left(\frac{\eta_{m\nu} r}{R_c} \right) J_m(\alpha_{mn}^{*\pm} r) r dr = \frac{R_c^2}{\eta_{m\nu}^2 - R_c^2 \alpha_{mn}^{*\pm 2}} \left[\eta_{m\nu} J_{m+1}(\eta_{m\nu}) J_m(\alpha_{mn}^{*\pm} R_c) - R_c \alpha_{m\nu}^{*\pm} J_{m+1}(\alpha_{m\nu}^{*\pm} R_c) J_m(\eta_{m\nu}) \right] . \quad (4.18)$$

In matrix vector notation and using the vectors $\vec{q} = [F_{m0}, G_{m0}, F_{m1}, G_{m1}, \ldots, F_{mn_r}, G_{mn_r}]^T$ and $\vec{q}^* = [F_{m0}^*, G_{m0}^*, F_{m1}^*, G_{m1}^*, \ldots, F_{mn_r}^*, G_{mn_r}^*]^T$ they can be written as:

$$\mathbf{Q} \vec{q} = \mathbf{Q}^* \vec{q}^* \quad , \quad (4.19)$$

with matrices $\mathbf{Q}$ and $\mathbf{Q}^*$ of size $2n_r \times 2n_r$ and entries:

$$Q(2\nu - 1, 2n - 1) = \zeta_{\nu n}(\kappa_{mn}^{+} M + 1) \quad , \quad Q(2\nu - 1, 2n) = \zeta_{\nu n}(\kappa_{mn}^{-} M + 1) \quad , \quad (4.20)$$

$$Q(2\nu \quad , 2n - 1) = \zeta_{\nu n}(\kappa_{mn}^{+} + M) \quad , \quad Q(2\nu, 2n) = \zeta_{\nu n}(\kappa_{mn}^{+} + M) \quad , \quad (4.21)$$

and:

$$Q^*(2\nu - 1, 2n - 1) = \zeta_{\nu n}^{*+}(\kappa_{mn}^{*+} M + 1) - i \frac{M \bar{c} R_c}{\omega Z} J_m(\eta_{m\nu} R_c) J_m(\alpha_{mn}^{*+} R_c) \, , \quad (4.22)$$

$$Q^*(2\nu - 1, 2n \quad) = \zeta_{\nu n}^{*-}(\kappa_{mn}^{*-} M + 1) - i \frac{M \bar{c} R_c}{\omega Z} J_m(\eta_{m\nu} R_c) J_m(\alpha_{mn}^{*-} R_c) \, , \quad (4.23)$$

$$Q^*(2\nu \quad , 2n - 1) = \zeta_{\nu n}^{*+}(\kappa_{mn}^{*+} M + 1) \, , \quad (4.24)$$

$$Q^*(2\nu \quad , 2n \quad) = \zeta_{\nu n}^{*-}(\kappa_{mn}^{*-} M + 1) \, . \quad (4.25)$$

Due to the orthogonality of the weighting functions, $\mathbf{Q}$ is a block diagonal matrix. Using this notation, the transfer matrix of a jump in shell impedance can finally be expressed in terms of these two matrices. For the jump from the hard-wall into the

soft-wall, the transfer matrix is $\mathbf{T}_{hs} = \mathbf{Q}^{-1}\mathbf{Q}^{*}$. For the jump in the opposite direction, the transfer matrix is $\mathbf{T}_{sh} = \mathbf{T}_{hs}^{-1} = (\mathbf{Q}^{*})^{-1}\mathbf{Q}$.

Since matrix inversion is needed, the condition number of the involved matrices is important. As pointed out in [39], in some cases, the choice of the hard-wall modes as weighting functions might lead to ill conditioned matrices. Gabard et al. suggest to use then a different set of weighting functions to improve the accuracy.

Physically, the scattering matrix notation introduced in Sec. 2.2.3 offers a more descriptive characterization of the problem that preserves causality. In this case, the system is described by a matrix $\mathbf{S}_{sh}$ that relates the incoming to the outgoing waves at the jump position:

$$\begin{pmatrix} f_{m0}^{*} \\ g_{m0} \\ \vdots \\ f_{mn}^{*} \\ g_{mn} \end{pmatrix}_{\text{out}} = \mathbf{S}_{sh} \begin{pmatrix} f_{m0} \\ g_{m0}^{*} \\ \vdots \\ f_{mn} \\ g_{mn}^{*} \end{pmatrix}_{\text{in}} = \begin{bmatrix} [2\times 2]_{0\to 0} & \cdots & [2\times 2]_{n\to 0} \\ [2\times 2]_{0\to 1} & & \vdots \\ \vdots & \ddots & \\ [2\times 2]_{0\to n} & & [2\times 2]_{n\to n} \end{bmatrix} \begin{pmatrix} f_{m0} \\ g_{m0}^{*} \\ \vdots \\ f_{mn} \\ g_{mn}^{*} \end{pmatrix}_{\text{in}} . \tag{4.26}$$

The scattering matrix can be divided into $[2\times 2]$ sub-block matrices that allow a physical representation of the different entries as explained in Sec. 2.2.3. Each sub-block matrix represents the coupling between two radial mode orders as shown by the arrows in the indices of Eq. (4.26). Thus, within each sub-block, the diagonal entries represent transmission, while the off-diagonal elements reflection of the corresponding traveling waves into a different mode order. As an example consider the coupling of the radial order $n = 0$ into order $n = 1$:

$$[2\times 2]_{0\to 1} = \begin{bmatrix} T_{0\to 1}^{+} & R_{0\to 1}^{+} \\ R_{0\to 1}^{-} & T_{0\to 1}^{-} \end{bmatrix} . \tag{4.27}$$

4.3.3 Acoustic Network Approach Above Cut-on and Mode Coupling

The low order acoustic network approach introduced in Sec. 2.2.3 has been extensively applied for systems in which mainly plane waves propagate. For higher frequencies above the cut-on, $\omega > \omega_c$, transverse modes have to be taken into account, too. This is the case in rocket thrust chambers, where the strongest and most dangerous instabilities occur at high frequencies. Due to linearity of the solution and assuming no interaction between the different mode orders at discontinuities, each mode can be treated independently. As pointed out in [107], for each transverse mode order the network can still be built by single mode elements using the corresponding wave numbers $k_{mn}^{\pm}$ and $\alpha_{mn}^{\pm}$ connected by two pins. Thus, each transverse mode order mn is treated independently with a system of linear equations:

$$\mathbf{A}_{mn}\vec{x}_{mn} = \vec{b}_{mn} . \tag{4.28}$$

Even if the modes behave independently along the element segments, this does not necessarily have to always be valid at connecting planes. At discontinuities like area changes or shell impedance jumps, the matching conditions may lead to mode coupling.

In this more general case, several mode orders have to be taken into account. So-called multi-mode elements in the network can thus have several pairs of connecting pins per port. The low order network can still be described by a system of linear equations:

$$\mathbf{A}_{\text{coupl}}\vec{x}_{\text{coupl}} = \vec{b}_{\text{coupl}} \quad , \tag{4.29}$$

where the system matrix $\mathbf{A}_{\text{coupl}}$, state $\vec{x}_{\text{coupl}}$, and excitation vector $\vec{b}_{\text{coupl}}$ are concatenations of their single mode counterparts $\mathbf{A}_{mn}$, $\vec{x}_{mn}$, and $\vec{b}_{mn}$, respectively. The size of the linear system depends on the number of modes considered in the coupling.

4.3.4 Generalized Nyquist Criterion for Systems Above Cut-on and Mode Coupling

The application of the Nyquist method presented in Sec. 2.2.5 for linearly independent higher order modes is quite straightforward. The diagnostic dummy and the acoustic elements are evaluated with the wave numbers $\alpha_{mn}^{\pm}$, m and $k_{mn}^{\pm}$ of the mode order of interest. An $OLTF$ curve can then be evaluated for each mode $OLTF_{mn}$ and the linear stability predicted. However, it has not yet been validated for transverse modes.

When radial mode coupling has to be taken into account, due to interactions at discontinuities combined with frequencies beyond the radial cut-on, the method has to be extended. In fact, due to the coupling, a multiple input and multiple output analysis has to be considered [120]. As mentioned before, in this study the coupling is restricted to the vicinity of the resonator ring and the modes are treated independently when performing the global stability analysis. This procedure will be explained in the next section where the resonator ring element is described.

4.4 Resonator Ring Element

The methodologies presented in Sec. 4.3 allow to model a resonator ring in a low order element sense. With integral mode matching, the resonator ring element that accounts for scattering and mode coupling can be modeled as a combination of two jumps with a soft-wall duct segment of homogeneous shell impedance of length d in-between, see Fig. 4.6. The impedance jumps are characterized by the transfer matrices $\mathbf{T}_{hs}$ and $\mathbf{T}_{sh}$. The soft-wall duct segment can be characterized by a diagonal matrix, whose exponential entries describe the axial propagation of the up- f_{mn}^{*} and downstream traveling waves g_{mn}^{*} in terms of the axial wave numbers $k_{mn}^{*\pm}$ of the different modes:

$$\mathbf{T}_s = \begin{bmatrix} e^{-ik_{m0}^{*+}L} & 0 & \cdots & 0 \\ 0 & e^{-ik_{m0}^{*-}L} & & \vdots \\ \vdots & \ddots & \ddots & \\ & & e^{-ik_{mn_r}^{*+}L} & 0 \\ 0 & \cdots & 0 & e^{-ik_{mn_r}^{*-}L} \end{bmatrix} \tag{4.30}$$

Taking advantage of the transfer matrix notation the resonator ring element can simply be described by:

$$\mathbf{T}_{\text{ring}} = \mathbf{T}_{sh}\mathbf{T}_s\mathbf{T}_{hs} \quad . \tag{4.31}$$

For each tangential mode order it relates all radial orders with each other. In general, depending on how many radial modes n_r are considered in the coupling, it is a $2n_r \times 2n_r$ square matrix.

The scattering matrix $\mathbf{S}_{\text{ring}}$ gives the response of the ring to multi-mode excitation. However, it is not trivial to derive the scattering matrix of a system from the individual element transfer matrices. In this thesis, a method based on matrix manipulation is proposed.

The starting point is the factorization of the state vector at the upstream position (index $_u$ in terms of incoming $\vec{x}_{\text{in}}$ and outgoing $\vec{x}_{\text{out}}$ vectors:

$$\begin{pmatrix} f_{m0} \\ g_{m0} \\ \vdots \\ f_{mn} \\ g_{mn} \end{pmatrix}_u = \underbrace{\begin{bmatrix} 1 & 0 & & \cdots & & 0 & 0 \\ 0 & 0 & & & & & \\ & & 1 & & & & \\ \vdots & & & \ddots & & & \vdots \\ & & & & 0 & & \\ 0 & & & & & 1 & 0 \\ 0 & & & \cdots & & 0 & 0 \end{bmatrix}}_{\mathbf{E}^{(1)}} \underbrace{\begin{pmatrix} f^u_{m0} \\ g^d_{m0} \\ \vdots \\ f^u_{mn} \\ g^d_{mn} \end{pmatrix}}_{\vec{x}_{\text{out}}} + \underbrace{\begin{bmatrix} 0 & 0 & & \cdots & & 0 & 0 \\ 0 & 1 & & & & & \\ & & 0 & & & & \\ \vdots & & & \ddots & & & \vdots \\ & & & & 1 & & \\ 0 & & & & & 0 & 0 \\ 0 & & & \cdots & & 0 & 1 \end{bmatrix}}_{\mathbf{E}^{(2)}} \underbrace{\begin{pmatrix} f^d_{m0} \\ g^u_{m0} \\ \vdots \\ f^d_{mn} \\ g^u_{mn} \end{pmatrix}}_{\vec{x}_{\text{in}}} \quad . \tag{4.32}$$

Doing the same for the state vector at the downstream position, the transfer matrix can be written as:

$$\mathbf{E}^{(1)}\vec{x}_{\text{out}} + \mathbf{E}^{(2)}\vec{x}_{\text{in}} = \mathbf{T}_{\text{ring}}(\mathbf{E}^{(1)}\vec{x}_{\text{in}} + \mathbf{E}^{(2)}\vec{x}_{\text{out}}) \quad . \tag{4.33}$$

After some rearrangement, the scattering matrix notation is given then by:

$$\vec{x}_{\text{out}} = (\mathbf{E}^{(1)} - \mathbf{T}_{\text{ring}}\ \mathbf{E}^{(2)})^{-1}\ (\mathbf{T}_{\text{ring}}\ \mathbf{E}^{(1)} - \mathbf{E}^{(2)})\vec{x}_{\text{in}} \quad . \tag{4.34}$$

This method can be applied for any transfer matrix. However, the inversion of the matrix $(\mathbf{E}^{(1)} - \mathbf{T}_{\text{ring}}\ \mathbf{E}^{(2)})^{-1}$ can be mathematically difficult if the transfer matrix is ill-conditioned. This can happen for systems in which some radial orders are highly evanescent. Thus, the number of radial mode orders considered for the analysis is restricted by the robustness of the method used for matrix inversion.

For a more descriptive interpretation, the scattering matrix can be divided into 2×2 blocks that express the interaction between the different mode orders. The diagonal

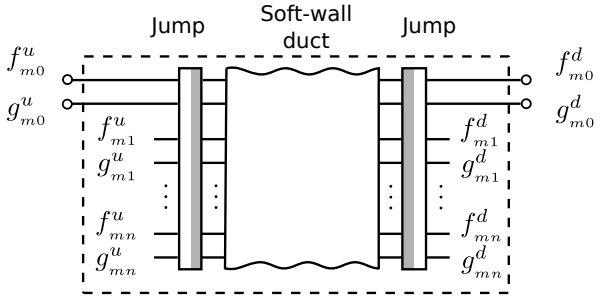

Figure 4.6: Resonator ring element for network approach.

blocks represent scattering of a mode into itself. The off-diagonal blocks represent the coupling between radial modes of different order.

The stronger the difference between the transverse mode shape across the jump, the more significant the contribution of the off-diagonal blocks. In other words, if the mode shape across the jumps differs strongly, a wave passing through the resonator scatters into higher radial modes in order to satisfy conservation of mass and momentum. This is an important feature of resonator rings that can have a considerable impact on their stabilizing influence, as shown later in this thesis.

In the scope of the network approach, the resonator ring would have to be modeled as a multi-mode element with $2n_r$ pins per connecting port. However, at frequencies below the radial cut-on, the radial modes will mainly propagate along the soft-wall section. On the hard-wall side of the jumps, these modes will decay exponentially. At low frequencies, the system matrix $\mathbf{A}_{\text{coupl}}$ would get ill conditioned and numerically difficult to invert at low frequencies because the entries of the radial modes in the system would be orders of magnitude smaller than the rest of the network. It is thus not only a very plausible approximation to uncouple these modes from the rest of the network, but also a strategy to increase numerical robustness of the method. Figure 4.6 describes schematically the procedure, where only the pins $_{m0}$ of the resonator element are connected to the rest of the network. Mathematically, this corresponds to considering only the first 2×2 diagonal block of the general transfer matrix.

4.5 Model of Representative Thrust Chamber

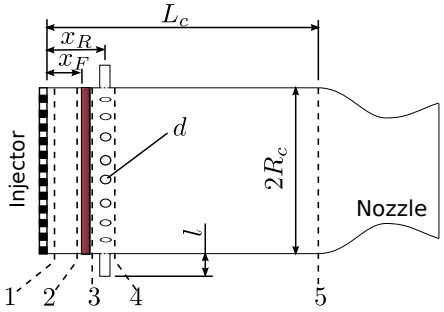

Figure 4.7: Sketch of a representative thrust chamber used as test case.

A representative thrust chamber configuration displayed in Fig. 4.7 is chosen to demonstrate the applicability of the method proposed in this thesis. The configuration is also suitable for the evaluation of resonator rings with regard to their stabilizing influence. The thrust chamber of radius R_c, length L_c and mean flow mach number M is bounded on the left by the injector plate as well as on the right by the nozzle. Near the injector plate at distance x_F, the combustion front with an excess temperature $\Xi = \bar{T}_h/\bar{T}_c - 1$ and ratio of acoustic impedances $\xi = \bar{\rho}_c\bar{c}_c/(\bar{\rho}_h\bar{c}_h)$ is expected. At distance x_R from the injector plate, a resonator ring with n_R cavities of the quarter wave type is placed. All cavities have the same diameter d and length l and are equally distributed in the azimuthal direction. The length of the quarter wave tubes is chosen to approximately match the eigenfrequency of the first tangential mode of the chamber $l \approx R_c/2$. Table (4.1) summarizes the values used for the test case, where the geometrical dimensions

are non-dimensionalized by the chamber radius. The eigenfrequency of the first tangential mode without mean flow and closed boundaries $f_o = \bar{c}\eta_{10}/(2\pi R_c)$ is used to non-dimensionalize all frequencies and time scales throughout this study. All thermodynamic properties are assumed homogeneous over the transverse chamber plane and the spatial average operator is omitted for clarity.

Table 4.1: Geometrical and thermodynamical parameters of the test case in non-dimensional form.

$\frac{R_c}{R_c}$	$\frac{L}{R_c}$	$\frac{x_F}{R_c}$	$\frac{x_r}{R_c}$	$\frac{d}{R_c}$	$\frac{l}{R_c}$	$\frac{l_r}{R_c}$	Ξ	ξ	γ	n_r	n	τf_o	M_h
1	2.86	0.11	0.16	0.089	0.466	0.179	12	3.85	1.13	22	1.1	0.55	0.25

4.5.1 Network Model of Representative Thrust Chamber

The generic thrust chamber presented in Sec. 4.5 is modeled here as a network of low order elements. Using the notation shown in Fig. 4.7, the mathematical description of the particular elements is given here, from which the transfer matrices can easily be determined. The numbered indices denote the axial position in the chamber according to Fig. 4.7. For better readability, the mode indices $_{mn}$ are omitted in this part, however the expressions are valid for any mode order.

- For the injector plate at position 1, the acoustic mass flow fluctuations are set to zero $(\rho_1 u_1)' = 0$. This follows from the assumption of critical mass flow rate through the injectors. Written in terms of Riemann-Invariants, the boundary condition is given by [67]:

$$(\kappa_1^+ + M_1) f_1 + (\kappa_1^- + M_1) g_1 = 0 \quad . \tag{4.35}$$

- For a short duct with hard walls of length $L_{12} = x_F$ with wave numbers given by Eq. (2.37), it follows:

$$f_2 = f_1 e^{-ik_1^+ L_{12}} \quad , \tag{4.36}$$

$$g_2 = g_1 e^{-ik_1^- L_{12}} \quad . \tag{4.37}$$

- The combustion process is modeled as a compact heat source of zero thickness $L_{23} \approx 0$. Matching conditions are not needed, because the radial wave numbers do not change across the jump. The linearized Rankine-Hugoniot equations [107] relate the acoustic primitive variables across the flame front:

$$p_3' = p_2' - \bar{\rho}_2 \bar{u}_2^2 \Xi \left(\frac{u_2'}{\bar{u}_2} + \frac{\dot{Q}'}{\bar{\dot{Q}}} \right) \quad , \tag{4.38}$$

$$u_3' = u_2' + \bar{u}_2 \Xi \left(\frac{\dot{Q}'}{\bar{\dot{Q}}} - \frac{p_2'}{\bar{p}_2} \right) \quad , \tag{4.39}$$

where $\Xi = (\bar{T}_3/\bar{T}_2 - 1)$ is the excess temperature. Only for vanishing Mach numbers,

the pressure fluctuations at both sides are approximately equal $p_3' \approx p_2'$. Entropy inhomogeneities are neglected upstream of the flame front. To close the expressions, the variation of heat release rate $\dot{Q}'$ has to be given in terms of the acoustic quantities. Using the n-τ sensitive time lag model proposed by Crocco [23], the heat release fluctuations are linked to the pressure fluctuations on the cold side and can be given by [101]:

$$\frac{\dot{Q}'}{\bar{\dot{Q}}} = n\left(1 - e^{i\Omega\tau}\right)\frac{p_2'}{\bar{p}_2} \quad . \tag{4.40}$$

This assumes that in the chain of processes taking part in the combustion, the most sensitive one responds to pressure excitation [100]. Using the ratio of specific impedances ξ and the isentropic exponent γ, substitution of Eq. (4.40), and the general solution Eq. (2.49) and Eq. (2.51) in the Rankine-Hugoniot equations leads to:

$$\begin{aligned} f_3 + g_3 = \xi\left[1 - M_2\Theta\left(\gamma M_2 n(1 - e^{i\Omega\tau}) + \kappa_2^+\right)\right] f_2 \\ + \quad \xi\left[1 - M_2\Theta\left(\gamma M_2 n(1 - e^{i\Omega\tau}) + \kappa_2^-\right)\right] g_2 \quad , \end{aligned} \tag{4.41}$$

$$\begin{aligned} \kappa_3^+ f_3 + \kappa_3^- g_3 = \left[\kappa_2^+ + M_2\gamma\Theta\left(n(1 - e^{i\Omega\tau}) - 1\right)\right] f_2 \\ + \quad \left[\kappa_2^- + M_2\gamma\Theta\left(n(1 - e^{i\Omega\tau}) - 1\right)\right] g_2 \quad . \end{aligned} \tag{4.42}$$

Note that from the conservation equations across the flame, a relation for the mean properties exists between the excess temperature Ξ, the ratio of specific impedances ξ and the Mach number on the hot side M_2, see App. A.3. Thus, only two of these three parameters can be chosen independently. The fourth and fifth parameters given by the interaction index n and the time lag τ are assumed to be independent and can be arbitrarily chosen. In practice, they depend on the propellant and feed system.

- For the resonator ring element of length $L_{34} = d$, the first 2×2 diagonal block of the discrete transfer matrix $\mathbf{T}_{\text{ring}}$ is taken, see Sec. 4.4. Depending on the test case, the impedance expression for a quarter wave cavity is applied as shell boundary condition using either Eq. (3.23) for the homogeneous approach or Eqs. (3.22) and (3.44) for the polynomial approach. The tabulated values for real valued frequencies $\omega \in [0.027 : 2.194]$ with frequency increment $\Delta\omega = 0.0017$ is used to estimate the radial $\alpha_{mn}^{\pm}$ and axial $k_{mn}^{\pm}$ wave numbers:

$$\begin{pmatrix} f_4 \\ g_4 \end{pmatrix} = \begin{bmatrix} T_{\text{ring}}(1,1) & T_{\text{ring}}(1,2) \\ T_{\text{ring}}(2,1) & T_{\text{ring}}(2,2) \end{bmatrix} \begin{pmatrix} f_3 \\ g_3 \end{pmatrix} \quad . \tag{4.43}$$

- A second duct of length $L_{45} = L_c - x_R - d/2$ with hard walls and wave numbers given by Eq. (2.37) follows:

$$f_5 = f_4 e^{-ik_x^+ L_{45}} \quad , \tag{4.44}$$

$$g_5 = g_4 e^{-ik_x^- L_{45}} \quad . \tag{4.45}$$

- For the application of the Nyquist method, the diagnostic element is placed at

position 5. The position just across the cut is denoted by $5'$. The relation for the Riemann-Invariants write then:

$$f_{5'} = 1 \quad , \tag{4.46}$$

$$g_{5'} = g_5 \quad . \tag{4.47}$$

- For the choked nozzle, restricting to homentropic flows and assuming acoustic compactness, the relation between the Riemann-Invariants is given by [107]:

$$\left(\kappa^+_{5'} - \frac{\gamma-1}{2} M_{5'}\right) f_{5'} + \left(\kappa^-_{5'} - \frac{\gamma-1}{2} M_{5'}\right) g_{5'} = 0 \quad , \tag{4.48}$$

where $M_{5'}$ denotes the Mach number at the section just before the converging part of the nozzle. Due to the requirement of compactness, the expression given by Eq. (4.48) is commonly referred to as *short-nozzle*. For geometrical dimensions leading to a short convergent section of the nozzle, the simplified approach delivers a reasonable approximation.

It has to be conceded that, apart from the resonator ring element, the models for the remaining components are rather simple. But nevertheless they reflect the essential behavior of the components. The aim of this study is to demonstrate the applicability of the method and to give some insight in the stabilizing influence of resonator rings. More elaborated models for the other components can be used without significant difficulty. For the combustion, the heat release fluctuation can be incorporated as a source term in the wave equation and solved for a portion of the chamber. For the nozzle, the semi-analytical approach proposed by Bell and Zinn [9] can be used to determine a more accurate admittance. This flexibility to incorporate easily various models is one of the major advantages that the here proposed method provides.

4.5.2 Test Case Configurations

The representative rocket thrust chamber introduced in Sec. 4.5 is now described as a network of low order elements. Throughout this thesis, several test case configurations given in in Tab. 4.2 are studied. For the cases without resonator ring, a slightly longer duct segment between injector and flame front is used. The basic geometrical and thermodynamical parameters have been already given in Tab. 4.1. Some of these parameters have been varied systematically in a range of test cases. An overview of these parametric studies is given in Tab. 4.3.

Table 4.2: Test case configurations considered in this study.

	Injector	Duct	Flame	Ring	Duct	Nyquist	Nozzle
Case A	✓	✓	✓	×	✓	×	✓
Case B	✓	✓	✓	×	✓	✓	✓
Cases C, D, E, F, G, H	✓	✓	✓	✓	✓	✓	✓

Table 4.3: Geometrical and thermodynamical parameters of the various test cases in non-dimensional form.

Case	Ring	l_a/R_c	ϵ_{nl}	χ	Impedance model
A	×	–	–	–	–
B	×	–	–	–	–
C	✓	0.466	50	6.2	Hom.
D	✓	$0.22 - 0.67$	50	6.2	Hom.
E	✓	0.466	$20 - 200$	6.2	Hom.
F	✓	0.466	50	6.2	Poly.
G	✓	0.466	50	$1.1 - 12.6$	Poly.
H	✓	0.466	50	$1.1 - 12.6$	Hom.

4.6 Validation: Linear Stability Without Resonator Ring

At the beginning, a thrust chamber without resonator ring is investigated for two reasons. Firstly, without resonator ring, all elements in the system can be described in closed form, and thus, the characteristic equation can be solved to obtain the eigenfrequencies and growth rates. The Nyquist plot method can then be validated against these results. And secondly, an unstable operation point with at least one unstable transverse mode had to be found in order to serve as a reference case in which the functionality of resonator rings can be evaluated.

The network of this reference case is shown in Fig. 4.8 and corresponds to the chamber already introduced in Sec. 4.5, however omitting the resonator ring element. Therefore, a slightly longer hard wall duct segment is used for the section $3 \rightarrow 5$. The parameters of the flame transfer function n and τ have been varied until an instability was encountered. Given in non-dimensional form, a combination of $n = 1.1$ and $\tau f_o = 0.551$ has been chosen. These values lie in the order of magnitude of widely observed for hypergolic bi-propellants [101].

Without resonator ring no mode coupling occurs and all modes can be treated separately. Furthermore, the cut-on frequencies of the radial modes are beyond the frequency range of interest and thus, the stability analysis has been performed for plane waves $\alpha_{00} = 0$ and first tangential mode $\alpha_{10} = \eta_{10}/R_c$. After setting up the system matrix $\mathbf{A}_{\text{ref}}$ using the relations given in the previous section, the resonant frequencies of the system are determined by solving the characteristic equation $\det\{\mathbf{A}_{\text{ref}}\} = 0$.

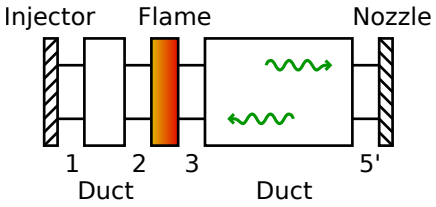

Figure 4.8: Network of reference case.

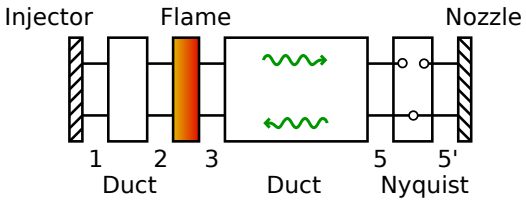

Figure 4.9: Network of reference case with diagnostic dummy.

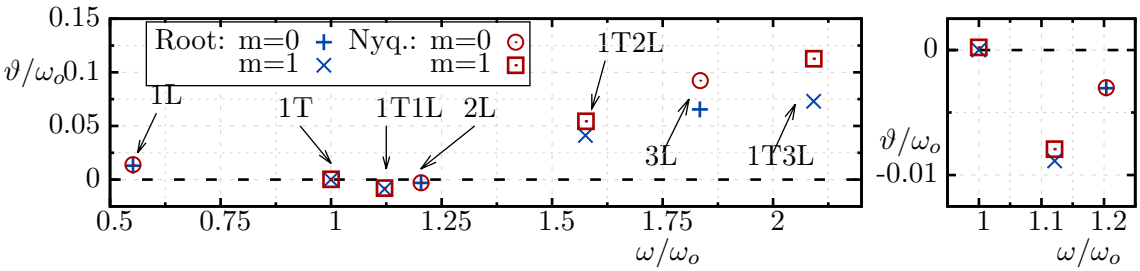

Figure 4.10: Resonant frequencies of the reference case without resonator ring. Comparison of exact values determined by the roots of the characteristic equation and values estimated from the Nyquist-Plot method.

Figure 4.10 depicts the computed eigenfrequencies Ω_{eig} in the complex plane. Under this conditions the $1T1L$ and $2L$ modes are unstable, with cycle increments of $\Gamma_{1T1L} = +8.0\%$ and $\Gamma_{2L} = +0.56\%$, respectively. Even if the rates seem to be small, at high frequencies the amplitude of the oscillations would increase very fast. The chosen configuration is thus suitable for the testing of resonator cavities as dampers.

A pure tangential mode $1T$ is also found with a metastable growth rate of $\Gamma_{1T} = 0\%$. There is some confusion in the linear acoustic community concerning pure transverse modes. As pointed out by Kathan [61], a pure transverse mode should not exhibit any axial dependency and thus, the axial pressure gradient should vanish: $\partial p'/\partial x$. As shown in [61], two conditions are necessary to fulfill this requirement: a) ideal axial terminations with either fully or non reflective properties and b) equal axial wave numbers for the up- and downstream traveling waves. For configurations with mean flow, this condition holds only at the cut-on frequency where the two branches of the dispersion relation join. Thus, this eigenfrequency might be caused by the singularity in the mathematical model and its physical validity is questionable. Although this issue is not totally clarified, this singular mode is still mentioned in the rest of this study and should be interpreted with caution.

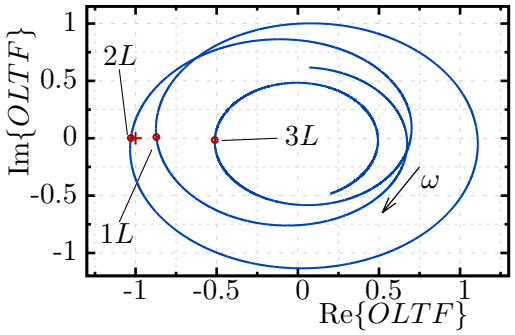

Figure 4.11: Nyquist plot of thrust chamber without resonator ring. Longitudinal modes, $m = 0$.

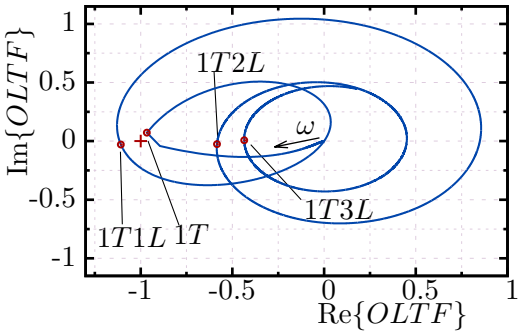

Figure 4.12: Nyquist plot of thrust chamber without resonator ring. First tangential mode, $m = 1$.

According to the extended Rayleigh criterion, the correlation between the pressure and heat release fluctuations should be larger than the acoustic losses of the system for thermoacoustic instabilities to appear. Thus, the thrust chamber studied in this paper

Table 4.4: Resonant frequencies and corresponding growth rates. Deviation of Nyquist-Plot estimation from the exact values determined by the roots of the system matrix determinant.

Mode	1L	1T	1T1L	2L	1T2L	3L	1T3L
ε_ω [%]	0.009	0.004	0.018	0.001	0.076	0.06	0.006
ε_ϑ [%]	7.2	0.0	10.6	1.4	32.0	41.1	54.3

is more likely to be unstable when the phase lag between pressure and heat release fluctuations is minimal. The heat release fluctuations in this study using the sensitive time-lag model are given by the expression:

$$\dot{Q}' \sim \left(1 - e^{i\omega\tau} e^{-\vartheta\tau}\right) p' \quad , \tag{4.49}$$

and thus, the term $\omega\tau$ should take values close to odd multiples of π to maximize the correlation. In non-dimensional form, this condition can be expressed as:

$$\frac{\omega}{\omega_o} \approx \frac{2j+1}{2\tau f_o} \quad , \qquad \text{for} \qquad j = 0, 1, 2, \ldots \quad . \tag{4.50}$$

Substitution of the imposed value for the time lag τ gives the following series of values $\omega/\omega_o = 0.91, 2.72, 4.54, \ldots$. This is in accordance to the results presented in Fig. 4.10, where the unstable modes are indeed close to these values and the stable ones lie between them.

In addition to the exact solution, the resonant frequencies of the reference case are also determined by application of the Nyquist-plot method. The $OLTF$ of the system is calculated by placing a Nyquist "dummy" close to position 5 as shown in Fig. 4.9. The Nyquist plots for the two investigated mode orders ($m = n = 0$) and ($m = 1,\ n = 0$) are shown in Figs. 4.11 and 4.12, respectively. The locations of the $OLTF$ curves with minimal distance to the critical point are also indicated in those figures by circular markers placed on the $OLTF$ curve.

An eigenfrequency for the pure $1T$ mode is found by the Nyquist-plot method, in accordance to the exact solution deduced from the roots of the characteristic equation $\det\{\mathbf{A}_{\text{ref}}\} = 0$. The singularity in the hard-wall axial wave numbers $k_{mn}^{\pm}$ at the cut-on frequency of the $1T$ modes leads also to a singularity in the $OLTF$ curve. In addition to the discussion about the physical validity of this mode, it has to be mentioned that the Nyquist criterion cannot be applied close to singularities in the $OLTF$ curve. Close to a singularity, the derivatives go to infinity and the conformal properties of the mapping are not valid in these regions [59].

Using the expression given by Eq. (2.83), the corresponding eigenfrequencies are graphically determined. The values computed via eigenvalue solver are included for comparison in Fig. 4.10, too. It can be seen that the Nyquist-plot method performs very well. The method is able to find all resonant frequencies in the range of interest and to effectively estimate their stability. In Tab. 4.4, the deviation of the estimated values towards the exact solution determined by the roots of the characteristic equation for eigenfrequency $\varepsilon_\omega = |\omega - \omega_N|/\omega$ and growth rates $\varepsilon_\Gamma = |\Gamma - \Gamma_N|/\Gamma$ is given. Quantitatively, the accuracy of the method is remarkably good concerning the real values of the

eigenfrequencies. For all considered modes, the deviation from the exact values is below 1%. Concerning the growth rates, the accuracy of the method is not always that high. Inspection of the corresponding Nyquist plots gives the reason for this behavior. When the $OLTF$ curve passes far away from the critical point, the method can estimate the growth rates only qualitatively since the conformal properties of the mapping are only locally preserved. Nevertheless, the method is able to predict the trends correctly. In cases where the curve passes close to the critical point, the accuracy of the method increases considerably. From a global point of view, this is a positive property of the method, because it is especially accurate close to the stability margin, where small deviations can have a strong influence on the stability prediction, as pointed out by Kopitz et al. [66].

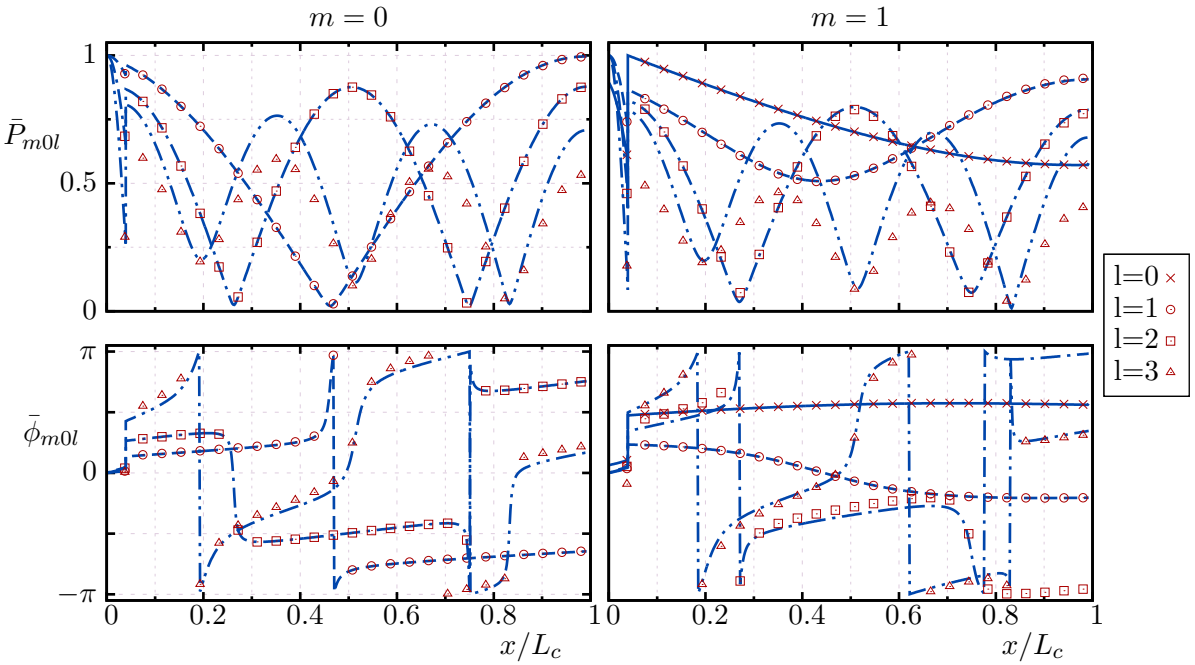

Figure 4.13: Longitudinal mode shapes for the reference case without resonator ring. Lines correspond to the solution via root finding technique; markers to the solution via Nyquist plot.

Knowing the eigenfrequencies of the system, the corresponding eigenvectors or characteristic amplitudes at discrete ports of the network are then calculated and the three-dimensional acoustic field at resonance is reconstructed. In the reference case having only hard-wall elements, the modal contributions to the pressure field can be easily brought into the following form:

$$\frac{p'_{mnl}}{\bar{\rho}\bar{c}} = J_m(\eta_{mn} r/R_c)\ \hat{P}_{mnl}(x)\ \cos(m\theta)\ e^{i\omega_{mnl}t}\ e^{-\vartheta_{mnl}t}\quad , \tag{4.51}$$

where the axial dependency is present in the term $\hat{P}_{mnl}$. Note that a third index $_l$ is introduced. It corresponds to the different longitudinal modal orders of the system.

Figure 4.13 shows the axial distribution of normalized amplitude $\bar{P}_{mnl}$ and phase $\bar{\phi}_{mnl}$ defined as:

$$\bar{P}_{mnl} = \frac{|\hat{P}_{mnl}|}{|\hat{P}_{mnl}|_{\max}} \quad , \quad \bar{\phi}_{mnl} = \angle\hat{P}_{mnl}(x) - \angle\hat{P}_{mnl}(0) \quad , \tag{4.52}$$

for the considered mode orders. All modes depict oscillatory dependency with a discontinuity at the position of the flame. As validation, the mode shapes using the eigenfrequencies estimated by the Nyquist-plot method are also given in the set of figures. The agreement for both the amplitude and phase is remarkably good in all cases, even for the modes with high growth rates. It is thus valid to use the Nyquist-plot method also to study the three-dimensional acoustic field of the thrust chamber at resonance. For the hard wall case, the transverse mode shapes $J_m(\alpha_{mn}r)$ are trivial and frequency independent and will not be discussed here.

4.7 Stabilizing Influence of a Resonator Ring

The proposed method is used to investigate the stabilizing influence of resonator rings. To bring some clarity in the damping behavior of resonator rings, a preliminary analysis with a ring of quarter wave tubes of small temperature inhomogeneity is performed. Thus, assuming an almost homogeneous temperature distribution inside the cavities, the impedance condition based on the homogeneous approach can be used. The intention is to characterize the coupled system of thrust chamber and resonator ring and have a reference state before the influence of inhomogeneities is studied.

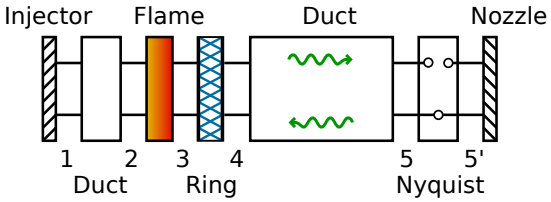

Figure 4.14: Network of a generic chamber with resonator ring and diagnostic dummy.

The thermoacoustic stability of the generic thrust chamber with a resonator ring is investigated using the network shown in Fig. 4.14 denoted as test case C. A non-linear resistance factor of $\epsilon_{nl} = 50$ corresponding to moderate sound pressure levels in the chamber is assumed. The resonator ring described by the discrete transfer matrix presented in Sec. 4.4 is used. Even if several radial mode orders are considered in the mode matching at the jumps, the global transfer matrix of the resonator ring is decoupled from the radial modes of the remaining network and thus only the first diagonal block of the transfer matrix is used. This is justified because the radial cut-on frequencies lie beyond the frequency range of interest. The geometrical quantities of the ring are listed in Tab. 4.3. The transfer matrix of the ring is computed according to the procedure proposed in Sec. 4.4 and tabulated only for real frequencies. The overall stability of the system is then estimated by the Nyquist plot method.

Figure 4.15 shows the eigenfrequencies and corresponding growth rates and summarizes the influence of the resonator ring on the global stability of the thrust chamber. The

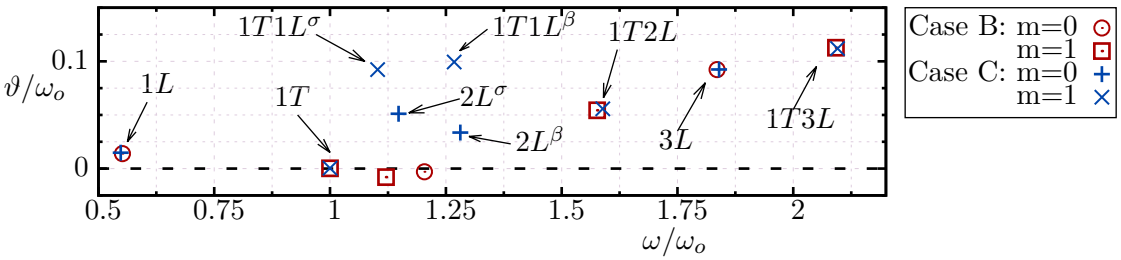

Figure 4.15: Eigenfrequencies of thrust chamber with resonator ring (case C). For comparison the eigenfrequencies of the chamber without resonator ring (case B) are also plotted.

eigenfrequencies of the reference case without ring are also shown for comparison. The stability of modes with eigenfrequencies beyond the resonator bandwidth of operation are not affected. In contrast, for the modes close to the resonant frequency of the cavities, two major effects can be seen. Firstly, additional modes appear that were not present in the undamped reference case. And secondly, these new modes are more stable than the original ones. One well accepted reason for this stabilizing influence is the dissipation of acoustic energy by viscous and turbulent losses described by the resistance of the equivalence impedance.

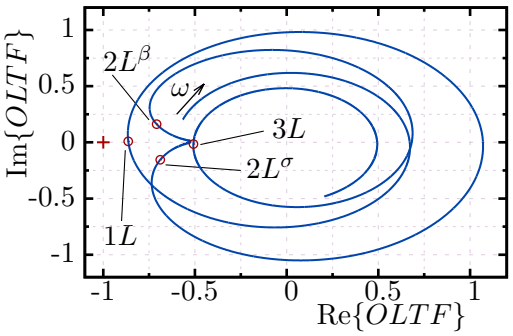

Figure 4.16: Nyquist plot of thrust chamber with resonator ring. Longitudinal modes, $m = 0$.

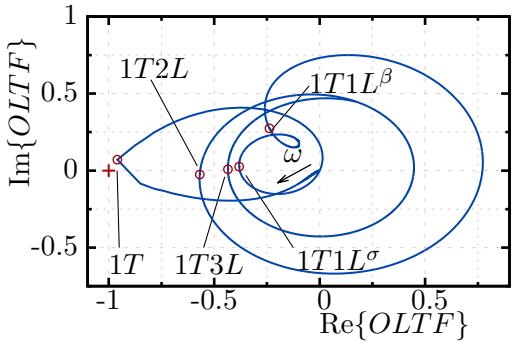

Figure 4.17: Nyquist plot of thrust chamber with resonator ring. First tangential modes, $m = 1$.

The corresponding Nyquist plots, from which the eigenfrequencies are estimated, are shown in Figs. 4.16 and 4.17. A close look on the $OLTF$ curves reveals that for each affected mode in the reference case two additional modes emerge close to the original eigenfrequencies, denoted by the superscripts σ and β in the figures. The corresponding eigenfrequencies and growth rates are also given in Tab. 4.5 for both the damped and undamped case. The emergence of additional, but more stable modes in the presence of resonators has already been observed in both experimental [95, 96] and theoretical investigations [100]. They can be interpreted as an increment in degrees of freedom of the acoustic system. In the $OLTF$ curve, this can be observed by the appearance of an additional loop for each azimuthal order m at a frequency close to the eigenfrequency of the cavities. However, it is important to note that in the coupled system the σ- and β-mode lie slightly shifted from the eigenfrequency of the cavity.

Table 4.5: Eigenfrequencies and cycle increments for various modes in the damped and reference case.

	Case B: undamped						
	$1L$	$1T$	$1T1L$	$2L$	$1T2L$	$3L$	$1T3L$
ω/ω_o	0.53	0.97	1.08	1.16	1.52	1.78	2.02
Γ	-13.7%	0%	5.09%	1.61%	-15.15%	-20.1%	-19.69%
	Case C: damped						
	$1L$	$1T$	$1T1L^{\sigma}$	$1T1L^{\beta}$	$2L^{\sigma}$	$2L^{\beta}$	$1T2L$	$3L$	$1T3L$
ω/ω_o	0.51	0.97	1.07	1.19	1.11	1.21	1.56	1.80	2.03
Γ	-73.3%	-0.3%	-47%	-13.6%	-56.4%	-5.1%	-21.9%	-26.4%	-25.1%

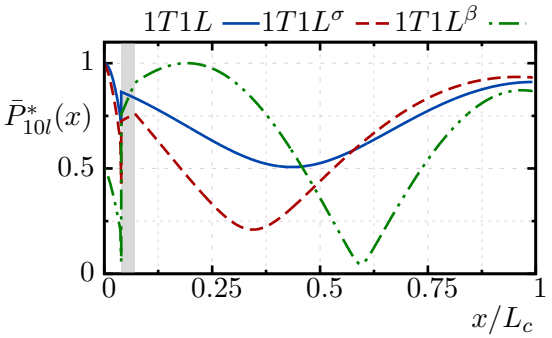

Figure 4.18: Longitudinal mode shapes for damped $1T1L$ modes at location $r = R_c$ (dashed lines) compared to the undamped case (full line).

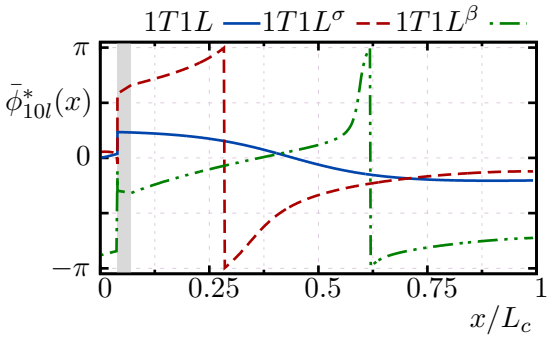

Figure 4.19: Axial phase for damped $1T1L$ modes at location $r = R_c$ (dashed lines) compared to the undamped case (full line).

Because the transverse mode shape of the upstream and downstream traveling waves are different in the soft wall section, it is not possible to bring the modal pressure into the form of Eq. (4.51). Instead, the radial and axial dependency have to be considered in a single term:

$$\frac{p'_{mnl}}{\bar{\rho}\bar{c}} = \hat{P}^*_{mnl}(r,x)\ \cos(m\theta)\ e^{i\omega_{mnl}t}\ e^{-\vartheta_{mnl}t} \quad . \tag{4.53}$$

For the mode shape analysis, only the mode $1T1L$ ($m = 1,\ n = 0,\ l = 1$) will be presented because the results are similar for the mode $2L$ and the remaining modes have not been changed by the resonator ring. Figures 4.18 and 4.19 show the axial distribution of normalized amplitude $\bar{P}^*_{10l} = |\hat{P}_{10l}|/|\hat{P}^*_{10l}|_{\max}$ and phase $\bar{\phi}^*_{10l} = \angle(\hat{P}^*_{10l}) - \angle(\hat{P}^*_{10l}(0))$ of the $1T1L$ modes. Note that the radial position at the cylinder boundary $r = R_c$ is chosen. For comparison, the mode shape of the undamped case $J_1(\eta_{10}R_c)\hat{P}_{101}(x)$ is also shown in the same figures. The region filled by the gray area denotes the location of the resonator ring. The additional axial mode shapes are possible at slightly different frequencies compared to the undamped case. The situation is similar when looking at the transverse mode shape. Figure 4.20 shows the normalized pressure amplitude of the $1T1L$ modes at the axial position x_R. For the reference case, the first tangential shape with zero gradient at the boundary is clearly displayed. In contrast, the gradient of the

σ and β modes is not zero. At the corresponding slightly lower and higher frequencies, the magnitude of the gradient is equal, once with positive and once with negative step.

To prove the validity of the mode matching conditions, the normalized pressure distribution at one of the jumps is given in Figs. 4.22 and Fig. 4.23. At one of the eigenfrequencies, they show the pressure and radial velocity amplitudes on both sides of the first jump. The matching condition proposed in this study is capable of handling this discontinuity in shell impedance remarkably good. From the figures, it is also clear that this is only possible if higher radial mode orders are present, even at frequencies below their cut-on. This scattering into higher mode orders can also have an stabilizing influence, as shown recently by McAlpine et. al [81], who exploited this mechanism in the optimization of acoustic liners for noise reduction in aero engines. A detailed analysis of the transport of acoustic energy for both propagating and evanescent modes is given by Morfey [85]. He shows that, even though a single evanescent wave is not able to transport acoustic energy, the interaction between up- and downstream evanescent waves does actually lead to a non zero transport. This holds even for ducts without mean flow. In the literature of resonator rings for rocket thrust chambers, this mechanism is not mentioned at all yet. The low-order model is capable to handle these 3D-effects remarkably good.

Three major stabilizing effects of the resonator rings have been identified:

(i) The eigenfrequencies of the system close to the design point of the cavities are shifted to slightly different frequencies. The coupling between driving mechanisms and acoustic might be weakened in this way.
(ii) Dissipation of acoustic energy by viscous effects described by the real part of the shell impedance stabilizes the system.
(iii) At connecting planes of the resonator ring, the traveling waves are scattered into higher order, evanescent modes reducing the acoustic energy present in the resonant mode.

To further clarify these three mechanisms, a series of parametric studies have been performed and the results will be presented in the next subsections. The information obtained from these parametric studies should serve as a basis for the interpretation of further results concerning the sensitivity to cavity temperature inhomogeneities caused by EHT.

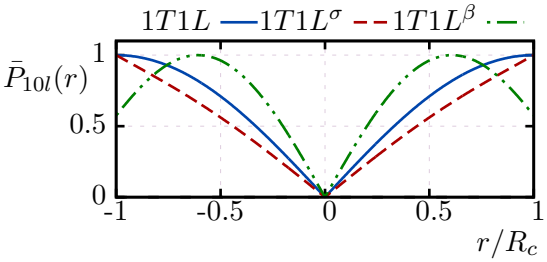

Figure 4.20: Normalized Pressure amplitude of $1T1L$ modes at axial position x_R.

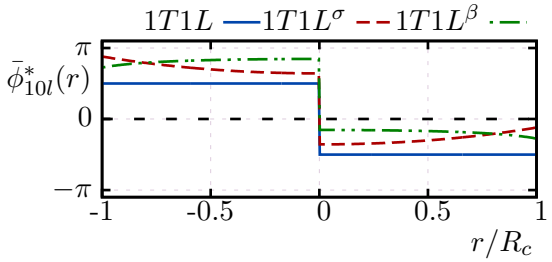

Figure 4.21: Phase of $1T1L$ modes at axial position x_R.

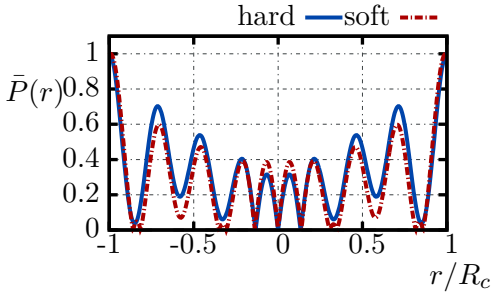

Figure 4.22: Pressure across first jump at the eigenfrequency of the mode $1T1L^{\sigma}$.

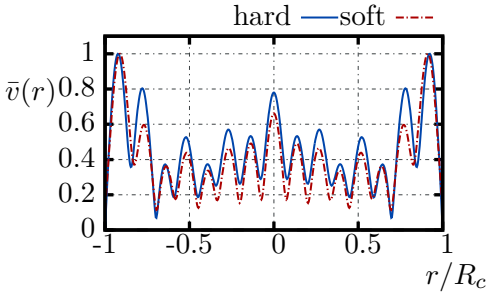

Figure 4.23: Radial velocity across first jump at the eigenfrequency of the mode $1T1L^{\sigma}$.

4.7.1 Influence of Cavity Length

It has been shown that a resonator ring brings additional degrees of freedom per azimuthal order and that the eigenfrequencies of the coupled system do not match the ones of the individual components. Thus, the optimum design of the ring cannot be determined by the mere consideration of the quarter wave cavities. To gain a better understanding, a parametric analysis that systematically varies the length of the cavities in the ring has been performed. The network described by Fig. 4.14 with parameters given by the test case D in Tab. 4.3 is used for the parametric study. Both the eigenfrequencies and growth rates of the coupled system are monitored.

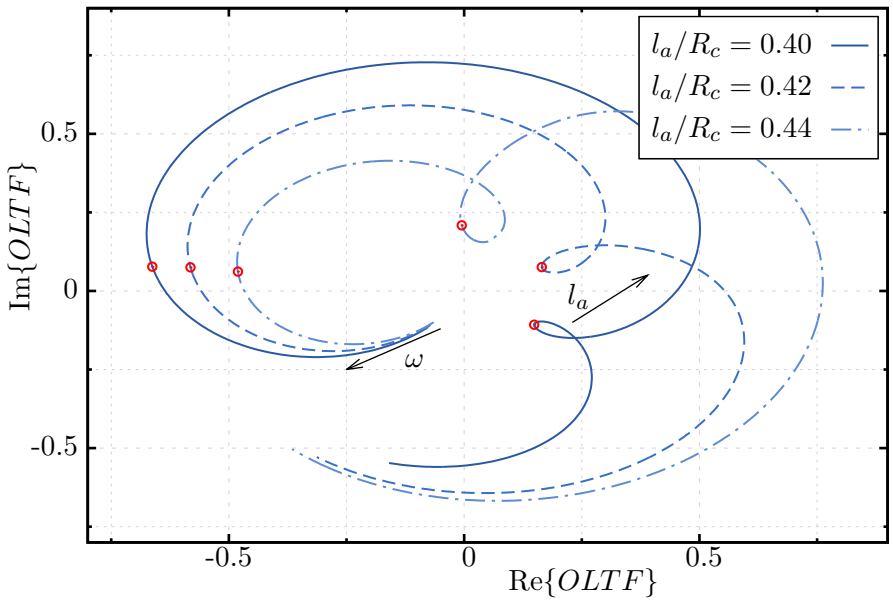

Figure 4.24: $OLTF$ curves of the representative chamber with ring and three different cavity lengths for the azimuthal order $m = 1$. The frequency range displayed spans the region close to the $1T1L$ mode.

Analyzing the problem via the Nyquist plots, the resonator ring becomes noticeable through an additional small loop in the $OLTF$ curve. As said before, the position of this loop depends on the eigenfrequency of the cavities. For increasing cavity lengths, the eigenfrequency of the cavities becomes smaller and the loop slides in counterclockwise

direction along the $OLTF$ curve, as shown in Fig. 4.24. Accordingly, the points with minimal distance to the critical point -1 slide towards lower frequencies.

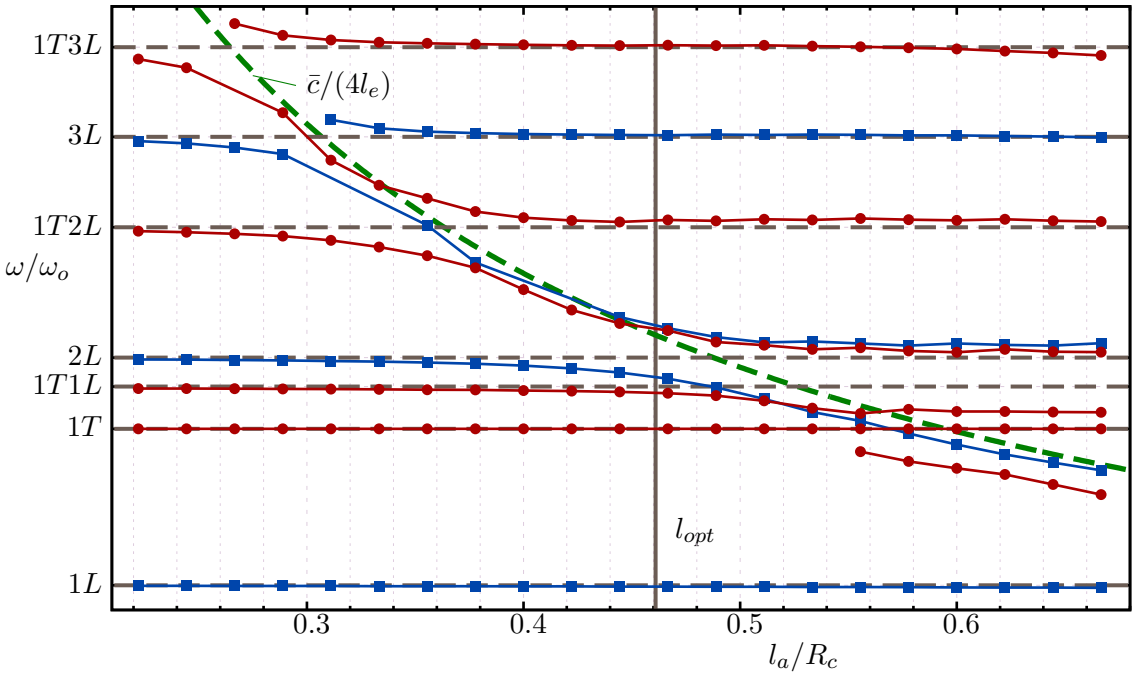

Figure 4.25: Case D: Real part of eigenfrequencies for various cavity lengths.

The results of the complete parametric study can be summarized in Fig. 4.25, where the real part of the eigenfrequencies are plotted against the non-dimensional cavity length. For very small lengths, the eigenfrequency of the cavities lie beyond the investigated frequency range. Thus, as seen in Fig. 4.25, the eigenfrequencies of the coupled system within this range remain unaffected and almost equal to those of the reference case without ring denoted by the dashed horizontal lines. As the cavity length increases, the resonator ring starts to interact with the chamber, more precisely with the $1T3L$ mode. The frequency of the pure $1T3L$ mode decreases and from a certain length on, an additional mode appears at a slightly higher frequency. According to the previous notation, these two modes are denoted as $1T3L^{\sigma}$ and $1T3L^{\beta}$, respectively. For larger cavity lengths, the $1T3L^{\beta}$ frequency approaches more and more the frequency of the pure $1T3L$ mode. Similarly, the $1T3L^{\sigma}$ slides toward the pure $1T2L$ mode. This behavior reiterates for the next modes: the $1T2L$ mode transmutes gradually into the $1T1L$ mode and so on. The same behavior can be observed for the pure longitudinal modes. Due to the influence of the resonator ring, a higher mode transmutes gradually into the adjacent transverse mode of lower longitudinal order. As expected, the course of these mode conversions lies close to the eigenfrequency curve of the cavities $f_R \sim \bar{c}/(4l_e)$ denoted by the green dashed line in the figure. The results are in close agreement with the FEM analysis of Oschwald and Farago [95].

The stability of both the pure and the additional modes depends on the imaginary part of the eigenfrequencies. Figure 4.26 shows the corresponding growth rates as a function of the cavity length. For clarity, each mode transformation is shown in a different subfigure with horizontal dashed lines, that denote the values of the undamped system. Again, for small lengths, the growth rates tend to the values of the reference case

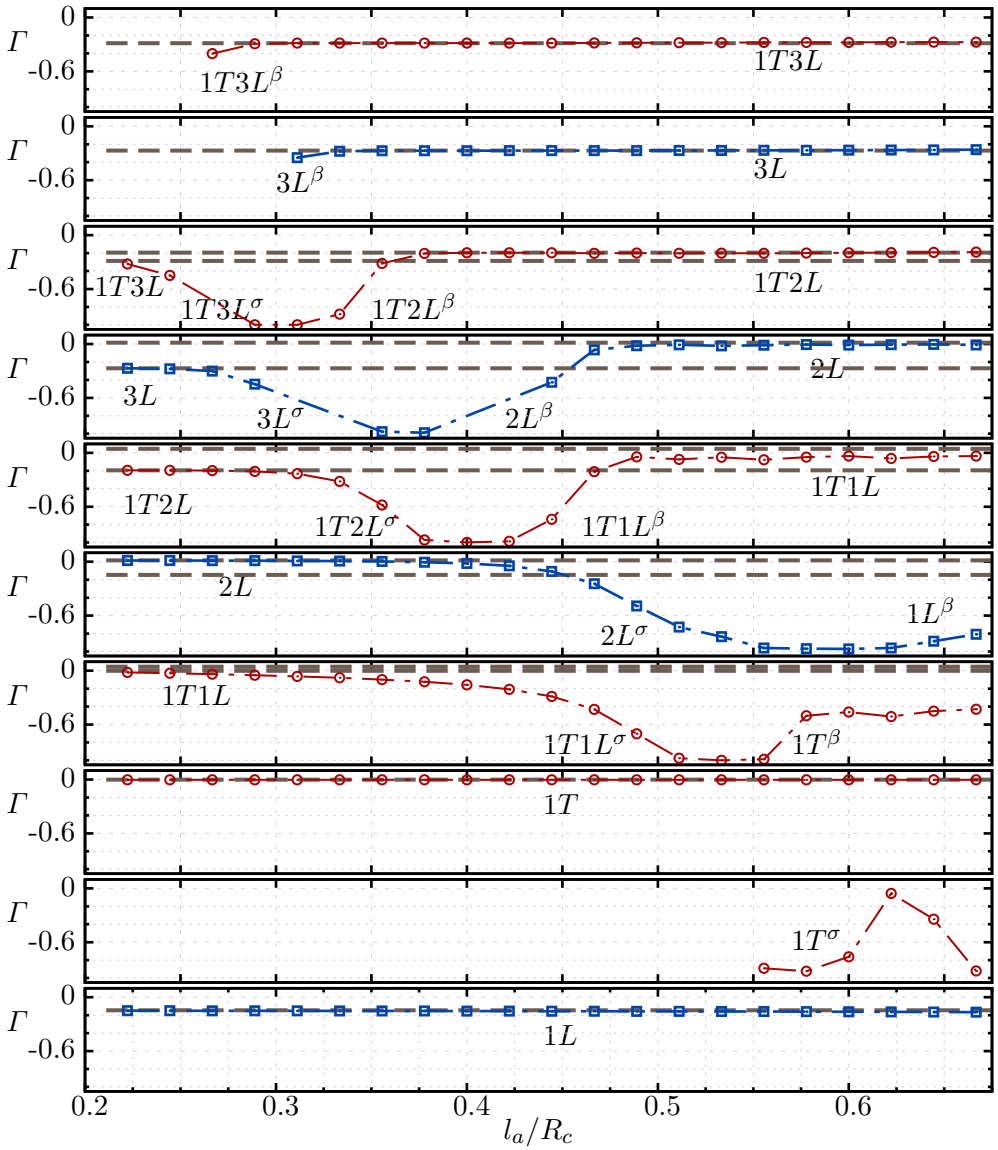

Figure 4.26: Case D: Growth rates of different modes for various cavity lengths.

without ring, where the modes $1T1L$ and $2L$ are slightly unstable. Due to the coarse resolution, this fact is not clearly visible in Fig. 4.26. For increasing length, the ring starts to modify the growth rate close to the eigenfrequency of the cavities. The behavior is very similar as for the real part of the eigenfrequencies: the growth rate of a mode transmutes gradually into the adjacent longitudinal mode of lower order. However, before reaching the value of the adjacent mode, the growth rate decreases almost to its minimum possible value of $\Gamma_{min} = -100\%$. This means that even though the mode is mathematically possible, physically it would unlikely appear because it would decrease almost immediately. In this context, additional modes in the coupled system emerge only when both cavities and combustion chamber share a similar eigenfrequency.

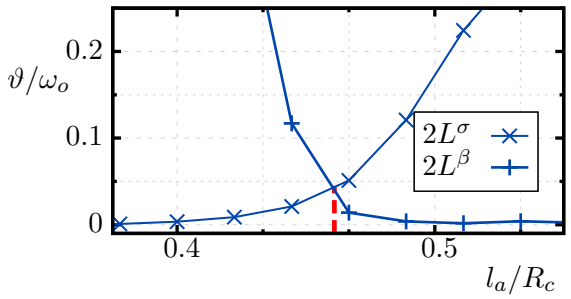

Figure 4.27: Case D: imaginary component of $2L^\sigma$ and $2L^\beta$ modes as a function of cavity length.

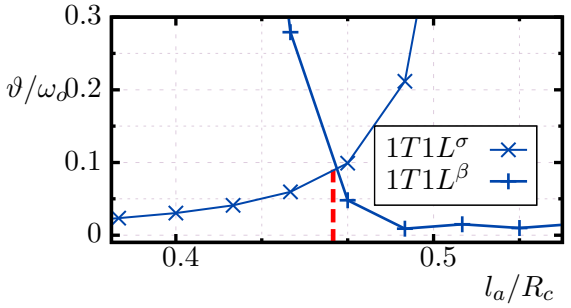

Figure 4.28: Case D: imaginary component of $1T1L^\sigma$ and $1T1L^\beta$ modes as a function of cavity length.

Depending on the mode to be damped, the optimal cavity length is that for which the decay rate of both σ and β modes is strongest. However, the decay rate per cycle is not suitable for this comparison because the normalizing frequency, and thus the cycle period, is different for the different modes, see [35]. Instead, the imaginary part of the eigenfrequencies normalized with the same reference frequency should be used. This procedure is shown in Figs. 4.27 and 4.28 for the previously unstable modes $2L$ and $1T1L$, respectively. For the length range of interest, the $2L^\sigma$ mode arises when the $3L$ mode transmutes into the $2L$ mode. Similarly, the $2L^\sigma$ mode arises when the $2L$ mode transmutes into the $1L$ mode. The intersection of these two curves in Fig. 4.27 marked with a red dashed line denotes the optimal length at which the imaginary part of the eigenfreqeuencies is maximal for both modes. The same procedure is followed for the $1T1L^\beta$ and $1T1L^\sigma$ modes shown in Fig. 4.28. In both cases, the optimal length is approximately equal $l_{opt,1T1L} \approx 0.461 \approx l_{opt,2L}$. This optimal length is also marked in Fig. 4.25 by a vertical line.

It is interesting to compare this optimum length to the one predicted by the decoupled analysis, since it is a common practice to design the resonator cavities to match the eigenfrequency of the undamped system. In this case, the effective length of the cavities can be determined from Eq. (3.16) by substitution of the eigenfrequency f_{1T1L} of the chamber without ring. Subtraction of the end correction length according to Eq. (3.5) gives then the geometrical length. Substitution of the values for the representative chamber gives:

$$\frac{l_{opt,de}}{R_c} = \frac{\bar{c}_r}{\bar{c}_c}\frac{\pi}{2\eta_{10}}\frac{f_{ref}}{f_{1T1L}} - \frac{4}{3\pi}\frac{d}{R_c} \approx 0.526 \quad , \tag{4.54}$$

which is considerably larger than the one determined from the stability of the coupled system. From this example it is clear that the coupled system of combustion chamber and damping devices has to be considered in order to optimize resonator cavities.

4.7.2 Influence of Non-Linear Dissipation at the Cavity

In the decoupled analysis, the absorption coefficient has been used to evaluate the efficiency of resonator rings. The maximum in absorption occurs at the cavity resonances and the equivalent resistance plays a decisive role for its magnitude. However, it has been suggested that sound absorption through dissipation is not the only stabilizing mechanism of resonator rings when coupled to the chamber. To bring some insight into the influence of acoustic dissipation on the efficiency of resonator rings, a parametric study that varies the non-linear resistance factor in the impedance expression of the quarter wave cavities has been performed. Test case E in Tab. 4.3 gives the geometrical parameters used in this analysis.

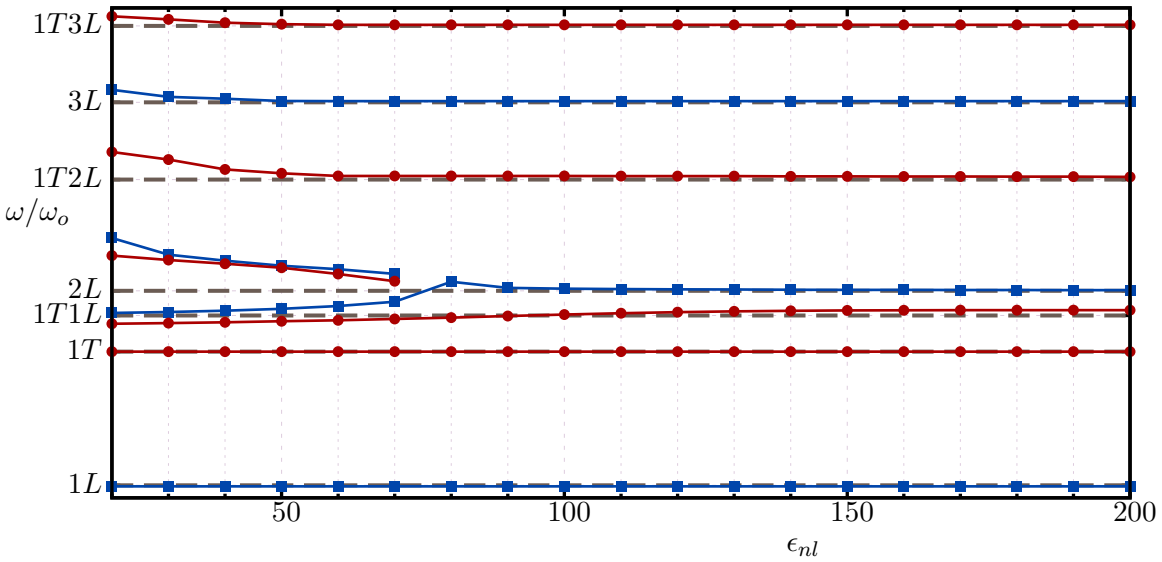

Figure 4.29: Real part of eigenfrequencies for various non-linear resistance factors calculated from test case E.

Figure 4.29 shows the eigenfrequencies of the coupled system as a function of the non-linear resistance factor. Again, the dashed horizontal lines denote the frequencies of the undamped case without ring and serve as reference. For non-linear resistance factors larger than $\epsilon_{nl} \gtrsim 100$, the eigenfrequencies of the coupled system are almost equal to the ones of the undamped case and no additional DOF's appear. For such high non-linear factors, the resonator ring's equivalent resistance is large and the cavities are overdamped. Thus, the soft shell modeling the resonator ring behaves actually more like a hard boundary. The additional DOF's appear only for lower resistance values of about $\epsilon_{nl} \lesssim 80$. Since the cavities' length for this test case are chosen to mainly interact with the $2L$ and $1T1L$ modes, these modes are split into β and σ modes at a slightly higher and lower frequencies, respectively. The stability dependency of the coupled system is given in Fig. 4.30, where the growth rates of the modes are plotted

against the non-linear factor. As expected, only the growth rates of the $2L$ and $1T1L$ modes are influenced by the ring.

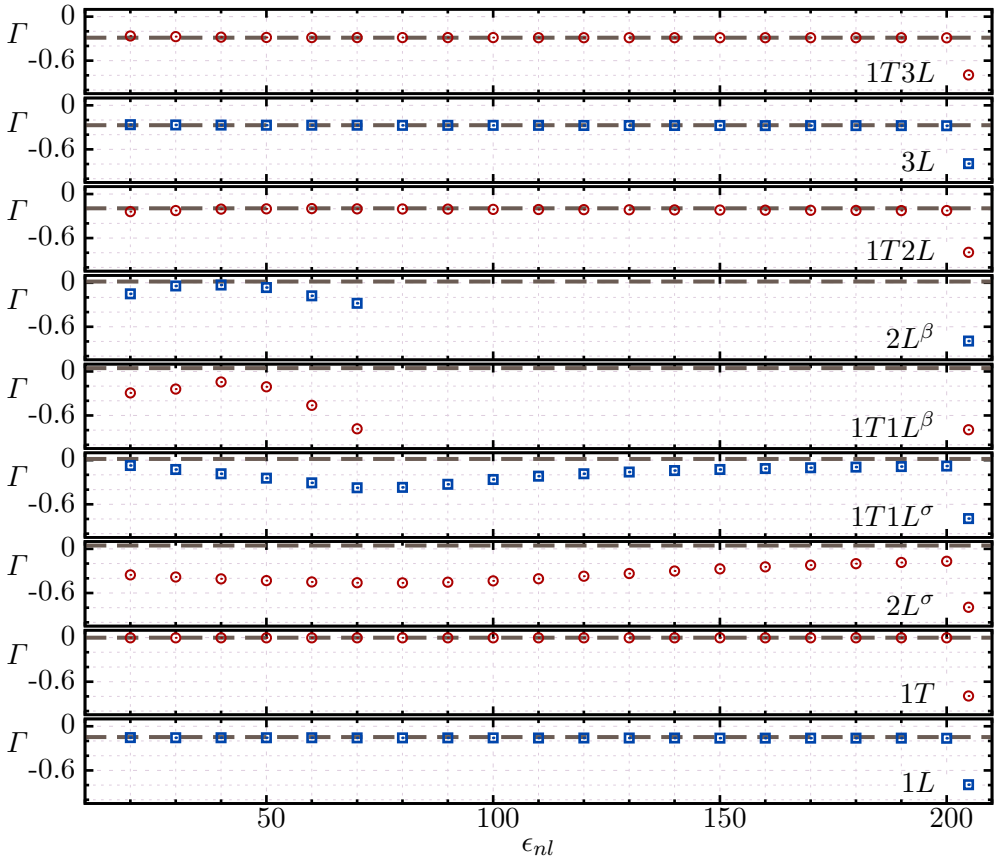

Figure 4.30: Growth rates for various non-linear resistance factors computed from test case E. Markers denote the damped case, dashed lines the reference values from the undamped case A.

Again, rather than the growth rates, the imaginary part of the eigenfrequencies should be used to estimate the optimal non-linear factor that leads to maximum stabilization. For this purpose, dissipation is given in Figs. 4.31 and 4.32. For large non-linear factors the system is only barely damped. For lower values, the system stabilizes and the damping increases, while the additional DOF's also appear. This trend continues until a maximum is reached in the $2L^{\sigma}$ and $1T1L^{\sigma}$ modes and the imaginary part starts to decrease again. Thus, at this points the coupled system is optimally damped for the given configuration. The optimal values of the non-linear resistance factor are approximately equal for both modes $\epsilon_{nl,opt,2L} \approx \epsilon_{nl,opt,1T1L} \approx 80$.

Again, it is interesting to compare this optimal value against the one predicted by the decoupled analysis. According to Fig. 3.20, the absorption coefficient of the equivalent resonator ring has its maximum of $\alpha_{max} = 1$ at a non-linear factor of $\epsilon_{nl,opt,de} \approx 140$. The value considerably differs from the one determined by the parametric study of the coupled system. One major conclusion of this result is that, when considering the coupled system of chamber and resonator ring, the strongest stabilization does not necessarily occurs when the absorption of the ring is maximum. This means that the dissipation of acoustic energy is not the solely stabilization mechanism of resonator rings. As suggested at the end of Sec. 4.7, the additional stabilization comes from weak-

ening the coupling between combustion dynamics and acoustics and from the scattering of acoustic waves at connecting planes of the resonator ring. These two mechanism are stronger when additional DOF's appear in the coupled system because then, the eigenfreqeuencies of the additional modes are shifted and their transverse mode shapes differ from the hard walled modes.

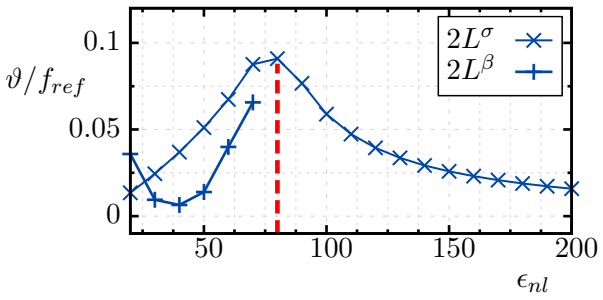

Figure 4.31: Imaginary component of $2L^\sigma$ and $2L^\beta$ modes as a function of non-linear resistance factor computed from test case E.

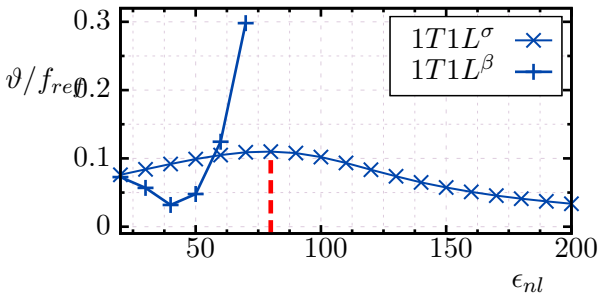

Figure 4.32: Imaginary component of $1T1L^\sigma$ and $1T1L^\beta$ modes as a function of non-linear resistance factor computed from test case E.

4.7.3 Influence of Inhomogeneous Temperature Distribution Inside the Cavities

In this section, the influence of a moderate cavity temperature inhomogeneity is evaluated. A simple polynomial temperature profile is assumed along the cavity axis. For this purpose, the stability of the coupled system defined by the test case F in Tab. 4.3 is estimated using the polynomial approach and the results compared against the ones of test case C using the homogeneous approach.

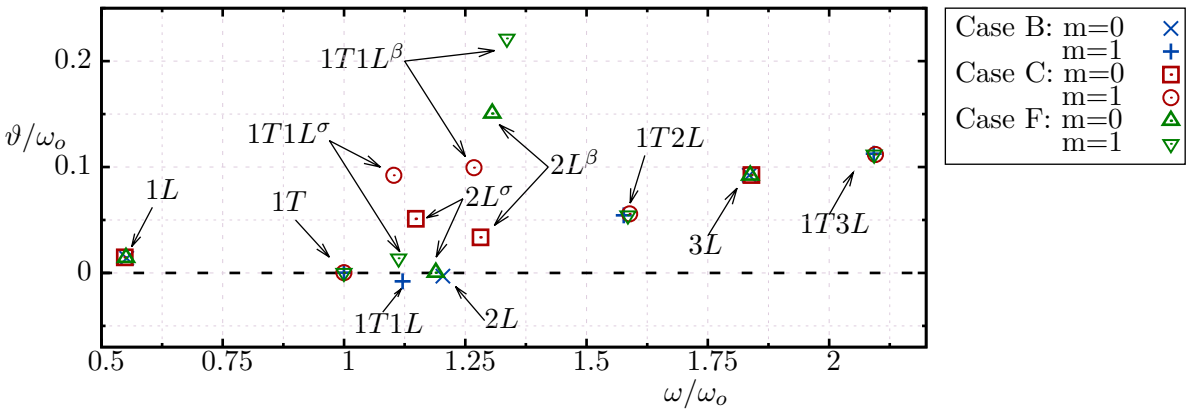

Figure 4.33: Eigenfrequencies of representative thrust chamber with resonator ring. Comparison between homogeneous and polynomial approach. Case B, undamped. Case C, damped with homogeneous approach; Case F, damped with polynomial approach.

The results of this comparison are given in Fig. 4.33, where the normalized eigenfrequencies of the coupled system are plotted in the complex plane. As a reference, the eigenfrequencies of the undamped case are also given. It can be seen that only the eigenfrequencies close to the resonant frequency of the cavities are affected by the ring in accordance to all previous observations. Furthermore, the appearance of additional DOF's is predicted by the two modeling approaches. However, even for this moderate inhomogeneity ratio of $\chi = 6.2$, the eigenfrequencies and growth rates of the system modes differ slightly depending on the approach used. Since the same resistance dependency is used for the two approaches, the discrepancy can only come from the reactance.

4.8 Consequences of EHT on the Damping Behavior of Resonator Rings

The previous Sec. 4.7 has validated the low-order method and has demonstrated its applicability to qualitatively predict the stability of rocket thrust chambers. For an idealized representative chamber, the stabilizing influence of a resonator ring of the quarter wave type has been described. The influence of some design parameters on the stability of the coupled system has been also estimated. Furthermore, the necessity to account for temperature inhomogeneities inside the cavities has been demonstrated. Based on these findings, the impact of stronger thermal loads in the vicinity of the resonator rings during transient operation (EHT) on their damping behavior and the stability of the coupled system can be now qualitatively predicted.

In Sec. 3.6, an idealized radial temperature distribution has been defined. In this simplified temperature distribution, the influence of EHT is qualitatively modeled by an increase of the chamber wall temperature. This assumed radial temperature distribution shown in Fig. 3.12 is used again to estimate the consequences of EHT on the stabilizing influence of resonator rings for the coupled system. Again, the cooling $\bar{T}_{\mathrm{cool}}$ and combustion temperatures $\bar{T}_{\mathrm{comb}}$ are assumed to be constant. Upon the occurrence of EHT, the cavity mouth temperature T_n is expected to rise to higher values changing both the cavity's average temperature $\bar{T}_r$ and inhomogeneity ratio $\chi = \bar{T}_n/\bar{T}_{\mathrm{cool}}$. On the chamber side, the change in average chamber temperature due to the higher wall temperature is assumed to be small $\bar{T}_c \approx const.$ Table 4.3 gives the geometrical and thermodynamical values used in this test case G.

The stability of the coupled system is monitored within the frequency range of interest. The real part of the eigenfrequencies for various inhomogeneity ratios is given in Fig. 4.34. For increasing cavity mouth temperature both the inhomogeneity ratio and average temperature inside the cavities rise. Thus, the eigenfrequency of the resonator cavities also increases. According to Fig. 3.15, the eigenfrequency of the cavities can be approximated by the simple homogeneous approach using the average temperature inside the cavities given by Eq. (3.16). This approximated dependency $f_r \approx \bar{c}_r/(4l_e)$ is also plotted in the figure. The behavior is very similar to the previous observations: additional DOF's appear and, as the eigenfrequency of the cavities changes, the modes of the coupled system gradually transmute into the adjacent modes of longitudinal order. These transmutations take place close to the approximated cavity resonant curve.

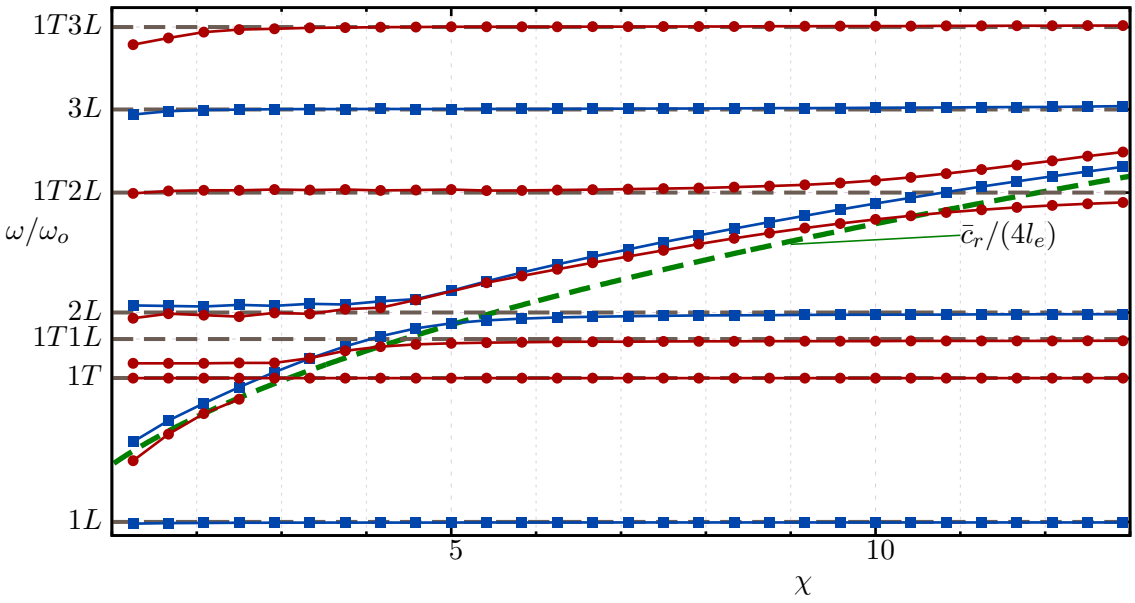

Figure 4.34: Real part of eigenfrequencies against the temperature inhomogeneity ratio in the cavities. Computed using case G.

Accordingly, the growth rates of the coupled system modes shown in Fig. 4.35 decrease to their minimum value of $\Gamma_{min} = -1$ before reaching the value of the adjacent longitudinal mode. The conclusions addressed in Sec. 4.7.1 can also be applied here, with the difference that upon the occurrence of EHT, the equivalent resistance of the resonator ring increases.

To determine how important it is to account for the temperature inhomogeneity in the global stability analysis of the representative chamber, the results using the polynomial approach are compared against those from the simplified homogeneous approach (Case H). The analysis focus on the previously unstable modes $2L$ and $1T1L$. Again, the imaginary part of the eigenfrequencies is used for the comparison. Figure 4.36 shows the results of this comparison. For small inhomogeneity ratios, both approaches predict approximately the same stability margin. The wiggles in the curves at regions of small inhomogeneity ratio are caused by a singularity in the Nyquist-curve close to the points of minimal distance. As explained by Kaess [59], such discontinuities may appear when portions of the network uncouple from the rest of the system. The discontinuity reduces the accuracy of the Nyquist-plot method leading for example to such oscillations. Fortunately, the method is still able to predict the trends of the system. For increasing inhomogeneity ratio, the homogeneous approach predicts a larger imaginary part for the eigenfrequencies. This is especially critical for modes close to neutral stability, as is the case of the $2L^{\beta}$ and $1T1L^{\beta}$. Thus, from the homogeneous approach, the stability of the coupled system appears to have a larger stability margin and to be less sensitive to EHT, while in reality the system is closer to neutral stability. This is in accordance to the results predicted by the decoupled analysis performed in Sec. 3.6.

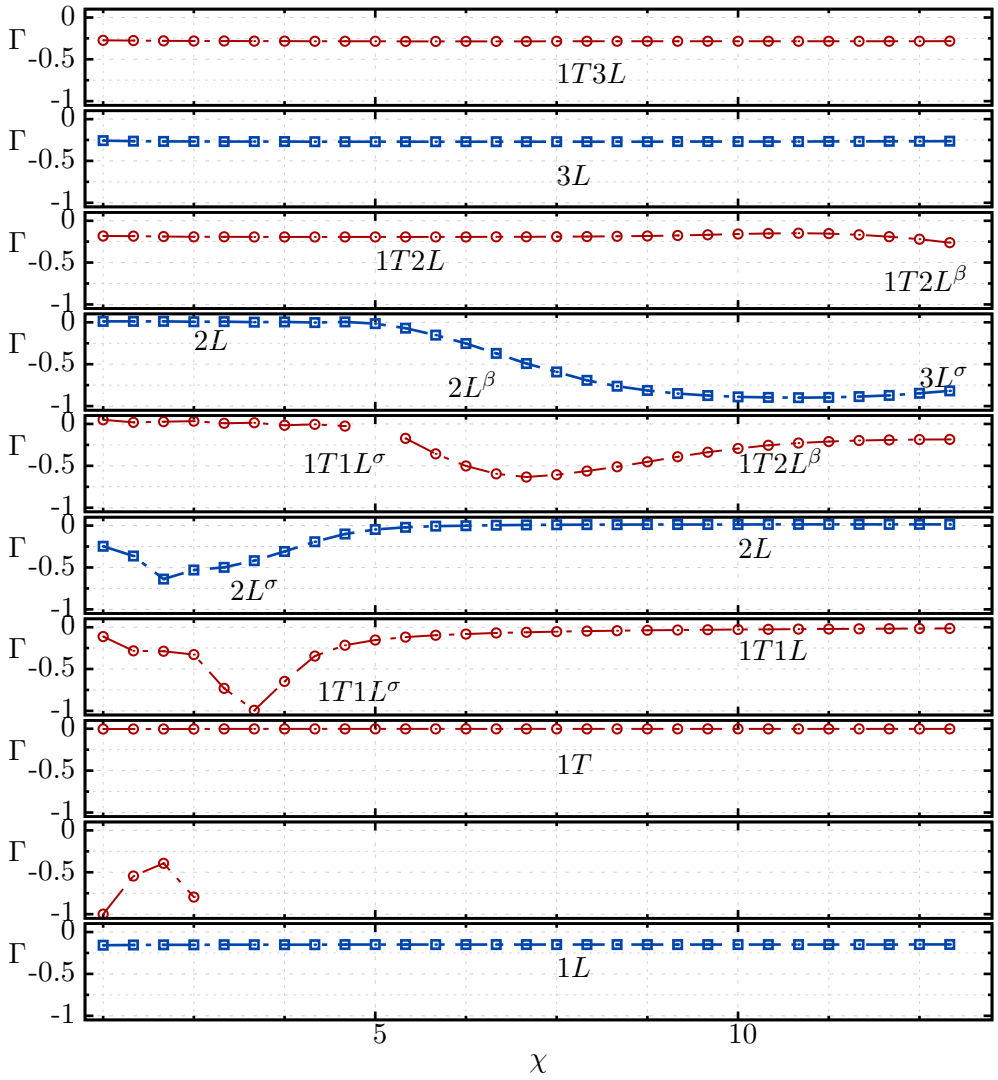

Figure 4.35: Growth rates against the temperature inhomogeneity ratio in the cavities. Computed using case G.

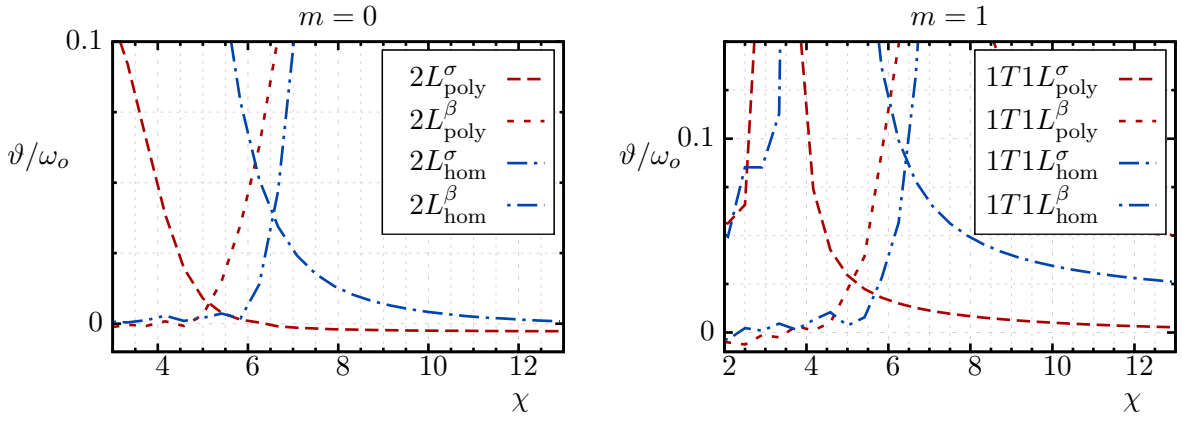

Figure 4.36: Imaginary component of eigenfrequencies for the $2L$ and $1T1L$ modes against the temperature inhomogeneity ratio in the cavities. Comparison of case G and H.

5 Enhanced Heat Transfer in Pulsating Flows

In devices suffering from self-sustained combustion oscillations, the resulting acoustic field with periodic pressure and velocity fluctuations has been reported to lead to considerably enhanced heat transfer coefficients [29, 49, 99]. In the literature, these phenomena have been repeatedly reported not only in rocket thrust chambers, but also in tail pipe pulse combustors. While the enhancement can be considered as beneficial in the later devices due to the possible reduction of required heat transfer area, the enhancement can actually decrease the performance and reliability of the engine in rocket motors. The higher thermal loads can change the temperature distribution in the chamber, including the gas inside the resonators used as damping devices. The damping behavior of these cavities can degrade due to the different temperature distribution. As demonstrated in Ch. 4, even moderate temperature changes of the gas inside the cavities can lead to the destabilization of the engine. In extreme cases, the reported enhancement has reached such intense values that the thermal integrity of the chamber is compromised. It is thus very important to understand the mechanisms leading to this heat transfer enhancement in order to accurately predict the thermal loads under real operating conditions. The literature review given in Sec. 5.1 illustrates the necessity of additional fundamental research in this area. Yet, it has not been possible to reproduce in theoretical or numerical approaches the higher heat transfer rates observed in some striking experiments. Even contradictory results can be found in the literature, which report enhanced as well as decreased heat transfer.

Of particular interest for the present study is hereby, how far can the periodic transient conditions present in rocket thrust chambers lead to heat transfer enhancement and up to what extent can this modify the temperature distribution in the chamber and the resonator cavities. The former concerns the thermal integrity of the chamber walls, while the latter the proper design of damping cavities. In the second part of this thesis, a detailed analysis of the problem is given, which tries to clarify these questions. Due to the complexity of the problem, a divide and conquer strategy presented in Sec. 5.2 is followed. Part of the results presented in this chapter have been published previously by the author in [15, 32] or are based on the results of supervised student thesis [31].

5.1 Literature Review Concerning Enhanced Heat Transfer in Pulsating Flows

In the literature, the phenomenon of enhanced heat transfer in pulsating flows has been reported repeatedly. For the case of rocket motors, Harrje [49] gives an overview of early observed incidents and argues that, due to the aggressive conditions in the chambers, most of the experimental information is limited and of rather qualitative

nature. Under representative conditions, unstable operation does not permit reliable measurements and often only a severe hardware damage can be attested. Nevertheless, he listed a few references where some measurements could be achieved leading to a relative heat transfer enhancement ranging from 170% to even 400%. From these early qualitative observations, he summarizes that

a) both transverse and longitudinal instabilities of significant amplitude can lead to heat transfer enhancement,
b) the enhancement for transverse modes tends to be stronger, and
c) devices operated at lower pressure are more susceptible to higher normalized enhancement.

At Princeton University, the heat transfer in oscillating flows driven by acoustic waves has been studied primarily experimentally by the group of Harrje et al. under idealized academic conditions. In a final report [50], Harrje concludes that the heat transfer under periodic unsteady conditions can indeed be considerably higher than in steady state by more than 100%. The enhancement seems to be maximal close to the velocity antinode of the oscillating modes. Furthermore, the degree of flow reversal plays a decisive role for the enhancement. Viscous dissipation and acoustic streaming appear to be of secondary order for the cases representative of thrust chambers. Harrje suggests that an interaction between the oscillations and the turbulent exchange properties offers the more plausible mechanism that controls the heat transfer enhancement in the flow.

In a laboratory scale, Perry and Culick [99] also studied the overall heat transfer in a solid propellant T-burner triggered to display combustion instabilities. In the presence of the oscillations, they found a definite heat transfer enhancement proportional to the square root of the oscillation amplitudes and the fourth root of the frequency.

Later on, the group of Dec et al. studied the problem experimentally with the help of a pulse combustor, which they managed to systematically trigger at various amplitudes and frequencies. The amplitude range was high enough to allow for flow reversal. In a series of papers [6, 27–29] they measured heat transfer enhancement that locally increased by 300%. The novelty compared to the investigations listed before was that they were able to perform detailed measurements of velocity, temperature and heat flux rates. They also share the hypothesis that a combination of increased turbulence at the shear layer and strong convection, driven by transverse flows at times of flow reversal, provide the most plausible explanation for the phenomenon. However, they were not able to explain the mechanism leading to these transverse flows during flow reversal.

While heat transfer enhancement has been experimentally reported several times, the responsible mechanisms have not been totally clarified yet. Neither in analytical nor in numerical approaches was it possible to reproduce those high enhancement ratios. Definitely, the large number of effects involved in the process of heat transfer in pulsating flows makes an accurate simulation difficult, especially in the case of turbulent pulsating flows. Due to the wide range of perturbation frequencies and the mean flow Reynolds numbers used in the different investigations, apparently contradictory arguments can be found in the literature, with both enhancement and decrease of heat transfer being reported.

Hemida et al. [51] attempted to clarify these issues with a theoretical analysis of heat transfer in laminar pulsating flow in a tube with constant wall heat flux. They found

that the local Nusselt number exhibits a spatial modulation along the tube with both higher and lower values compared to the stationary case. The perturbations are mostly present in the thermally developing region and are damped out further downstream. However, their studies are restricted to pulsating flow without center-line flow reversal. In an experimental study of laminar pulsating pipe flow, Habib et al. [47] studied the heat transfer characteristics at various pulsation frequencies. They again found cases with higher as well as lower Nusselt numbers and confirmed that the effects are primarily present in the thermally developing region.

In an analytical approach, Lundgren et al. [78] were able to resolve the flow field and heat transfer in pulsating flows in channel configurations including pipe flow. They treated the flow field as fully developed and imposed pressure, and velocity gradients in the axial direction that oscillated harmonically in time. Due to the symmetry of their formulation, they solved the governing equations of motions and energy in the transverse direction. While their study is restricted to laminar flows, they considered large amplitudes with center-line flow reversal. The consideration of an oscillating axial temperature gradient is the most important novelty of their study. Qualitatively, their results match the behavior of the experiments performed by Dec et al. very well, displaying second harmonics in the channel bulk temperature modulation. However, the results cannot be compared quantitatively because of the absence of turbulent scales. Nevertheless, the study also demonstrates the possibility of both enhanced and decreased heat transfer depending on the phase between the temperature and the velocity fluctuations.

One of the strongest limitations faced by CFD based simulations of turbulent pulsating flows is the required number of cells to properly resolve the turbulent scales. In addition to this, depending on the frequency of the organized motions, large integration times of several periods are necessary to achieve statistical convergence. For this reasons, DNS investigations are only feasible for academic conditions at low Reynolds numbers. On the other hand, computationally more efficient approaches like URANS generate unclosed terms that have to be modeled. For stationary turbulent flows accurate models exist. However, these conventional models fail to properly predict the flow dynamics in unsteady flows, as shown by Scotti and Piomelli [122]. Thyageswaran intended to simulate the turbulent flow in a pulse combustor tail pipe [126] and reproduce the high heat transfer rates reported by Dec et al. In order to resolve the whole tail pipe domain, his simulations were based on the use of wall models and URANS. They tested well established wall models, which however failed to reproduce the transient behavior of the heat transfer. They proposed an improved model which was only capable to reproduce the higher heat transfer rates qualitatively. Thus, while the investigation is able to approximately describe the heat transfer, it does not give insight into the mechanisms leading to the enhancement.

In this context, the trade-off between resolution and computational costs offered by the LES approach can be exploited in the study of turbulent pulsating flows. The validity and advantages of the LES approach to study unsteady problems as turbulent pulsating flows has been demonstrated by Scotti and Piomelli [121] for a wide range of frequencies. They showed that dynamic sub-grid scale models, which can be seen as state of the art, are capable of modeling accurately the unclosed terms in transient cases, too. This is not valid if conventional wall models are used. The near wall region has to be fully resolved, making the necessity of dynamically adapted coefficients evident. The study

of Scotti and Piomelli is restricted to incompressible flows without heat transfer using the dynamic Smagorinsky sub-grid scale model. Thus, the focus of their investigation lies on the momentum transfer. They concluded that the fluctuations generated in the near wall region by the influence of the pulsating pressure gradient do not propagate beyond a characteristic distance. They were able to estimate this so-called turbulent Stokes length l_τ using the sum of the molecular and turbulent diffusivities.

Wang and Lu applied the same LES methodology combined with the dynamic Smagorinsky sub-grid scale model to study the turbulent structure and the passive heat transfer [129] in turbulent pulsating flows between parallel plates. They investigated the influence of the Prandtl number and a turbulent Reynolds number of $\mathrm{Re}_\tau = 350$ on the thermal response of the flow. They confirmed that for high Prandtl numbers the temperature fluctuations and the mechanisms involved in the heat transfer process are confined to a very thin region close to the wall. Furthermore, the influence of the organized pulsations on the time average quantities are marginal under the investigated conditions without center-line flow reversal. Thus, heat transfer enhancement could not be predicted in that study.

This literature review gives an overview of the heat transfer in pulsating flows. The overall picture concerning enhanced heat transfer is that while serious evidence on its occurrence exists, a fully satisfactory explanation of the responsible mechanisms has not yet bin given. This is specially true for the turbulent case. Thus, fundamental research in this area is still highly necessary.

5.2 Identification of Relevant Mechanisms for EHT in Rocket Chambers

In order to perform a systematic study and to track the responsible mechanisms leading to enhanced heat transfer in rocket thrust chambers and resonator rings, the involved mechanisms and their possible interaction with heat transfer have to be identified.

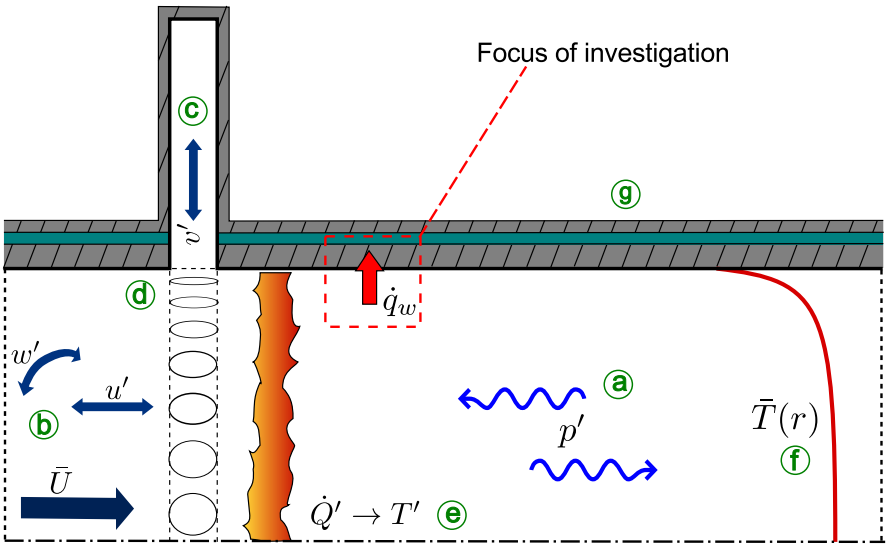

Figure 5.1: Possible mechanisms involved in the occurrence of enhanced heat transfer.

The situation in the vicinity of the resonator cavities is sketched in Fig. 5.1. A series of effects that could interact directly or indirectly with the heat transfer are marked in this figure with small letters and their description is given in the following list:

a) **Acoustic waves:** First of all, in rocket chambers, as in the majority of the devices where enhanced heat transfer has been observed, the driving force (mechanism) leading to the periodic oscillations are standing acoustic waves. These waves can have both longitudinal and transverse mode shapes, and their frequency is given by the chamber geometry.
b) **Pulsating flow:** Due to the axial mean flow $\bar{U}$, the velocity fluctuations induced by the acoustic waves present in the thrust chamber lead to a pulsating flow. Depending on the mode shape of the waves, the pulsating component can be in axial, tangential and radial direction.
c) **Oscillating flow:** In contrast, inside the cavities, the velocity fluctuates primarily in the chamber radial direction (or cavity local axial direction) due to the small transverse dimensions of the resonators. Furthermore, a pure oscillating flow is expected inside the cavities since no purge flow is used in rocket chambers. As explained in Sec. 2.5, oscillating flows are quite well understood, see [45, 121].
d) **Turbulence:** The flow field in the chamber is highly turbulent. At high oscillating amplitudes, jets emerge from the cavity mouths creating a very complex three dimensional flow field at this location.
e) **Temperature fluctuations:** Due to the coupling between the acoustic field and the local heat release of the combustion front, it can be expected that temperature fluctuations also occur.
f) **Stratification:** The high combustion temperatures coupled with the wall cooling lead to strong temperature gradients especially at the boundary layer. Thus, the flow field is expected to be stratified.
g) **Conjugate heat transfer:** The thermal inertia of the wall leads to a conjugate heat transfer problem.

This list of effects might be incomplete, but it gives a picture of the complexity exhibited by an environment representative of rocket thrust chambers. In the second part of this thesis, the intention is to evaluate the relevance of these effects concerning enhanced heat transfer and to characterize the conditions leading to its occurrence. However, not all effects listed will be handled in the same extent. Emphasis has been put on the most promising ones.

5.2.1 Definition of a Representative Domain

Going directly to the study of heat transfer under real rocket chamber operation conditions is not convenient or even feasible. The large number of involved effects and the complexity exhibited by each one of them would make the characterization unclear and confusing. The same holds for the different flow regimes at certain locations in the geometry. Certainly, the flow field close to the resonator cavity mouths is the most complex one due to the jets emerging at high amplitudes. The study of the heat transfer in this region would extend far beyond the goals of the first stage of the transregio TRR40. In contrast, the oscillating flow field inside the cavities is already well understood [45, 46, 121].

Thus, in order to understand first the general mechanisms leading to enhanced heat transfer under more definite conditions, only a small portion of the chamber flow field close to the cooled wall has been chosen. This small domain, enclosed by the red rectangle in Fig. 5.1, excludes the complex jets emerging from the cavity mouths and has a more homogeneous velocity distribution. Furthermore, the localized heat flux from the hot gases to the wall can be approximately handled as one dimensional. The conditions inside this cell can be identified in a more general sense allowing a more fundamental investigation. The local heat transfer inside this definite cell should give a qualitative picture of the possible enhancement intensity that can serve for future investigations on more complex geometries.

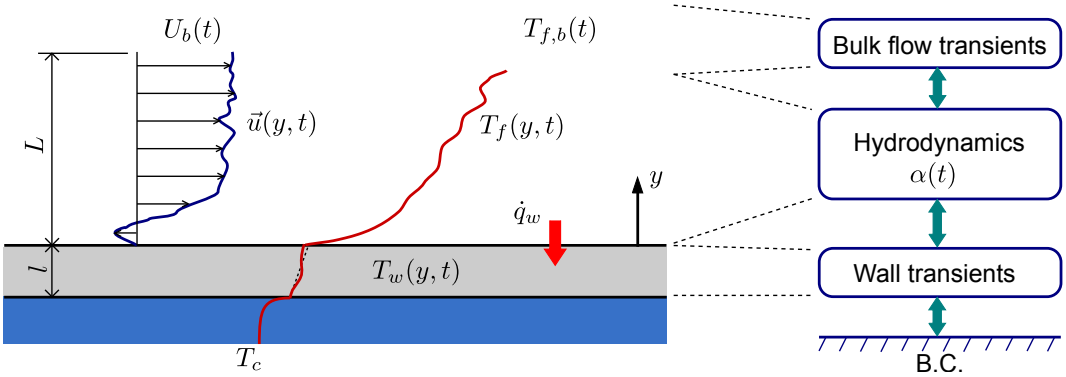

Figure 5.2: General representation of transient conjugate heat transfer from the hot gases to a small portion of the chamber wall cooled on the opposite side by liquid fuel.

Figure 5.2 gives a close up of the chosen cell. The size of the cell is small enough such that the curvature of the wall can be neglected. In wall normal direction, the cell extends so far that the boundary layer on the chamber side is fully enclosed up to a region in which the flow dynamics can be described as a bulk flow. This bulk flow can be of course highly turbulent and might experience velocity pulsations. The temperature of the bulk flow can also fluctuate in time due to the heat release fluctuations in the chamber. The stream- and spannwise dimensions of the cell are small compared to the dimensions of the chamber such that the system can be simplified as quasi one-dimensional. The chamber wall of finite thickness l_w and properties λ_w, ρ_w and c_v is cooled on the other side.

At the fluid-solid interface, the heat flux can be given by Fourier's law evaluated either on the solid or fluid side:

$$\dot{q}_w = -\lambda_f \left.\frac{\partial T_f}{\partial y}\right|_{y=0} = -\lambda_w \left.\frac{\partial T_w}{\partial y}\right|_{y=0} \quad . \tag{5.1}$$

Considering convective heat transfer, the classical Newton's law of cooling is also commonly used for the characterization of the heat flux:

$$\dot{q}_w = \alpha(t)\left[T_{f,b}(t) - T(0,t)\right] \quad . \tag{5.2}$$

However, under transient conditions, all quantities sketched in Fig. 5.2 can vary in time leading to some complications. Due to the system dynamics in both the solid and the fluid side, the proper definition of the reference temperature difference is difficult.

From Eq. (5.2), a change in the temperature difference leads also to a change in heat transfer coefficient, even if the net heat flux remains constant. A more striking difficulty arises if the local heat flux at the wall temporarily changes direction due to the system dynamics. This can lead to temporarily negative heat transfer coefficients, and also Nusselt numbers [77, 79], which is of course non-physical.

To avoid these complications, the present study follows numerical approaches that allow the direct computation of the flux via Fourier's law. Taking these considerations into account, the Nusselt number can be subsequently evaluated and used for the quantification of the heat transfer if the following condition is valid at all times:

$$\alpha = \frac{\dot{q}_w L}{\lambda_f \left(T_{f,b} - T_w(0,t)\right)} \geq 0 \quad . \tag{5.3}$$

Even if the condition given by Eq. (5.3) holds, care has to be taken when applying any kind of averaging operator for the characterization [134]. Zudin explain this introducing a *true heat transfer coefficient*:

$$\bar{\alpha}_{true} = \overline{\left(\frac{\dot{q}_w(t)}{T_b(t) - T_w(t)}\right)} \quad , \tag{5.4}$$

that can only be determined if all quantities are known at all instants. In contrast, he names the more practicable definition:

$$\bar{\alpha}_{exp} = \frac{\bar{\dot{q}}_w}{(\bar{T}_b - \bar{T}_w)} \quad , \tag{5.5}$$

as *experimental heat transfer coefficient*. Depending on the boundary conditions, the ratio $\bar{\alpha}_{true}/\bar{\alpha}_{exp}$, denoted by Zudin [134] as the factor of conjugation, can take values different from unity. This fact is mentioned in this section for completeness since the boundary conditions are left as general as possible. Later on, they will be of course restricted to specific cases. For simplicity, the true averaging procedure is meant if not specified.

Concerning the possible rise in heat transfer, a *ratio of enhancement* is defined comparing the average heat flux under pulsating conditions and a reference value without organized fluctuations:

$$EHT = \frac{\bar{\dot{q}}_w - \dot{q}_{w,\mathrm{ref}}}{\dot{q}_{w,\mathrm{ref}}} \quad . \tag{5.6}$$

Within this convention, positive values denote enhancement while negative values diminishment.

5.2.2 Strategy

As sketched in Fig. 5.2, the system dynamics have been divided into three major groups: the wall transients due to the thermal inertia, the hydrodynamics of the flow close to the hot side of the wall eventually abstracted into a heat transfer coefficient and finally, the bulk flow transients. On the cold side of the wall, the cold flow is assumed as a constant boundary condition due to the high mass flow rate of the cooling fluid in liquid state.

Thus, a constant cooling heat transfer coefficient and temperature is assumed. Even though the specific problem of heat transfer in rocket chambers has been generalized into a more academic configuration, if all three mentioned groups are considered at the same time, the chosen cell with definite conditions still exhibits a high complexity. For this reason, this thesis attempts to evaluate first the influence of each of these blocks separately in a divide and conquer strategy.

The steps followed in this strategy increase gradually in complexity and are organized as following:

- The first step in this strategy is the estimation of the wall dynamics. The interaction with a transient pulsating bulk flow should also be estimated. The question is valid since many engineering applications like thermoacoustic engines or Stirling engines rely on this interaction.
- In a subsequent step, as a preliminary study concerning the hydrodynamic response of pulsating flows, a laminar test case of a pulsating flow past a cooled plate is studied. The goal of this preliminary investigation is to gain some experience in the numerical simulation of pulsating flows and in post-processing transient data.
- Finally, building upon the preliminary investigations, the hydrodynamic response of a fully developed turbulent flow to periodic pulsations will be studied. Due to its relevance and complexity, this study focuses on this characterization and a separate Ch. 6 is devoted to it.

5.3 Low Order Model for the Heat Flux

To gain a more global insight into the dynamics of heat transfer in pulsating flows driven by thermoacoustic instability, a low order model that takes wall thermal inertia and also some flow transients into account is proposed in this thesis. As explained in Sec. 5.2.1, the convective heat transfer under transient conditions depends not only on the hydrodynamic inertia of the near wall flow, but also on the thermal inertia of wall and bulk-flow. The low-order model presented in the following is not intended to explain or predict the hydrodynamic mechanisms leading to the heat transfer modulation. Thus, the temporal dependency of $\alpha(t)$ is assumed to be known and the model should be specifically used to estimate the possible contribution of the thermal inertia of wall and bulk-flow on the overall heat flux. The model has been developed and analyzed by Emmert [31] in the framework of his Master-thesis under supervision of the present author and subsequently published by Emmert et al. [32].

The low-order model describes the unsteady conjugate heat transfer trough a wall of finite thickness l_w and constant properties λ_w, c_v and ρ_w. The flow on the inner side of the wall is heated by a pulsating hot flow assuming a transient but known heat transfer coefficient $\alpha_h(t)$. Furthermore, regularly distributed hot spots are convected downstream by the flow and thus, the bulk temperature $T_h(t)$ is also a known function of time. The outer side of the wall is cooled by a convective flow with constant heat transfer coefficient $\alpha_c = const$ and constant Temperature $T_c = const$. The length of the

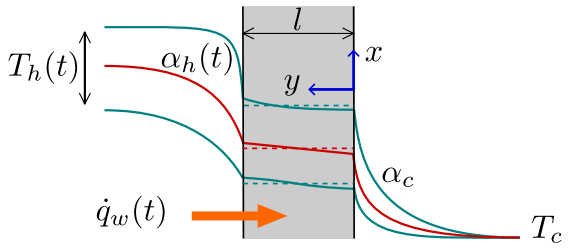

Figure 5.3: Qualitative temperature profiles across a wall of finite thickness l at various instants for a transient conjugate heat transfer problem.

plate is assumed to be large compared to its thickness $L/l_w \gg 1$ and thus, temperature gradients in axial direction are neglected compared to the ones in wall normal direction. Under this assumptions, the problem reduces to a one dimensional heat conduction problem inside the wall with transient boundary conditions of the third kind. The situation is sketched in Fig. 5.3 for a portion of the wall, where the temperature profiles are schematically given as a function of the wall normal coordinate y at three different time instants. As pointed out by Luikov [77], to maintain the physical validity of Newton's cooling law, transient problems represented by a boundary condition of the third kind are restricted to cases with positive valued heat transfer coefficients at all times. This restriction implies that the temperature profiles in the flow respond in a quasi steady manner. Otherwise the full conjugate problem using Fourier's law for the heat flux on the fluid side has to be solved.

The governing equation of the problem can be derived from an internal energy balance of a wall segment of infinitesimal length but finite thickness l_w:

$$\rho_w c_v \frac{\partial}{\partial t} \int T_w(t,y)\, dy = \alpha_h(t)\left[T_h(t) - T_w(t,l)\right] - \alpha_c\left[T_w(t,0) - T_c\right] \quad , \tag{5.7}$$

where the volumetric internal energy is expressed as $u = \rho_w c_v T_w$ and the heat fluxes at the boundaries are expressed via Newton's cooling law:

$$\alpha_h(t)\left[T_h(t) - T_w(t,l)\right] = -\lambda_w \left.\frac{\partial T_w(t,l)}{\partial y}\right|_{y=l} \quad . \tag{5.8}$$

It corresponds to an inhomogeneous partial differential equation of first order for the temperature inside the wall T_w. The transient boundary conditions on the hot side are given by the following harmonic functions:

$$\alpha_h(t) = \alpha_{h0} + \alpha_{h1}\cos(\omega t) \quad , \tag{5.9}$$

$$T_h(t) = T_{h0} + T_{h1}\cos(\omega t + \phi_T) \quad . \tag{5.10}$$

They represent an harmonic pulsating flow with convection of hot spots caused by heat release fluctuations of the same frequency but with a phase lag ϕ_T. This should mimic the response of the heat flux to perturbations caused by thermoacoustic instabilities. For the case of turbulent pulsating flows, the coefficients in Eqs. (5.9) and (5.10) can be thought as the ensemble averages at the corresponding phase ωt.

For generality, after substitution of the time dependent boundary conditions, and using the following set of non-dimensional parameters:

$$\xi = \frac{y}{l} \quad , \quad \vartheta = \frac{T - T_c}{T_{h0} - T_c} \quad , \quad \theta = \frac{T_{h0}}{T_{h0} - T_c} \quad , \quad \epsilon_\alpha = \frac{\alpha_{h1}}{\alpha_{h0}} \quad , \quad \epsilon_T = \frac{T_{h1}}{T_{h0}} \quad ,$$
$$\alpha_{\bar{h}} = \frac{\alpha_{h0}}{\alpha_{h0} + \alpha_c} \quad , \quad \alpha_{\bar{c}} = \frac{\alpha_c}{\alpha_{h0} + \alpha_c} \quad , \quad \tau = \frac{\alpha_{h0}(1+\epsilon_\alpha)}{\rho_w c_v l_w} t \quad , \tag{5.11}$$

Eq. (5.7) can be non-dimensionalized as:

$$[1+\epsilon_\alpha] \frac{\partial}{\partial t} \int \vartheta(\tau, \xi)\, d\xi = \alpha_{\bar{h}} \left[1 + \epsilon_\alpha \cos(\tilde{\omega}\tau)\right] \left[\epsilon_T \theta \cos(\tilde{\omega}\tau + \phi_T) - \vartheta(\tau, 1) + 1\right] - \alpha_{\bar{c}} \vartheta(\tau, 0) \quad . \tag{5.12}$$

Note that θ is a non-dimensional parameter fixed by a given problem, while ϑ corresponds to the time and location dependent variable. The resulting non-dimensional frequency:

$$\tilde{\omega} = \frac{\rho_w c_v l_w}{\alpha_{h0}\left[1+\epsilon_\alpha\right]} \omega \;\sim\; \frac{1}{\mathrm{Fo}\ \mathrm{Bi}_h \left[1+\epsilon_\alpha\right]} \tag{5.13}$$

corresponds to the ratio of oscillation period to a characteristic time of the unit impulse response of the temperature distribution [105]. This choice is important because it makes clear whether the oscillation frequency is large or small compared to the transients in the wall. To clarify this, consider first the steady state problem. In this case, the wall temperature profile is linear and the relation between the left and right temperatures is given by:

$$\vartheta(1) = \frac{\mathrm{Bi}_h + \vartheta(0)}{1 + \mathrm{Bi}_h} \quad , \tag{5.14}$$

where the Biot number on the hot side $\mathrm{Bi}_h = \alpha_{h0} l_w / \lambda_w$ is taken as the controlling parameter. The simplification into a lumped capacity, in which the temperature gradients inside the wall are assumed to be negligible, is valid for small Biot numbers $\mathrm{Bi}_h \lesssim 0.2$ [105]. In addition, if the ratio of heat transfer coefficients is small $\Gamma_\alpha = \alpha_{\bar{h}} / \alpha_{\bar{c}} \ll 1$, then the wall temperature can be assumed as constant $\vartheta \approx 0$. The wall transients can be completely neglected and an ideal BC of the first kind can be used for the hydrodynamic problem.

For transient periodic cases, the two just mentioned conditions are necessary but not sufficient for the same simplification. It has to be additionally ensured that the period of oscillation is large enough so the whole wall can respond to the new boundary condition as sketched in Fig. 5.3 by the horizontal dashed lines. Emmert et al. decided to approximate the sinusoidal excitation by a square wave signal and compare the characteristic time of the step response to one fourth of the excitation period $t_{crit} \approx 1/(8\pi\omega)$. The step response of a plate under the lumped capacity approximation to a sudden change in temperature ϑ_{step} can be given by the following relation:

$$\frac{\vartheta(t) - \vartheta_{ref}}{\vartheta_{step} - \vartheta_{ref}} = e^{-\frac{\alpha_{h0}(1+\epsilon_\alpha)}{\rho_w c_v l_w} t} = e^{-\tau} \quad . \tag{5.15}$$

Here, a conservative simplification using the maximum heat transfer coefficient $\alpha_{h0}(1+\epsilon_\alpha)$ has been applied. To find the threshold value, the specification of a 90% response is used as the critical time scale under pulsating conditions:

$$0.1 = e^{-\tau_{crit}} \quad \rightarrow \quad \tau_{crit} = -\ln(0.1) \quad . \tag{5.16}$$

This leads to the following threshold value for the non-dimensional frequency:

$$\tilde{\omega}_{crit} = \frac{2\pi}{-\ln(0.1)} \approx 0.87\pi \quad . \tag{5.17}$$

Thus, in order to estimate the importance of the wall transients in the overall dynamic system these three parameters can be used. If the following three conditions:

$$\mathrm{Bi}_h \ll 1 \quad \& \quad \Gamma_\alpha \ll 1 \quad \& \quad \tilde{\omega} \lesssim 0.87\pi \quad , \tag{5.18}$$

hold, the wall transients are negligible and an ideal BC of the first kind can also be applied for transient problems. For rocket chambers, these three conditions are mostly valid.

In addition, Emmert studied two cases of increasing complexity in which wall transients do occur [31]. The first one allows wall transients assuming a finite ratio $\Gamma_\alpha \gg 0$, but treating the wall as a lumped capacity $\tilde{\omega} < 0.87\pi$ and $\mathrm{Bi}_h \ll 1$. Under these assumptions, Eq. (5.12) reduces to a simple inhomogeneous differential equation of first order:

$$\begin{aligned}[1+\epsilon_\alpha]\frac{d\vartheta_w}{d\tau} + [1+\epsilon_\alpha\alpha_{\bar{h}}\cos(\tilde{\omega}\tau)]\,\vartheta_w = \\ \alpha_{\bar{h}}\left[1+\epsilon_\alpha\cos(\tilde{\omega}\tau)+\epsilon_T\theta\cos(\tilde{\omega}\tau+\phi_T)\right] + \frac{\alpha_{\bar{h}}\epsilon_\alpha\epsilon_T\theta}{2}\left[\cos(2\tilde{\omega}\tau+\phi_T)+\cos(\phi_T)\right]\end{aligned} \tag{5.19}$$

where the trigonometric functions have been expanded using the identity:

$$\cos(\tilde{\omega}\tau)\cos(\tilde{\omega}\tau+\phi_T) = \frac{1}{2}\left[\cos(2\tilde{\omega}\tau+\phi_T)+\cos(\phi_T)\right] \quad . \tag{5.20}$$

Note also that $\alpha_{\bar{h}} + \alpha_{\bar{c}} = 1$. Three important features concerning the system dynamics can already be identified: Firstly, due to the oscillations of heat transfer coefficient on the hot side, the differential equation is non-linear with time dependent coefficients. Secondly, the response of the system will also display higher harmonics due to the term oscillating with the frequency $2\tilde{\omega}$ in the inhomogeneous part. And thirdly, the average wall value will be offset by the time independent term $\sim \epsilon_\alpha\epsilon_T\cos(\phi_T)$. Concerning enhanced heat transfer, the third conclusion is definitely the most important one. It implies that the unsteadiness will induce a permanent, time independent change only when both the temperature and the heat transfer coefficient fluctuate. Furthermore, this permanent change can be positive or negative, depending on the relative phase between these oscillations leading either to heat transfer enhancement or diminishment. The concordance between these observations and the results of Lundgren et al. [78] for the heat transfer in pulsating pipe flow are remarkably good.

Before analyzing the temporal evolution of the heat transfer, important conclusions can be developed concerning the long time average solution. The permanent changes in overall heat transfer, can be estimated by averaging Eq. (5.19) over an oscillating period after the homogeneous solution vanishes. As shown by Emmert et al. [32] the transient term on the left-hand side vanishes due to the periodicity of the solution. The same holds for all harmonic terms of the inhomogeneous part and only the time independent terms are retained. Denoting this long time average operator by an overbar, the averaged equation can be written as:

$$(1+\epsilon_\alpha)\bar{\vartheta}_w + \alpha_{\bar{h}}\epsilon_\alpha\overline{\cos(\tilde{\omega}\tau)\vartheta_w} = \alpha_{\bar{h}} + \frac{\alpha_{\bar{h}}\epsilon_\alpha\epsilon_T\theta}{2}\cos(\phi) \quad . \tag{5.21}$$

The complications induced by the time dependent coefficient on the left-hand side become evident. Since the general solution for the wall temperature ϑ_s is also a function of time, a non-linear term arises. The average of this non-linear term can only be calculated if the temporal evolution of the wall temperature is known. This implies the knowledge of a closed form solution of Eq. (5.19).

To overcome the non-linear problem, Emmert et al. proposed two approximations for low and high frequencies, respectively:

- *Quasi-steady regime:* For low frequencies, the time derivative term in Eq. (5.19) is small $d\vartheta_w/d\tau \ll 1$ and thus can be neglected leading to a closed form expression for the wall temperature:

$$\vartheta_{w,lf} = \frac{\alpha_{\bar{h}}\left[1+\epsilon_T\cos(\tilde{\omega}\tau+\phi)\right]+\epsilon_\alpha\alpha_{\bar{h}}\cos(\tilde{\omega}\tau)+\frac{\epsilon_\alpha\alpha_{\bar{h}}\epsilon_T}{\cos}(2\tilde{\omega}\tau+\phi)+\frac{\epsilon_\alpha\epsilon_T}{2}\cos(\phi)}{1+\epsilon_\alpha\alpha_{\bar{h}}\cos(\tilde{\omega}\tau)} \quad . \tag{5.22}$$

  Unfortunately, the attempt to evaluate the long time average of the low frequency approximation analytically failed. No closed form has been found for the expression $\int \vartheta_{w,lf}\ dt$. Nevertheless, the ratio of enhancement can be computed numerically.

- *High frequency regime:* At high frequencies, the transient term dominates the dynamic behavior in Eq. (5.19). The non-linear term $\epsilon_\alpha\alpha_{\bar{h}}\cos(\tilde{\omega}\tau)\vartheta_w$ can be approximated using the time independent parts of the inhomogeneous right hand side:

$$\epsilon_\alpha\alpha_{\bar{h}}\cos(\tilde{\omega}\tau)\vartheta_w \approx \epsilon_\alpha\alpha_{\bar{h}}\cos(\tilde{\omega}\tau)\left[1+\frac{\epsilon_\alpha\epsilon_T\theta}{2}\cos(\phi_T)\right] \quad . \tag{5.23}$$

  The resulting linear ODE is written as:

$$\begin{aligned}(1+\epsilon_\alpha)\frac{d\vartheta_{w,hf}}{d\tau}+\vartheta_{w,hf} &= -\ \epsilon_\alpha\alpha_{\bar{h}}\cos(\tilde{\omega}\tau)\left[1+\frac{\epsilon_\alpha\epsilon_T\theta}{2}\cos(\phi_T)\right] \\ &+\ \alpha_{\bar{h}}\left[1+\epsilon_T\theta\cos(\tilde{\omega}\tau+\phi_T)+\epsilon_\alpha\cos(\tilde{\omega}\tau)\right] \\ &+\ \frac{\epsilon_\alpha\alpha_{\bar{h}}\epsilon_T\theta}{2}\left[\cos(2\tilde{\omega}\tau+\phi_T)+\cos(\phi_T)\right] \quad . \end{aligned} \tag{5.24}$$

  In a general sense, the solution of an inhomogeneous linear ODE can be decomposed into homogeneous, particular and stationary part:

$$\vartheta_{w,hf}(\tau) = \vartheta_{hom}(\sim e^{-\tau}) + \vartheta_{part}(\tau) + \vartheta_{stat} \quad . \tag{5.25}$$

  The homogeneous part depends on the initial conditions and vanishes at long times. The stationary part accounts for the contributions of the time independent terms of the right-hand side. Finally, the particular solution depends on the transient excitation terms of the right-hand side. The average wall temperature can be determined through the long time average of Eq. (5.24):

$$\bar{\vartheta}_{w,hf} = \alpha_{\bar{h}} + \frac{\epsilon_\alpha\alpha_{\bar{h}}\epsilon_T\theta}{2}\cos(\phi_T) \quad , \tag{5.26}$$

  where a permanent offset compared to the reference case is only possible when both the temperature and the heat transfer coefficient fluctuate. The sign of the

relative change depends on the phase angle between the fluctuations. The ratio of heat flux enhancement can be finally written as:

$$EHF = \frac{\bar{\vartheta}_{w,hf} - \vartheta_{w,ref}}{\vartheta_{w,ref}} = \frac{\epsilon_\alpha \epsilon_T \theta}{2} \cos(\phi_T) \quad . \tag{5.27}$$

The second configuration studied by Emmert et al. [32] considers the case in which $\Gamma_\alpha \gg 0$ and $\tilde{\omega} > 0.87\pi$. For higher frequencies, the assumption of an homogeneous temperature distribution in the wall starts to lose its validity. Even if the Biot number is small, for strong amplitudes at high frequencies the response of the wall on the cold side would start to lag behind the excitation acting as a low pass filter. This leads temporarily to temperature gradients in the wall. For this situation, Emmert developed then a semi-analytical approach based on finite volume discretization of the wall, see [31]. Each of the finite volumes in the wall is treated as a lumped capacity element, and thus, the necessary discretization accuracy depends on the ratio Bi Fo. The results of this second approach are not given in this thesis, because they are very similar to the ones of the lumped capacity approach. Merely the magnitude of the heat fluxes is smaller due to the gradients in the wall, but the conclusions concerning the relative enhancement are equal.

To conclude this section, three important results can be pointed out:

- Transients in the bulk flow can indeed lead to a heat transfer enhancement, provided that both temperature and heat transfer coefficient fluctuate. The phase between these fluctuations decides whether enhancement or diminishment occurs. This is in perfectly agreement with the results of Lundgren et al. [78].
- In absence of heat sources inside the wall, the transient response of the wall to harmonic perturbations of the bulk flow does not contribute to the enhancement. The thermal inertia of the wall works always against the heat flux. This is in accordance with the results of Mathi and Markides [79], and Zudin [134] .
- For transient problems, the Biot number condition $\mathrm{Bi} \ll 1$ and $\alpha_c \gg \alpha_h$ is a necessary, but not sufficient condition to decide whether an ideal boundary condition of the first kind $T_w \approx const.$ is valid or not. Additionally, the condition $\tilde{\omega} \lesssim 0.87\pi$ has to be fulfilled to assure that the response of the wall can react fast enough to the perturbations.

5.4 Laminar Pulsating Flow Past a Flat Plate

In the previous section, the interaction between wall and bulk-flow transients have been studied using a fluctuating heat transfer coefficient. All hydrodynamic effects were abstracted into this time dependent coefficient and thus, the response of the boundary layer to perturbations of the bulk flow was assumed known a priori. The aim of this section is to specifically study the response and dynamic behavior of a near wall flow subjected to bulk flow fluctuations and estimate the consequences on the heat transfer. Then results given in this section have been previously published by the author [15].

5.4.1 Test Case Set-up and Simulation Approach

A two dimensional configuration of a pulsating flow past a flat plate is chosen for the investigation. As shown in the previous section, concerning enhanced heat transfer, the wall dynamics play a negligible role and thus, ideal boundary conditions of the first kind are used. The investigation is limited to low Mach number laminar flows with small temperature ranges and thus, the Navier-Stokes equations can be simplified into:

$$\frac{\partial \vec{u}}{\partial t} + \vec{u} \cdot \vec{\nabla} \vec{u} = -\frac{1}{\rho} \vec{\nabla} p + \nu \vec{\nabla}^2 \vec{u} \quad , \tag{5.28}$$

$$\frac{\partial T}{\partial t} + \vec{u} \cdot \vec{\nabla} T = a \vec{\nabla}^2 T \quad , \tag{5.29}$$

with the constant kinematic viscosity ν and the constant thermal diffusivity $a = \lambda/(\rho c_p)$. The momentum conservation expressed in the form of Eq. (5.28) presumes inherently the mass conservation $\vec{\nabla} \cdot \vec{u} = 0$. Equation (5.29) corresponds to a transport equation for the temperature as a passive scalar and is a special simplified form of the energy conservation equation. In this way momentum and energy equations are only weakly coupled, since the velocity field is uncoupled from the temperature field, but not the other way around.

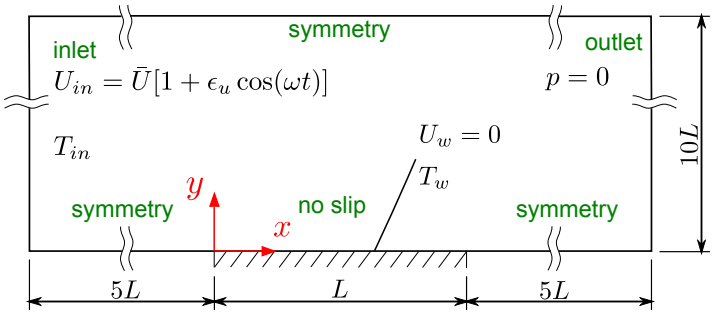

Figure 5.4: Sketch of simulation domain for pulsating flow past a flat plate.

Figure 5.4 depicts a sketch of the simulation domain. A flat plate of length L with no slip condition and surface temperature T_w is placed far enough from the boundaries in order to avoid distortion effects at times of flow reversal. The coordinate system origin is placed at the beginning of the plate. At the inlet the bulk velocity with time average value of $\bar{U}$, harmonic oscillations of order ϵ_u, frequency ω and the constant bulk temperature T_{in} are imposed, while the outlet is kept at constant pressure with zero gradient for the temperature. For reasons of accuracy and since the flow is treated as incompressible, a relative pressure of $p = 0$ is chosen. For high amplitude ratios, when flow reversal occurs, the temperature boundary condition of these two patches switches.

For generality, consider now the system of Eqs. (5.28) and (5.29) in dimensionless form:

$$\frac{\partial \vec{u}^*}{\partial t^*} + \vec{u}^* \cdot \vec{\nabla}\vec{u}^* = \frac{\mathrm{Sr}_s}{\mathrm{Re}_s}\left[-\vec{\nabla}p^* + \vec{\nabla}^2\vec{u}^*\right] \quad , \tag{5.30}$$

$$\frac{\partial \vartheta}{\partial t^*} + \vec{u}^* \cdot \vec{\nabla}\vartheta = \frac{\mathrm{Sr}_s}{\mathrm{Pr}\ \mathrm{Re}_s}\vec{\nabla}^2\vartheta \quad , \tag{5.31}$$

where the following substitutions have been used:

$$t^* = t\omega \ , \ \xi = \frac{x\omega}{\bar{U}} \ , \ \zeta = \frac{y\omega}{\bar{U}} \ , \ \vec{u}^* = \frac{\vec{u}}{\bar{U}} \ , \ p^* = \frac{p}{\nu\rho\omega} \ \text{ and } \ \vartheta = \frac{T_w - T}{T_w - T_{in}} \quad . \tag{5.32}$$

Furthermore, a Strouhal $\mathrm{Sr}_s = \delta_s\omega/\bar{U}$ and Reynolds number $\mathrm{Re}_s = \delta_s\bar{U}/\nu$ based on Stokes' length have been introduced. The chosen dimensionless coordinate represents a local Strouhal number $\xi \sim (\delta/\delta_s)^2$, which gives the ratio of boundary layer thickness to Stokes' length. The motivation for this choice of non-dimensionalization can be explained with the help of Fig. 5.5. The velocity boundary layer $\delta(x)$ grows unobstructedly along the plate, while the laminar Stokes length δ_s is only a function of viscosity and forcing frequency. The ratio between these two length scales gives an appropriate similarity parameter. Thus, for a given frequency ω, the low frequency regime is expected close to the left stagnation point, while far from it the high frequency regime appears.

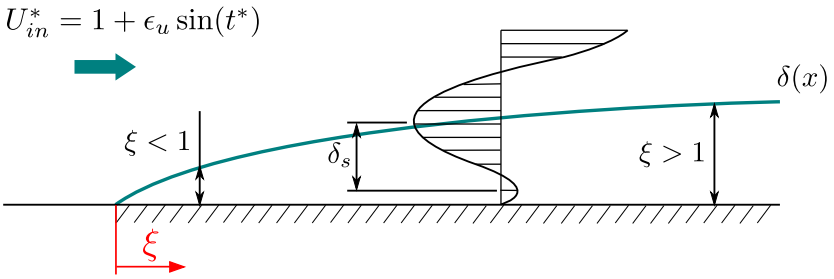

Figure 5.5: Schematic comparison of length scales in a laminar pulsating flow past a flat plate.

The skin friction and wall heat flux have been non-dimensionalized by:

$$\tau_w^* = \frac{\tau_w}{\rho\bar{U}^2} \quad , \quad \dot{q}_w^* = \frac{\dot{q}_w}{c_p\rho(T_w - T_{in})} \quad . \tag{5.33}$$

For clarity, Fig. 5.6 depicts the sketch of the simulation domain with the applied boundary conditions in their dimensionless form. The imposed bulk velocity at the inlet has now the form $U^*_{in} = 1 + \epsilon_u \sin(t^*)$. Note that the wall temperature has a value $\vartheta_w = 0$, while the bulk temperature a value of $\vartheta_{in} = 1$. The coordinate system origin placed at the beginning of the plate is scaled in the streamwise direction as the local Strouhal number ξ.

For the numerical solution of the problem, the open-source package *openFoam* has been chosen, where the system of partial differential equations has been discretized by finite volume approach and solved iteratively with the PISO method introduced in

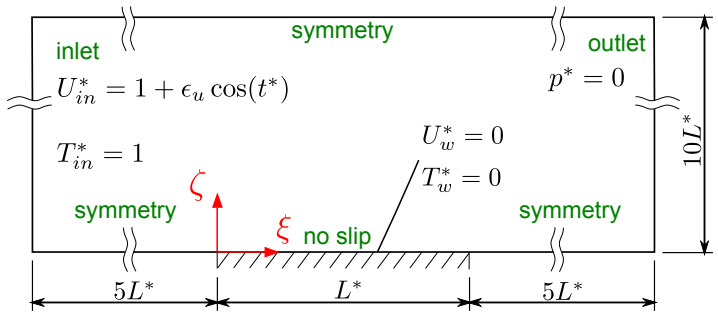

Figure 5.6: Sketch of simulation domain for pulsating flow past a flat plate in dimensionless form.

Sec. 2.4.3.1 performing two momentum corrector steps [56]. The simulation domain has been spatially discretized by a non-uniform unstructured hexahedral mesh with a total number of 70091 cells. For the heated plate of length L^* 249 cells have been used. In wall normal direction, 133 cells with an expansion ratio of 1.0607 have been used. For the time integration, the second order Crank-Nicholson scheme was applied. Spatial discretization of the convective fluxes were performed through a second order Gauss scheme, for which the face fluxes are interpolated through a second order upwind differencing scheme bounded by a van Leer function. The diffusive fluxes are discretized through a second order Gauß scheme, for which the surface normal gradients are interpolated through a second order upwind differencing scheme. For pressure and velocity, the iterations are stopped for residuals lower than 10^{-6}, while 10^{-11} is used for the temperature.

Solver and domain setup have been first validated by a stationary test case without any pulsations. This case served as well as a reference to compare and define the ratio of heat transfer enhancement. The resolution of the mesh proved to be fine enough to resolve the boundary layer, both thermally and hydrodynamically. This has been proved comparing the velocity profiles of the stationary test case against well-known analytical solutions, e.g. Karman and Pohlhausen [44] and Luikov [77]. The integration errors of the solver for mass and energy conservation lie below 0.3%. The temperature range used in all simulations is small enough so the passive scalar simplification for the temperature remains valid. Table 5.1 gives a brief overview of the parameter ranges studied using this test case.

Table 5.1: Simulation parameters for the reference and the two simulation campaigns.

	Pr	Re_s	Sr_s	$\xi(L)$	ϵ_u	ϵ_T
Reference	0.71	27	0.036	0.38	0	0
Const. ϑ_w	0.71	27	0.036	0.38	0.1 . . . 2.5	0

5.4.2 Low amplitudes

To validate the solver and test case set up in the pulsating case, a first transient simulation with small amplitude ratio $\epsilon_u = 0.1$ has been performed and compared against the analytical solution of Lighthill introduced in Sec. 2.5. To do this, the

velocity field computed by the CFD simulation has been expressed in the following form:

$$u = \bar{u} + |\hat{u}| \cos(\omega t + \phi_u) \quad . \tag{5.34}$$

Figure 5.7 shows the skin friction phase lag $\phi_{\tau_w} = \phi_u(y = 0)$ plotted against the frequency parameter ξ along the surface of the plate. As expected, it starts with a value of 0 and approaches asymptotically to the maximum value of $\pi/4$ predicted by Lighthill. This figure demonstrates the possibility of having both frequency regimes in one simulation [125]. The red dashed line corresponds to Lighthill's high frequency approximation Eq. (2.135) evaluated for $y \to 0$. The high frequency regime is clearly displayed at frequency parameter $\xi > 4$. The green dashed line corresponds to the low frequency approximation given by Eq. (B.22).

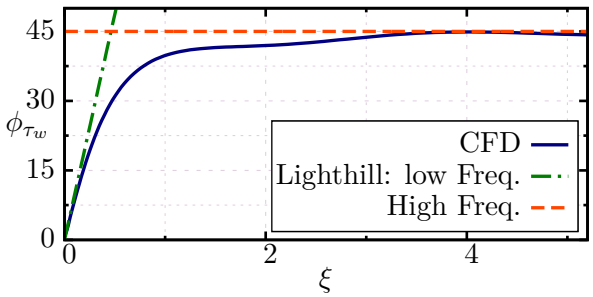

Figure 5.7: Skin friction phase along the plate for amplitude ratio $\epsilon_u = 0.1$ and constant frequency. Dashed lines denote Lighthill's approximation [75].

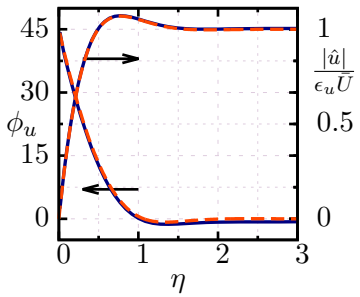

Figure 5.8: Gain and phase of skin friction in the high frequency regime for amplitude ratio $\epsilon_u = 0.1$ and constant frequency. Dashed lines denote Lighthill's high freq. approximation [75].

Figure 5.8 shows the phase ϕ_u and gain $g = |\hat{u}|/\epsilon_u \bar{U}$ of the boundary layer velocity at the axial location $\xi = 5$ corresponding to the high frequency regime. The results are plotted against local wall units $\eta = y/\delta$. The CFD results are compared against the analytical solution of Lighthill, Eqs. (2.134) for the gain and (2.135) for the phase. As expected and due to the lower inertia of the fluid near the wall, the velocity fluctuations in the boundary layer advance the far field oscillations. The phase advance starts with a value of $\pi/4$ just above the wall and decreases with distance to it until it finally vanishes at the end of the local boundary layer $\eta = 1$. The gain of the velocity fluctuations grows with distance to the wall and reaches its maximum shortly before the end of the boundary layer. It has a small overshoot before it reaches the expected value of 1 far away from the wall.

Excellent agreement between the CFD simulation and the analytical solution of Lighthill can be observed in Figs. 5.7 and 5.8.

5.4.3 High amplitudes

After validating the solver and test case, several simulations at various amplitude ratios have been conducted, see Tab. 5.1. The main results of the investigation can be expressed in terms of the previously defined EHT ratio (Eq. (5.6)). Figure 5.9 gives

the local ratio of enhancement along the plate in terms of the frequency parameter ξ for various amplitude ratios ϵ_u. It is interesting that regions of locally enhanced as well as decreased heat transfer are present, with a periodic dependency in axial direction in accordance to the results of Hemida et al. [51], and Mathie and Markides [79]. As expected, the heat flux perturbations are stronger near the leading edge in the thermally developing region. Further downstream the perturbations are damped out. For the frequency range considered, the maximum enhancement found was about $EHT \approx 1.17$ for an amplitude ratio of $\epsilon_u \approx 1.25$ at position $\xi \approx 2.6$.

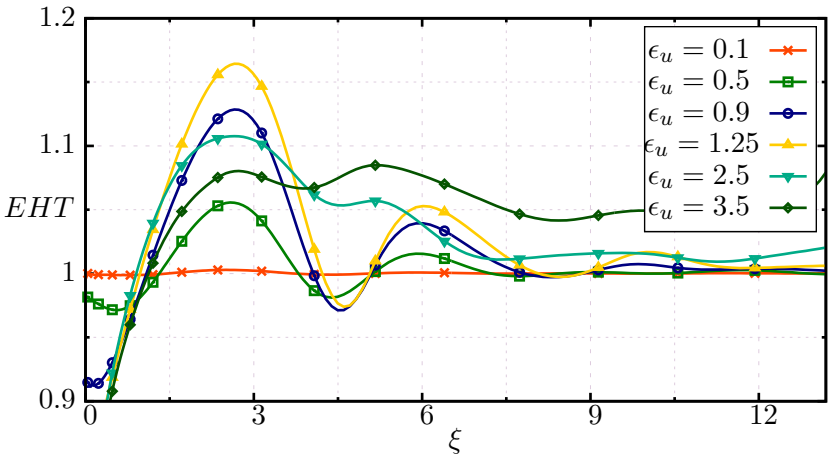

Figure 5.9: Enhanced heat transfer for various amplitude ratios and constant plate temperature.

Up to an amplitude ratio of approximately $\epsilon_u \approx 1.75$ the enhancement is proportional to the amplitude ratio ϵ_u and its periodic behavior similar, with maxima and minima located at the same position. The modulation of the ratio of enhancement in axial direction can be explained by following a small package of fluid representative of the local boundary layer in a Lagrangian manner. Due to the mean flow, the package is convected downstream while being heated up by the plate. The local velocity amplitude is $|\hat{u}(y)|/\bar{u}(y) > 1$ close to the wall. This means that even if the bulk flow does not experience flow reversal, the fluid package close to the wall does. The axial locations at which this flow reversal occur will experience in average a lower heat transfer, since the fluid package is already heated up. Similarly, at other axial locations the fluid package will have in average a lower temperature because it flows faster, leading to an enhanced heat transfer. The corresponding discrete axial locations can be approximated using the average boundary layer velocity $\bar{u}_\delta \approx \bar{U}/2$ and the frequency of oscillation. The distance between two peaks correspond to the distance that the fictive fluid package passes during one period of oscillation:

$$\Delta x \approx \bar{u}_\delta \frac{2\pi}{\omega} \quad \rightarrow \quad \Delta\xi = \frac{\Delta x \omega}{\bar{U}} = \frac{\bar{u}_\delta 2\pi}{\omega}\frac{\omega}{\bar{U}} = \pi \quad . \tag{5.35}$$

At higher amplitude ratios $\epsilon_u > 1.75$, the dependency of EHT on ξ starts to change with the maxima and minima being softened and leading to a decrease in magnitude of the enhancement. At high amplitude ratios with strong flow reversal, secondary flows ("streaming") appear. Their structure depends on the overall geometry and the location of the stagnation points [116]. In the geometry used for this study, these secondary flows reduce the velocity at the boundary layer close to the leading edge of the plate.

5.5 Conclusions Concerning Preliminary Studies

After giving some introduction to heat transfer in pulsating flows, with special attention to the conditions present in rocket thrust chambers, this chapter presented the strategy to study these phenomena, that has been followed in this thesis. The steps in this strategy increase gradually in complexity.

The first preliminary investigation included a low order model for heat flux through a wall of finite thickness subjected to transient boundary conditions similar to those expected in devices suffering from thermoacoustic instabilities. Two major results can be formulated from this investigation: Firstly, for most combinations of parameters, the wall thermal inertia plays a minor role in the heat transfer under transient conditions and leads always to a reduction of the heat flux through the wall. These results are in accordance to similar investigations available in the literature [51, 79, 134]. And secondly, the bulk flow transients can indeed lead to a permanent time averaged heat transfer change, provided that both the temperature and the heat transfer coefficient fluctuate in time. As predicted by Lundgren et al. [78], the phase between the oscillations plays the decisive role concerning the sign of the offset. The magnitude of the offset is proportional to the amplitudes of the heat transfer coefficient and temperature oscillations.

The second step performed in the strategy treated the heat transfer in pulsating flow past a flat plate. A numerical CFD approach was used in the investigation. Based on the results gained from the low order model, an ideal temperature boundary condition for the wall has been used, because no major contributions are expected from its thermal inertia. Apart from serving as a validation for some numerical simulation tools and post-processing utilities, this test case produced some interesting results concerning the thermally developing region. Indeed, pulsating flow can lead locally to both enhancement and diminishment of time averaged heat transfer. The changes are more predominant in the thermally developing region and are damped out downstream, in good agreement with results available from the literature [51, 79].

The results of these preliminary investigations are in good agreement, both qualitatively and quantitatively, with other theoretical and numerical investigations available from the literature. Quantitatively, the possible heat transfer enhancement accounts merely few percent. Thus, the mechanisms found in this preliminary investigation cannot explain the large heat transfer enhancement rates observed in some experimental investigations [29, 49]. However, turbulence phenomena have been left aside in these preliminary investigations. Chapter 6 will deal precisely with these phenomena.

6 Turbulent Pulsating Channel Flow with Heat Transfer

Turbulent pulsating flows exhibit a high degree of complexity due to the wide range of time and length scales involved in the problem. A test case appropriate for the numerical study of heat transfer in turbulent pulsating flows has to be chosen carefully. In this context, two major difficulties have to be overcame. The first one is the allocation of a physical and fully developed turbulence field containing a healthy spectrum. The direct imposition of such a field is an issue itself. The indirect imposition through small perturbations that develop into turbulence is a more practical approach.

The second difficulty is the computational cost associated with the numerical simulation of turbulence. Despite the tremendous advances in the field of computational fluid dynamics, the simulation of turbulent pulsating flows is still very challenging. While DNS offers a straight forward approach with very low modeling uncertainty, the large number of mesh points of the order $\mathrm{Re}^{9/4}$ for $\mathrm{Pr} < 1$ or $\mathrm{Pr}^3\ \mathrm{Re}^{9/4}$ for $\mathrm{Pr} > 1$ [129] required to resolve all scales in the flow makes the numerical solution very expensive and time consuming. On the other hand, more efficient approaches like RANS require a higher degree of modeling to describe the unclosed terms that may lead to erroneous results if conventional models are used, see for example the study performed by Scotti and Piomelli [122]. In this context, the LES approach provides an effective alternative to study turbulent flows. Their validity in combination with dynamic eddy viscosity models describing the subgrid-scales has been demonstrated by Scotti and Piomelli in a thorough investigation [121]. Their methodology requires the full resolution of the near wall region in combination with a dynamic sub-grid model. The reason for this requirement is that the state of the art wall models are not capable of accurately reproducing the boundary layer response.

As mentioned in Sec. 5.1, the experimental results concerning heat transfer in turbulent pulsating flows have not yet been reproduced by numerical investigations. One possible cause for the strong discrepancies might be a fragmentary consideration of effects involved in pulsating flows driven by acoustic fields. To explain this situation, the first section in this chapter presents a thorough description of the acoustic mechanisms leading to mean flow pulsations. In accordance to the strategy followed in this thesis, two studies of increasing complexity are presented in this chapter. Both are based on an acoustic compact approach: The first one gives a detailed analysis of both the hydrodynamic and heat transfer response to bulk flow pulsations close to a pressure node. Thus, only velocity fluctuations are considered omitting acoustic pressure fluctuations. In this fundamental analysis, an extensive simulation campaign has been performed assuming an incompressible flow with constant properties. Based on these results, a second campaign intends to estimate the possible influence of temperature dependent properties and acoustic pressure fluctuations. For the second study only a reduced number of simulations has been performed.

6.1 Acoustic Field as Driving Mechanism

In the majority of the investigations of pulsating flows, the pulsating motions of definite frequency are assumed as present and only minor attention is paid to the driving source. This deficiency may impede the proper comparison of the results of both numerical and experimental nature. Organized velocity pulsations can be induced by several mechanisms. This thesis intends to study pulsating flows driven by acoustic fields. This section describes these acoustic fields and gives the resulting boundary conditions of the problem.

In Sec. 2.2.1, three dimensional acoustic waves have been introduced. A general acoustic field can be decomposed into several traveling waves. Depending on the boundary conditions, these traveling waves can form standing waves. This is the case for the majority of self-sustained oscillations as such encountered in rocket chambers. This thesis assumes thus acoustic fields composed solely of standing waves.

The standing waves can be described by one dimensional linear acoustics solving the inviscid convective Wave-Equation for simple ducts as shown in Sec. 2.2.2. In Sec. 2.2.2.3, the acoustic field in a simple channel has been given by Eqs. (2.54) and (2.55). For the characterization, the mode shape of the second harmonic $l = 2$ will be used:

$$\frac{p'}{\bar{\rho}\bar{c}}(x,t) = 0.5A\cos(2\pi x/L)\cos(\omega t) = \hat{P}(x)\cos(\omega t) \quad , \tag{6.1}$$

$$u'(x,t) = -0.5A\sin(2\pi x/L)\sin(\omega t) = \hat{U}(x)\sin(\omega t) \quad , \tag{6.2}$$

where A denotes the forcing amplitude and small Mach numbers $M \ll 1$ are assumed. Figure 6.1 shows schematically the normalized amplitudes $\hat{P}(x)/A$ and $\hat{U}(x)/A$ of the velocity and pressure waves along the channel. The alternation between pressure and velocity nodes in periods of $L/4$ can clearly be seen in the figure. Four axial locations a to d are also shown in Fig. 6.1 to illustrate the different local environments. Location a is placed on a pressure node. For a given wave amplitude A, the velocity fluctuations reach a maximum at this location, while the pressure remains constant. The opposite situation is given at location c placed at a velocity node where only pressure fluctuations are observed. At positions b and d, both velocity and pressure fluctuations arise. At position c the velocity advances the pressure by $\pi/2$, while at position d it lags the pressure by the same phase.

It is thus important to remark, that velocity pulsations will in general be accompanied by pressure fluctuations, if acoustic waves are the cause of the periodic unsteadiness.

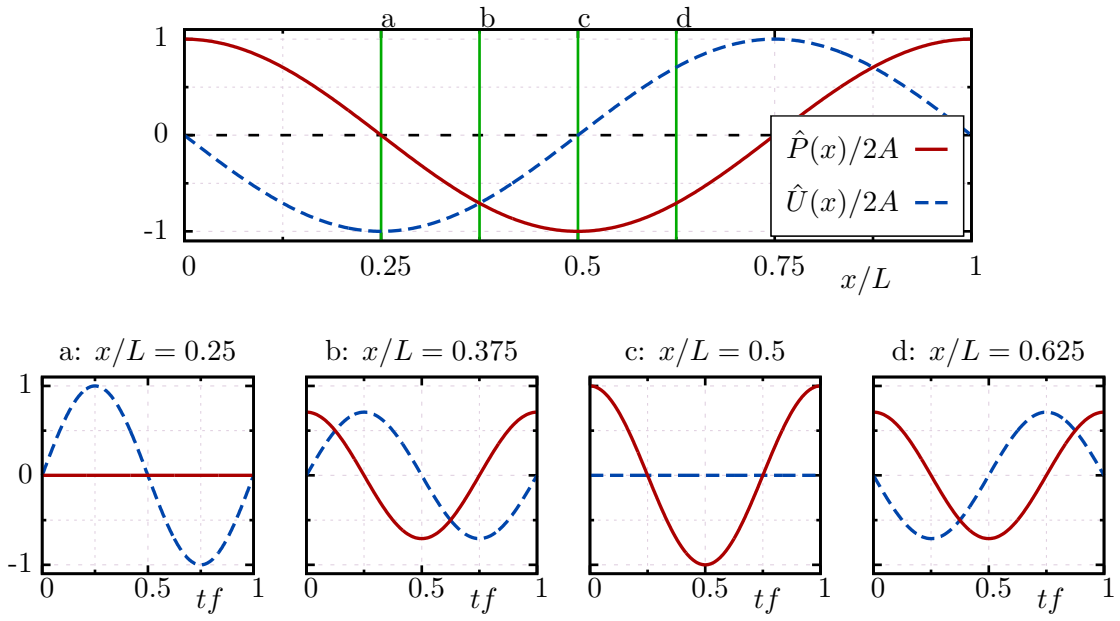

Figure 6.1: Pressure and velocity amplitudes in a channel with two acoustically closed ends and a standing wave. Upper plot, normalized amplitudes as a function of space. Lower plots, local amplitudes as a function of time.

6.2 Incompressible Case with Constant Properties

6.2.1 Problem Formulation and Test Case Set-up

The test case chosen for the investigation is a fully developed turbulent flow between two parallel walls, that are of infinite extent in the stream- and spanwise direction. The major advantage of this configuration is that the turbulent structures are not imposed explicitly in the form of velocity perturbations, but inherently by the influence of the wall itself. Thus, when fully developed, the turbulence spectrum should be physical. Furthermore, the case is well documented in the literature. The simulation domain is sketched in Fig. 6.2, where the channel half height h is the characteristic geometry length scale. Due to the symmetry of the problem, cyclic boundary conditions are imposed on the stream- and spanwise boundaries, respectively. In order to resolve the large turbulent structures, the domain extends $2\pi h$ in the streamwise and πh in the spanwise direction. Non-slip conditions are imposed at the top and bottom walls. Furthermore, to induce heat transfer, the walls are kept at different temperatures T_H and T_C, respectively. The flow is driven by an externally imposed momentum source term $\vec{S}_M$ that mimics the influence of the pressure gradient and overcomes the friction losses at the walls as shown in Fig. 6.2.

The resulting mean flow velocity is high enough to develop turbulence. The temperature difference between the plates is chosen to be small, and since the Mach number remains small too, the fluid properties can be treated as constant.

In the presence of an acoustic field with standing waves, the axial pressure distribution along the channel at an instant t_0 is sketched in Fig. 6.3. The pressure gradient oscillates

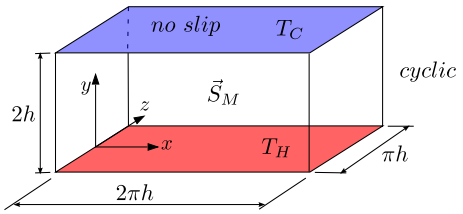

Figure 6.2: Simulation domain for a channel with cyclic boundary conditions in the stream- and spanwise directions.

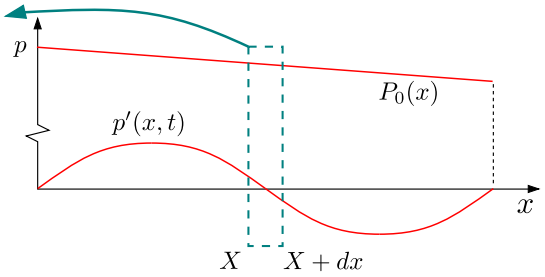

Figure 6.3: Acoustically compact approximation for a section small compared to the acoustic wavelength.

harmonically around a non zero mean value. Thus, the momentum source term driving the flow is proportional to this axial pressure gradient:

$$\vec{S}_M(\vec{x},t) \sim \left(\frac{dP_0}{dx} + \frac{\partial p'(\vec{x},t)}{\partial x} \right) \vec{e}_x \quad . \tag{6.3}$$

The mean pressure gradient is constant and homogeneous in space $dP_0/dx = const.$ The oscillating component is actually a function of time and space. However, when the wavelength of the acoustic oscillations is large compared to the channel half height, the source term can be treated as homogeneous in space within a small channel section denoted by the dashed box in Fig. 6.3:

$$\vec{S}_M(t) \approx \left(\frac{dP_0}{dx} + \left. \frac{\partial p'(\vec{x},t)}{\partial x} \right|_{x=X} \right) \vec{e}_x = \left(P_{0x} + P_{1x} \cos(\omega t) \right) \vec{e}_x \quad , \tag{6.4}$$

where P_{0x} and P_{1x} are constants.

In this preliminary simulation campaign, only the location close to a pressure node is studied because of two reasons: Firstly, according to the observations of Bogdanoff [10], the strongest enhancement is apparently occurring here. And secondly, since no acoustic pressure fluctuations are present, the flow can be treated as incompressible. This leads not only to a considerably simplification of the governing equations, but also to the exclusion of acoustic length and time scales.

It is important to remark that the problem formulation is based on the assumption of acoustic compactness. This is valid when the domain size is small compared to the wavelength of the acoustic waves. In other words, the Helmholtz number based on the forcing frequency, speed of sound and domain length should be small, $\mathrm{He} = \frac{\omega h}{\bar{c}} \ll 1$. Only under this circumstances the momentum source term can be treated as homogeneous in space.

For stationary pressure gradients, the friction forces characterized by the skin friction $\tau_w = \mu \partial u/\partial y|_{y=0}$ are in equilibrium with the pressure gradient as sketched in Fig. 6.4:

$$\tau_w = h \frac{\Delta P_0}{\Delta x} \approx h \frac{\partial P_0}{\partial x} = h P_{0x} \quad . \tag{6.5}$$

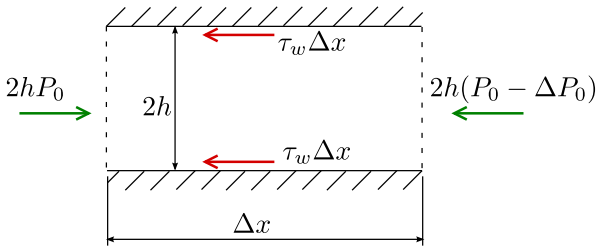

Figure 6.4: Balance of forces in channel flow driven by a stationary pressure gradient.

Using the constant part of the imposed momentum source term, the friction velocity can be determined from:

$$u_\tau = \sqrt{\frac{\tau_w}{\rho}} = \sqrt{\frac{h}{\rho} P_{0x}} \quad . \tag{6.6}$$

When heat transfer is considered, additional parameters are necessary to characterize the problem. In the incompressible case with constant properties, the Nusselt number corresponds to a non-dimensionalized wall normal temperature gradient:

$$\mathrm{Nu} = \frac{\dot{q}_w}{\Delta T_b} \frac{h \,\mathrm{Pr}}{\nu \rho c_p} = \frac{h}{\Delta T_b} \left. \frac{\partial T}{\partial y} \right|_{wall} \quad , \tag{6.7}$$

where the heat transfer coefficient α is given as the ratio of the wall heat flux $\dot{q}_w$ and the temperature difference. For the case of constant wall temperatures, the bulk flow temperature at the channel center ΔT_b can be approximated as $(T_H - T_C)/2$ due to the symmetry of the problem. Furthermore, the fluid thermal conductivity is given as a function of the Prandtl number. Using the friction temperature T_τ, the Nusselt number can be written in terms of the previously introduced parameters as:

$$\mathrm{Nu} = \frac{T_\tau \,\mathrm{Re}_\tau \,\mathrm{Pr}}{\Delta T_b} \quad . \tag{6.8}$$

6.2.2 Characterization of Turbulent Pulsating Flows

Comparing the diffusion driven penetration time scales, Ramaprian and Tu [110] argued that a classical Stokes' number is not appropriate for the characterization of turbulent pulsating flows, since the effective diffusion can be considerable higher in turbulent flows. Instead, a non dimensional frequency widely used in the literature for the characterization of turbulent pulsating flows can be written as [124]:

$$\omega^+ = \frac{\omega \nu}{u_\tau^2} \quad . \tag{6.9}$$

This rather abstract quantity can be transformed into a more descriptive one:

$$l_s^+ = \sqrt{\frac{2}{\omega^+}} = \frac{\delta_s u_\tau}{\nu} \quad , \tag{6.10}$$

represented by the classical Stokes' length in non-dimensional wall units.

The strength of the pulsations driven by the oscillating axial pressure gradient can be characterized by an amplitude ratio. The most straight forward ratio would be that

of the center-line velocity ϵ_{uc}. In the current dominated flow ($\epsilon_{uc} < 1$), the flow is apparently controlled by the forcing frequency ω^+ [121, 124]. Scotti and Piomelli go further and propose a *turbulent Stokes length* l_τ in order to estimate the thickness of the layer to which the influence of the oscillations is confined. In an analogy to the laminar Stokes problem, they obtain this turbulent length scale by adding molecular and turbulent diffusivities:

$$l_t = \sqrt{\frac{2(\nu + \nu_\tau)}{\omega}} \quad . \tag{6.11}$$

Modeling qualitatively the influence of turbulence by an eddy viscosity model:

$$\nu_\tau = \kappa_\mathrm{K} u_\tau l_\tau \quad , \tag{6.12}$$

where κ_K is the von Karman constant, they derived to the following expression in non-dimensional wall units:

$$l_t^+ = l_s^+ \left[\left(\frac{\kappa_\mathrm{K} l_s^+}{2} \right) + \sqrt{1 + \left(\frac{\kappa_\mathrm{K} l_s^+}{2} \right)^2} \right] \quad . \tag{6.13}$$

Based on this expression, they characterize the different frequency regimes described by Gündoğdu and Çarpinlioğlu [46] in the current dominated case:

- quasisteady regime
- low-frequency regime
- intermediate frequency regime
- high frequency regime
- very high frequency regime (bursting frequency)

6.2.3 Governing Equations and Numerical Method

For low Mach numbers and small temperature gradients, the incompressible Navier-Stokes-Equations with constant properties can be used to describe the flow. In the LES context, they filtered counterparts can be written as:

$$\frac{\partial \vec{u}}{\partial t} + (\vec{u} \cdot \vec{\nabla})\vec{u} = -\frac{1}{\rho}\vec{\nabla} p + \vec{\nabla}\left[(\nu + \nu_{sgs})\vec{\nabla}\vec{u}\right] + \frac{1}{\rho}\vec{S}_M \quad , \tag{6.14}$$

$$\frac{\partial T}{\partial t} + (\vec{u} \cdot \vec{\nabla})T = \vec{\nabla}\left[(a + a_{sgs})\vec{\nabla} T\right] \quad . \tag{6.15}$$

For simplicity, the tilde denoting filtered variables is omitted. The effects of the subgrid scales are captured by a simple eddy viscosity ν_{sgs}. The momentum equation Eq. (4.2) satisfies inherently the mass conservation $\vec{\nabla} \cdot \vec{u} = 0$. The effects of the subgrid scales on the thermal diffusivity are approximated through a turbulent Prandtl number:

$$\mathrm{Pr}_t = \frac{\nu_{sgs}}{a_{sgs}} \approx \mathrm{Pr} \quad , \tag{6.16}$$

assumed to be constant. For the subgrid scales, a one equation eddy viscosity model based on the conservation of SGS turbulent kinetic energy is used, see Sec. 2.4.2.1. The model constants are dynamically adapted through the Germano identity [41] and the extension of Lilly [76]. Scotti and Piomelly [121] and later Wong and Lu [129] used the dynamic Smagorinsky model, which is based on the assumption of local equilibrium. In this study, the less restrictive one equation TKE model is consciously chosen because the unsteadiness might partially break the equilibrium assumed by the Smagorinsky model.

The simulations are run within the *openFoam* environment. The standard incompressible solver *pisoFoam* that solves Eq. (6.14) has been extended to solve also the transport equation for the temperature given by Eq. (6.15). Furthermore, the momentum source term with harmonic dependency given by Eq. (6.4) has been included in the solver where the parameters P_{0x}, P_{1x} and ω can be freely chosen. The system of partial differential equations is solved iteratively by the PISO algorithm [56] using two momentum correction steps. Time discretization is performed through a second order Crank-Nicholson scheme. Spatial discretization of the convective fluxes is performed through a second order Gauß scheme, for which the face fluxes are interpolated through a second order upwind differencing scheme bounded by a van Leer function. The diffusive fluxes are discretized through a second order Gauß scheme, for which the surface normal gradients are interpolated trough a second order upwind differencing scheme. Details concerning the discretization schemes and the chosen parameters can be found in [34, 69]. The mesh used for the spatial discretization is orthogonal with a stretching function in the wall normal direction and homogeneous distribution in the span- and streamwise directions, see App. C.1.

6.2.4 Data Reduction Through Averaging Operators

For the characterization of turbulent pulsating flows different averaging procedures of a quantity $\psi(\vec{x}, t)$ can be defined including spatial, temporal and combination of both.

Temporal averaging of a quantity will be denoted by an overbar and is defined as:

$$\bar{\psi}(\vec{x}) = \frac{1}{t_{tot}} \int_0^{t_{tot}} \psi(\vec{x}, t) dt \quad , \tag{6.17}$$

where t_{tot} denotes the total integration time. To increase the statistical validity of the mean quantities, spatial averaging in the directions of homogeneity can also be performed. This combination of temporal and spatial average operations will be denoted by angle brackets:

$$\langle\psi\rangle(y) = \frac{1}{t_{tot} L_x L_z} \int_0^{L_z} \int_0^{L_x} \int_0^{t_{tot}} \psi(\vec{x}, t) \; dt \; dz \; dx \quad , \tag{6.18}$$

where L_x and L_z denote the domain size in stream- and spanwise direction, respectively.

When dealing with pulsating flows driven at one given frequency $f = 2\pi\omega$, phase or ensemble averaging can help in the identification of coherent structures. As argued by Scotti and Piomelli [121], this assumes that the major contribution of the system

response occurs at the forcing frequency. This kind of operation will be denoted by subscripted angle brackets $\langle\ \rangle_p$ and is defined as:

$$\langle\psi\rangle_p(y,\varphi) = \frac{1}{N_t L_x L_z}\sum_{j=1}^{N_t}\int_0^{L_z}\int_0^{L_x}\psi\left(\vec{x},\frac{\varphi}{\omega}+2\pi\frac{(j-1)}{\omega}\right)dz\ dx \quad , \tag{6.19}$$

where N_t is the number of cycles considered in the ensemble averaging and $0 < \varphi \leq 2\pi$ represents the phase angle. The phase averaged quantities can be further decomposed into a mean, an harmonic and a non-linear component as proposed in [121]:

$$\langle\psi\rangle_p(y,\varphi) = \langle\psi\rangle(y) + a_\psi(y)\cos(\varphi+\phi_\psi(y)) + \psi_{ha}(y,\varphi) \quad . \tag{6.20}$$

Of course, the stationary component corresponds to the temporal and spatial average of the original quantity. The harmonic component can be seen as a real valued amplitude, and thus, a phase lag ϕ_ψ towards a reference value is necessary. Note that both the amplitude and the phase lag are functions of the wall distance. Usually, the phase lag is defined using the axial velocity oscillations at the channel center-line as reference. From the phase averaging definition, the oscillating component accounts only for the contribution of the forcing frequency. The contributions at higher harmonics are all added up in the term ψ_{ha} which is of course a function of the phase φ and the wall normal location y.

For the pulsating channel flow, the triple decomposition introduced in Sec. 2.5 and widely used in the literature can be written in terms of these average operators as:

$$\psi(\vec{x},t) = \langle\psi\rangle + a_\psi(y)\cos(\omega t+\phi_\psi(y)) + \psi'(\vec{x},t) \quad . \tag{6.21}$$

where $'$ denotes the chaotic turbulent fluctuations.

6.2.5 Stationary Validation and Reference Case

The first step in this study was the validation of the numerical solver used in the methodology for both stationary and pulsating case. Unfortunately, if heat transfer is considered, the available data in the literature is very sparse and a test case with the combination of parameters as those used in this study has not been found.

For the stationary case without pulsating forcing, App. C.1 gives a thorough validation for two different cases of turbulent Reynolds numbers $\mathrm{Re}_\tau = 150$ and $\mathrm{Re}_\tau = 180$ against DNS data available from the literature. The combination of solver, turbulence model and mesh performs very well and the agreement with the DNS data is very good. The details of the validation are given in the appendix.

Table 6.1: Reference case for turbulent channel flow with heat transfer.

Re_τ	Pr	Nu_{ref}	Logarithmic sublayer
179.9	0.71	6.26	$u^+ = 2.5\ln(y^+) + 5.5$
			$T^+ = 3.6\ln(y^+) + 0.3$

After the validation, a turbulent test case without acoustic pulsations has to be defined to serve as a reference for the evaluation of heat transfer enhancement. The test case

of Reynolds number $\mathrm{Re}_\tau = 180$ and Prandtl number $\mathrm{Pr} = 0.71$ already used for the stationary validation is chosen to serve as the reference case. Table 6.1 gives the key parameters of this simulation. This Reynolds number is lower than the one used in the two major publications cited in this thesis [121, 129], which was $\mathrm{Re}_\tau = 350$. However, in these studies, only the current dominated flow with velocity amplitudes at the center-line $\epsilon_{uc} = a_{uc}/\langle u(h)\rangle$ of $\epsilon_{uc} \lesssim 0.7$ and various frequencies was studied. In the research presented in this thesis, a wider range of amplitudes covering also at least partially the wave dominated flow $\epsilon_{uc} > 1$ are studied. Thus, a lower turbulent Reynolds number of $\mathrm{Re}_\tau = 180$ is chosen in order to save some computational resources. Nevertheless, as it will be shown later, the effective non-dimensional frequency ω^+ still allows the comparison against the data of these studies.

6.2.6 Pulsating Case Validation

As a starting point, three exemplary operation points are described and compared to some of the data available from the literature. This should serve as a validation for the turbulent pulsating case and help to elucidate the main hydrodynamic behavior of turbulent pulsating flows already observed in previous investigations. The cases correspond to the ones studied experimentally by Tardu et al. [124], which were subsequently also used in the numerical studies of Scotti and Piomelli [122] and Wang and Lu [129]. Table 6.2 lists the key parameters of the three different computed cases in the present study compared against the ones used by the mentioned investigations. All cases lie in the current dominated regime with *velocity center-line amplitude* of approximately $\epsilon_{uc} \approx 0.7$. It is important to remark that the turbulent Reynolds numbers of the different investigations are not always equal, ranging from $\mathrm{Re}_\tau = 432$ in the experimental study to $\mathrm{Re}_\tau = 180$ in the present study. The other two numerical studies use $\mathrm{Re}_\tau = 350$. However, the forcing frequencies are chosen in such a way that the resulting turbulent Stokes numbers l_s^+ are comparable, depicting the low, medium and high frequency regimes, respectively.

For the present study, the different cases are simulated using the solver and methodology presented in Sec. 6.2.3 and run for several periods to get accurate temporal and phase average statistics. Figure 6.5 shows the axial velocity components after performing the triple decomposition given by Eq. (6.20) and plotted in wall units. The profiles of the present LES simulations are compared against the results of the investigations listed in Tab. 6.2. The first row in the figure shows the time independent part of the axial velocity, which clearly follows the classical law of the wall. In the low and the high frequency regimes, the profiles collapse to the classical law of the wall $\langle u^+\rangle = 2.5\ln(y^+)+5$ and $\langle u^+\rangle = y^+$ denoted by the dashed lines and the agreement between the different investigations is very good. In the medium frequency regime, the present LES simulations match the experimental results somewhat better than the LES of Scotti and Piomelli. In this regime, it seems that the logarithmic region is shifted slightly to a lower wall normal coordinate. For the other frequencies, the average profiles lie close to the ones of the stationary case without pulsations. The middle row shows the ensemble averaged velocity amplitude a_u^+ normalized by its center-line value a_{uc}^+. As expected, the thickness of the turbulent Stokes' layer is inversely proportional to the forcing frequency ranging from 10 in the high to 500 in the low frequency regime. Again, the concordance between the three investigations is remarkably good. Finally, the third

Table 6.2: Key parameters of the three different test cases used for the validation of the solver and numerical set up.

	l_s^+			ϵ_{uc}	Re_τ	Pr	Nu_{ref}	$\langle \mathrm{Nu} \rangle$
	high	medium	low					
	7.1			0.70				6.26
Present		15.3		0.78	180	0.71	6.26	6.50
study			34.2	0.70				5.41
	8.1							
TBB[124]		16		0.64	432	-	-	-
			34					
	7			0.66				
SP[121]		14		0.70	350	-	-	-
			35	0.79				
	7			0.7				not given
WL[129]		14		0.7	350	1	28	not given
			35	0.7				not given

row in the figure gives the phase difference $\Delta\phi_u = \phi_u(y) - \phi_u(h)$ between the wall and channel center-line velocity fluctuations. Unfortunately, the wall normal profiles of this quantity are not given in the publication of Scotti and Piomelli. They provide merely the values for the skin friction phase and thus, only one value per frequency case is plotted in the third row of Fig. 6.5. For high frequencies, the behavior is almost identical to the one of laminar pulsating channel flow. Due to the lower inertia of the fluid close to the wall, it reacts faster to the pressure gradient pulsations, leading to a phase advance of $\pi/4$ as predicted by the analytical analysis. For lower frequencies this phase advance reduces. It is interesting that in the low frequency case, the phase of the near wall region decreases further taking negative values. The magnitude of this phase lag is of the order of $\pi/40$ in the case studied here. Concerning the phase, the degree of conformity between the three investigations is very good, too.

It is important to remark that the comparison between the three investigations is valid even though different turbulent Reynolds numbers are used in each of them. This preliminary comparison demonstrates that, concerning the momentum transfer, the proper similarity parameters are the non-dimensional frequency ω^+ or Stokes' length l_s^+ and the velocity amplitude ratio at the channel center-line.

The ensemble average at different phase angles of the forcing frequency helps to further explain the hydrodynamic response of turbulent pulsating flows to pressure gradient fluctuations. In Fig. 6.6, the evolution of the flow within a wave cycle is given by plotting the ensemble averaged velocity profiles at ten equally distributed phases $\varphi = 0, \pi/5, 2\pi/5, \ldots$. The graph on the left shows schematically these phases and the magnitude of the corresponding oscillating axial pressure gradient. For each frequency, the ten ensemble averaged velocity profiles are plotted in the same graph, but are separated from each other by multiples of 20 units in the vertical direction. The stationary velocity profile is also plotted ten times (red dashed lines) using the same

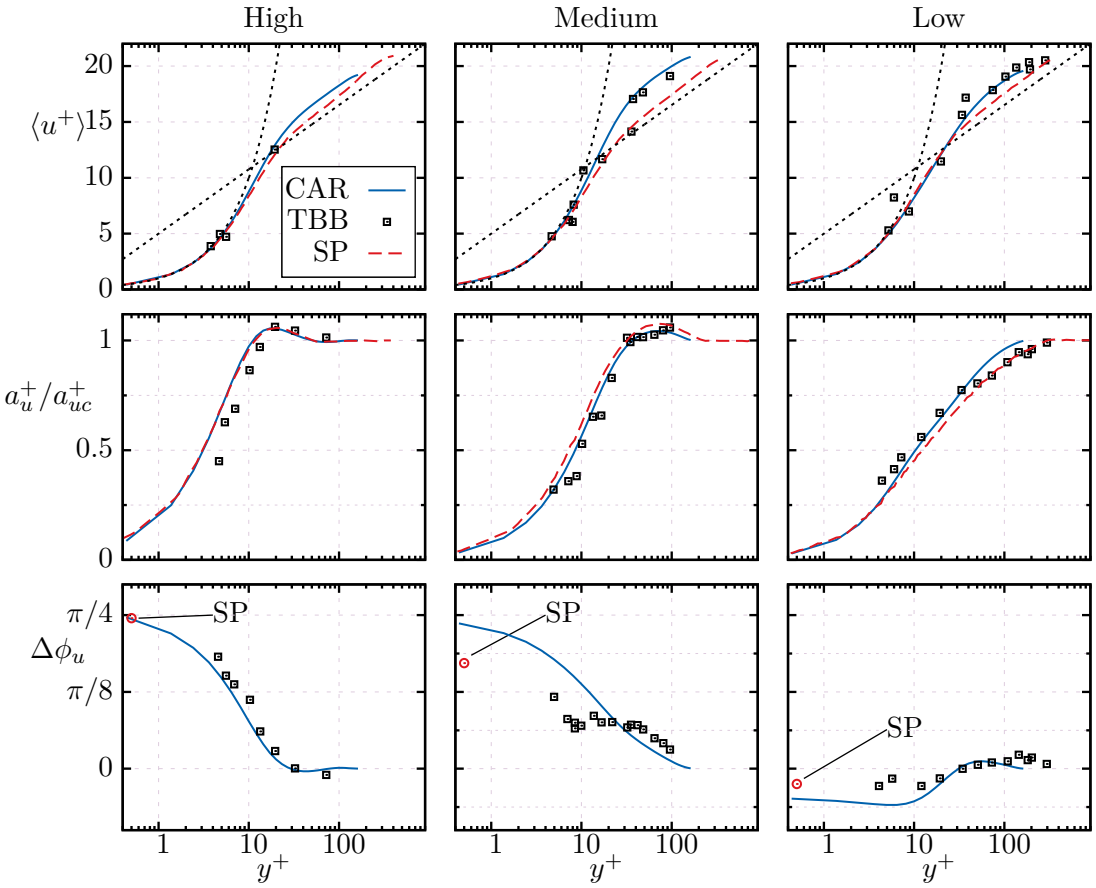

Figure 6.5: Triple decomposition $u^+ = \langle u^+ \rangle + \langle a_u^+ \rangle \cos(\omega t + \phi_u)$ according to Eq. (6.21) of axial velocity components for the three frequencies given in Tab. 6.2: CAR (present study), TBB [124] and SP [121]. The velocity amplitude is normalized by the center-line value a_{uc}^+, the phase at the center-line location is used as reference $\Delta\phi_u = \phi_u - \phi_{uc}$.

series of offsets to serve as a reference when comparing the ensemble profiles. Thus, the scale of the vertical axis provides relative instead of absolute values. Furthermore, the turbulent Stokes' number l_τ^+ proposed by Scotti and Piomelli [121] and estimated by Eq. (6.13) is also shown in the plots by vertical dashed lines. As explained by Scotti and Piomelli, this quantity estimates the penetration length of the perturbations. In the high frequency regime, it lies on the intermediate region between the viscous and the logarithmic layers. Thus, a plug flow behavior can be observed, in which the turbulent core region retains its slope, while the profile is simply shifted up- and downward by the modulation of the forcing pressure gradient. The pulsating flow in the viscous sublayer can be accurately described by the analytical laminar Stokes' solution with a phase advance of $\pi/4$. Note that for very high frequencies, the penetration length would even be confined within the viscous sublayer. As explained by Scotti and Piomelli [121], a possible interaction with the bursts generated in this region is widely suggested in the literature. Due to the required high resolution, this case is not treated in this study. In the medium frequency regime the perturbations can reach the logarithmic region.

However, a portion of the bulk region remains unaltered with frozen turbulence and being shifted up- and downstream by the modulation. In the low frequency regime, the penetration length is large enough to enclosure the whole half channel height. Thus, the complete flow is affected by the modulation of the pressure gradient. The slope of the curves in the logarithmic region changes during the cycle. Finally, for very low frequencies within the quasi steady regime, the flow at each phase of the cycle would have enough time to fully develop. In such a case, the quasi steady theory can accurately describe the response of the flow.

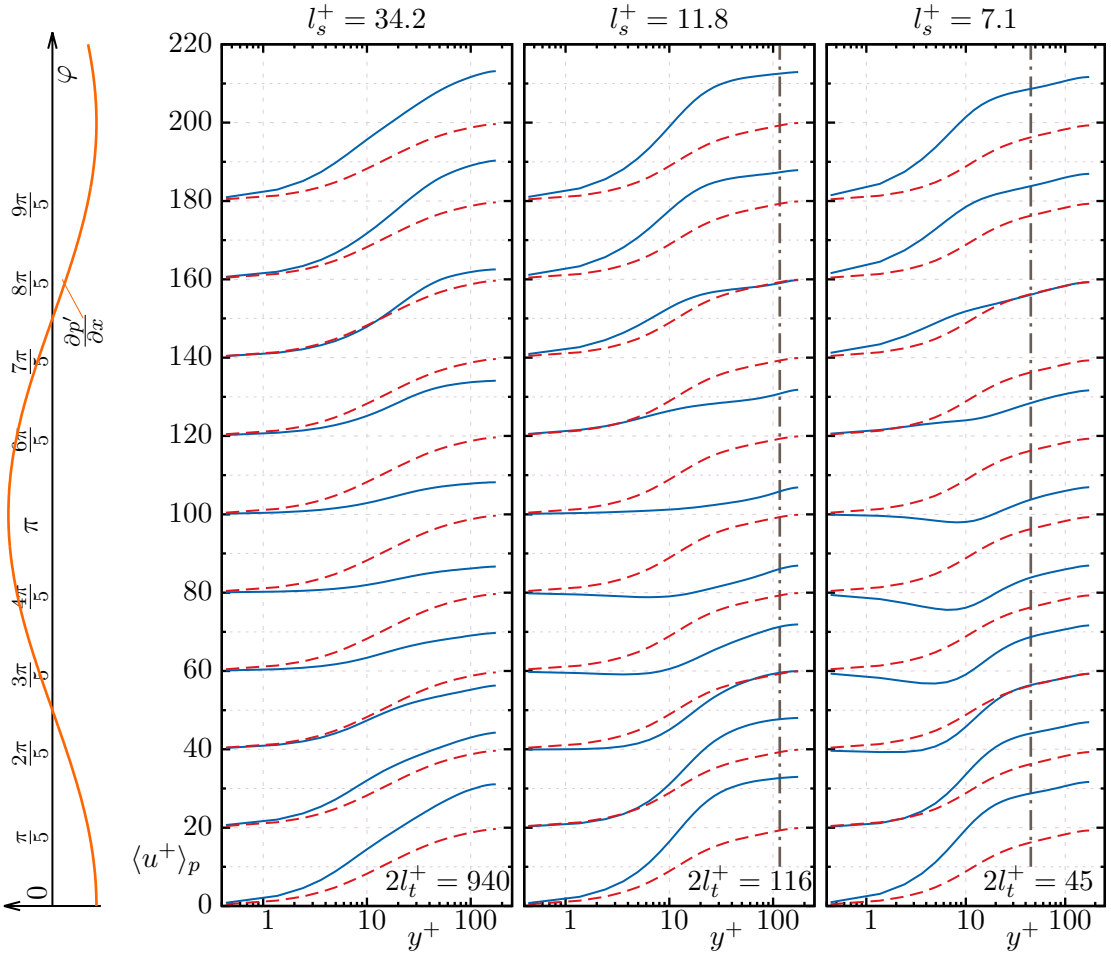

Figure 6.6: Blue lines, ensemble average profiles $\langle u^+ \rangle_p$ at various equally distributed phases φ of one cycle separated by 20 wall units in the vertical direction. Red dashed lines correspond to the time average profiles at the corresponding cases. The vertical dashed lines give the estimate for the turbulent Stokes' length l_t^+. The orange curve on the plot in the left show schematically the magnitude of the oscillating pressure gradient.

Concerning the thermal response of the flow to the harmonic unsteadiness, the situation only has limited similarity towards the hydrodynamic response. As already shown by Wang and Lu [129], for the three investigated cases, the time independent part of the non-dimensionalized temperature plotted in wall normal direction follows also the logarithmic law of the wall with a near wall buffer layer and a logarithmic bulk region. For this quantity, the Reynolds analogy with the Prandtl number dependency still holds and the profiles can be predicted accurately by the classical steady flow correlations. They showed that the thermal penetration length is strongly dependent on the fluid

properties described by the Prandtl number. They studied the response of a turbulent flow of Nu ≈ 28 and a series of Prandtl numbers Pr $= 0.1, 1, 10, 50$ and 100 to harmonic velocity fluctuations. Unfortunately, Wang and Lu do not provide the data in a way easy to reproduce and the comparisons can only be performed qualitatively. Figure 6.7 shows the triple decomposition components computed from the present LES plotted in wall normal direction. The plot on the left shows the time independent component for the three frequency regimes. It can clearly be seen that this component is relatively insensitive to the harmonic forcing of the flow, in agreement with the results of Wang and Lu. Concerning the organized oscillations given by the temperature amplitude a_T^+ and plotted in the center of the figure, the penetration length of the perturbations is also inversely proportional to the forcing frequency. However, the magnitude of the temperature oscillations strongly depends on the forcing frequency and the reference Nusselt number. At high frequencies, the oscillations are marginal. For the small Prandtl and Nusselt numbers used in the present investigation, the temperature oscillations become relevant only at lower frequencies. This is also in agreement with the observations of Wang and Lu. However, the strongest difference towards the hydrodynamic response is exhibited by the phase of the temperature oscillations shown on the right plot in the figure.

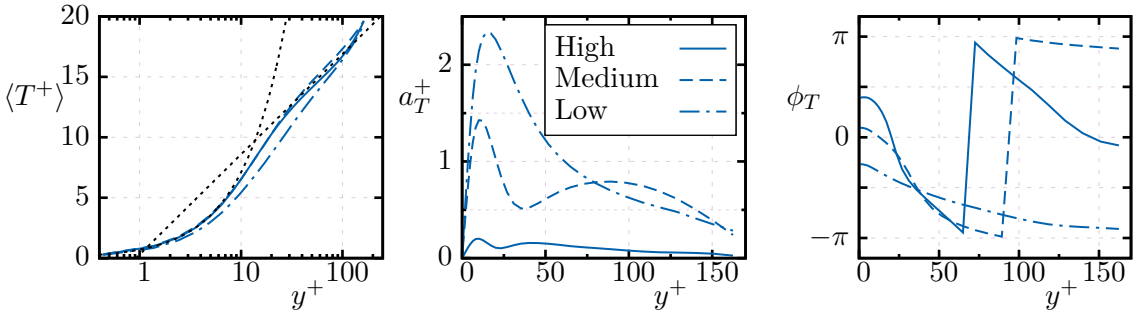

Figure 6.7: Triple decomposition of the temperature for the three exemplary cases given in Tab. 6.2.

Corresponding to Fig. 6.5 for the velocities, the evolution of the temperature ensemble averages within a cycle are given in Fig. 6.8 for the same three exemplary cases. Again, the profiles correspond to ten equally distributed phases and are separated from each other by multiples of 5 units in the vertical direction. The stationary profiles are denoted by red dashed lines. It can clearly be seen that both the penetration length and magnitude of the temperature oscillations strongly depend on the forcing frequency.

In a global sense, the magnitude of the skin friction and the wall heat flux give insight into the momentum and energy transfer in the domain. Figure 6.9 shows the skin friction evolution over one cycle normalized by its reference value without organized oscillations. It can clearly be seen that the skin friction response has also a linear sinusoidal dependency for all three exemplary frequencies. Furthermore, the amplitude is always higher than the velocity center-line amplitude and is frequency dependent. For high frequencies, the amplitude takes even values larger than unity. This means that locally, close to the wall the flow reverses during some phases of the cycle. In contrast, the cycle evolution of the normalized heat flux shown in Fig. 6.10 exhibits a totally different behavior. The amplitudes are rather small and most importantly, the response of the heat flux exhibits higher harmonics. Furthermore, there is a large

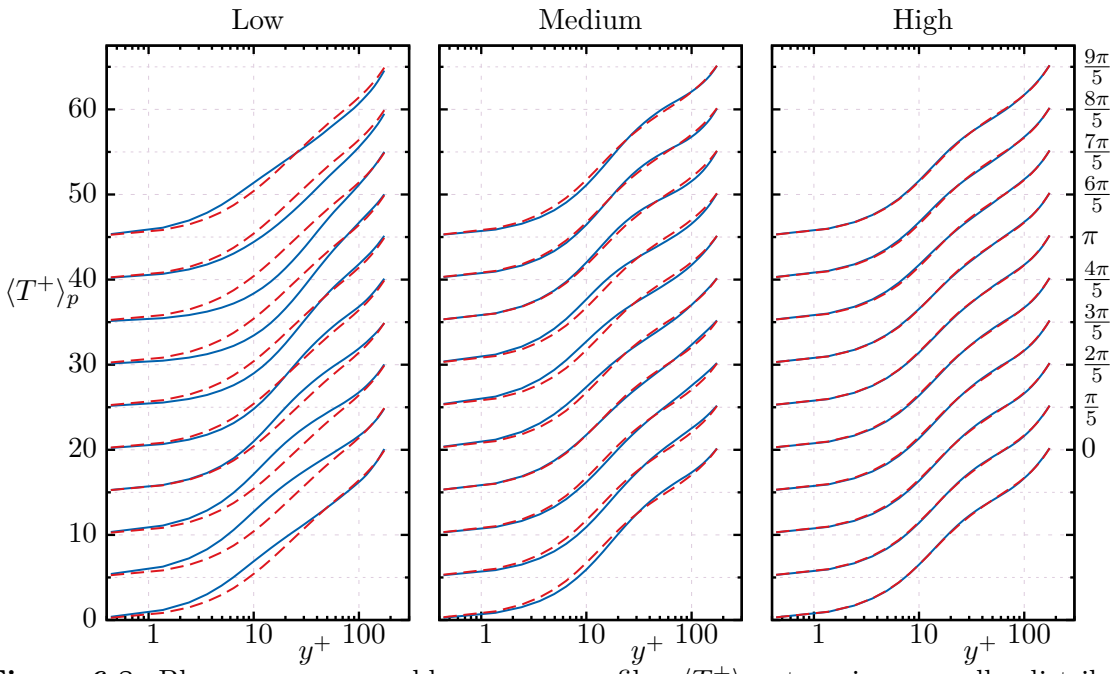

Figure 6.8: Blue curves, ensemble average profiles $\langle T^+ \rangle_p$ at various equally distributed phases ωt of one cycle separated by 5 wall units in the vertical direction. Dashed red curves correspond to the time average profiles at the corresponding frequencies.

phase change between the three frequencies considered. This behavior confirms the absence of the Reynolds analogy in the cycle resolved response of pulsating flows with heat transfer.

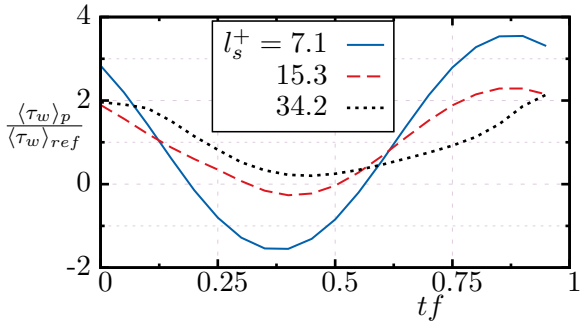

Figure 6.9: Cycle evolution of normalized skin friction for the cases listed in Tab. 6.2.

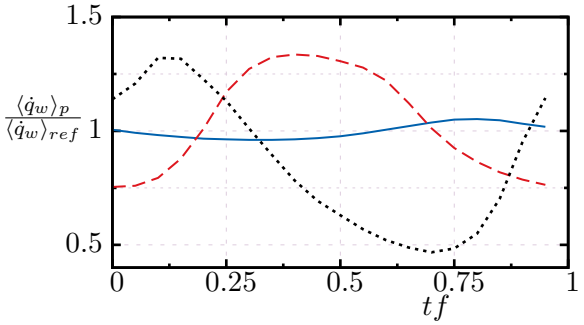

Figure 6.10: Cycle evolution of normalized heat flux for the cases listed in Tab. 6.2.

Based on the good agreement against the data of previous investigations, it can be stated that the test case set up and LES solver used in the present study reproduce the hydrodynamic and thermal behavior of turbulent pulsating flows correctly. To conclude this section, the key parameters and properties that characterize turbulent pulsating flows are reviewed:

1. The non dimensional frequency ω^+ or non dimensional Stokes length l_s^+ is the appropriate similarity parameter.

2. In the current dominated regime $\epsilon_{uc} \lesssim 0.7$, the time averaged velocity and temperature profiles are only weakly sensitive to the harmonic forcing.

3. The Reynolds analogy between skin friction and wall heat flux does not hold for the cycle resolved evolution.

6.2.7 Results of Simulation Campaign

After the validation of the LES solver and test case for three representative frequencies and amplitudes, an extensive simulation campaign with parameters listed in Tab. 6.3 has been carried out. The forcing frequency spans both the low and high frequency regimes according to the turbulence level of the test case. Furthermore, strong amplitude pressure gradient oscillations are imposed leading to large center-line velocity amplitudes. The novelty of the present investigation relies not only on the consideration of heat transfer, but specially on the consideration of large center-line velocity amplitudes. This is a very important feature, because the experimental investigations in which enhanced heat transfer has been observed are operated in the wave dominated regime $\epsilon_{uc} > 1$ displaying flow reversal throughout the channel. The goal was to clarify whether an increment in the forcing amplitude actually leads to higher energy transport rates. An attempt was made to span the parameter range as far as the available computational resources allow.

Table 6.3: Simulation parameters for the reference and the first simulation campaign.

Re_τ	l_s^+	(ω^+)	ϵ_{uc}	Pr	Nu_{ref}
180	5.9 to 37.4	0.0014 to 0.057	0.17 to 1.36	0.71	6.26

First, some results of the simulation campaign concerning the skin friction are discussed. Figure 6.11 shows the ratio of skin friction amplitude a_{τ_w} normalized by Stokes laminar solution [124]. The size of the markers denotes the amplitude of the velocity center-line amplitudes a_{uc}. At high frequencies, the Stokes length is small and is contained within the laminar sublayer of the flow. Thus, the ratio in the figure is close to unity. In contrast, for small frequencies, the Stokes length is large and extends well into the logarithmic bulk region. The flow has, in this case, time to develop into the corresponding turbulent regime and the amplitude of the skin friction increases. Interesting is that there is a frequency region in between ($l_s^+ \approx 15$), in which the skin friction amplitude of the turbulent flow is smaller than its laminar counterpart. This behavior has been already observed and discussed by Tardu et al. [124] in their experimental analysis.

Figure 6.12 shows the phase evolution of the skin friction and wall heat flux. The phase of the center-line velocity amplitude is taken as reference. The behavior of the skin friction phase is reproduced by Lighthills analytical solution remarkably well. For high frequencies, the limiting value of a $\pi/4$ phase advance can be observed clearly. This value changes gradually into a zero phase for lower frequencies. The transition occurs between the Stokes' lengths of approximately $l_s^+ \approx 13$ and $l_s^+ \approx 20$, respectively. Furthermore, the phase evolution is insensitive to the magnitude of the velocity center-line amplitudes, since all operation points collapse into a single curve.

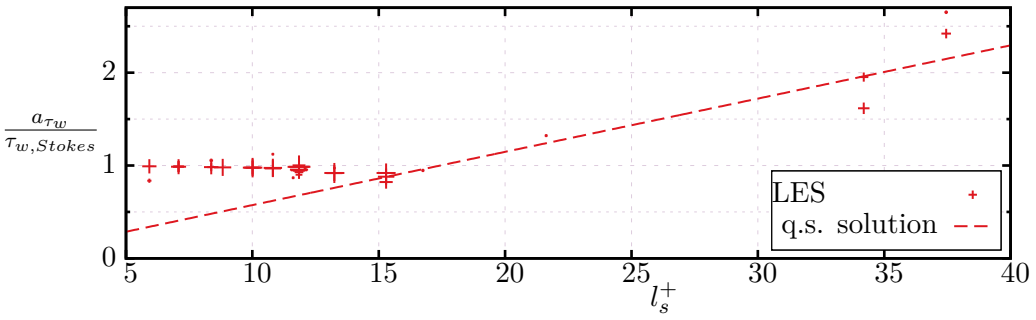

Figure 6.11: Comparison of the skin friction amplitude against the analytical solution of Stokes for laminar cases.

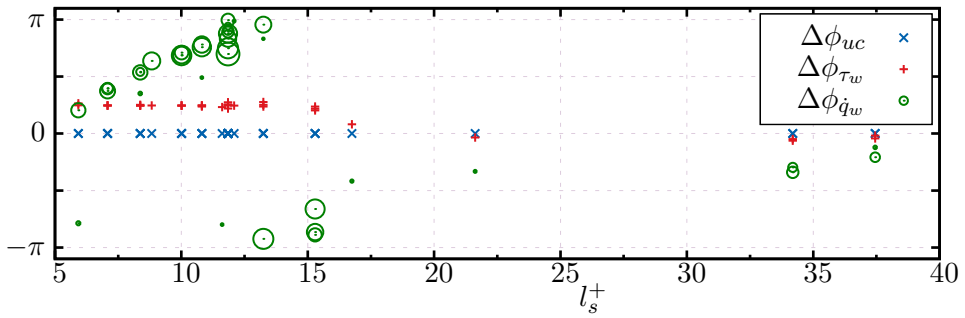

Figure 6.12: Comparison of the relative phases with the center-line velocity as reference.

The phase evolution of the wall heat flux also shown in Fig. 6.12 spans a broader range of values for the different operation points. At very high frequencies, the heat flux is in phase with the skin friction and grows rapidly as the frequency decreases. It reaches its maximum at a frequency parameter of approximately $l_s^+ \approx 12$. For lower frequencies, the phase reduces gradually into the expected quasi steady value of zero. While all operation points follow the same trend, the magnitude of the velocity oscillations denoted by the marker size seems to have a slight influence on the heat flux phase evolution. The scatter observed especially for small amplitude is caused by the harmonic decomposition. As demonstrated in the pulsating case validation in Sec. 6.2.6, small velocity amplitude lead to marginally ensemble averaged temperature oscillation and the decomposition looses quality.

Finally, the ratio of heat transfer enhancement defined by Eq. (5.6) is shown in Fig. 6.13 for all operation points summarizing the results of this simulation campaign. The crosses in this figure denote the computed operation points at various center-line velocity amplitudes and non-dimensional frequencies. The continuous surface plot has been computed via spline interpolation. Certainly, some regions in the interpolated map are not supported with simulated operation points and are thus, questionable. For this reason, they can be interpreted only qualitatively. The lack of operation points at low frequencies and high amplitudes is caused by the necessity of long integration times coupled with small time steps that were not affordable with the available computational resources. At high frequencies, the size of the mesh used restricted the imposition of larger amplitude ratios. Nevertheless, Fig. 6.13 shows that for small velocity amplitudes

and regardless of the forcing frequency, the heat transfer is insensitive to the pulsations. A noticeable change in the time averaged heat transfer can only be observed for large velocity amplitudes. Furthermore, depending on the frequency parameter l_s^+, both regions of enhancement and diminishment are exhibited. The maximum enhancement has been found for an operation point with center-line amplitude $\epsilon_{uc} \approx 1$ and frequency $l_s^+ \approx 12$. For higher frequencies, the enhancement vanishes due to the cut-off frequency that any dynamic system owns. For smaller frequencies, the ratio reduces and changes from enhancement to diminishment. The reason for this behavior is attributed to relaminarization effects.

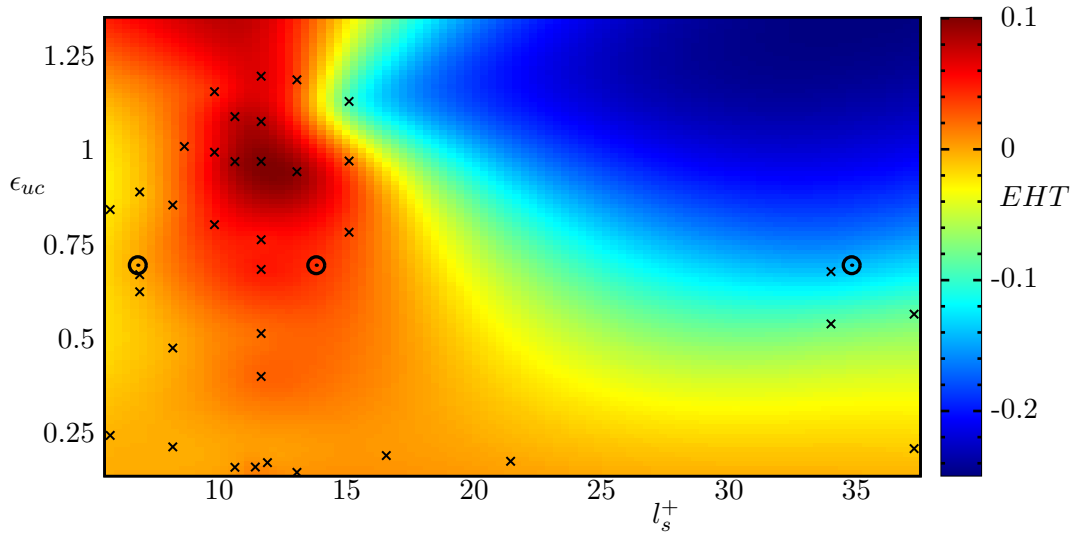

Figure 6.13: Enhanced heat transfer $EHT = (\langle \dot{q}_w \rangle - \langle \dot{q}_{w,\mathrm{ref}} \rangle)/\langle \dot{q}_{w,\mathrm{ref}} \rangle$ for a range of non-dimensional frequencies (l_s^+) and center-line velocity amplitude ratios ϵ_{uc}. The surface plot shows the spline interpolation supported by CFD simulations at the operation points denoted by the black crosses. Circles denote the three operation points studied by Wang and Lu [129].

In contrast to the momentum transfer, detailed CFD data concerning the heat transfer in turbulent pulsating channel flow is very sparse. Apart from the study of Wang and Lu [129], no other studies have been found in the literature. The operation points studied by Wang and Lu are marked also in Fig. 6.13 by circular markers. They correspond to the ones previously studied by Scotti and Piomelli [121] (note that they do not studied the heat transfer). Unfortunately, Wang and Lu do not provide quantitative results concerning the heat transfer enhancement. They state however, that the time averaged Nusselt numbers of the pulsating cases can be predicted with good accuracy by well established stationary correlations. Thus, they concluded that the pulsations do not lead to a noticeably permanent heat transfer enhancement. The simulation campaign shown in Fig. 6.13 gives similar results for these points, too, where $EHT \approx \pm 2\%$.

To finalize this section, the following conclusions can be addressed:

- This simulation campaign is novel, because it spans a wider range of frequencies and velocity amplitudes, and considers heat transfer.
- Concerning the momentum transfer, the results of the simulation campaign are in very good agreement with available numerical [121] and experimental [124]

data. It has been confirmed that the relevant similarity parameter is the non-dimensional frequency ω^+ or l_s^+.

- A noticeable permanent change in time averaged heat transfer is only observed at velocity amplitudes with considerable flow reversal, in accordance with some experimental observations. Depending on the non-dimensional frequency, both regions of enhancement and diminishment are possible. This may lead to contradictory results, if investigations of different non-dimensional frequency are compared with each other.
- However, the magnitude of the possible enhancement is much lower than the one predicted in some experimental investigations, e.g. [29], even if the non-dimensional frequency is similar. While the maximum enhancement found in the present investigation is of the order of magnitude of a few percent $EHT_{\max} \approx 8\%$, the aforementioned publications report ratios larger than 200%.

One possible reason for the discrepancies mentioned in the last point is that the experimental investigations reporting striking enhancement ratios exhibit large velocity amplitudes $\epsilon_{uc} \gg 1$. Furthermore, as explained in the introduction of this chapter, pressure fluctuations inherent of acoustic waves that have been neglected in this first campaign might also play a role. Finally, stratification caused by temperature dependent properties can lead to a destabilization of the turbulent pulsating flow, which was not considered in the present simulation campaign. Thus, further investigations are necessary to evaluate the influence of these effects. These additional investigations will be presented in the next section. However, the computational resources available in the present work are restricted, and it will not be possible to study the large velocity amplitudes.

6.3 Extension of the Solver to Handle Pulsating Pressure and Stratification

The NS-equations presented in Sec. 2.1.2 provide a general framework for the description of flows with strong temperature differences leading to stratification, and acoustic waves. However, the numerical treatment of such a set of equations is very challenging. In addition to the high resolution requirements, difficulties concerning the wave propagation arise. As explained in [103], the numerical schemes influence the wave propagation velocity and induce dispersion errors. Furthermore, spatial discretization induces also numerical errors at regions with step gradients. The consequence of these two issues are spurious non-physical waves of short wavelength and high propagation speed that are very sensitive to boundary conditions. The stabilization of the code against such *numerical waves* is a difficult task.

Certainly, the low Mach number simplification presented in Sec. 2.3 provides a robust solution to the issues just mentioned. Actually, the influence of stratification can be investigated directly by this approach in combination with the acoustically compact method presented in Sec. 6.2.1. However, this method completely suppress the acoustic waves in the system making only the simulation close to a pressure node feasible.

6.3.1 Generalized Acoustically Compact Approach

To account for acoustic pressure fluctuations, a generalized acoustic compact approach has been developed in the present study. This method avoids also the numerical issues leading to spurious waves by solving the low Mach number approximation of the NS-equations (Eqs. (2.90) to (2.92)), but introducing momentum and mass source terms that mimic the effects of acoustic standing waves.

The first step in the derivation splits the pressure into a thermodynamic and a hydrodynamic component:

$$p = p_{\mathrm{th}}(\vec{x}, t) + p_{\mathrm{hy}}(\vec{x}, t) \quad . \tag{6.22}$$

As explained in Sec. 2.1.3, each of this terms accounts the contributions of two scales of considerably different magnitude. Perturbations of the hydrodynamic component travel through the domain at velocities similar to the reference flow velocity and their magnitude is similar to the kinetic energy of the flow. In contrast, the isentroppic thermodynamic perturbations display small amplitudes and travel through the domain at the speed of sound. They can be linearized into a mean and a fluctuating component $p_{\mathrm{th}} = \bar{p}_{\mathrm{th}} + p'$. The mean component corresponds to the atmospheric pressure, which is constant for open configurations. As explained in Sec. 6.1, the spatio-temporal dependency of the acoustic perturbations can be predicted by linear theory. In the present study, the investigations focus on the channel flow test case with acoustic standing waves already introduced in Sec. 6.2.1, such that:

$$p = P_o + p'(x, t) + p_{\mathrm{hy}}(\vec{x}, t) \quad , \tag{6.23}$$

where P_o denotes the constant atmospheric pressure. Following the same principles of acoustic compactness described in Sec. 6.2.1, only the hydrodynamic component is used as primitive variable in the momentum equation. The gradient of the acoustic

perturbation is incorporated as a homogeneous source term that fluctuates in time. Up to here, the approach is equivalent to the one used for pressure nodes.

Within the low Mach number approximation, only the atmospheric pressure is considered in the ideal gas law. However, small prescribed perturbations are also introduced to account for the pressure fluctuations:

$$\rho = \frac{P_o}{R_s T(\vec{x},t)} + \rho'(t) \quad . \tag{6.24}$$

Neglecting the acoustic perturbations in Eq. (6.24) leads to the classical weakly compressible set of equations widely used in the literature [92, 97].

Numerically, the density oscillations can be incorporated effectively in the PISO loop via pressure equation. Substitution in Eq. (2.125) gives a new Poisson equation in the iterative PISO algorithm:

$$-\frac{\partial \rho_o}{\partial t} - \frac{\partial \rho'}{\partial t} = \nabla\left(\rho \mathbf{A}^{-1}\left[\vec{r} - \mathbf{H}'\vec{u}^*\right]\right) - \nabla\left(\rho \mathbf{A}^{-1} \nabla \vec{p_{\mathrm{hy}}}^*\right) \quad , \tag{6.25}$$

where $\rho_o = P_o/(R_s T)$ denotes the density at atmospheric pressure. Some assumptions are necessary to couple the density fluctuations to the prescribed pressure fluctuations. Restricting to small isentropic acoustic perturbations, the constitutive equation $\rho' = p'/\vec{c}^2$ can be used. The transient term for the fluctuations can be approximated as:

$$\frac{\partial \rho'}{\partial t} = \frac{\partial \rho'}{\partial p'}\frac{\partial p'}{\partial t} \approx \frac{1}{\vec{c}^2}\frac{\partial p'}{\partial t} = \frac{1}{\gamma R_s T_o}\frac{\partial p'(x,t)}{\partial t} \quad . \tag{6.26}$$

Furthermore, within an acoustically compact region at location X, the pressure fluctuations are

$$p' \approx a_p(X)\cos(\omega t) \quad , \tag{6.27}$$

with pressure amplitude $a_p \sim \cos(l\pi x/\lambda_a)$. Substitution in Eq. (6.25) gives after some rearrangement the following modified iterative pressure equation:

$$-\frac{\partial \rho_o}{\partial t} = \nabla\left(\rho \mathbf{A}^{-1}\left[\vec{r} - \mathbf{H}'\vec{u}^*\right]\right) - \nabla\left(\rho \mathbf{A}^{-1} \nabla \vec{p}^*_{\mathrm{hy}}\right) - \frac{\rho_o}{\gamma P_o}\omega a_p(X)\sin(\omega t) \quad , \tag{6.28}$$

where the third term on the right-hand side corresponds to an explicit source term. This method introduces source terms in the momentum and pressure equations to account for the influence of acoustic standing waves in a compact region. A similar approach has been proposed by Schmid et al. [119] by pumping mass through the boundaries instead of using source terms.

However, a conflict arises since the flow transfers heat with the boundaries and the assumption of isotropy is breach. Thus, it has to be noted that this method is only an approximation.

6.3.2 Demonstration of Applicability

To prove the applicability of the generalized acoustically compact approach, an academic case shown in Fig. 6.14 is computed. It corresponds to a two dimensional channel

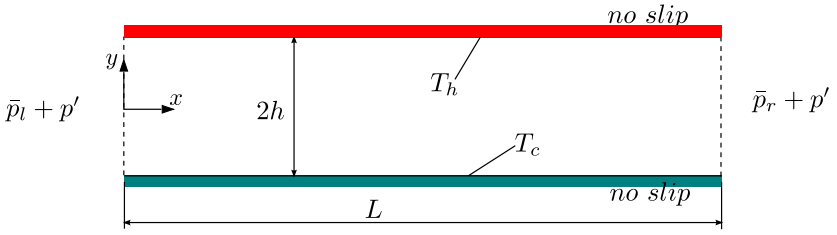

Figure 6.14: Sketch of a 2D-channel with laminar flow and and acoustic standing waves.

of length L and width $2h$ with walls kept at different temperatures T_c and T_h, respectively. It represents closely the case explained in Sec. 2.2.2.3 accounting for laminar viscous mean flow, heat transfer and variable fluid properties.

First, the whole domain is simulated with a fully compressible solver without source terms. By imposing pressure fluctuations $p' = a_p \cos(\omega t)$ at inlet and outlet, the second mode shape at a frequency $\omega = \bar{c}/(2\pi L)$ can be excited. Table 6.4 gives the relevant boundary conditions. The resulting Mach number is quite small $M = 0.002 \ll 1$ and its effects will be neglected. Thus, the analytical solution given by Eqs. (2.68) and (2.69) can be used as a reference.

Table 6.4: Laminar compressible channel flow with variable properties, simulation parameters.

L/h	Mesh	T_h/T_c	M	$a_p(0)/(\bar{p}_l - \bar{p}_r)$	γ	$\bar{c}$	ω
695.6	1000×60	1.5	0.002	46	1.4	$\sqrt{\frac{(T_h+T_c)}{2}\gamma R_s}$	$\bar{c}/(2\pi L)$

The flow field can be decomposed into a mean and a fluctuating component:

$$u = \bar{u}(y) + a_u(x, y)\cos(\omega t + \phi_u) \quad , \tag{6.29}$$

$$p = \bar{p}(x) + a_p(x)\cos(\omega t + \phi_p) \quad , \tag{6.30}$$

where the mean velocity field is assumed as fully developed and the pressure as constant in wall normal direction. Figure (6.15) shows the axial distribution of the computed velocity and pressure fluctuations along the channel center-line. The harmonic dependency of the axial amplitude distribution can be seen clearly. However, the analytical solution with velocity nodes at the boundaries is not reproduced perfectly. This behavior is attributed to the simplistic boundary conditions imposed. More sophisticated boundary conditions exist, which avoid spurious numerical waves, see [21]. When looking at the phase axial distribution, the picture is similar. The analytical solution can be reproduced only qualitatively. In addition to the boundary condition issues, the harmonic decomposition of the recorded signals losses quality at locations where the amplitude is small. Nevertheless, the test case reproduces qualitatively well the laminar flow field in the presence of standing acoustic waves and is suitable for testing the generalized acoustically compact approach.

For the validation, the flow field at certain axial positions is computed using the previously explained generalized acoustically compact approach considering only a small section $l = 0.01L$ of the domain. The chosen locations are denoted by vertical lines

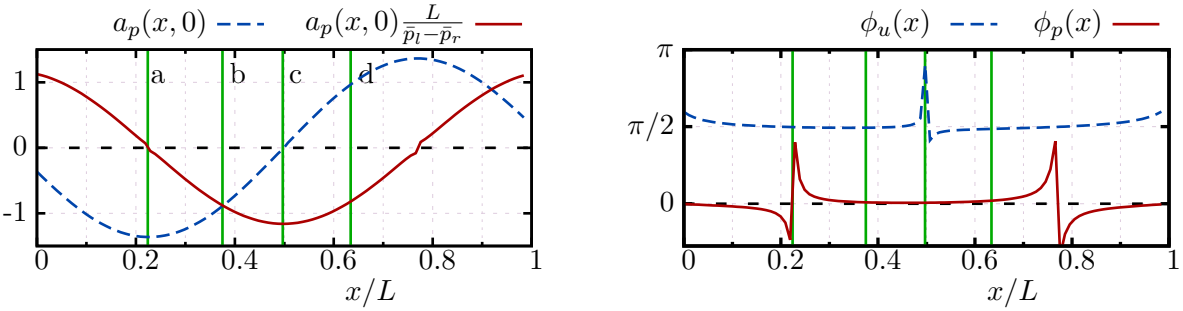

Figure 6.15: Axial profiles of velocity and pressure oscillations. Left: amplitudes, right: phases.

in Fig. (6.15). The flow is driven by a constant and homogeneous momentum source term:

$$\frac{\partial \bar{p}}{\partial x} = \frac{\bar{p}_l - \bar{p}_r}{L} \quad . \tag{6.31}$$

Fluctuations of pressure and velocity are induced by oscillating source terms proportional to the local pressure amplitude gradient and magnitude. The values for the various locations are taken from the fully compressible simulation and listed in Tab. 6.5 in non-dimensional form.

Table 6.5: Local values of pressure amplitudes employed in the generalized acoustically compact simulations.

	Location			
	a	b	c	d
$\frac{a_p}{\bar{p}_l-\bar{p}_r}$	-6	-26.8	-47.4	-36
$\frac{L}{\bar{p}_l-\bar{p}_r}\frac{\partial a_p}{\partial x}$	-268	-222	3.4	180

The results of these simulations are plotted in Fig. 6.16 to 6.17 for the four chosen locations and compared to the fully compressible simulation. The agreement between the fully compressible and the compact simulation is very good. As expected, the mean velocity profile $\bar{u}(y)$ driven by the mean pressure gradient is equal at all locations. The amplitude of the velocity oscillations a_u is not symmetric due to the temperature dependent viscosity. The phase of the velocity oscillations approaches at the channel center line the analytical value of $\pi/2$. Furthermore, a phase advance towards the center-line fluctuations of $\pi/4$ is present close to the walls at all locations as predicted analytically by Lighthill.

6.3.3 Weakly Compressible Turbulent Channel Flow: Reference Case

As in the fully incompressible case considered in Chap. 6.2.5, a turbulent test case without acoustic fluctuations is necessary to serve as a reference case and evaluate a possibly *EHT*. This reference case served also as a validation for the LES solver used in this weakly compressible approach.

The dynamic One-Equation eddy viscosity model was not available in the standard *openFOAM* version and it had to be implemented. Taking advantage of the C++

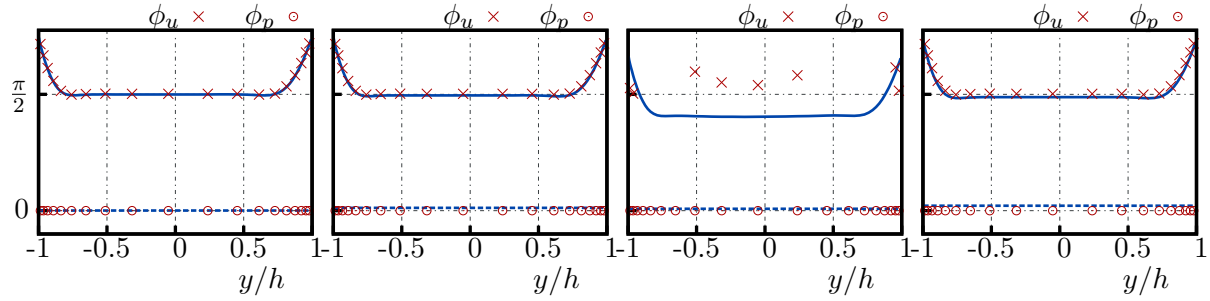

Figure 6.16: Comparison of compact approach to full domain simulation. Phases at the four locations a to d, from left to right.

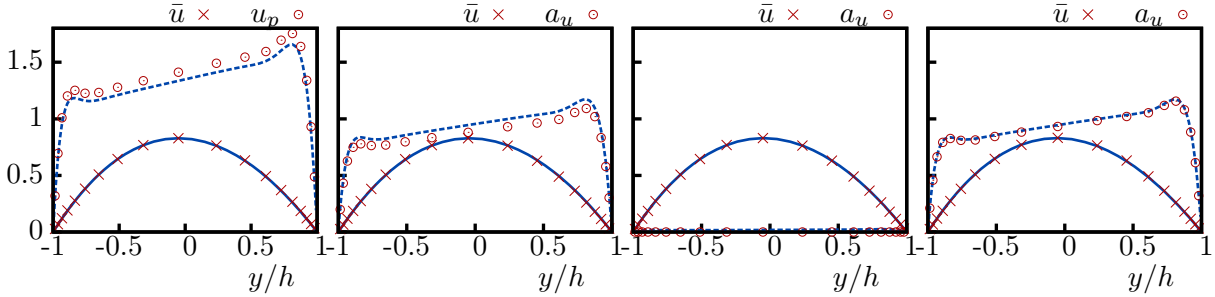

Figure 6.17: Comparison of compact approach to full domain simulation. Mean and amplitude components of velocity at the four locations a to d, from left to right.

structure of the package, the implementation was based on the incompressible formulation and only the additional terms present in compressible flows had to coded. The implementation is based on the derivation given by Fureby [36], and Chai et al. [20]. In contrast to the implementation for the fully incompressible case, the turbulent Prandtl number is computed here also dynamically. This decision has been taken, because the results of the first simulation campaign shown that the Reynolds analogy close to a boundary layer does not hold for pulsating flows. At first glance, the contribution of a variable turbulent Prandtl number is expected to be small. This is because the heat transfer is taking place in a region close to the wall, which is resolved very accurately leading to marginal subgrid scale diffusion. However, it was interesting to investigate whether this influence is important or not.

Table 6.6: Results of Weakly compressible reference case.

T_h/T_c	$\mathrm{Re}_{\tau c}$	$\mathrm{Re}_{\tau h}$	Nu_c	Nu_h	Pr
2	212.7	85.6	5.92	3.63	0.71

Details of the validation against data available from the literature are given in App. C.2. The agreement between the present LES simulation and the data of Lessani and Papalexandris [74] is not ideal. Especially the resolution of the flow close to the cold wall was challenging, and it seems that the resolution was not fine enough. Other reasons for the discrepancies might be slightly different Reynolds numbers and transport coefficients. Nevertheless, in view of the otherwise not manageable computational costs, the test case set-up has been kept as it is. Because of this reason, the results gained from this investigation should be understood as merely qualitatively correct.

The results of this reference test case are listed in Tab. 6.6. The major challenge of strong stratified test cases is that in one simulation with a homogeneous source term driving the flow, two turbulent regimes are displayed. On the cold side, the flow is fully developed in the turbulent regime. In contrast, the flow close to the hot wall is not fully turbulent due to the higher molecular viscosity and the Reynolds number is considerably lower. This leads to a asymmetric velocity field. The same holds for the thermal field. From energy conservation, the heat flux on both wall is equal. However, the local Nusselt numbers differ due to the different properties at the walls.

To characterize this flows, an average average friction velocity is introduced. From the momentum conservation, an average skin friction can be estimated as:

$$\tau_{\bar{w}} = h\frac{\partial \bar{p}}{\partial x} = \frac{1}{2}\left(\mu_c \left.\frac{\partial u}{\partial y}\right|_c + \mu_h \left.\frac{\partial u}{\partial y}\right|_h\right) \quad , \tag{6.32}$$

where the indices $_c$ and $_h$ denote the locations on the cold and hot wall, respectively, and $\frac{\partial \bar{p}}{\partial x}$ the homogeneous momentum source term. Similarly, an average friction velocity can be defined using the average density as:

$$u_{\bar{\tau}} = \sqrt{\frac{2\tau_{\bar{w}}}{\rho_c + \rho_h}} = \sqrt{\frac{2h}{(\rho_c + \rho_h)}\frac{\partial \bar{p}}{\partial x}} \quad . \tag{6.33}$$

6.3.4 Influence of Stratification Close to a Pressure Node

The question that arises is whether the asymmetry in a stratified flow field can lead to a destabilization in combination with acoustic pulsations. Due to constraints in available computational resources, the simulation campaign for stratified flows has been reduced to a single operation point. From the extensive campaign performed for the incompressible case, the operation point with the strongest heat transfer enhancement has been observed at a frequency parameter of $l_s^+ \approx 12$ and a center-line velocity amplitude close to unity $\epsilon_{uc} \approx 1$. Since the functional behavior is expected to be qualitatively similar, an operation point close to these conditions has been chosen here, too.

Table 6.7: Results of simulation at optimal operation point close to a pressure node.

$l_{\bar{s}}^+$	l_{sc}^+	l_{sh}^+	ϵ_{uc}	EHT	$\overline{\mathrm{Re}}_{\tau c}$	$\overline{\mathrm{Re}}_{\tau h}$	$\overline{\mathrm{Nu}}_c$	$\overline{Nu}_h$
10.2	13.46	9.79	1.05	6.1%	213.7	84.7	6.30	3.84

Close to a pressure node, the pressure remains constant and the source term in the Poisson equation vanishes. This is achieved by setting the input parameter for the pressure amplitude to zero in the solver described above. The imposition of the frequency parameter is not straight forward. This, because of the two turbulent regimes present in a stratified flow. Consequently, one forcing frequency will lead to two different non-dimensional frequencies: one on the cold l_{sc}^+ and one on the hot side l_{sh}^+, respectively. It was thus necessary to vary the forcing frequency until an appropriate pair of values was found. The same was necessary concerning the oscillating momentum source term to get a center-line velocity amplitude close to unity.

Table 6.7 gives the results of the simulation closest to the desired operation conditions. The essential parameter concerning heat transfer is again the ratio of enhancement. Under the given operation conditions, an enhancement of approximately 6.1% has been found. Compared to the value of 6.6% that the map of the fully incompressible campaign predicts for the operation point $l_s^+ = 10.2$ and $\epsilon_{uc} = 1.05$, no appreciable change can be observed. This means that the stratification does not change essentially the relative average heat transfer in pulsating flows.

6.3.5 Influence of Pressure Fluctuations

To get the general picture of heat transfer in pulsating flows driven by standing acoustic waves, three additional operation points have been computed. They corresponds to locations in an acoustic field others than the pressure node. To explain this simulation campaign, consider the acoustic field shown schematically in Fig. 6.18 by the dashed lines. It corresponds to standing acoustic waves of wavelength λ_a. The locations to be investigated are denoted by small dashed rectangles at positions $x = X_1$ to $x = X_4$. According to the linear theory presented in Sec. 2.2.2, the pressure field can be described by:

$$p' = P_1 \cos(2\pi x/\lambda_a)\cos(\omega t) = a_p(x)\cos(\omega t) \quad , \tag{6.34}$$

with pressure amplitude P_1. According to the compact approach presented above, the momentum source term is:

$$\vec{S}_M = \frac{\partial}{\partial x}\left[\bar{p} + P_1 \cos(2\pi x/\lambda_a)\cos(\omega t)\right] = P_{0x} - P_{1x}(x)\cos(\omega t) \quad , \tag{6.35}$$

where stationary and oscillating components are assumed homogeneous over a small portion of the channel for a given location $x = X$. To be consistent with the operation point presented in Sec. 6.3.4, the parameters used in that simulation are adopted here for position X_3. The normalized parameters for all positions are listed in the first three columns of Tab. 6.8.

Table 6.8: Parameters used in the simulation campaign for various compact axial locations and corresponding results.

Location	$\frac{P_{0x}}{\lvert P_{0x}(X_1)\rvert}$	$\frac{P_{1x}}{\lvert P_{1x}(X_3)\rvert}$	EHT	l_{sc}^+	l_{sh}^+	ϵ_{uc}	$\overline{\mathrm{Re}}_{\tau c}$	$\overline{\mathrm{Re}}_{\tau h}$	$\overline{\mathrm{Nu}}_c$	$\overline{Nu}_h$
X_1	1	0	−0.9%	13.69	9.66	1.05	216.3	84.4	5.89	3.58
X_2	$\sqrt{2}$	$-\sqrt{2}$	5.6%	13.43	9.94	1.05	212.2	86.9	6.27	3.84
X_3	0	−1	6.1%	13.46	9.79	1.05	213.7	84.7	6.30	3.84
X_4	$-\sqrt{2}$	$-\sqrt{2}$	5.6%	13.39	9.53	1.05	211.6	83.3	6.29	3.84

Again, the results concerning heat transfer are evaluated primarily through the ratio of enhancement, which is also listed in Tab. 6.8. For a better overview, the ratio of enhancement is also plotted in Fig. 6.18, where the profiles of acoustic pressure and velocity fluctuations are also sketched. The ratio of enhancement at locations X_2 and X_4 is almost identical to the ratio at the reference position X_3. In contrast, at position X_1 where only pressure fluctuations occur, the ratio of enhancement vanishes. The results of this simulation campaign show that the heat transfer enhancement is controlled solely by velocity fluctuations. The amplitude of the small acoustic pressure fluctuation does not influence the heat transfer.

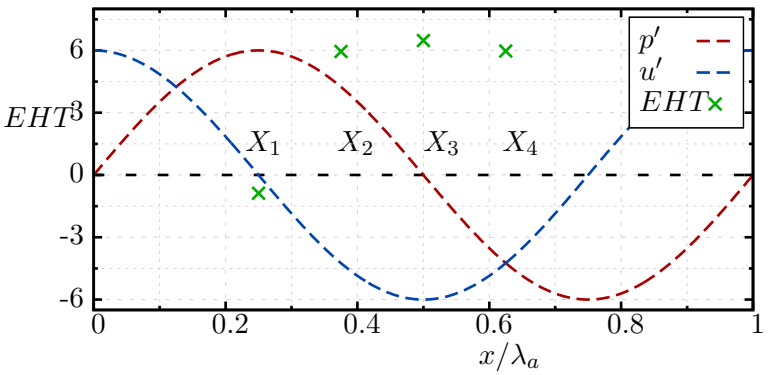

Figure 6.18: Ratio of heat transfer enhancement EHT at four representative locations in a channel with acoustic standing waves. The dashed lines denote the relative amplitude of the acoustic waves.

7 Summary and Conclusions

The long term objective of the project hosting this work is the development of reliable engineering tools to characterize the damping behavior of resonator rings in rocket thrust chambers under real operation conditions. Hereby, the influence of enhanced heat transfer presumably driven by the acoustic fluctuations should be considered in the analysis. The overall intention of the project is to clarify the following questions:

1. Should we expect significantly enhanced heat transfer in resonators or in the vicinity of the cavity mouths?
2. Does this enhanced heat transfer has any consequences on the damping behavior of resonators?

In order to provide satisfactory answers to these questions, fundamental research concerning two top level topics is necessary, namely: damping characteristics of resonator rings and heat transfer in pulsating flow. This fundamental research, and a preliminary estimation of possible consequences was the goal of this thesis.

The first part of this thesis dealt with the accurate description of the damping behavior of resonator rings under representative rocket chamber operation conditions. The characterization of the resonator rings is based on impedance expressions treated as boundary conditions. After giving some state of the art models for resonators, an extension to account for temperature inhomogeneities inside the cavities is proposed. Based on these equivalent impedance expressions, a preliminary decoupled analysis is presented that describes the dependency of the cavities to some design parameters and chamber conditions. Especial attention is given to the influence of an inhomogeneous temperature profile possibly caused by heat transfer enhancement. The results of this preliminary investigation show that the cavities frequency bandwidth of operation is considerably reduced by a temperature inhomogeneity. Furthermore, it has been shown that the models describing the non-linear losses exhibit a strong uncertainty.

To accurately predict the stabilizing influence of resonator rings, the main driving and damping mechanisms present in the thrust chambers have to be considered. For this purpose, a low-order method to predict linear stability is proposed, which is able to reproduce the essential driving and damping mechanisms present in the chamber, give especial attention to the resonator ring, and afford parametric studies. The method is based on a network representation of the chamber combined with a Nyquist-plot technique for the determination of the system eigenfrequencies. This method widely applied for configurations propagating only plane waves, has been extended to account for non-plane transverse acoustic modes of major importance in rocket chambers. The necessary modifications to the method have been discussed. The incorporation of the resonator ring element has been carefully accomplished, taking an accurate acoustic pressure field close to reactive and dissipative boundaries. This causes higher order

mode coupling at connections to the rest of the network. Studying a representative rocket thrust chamber configuration, three major stabilizing effects of resonator rings have been identified:

(i) The eigenfrequencies of the system close to the design point of the cavities are shifted to slightly different frequencies. The coupling between driving mechanisms and acoustic might be weakened in this way.
(ii) Dissipation of acoustic energy by viscous effects described by the real part of the shell impedance stabilizes the system.
(iii) At connecting planes of the resonator ring, the traveling waves are scattered into higher order, evanescent modes reducing the acoustic energy present in the resonant mode.

Furthermore, it has been demonstrated that the optimal design of resonator rings predicted by a decoupled analysis differs from the one predicted by the coupled analysis. The reason for this behavior is the emergence of additional modes in the coupled system, which can not be described by a mere analysis of the boundary conditions. This is in accordance to experimental and numerical investigations [96].

This framework allowed finally to study the sensitivity of resonator rings to changes in the chamber operation conditions. The occurrence of enhanced heat transfer has been modeled as a sudden increase of chamber wall temperature leading to a gas temperature inhomogeneity in the cavities. It has been shown that such a inhomogeneity can indeed lead to a destabilization of the engine that was no predicted by state of the art models. This highlights the necessity for an accurate knowledge of the temperature profiles in rocket chambers, especially in the resonator cavities and under real operation conditions.

Thus, a major long term goal of the project hosting this work is the prediction of reliable temperature profiles inside and in the vicinity of the cavities under pulsating conditions. However, to achieve this goal, a more concise understanding of the fundamental heat transfer phenomena under pulsating conditions as those induced by acoustic waves is necessary. This was the intention of the second part of this thesis. Because the system dynamics in representative rocket chambers are very complex, displaying bulk flow, near wall turbulent hydrodynamic and wall thermal transients, the problem has been divided into more definite work packages of increasing complexity. In a divide and conquer strategy, the influence of the different transients has been studied separately. The first preliminary investigation included a low order model for heat flux through a wall of finite thickness subjected to transient boundary conditions similar to those expected in devices suffering from thermoacoustic instabilities. The second step performed in the strategy treated the heat transfer in laminar pulsating flow past a heated flat plate using a numerical CFD approach. Based on these two preliminary investigations, various mechanisms leading to enhanced heat transfer have been identified and the following conclusions can be addressed:

- Bulk flow transients can indeed lead to a permanent time averaged heat transfer change, provided that both the temperature and the heat transfer coefficient fluctuate in time. The phase between the two pulsations decides whether enhancement or diminishment occurs. The magnitude of the offset is proportional to the

amplitudes of the heat transfer coefficient and temperature oscillations. A similar dependency has been predicted by Lundgren et al. [78].

- Two dimensional laminar hydrodynamic effects like flow reversal in a thermally developing flow can also lead to permanent time averaged heat transfer changes. Both enhancement and diminishment of time averaged heat transfer is locally possible, in agreement with theoretical and experimental observations [51, 79].
- For most combinations of parameters, the wall thermal inertia plays a minor role in the heat transfer under transient conditions caused by pulsations of the bulk flow. The thermal inertia does not contribute to any permanent enhancement and works always against the heat flux. These observations agree with the results of similar investigations available in the literature [51, 79, 134].

The magnitude of the enhancement induced by the mechanisms mentioned in the previous list is small. However, the interaction of turbulent scales with the organized pulsations was omitted in those preliminary analysis. To account for the influence of this interaction, the third step in the strategy focused on the more challenging study of heat transfer in turbulent pulsating flow.

First, a proper test case set-up has been defined, that makes the numerical treatment of turbulent flows feasible based on the large eddy simulation approach. The organized pulsations are imposed via an acoustically compact approach driven by source terms that allow the treatment of the problem within an incompressible formalism. This overcomes several numerical issues concerning spurious numerical waves. Periodicity boundary conditions in stream- and spanwise direction allowed the flow to develop turbulent fluctuations inherently. This leads to a physical turbulent spectrum and to a reduction of computational cost, because only a compact region of the channel has to be simulated. The novelty of this extensive simulation campaign is that it covers a wider range of frequencies and center-line velocity amplitudes, and considers heat transfer. The principal results of this study are:

- The momentum transfer exhibited by the simulation campaign is in very good agreement with available numerical [121] and experimental [124] data. It has been confirmed that the relevant similarity parameter is a non-dimensional frequency scaled by appropriate turbulent time scales.
- A noticeable permanent change in time averaged heat transfer is only observed at large velocity amplitudes, in accordance with some experimental observations. Depending on the non-dimensional frequency, both heat transfer enhancement and diminishment is possible. This may lead to contradictory results, if investigations of different non-dimensional frequency are compared with each other.
- However, the magnitude of the possible enhancement is only a few percent and is order of magnitudes lower than the one predicted in some experimental investigations, e.g. [29, 49], even if the non-dimensional frequency is similar.

In the first turbulent simulation campaign, stratification and acoustic pressure fluctuations have been neglected. In a subsequent final analysis, the method has been extended to account for temperature dependent properties and local pressure fluctuations

in a weakly compressible formalism. Again, the assumption of acoustic compactness allowed the incorporation of these effects via source terms in the momentum and iterative pressure equation. After validation of the extended method, the operation point that exhibited the maximum enhancement in the previous campaign has been investigated taking stratification and pressure fluctuations into account. However, these effects seem to play a negligible role concerning heat transfer enhancement.

A Linear Acoustics

A.1 Derivation of Wave Equation

This section reviews the derivation of a general inhomogeneous wave equation for the pressure fluctuations p' and is based on the analysis given by Culick [24].

The starting point of the derivation are the Navier-Stokes equations given in Sec. 2.1.2. However, it is more convenient to express the equation of energy in terms of the pressure. This can be done assuming ideal gas behavior with homogeneous and constant heat capacities (perfect gas). The set of equations in tensorial notation are:

$$\frac{\partial \rho}{\partial t} + \vec{u} \cdot \vec{\nabla}\rho = -\rho \vec{\nabla} \cdot \vec{u} \quad , \tag{A.1}$$

$$\rho \frac{\partial \vec{u}}{\partial t} + \rho \vec{u} \cdot \vec{\nabla}\vec{u} = -\vec{\nabla}p + \vec{\nabla} \cdot \boldsymbol{\tau} \quad , \tag{A.2}$$

$$\frac{\partial p}{\partial t} + \gamma p \vec{\nabla} \cdot \vec{u} = -\vec{u} \cdot \vec{\nabla}p + \frac{R_s}{c_v}\left[-\vec{\nabla} \cdot \vec{q} + \dot{Q}\right] \quad , \tag{A.3}$$

where $\boldsymbol{\tau}$ corresponds to the stress tensor, mass and momentum source terms are neglected, and $\dot{Q}$ represents a volumetric heat release rate. This heat release rate can be caused for example by combustion.

In a perturbation analysis, all variables are decomposed into time averaged (mean) and fluctuating parts. Apart from the mean pressure, all mean quantities might vary in space. A homogeneous averaged pressure assumption is valid for low Mach numbers. Under these assumptions, the set of perturbed equations can be written as:

$$\frac{\partial \rho'}{\partial t} + \vec{\bar{u}} \cdot \vec{\nabla}\rho' = -\vec{u}' \cdot \vec{\nabla}\bar{\rho} + \mathcal{O}^2 \quad , \tag{A.4}$$

$$\frac{\partial \vec{u}'}{\partial t} + \frac{1}{\bar{\rho}}\vec{\nabla}p' = -\left[\vec{\bar{u}} \cdot \vec{\nabla}\vec{u}' + \vec{u}' \cdot \vec{\nabla}\vec{\bar{u}}\right] + \frac{1}{\bar{\rho}}\vec{\nabla} \cdot \boldsymbol{\tau}' + \mathcal{O}^2 \quad , \tag{A.5}$$

$$\frac{\partial p'}{\partial t} + \gamma \bar{p} \vec{\nabla} \cdot \vec{u}' = -\vec{\bar{u}} \cdot \vec{\nabla}p' - \gamma p' \vec{\nabla} \cdot \vec{\bar{u}} + \frac{R_s}{c_v}\left[-\vec{\nabla} \cdot \vec{q}' + \dot{Q}'\right] + \mathcal{O}^2 \quad . \tag{A.6}$$

The perturbed form of the equation of state reads:

$$p' = R_s(\rho' \bar{T} + \bar{\rho} T') + \mathcal{O}^2 \quad . \tag{A.7}$$

Culick derived this equations up to second order in the fluctuations [24]. Here, these terms are not shown explicitly, but are denoted by $\mathcal{O}^2$ in the corresponding equations.

A general perturbed wave equation can be derived by differentiating Eq. (A.6) with respect to time and substracting the divergence of Eq. (A.5), such that the term $\vec{\nabla} \cdot \frac{\partial \vec{u}'}{\partial t}$ vanishes. This operation can be written, after some rearrangement as:

$$\frac{\partial^2 p'}{\partial t^2} - \vec{\nabla} \cdot \left(\bar{c}^2 \vec{\nabla} p'\right) = \wp \quad , \tag{A.8}$$

with inhomogeneous term $\wp$ on the right hand side. Note that this right hand side has, in general, terms that depend on the pressure and velocity fluctuations up to second order. Because of this, Eq. (A.8) can only be seen as a perturbed form of the wave equation.

For linear acoustics, the second order terms $\mathcal{O}^2$ are left aside. In this case, it can also be shown that the stress tensor and heat flux vector are of second order, too [115]. This leads to a simplified form of the perturbed wave equation based on linearized Euler equations:

$$\frac{\partial^2 p'}{\partial t^2} - \vec{\nabla}\cdot\left(\bar{c}^2\vec{\nabla}p'\right) = -\vec{\bar{u}}\cdot\vec{\nabla}p' - \gamma p'\vec{\nabla}\cdot\vec{\bar{u}} + \gamma\bar{p}\vec{\nabla}\cdot\left[\vec{\bar{u}}\cdot\vec{\nabla}\vec{u}' + \vec{u}'\cdot\vec{\nabla}\vec{\bar{u}}\right] + (\gamma-1)\dot{Q}' \quad . \tag{A.9}$$

Depending on the mean field, this equation can be simplified into the well established wave equations given at the beginning of Sec. 2.2.

A.2 Implications of Sign Convention for Time Dependency

Throughout this thesis, the sign convention

$$p'_{mn} \sim \; e^{+i\Omega t} e^{-ik^{\pm}_{mn}x}$$

is used for the harmonic time and axial dependency. This sign convention is frequently used in control theory and is therefore convenient when stability analysis are intended, because then, the control theory formalism can be adopted.

This decision has implications in the choice of branch for the axial wave numbers. In the hard wall case and for real valued frequencies, the axial wave numbers have two branches (positive $k^{\oplus}_{mn}$ and negative $k^{\ominus}_{mn}$ root) with a common value at the cut-on frequency, see Fig. (A.1) for the first tangential mode. To determine which branch corresponds to the up- and downstream traveling wave, the cut-on condition has to be analyzed. For frequencies below the cut-on value, the waves are evanescent and decay exponentially in the axial direction. Beyond the cut-on frequency, waves start to propagate. Furthermore, the axial wave length of the downstream traveling ones get stretched due to the mean flow.

In the special case of pure real valued frequencies, the direction of propagation is not associated with one of the branches throughout the whole frequency range. Instead, at the cut-on frequency (denoted by a circular marker in the figure) a switch must be imposed:

$$k^{+}_{mn} = \begin{cases} k^{\ominus}_{mn} = \frac{-M\omega/c - \sqrt{(\omega/c)^2 - (\eta_{mn}/R)^2(1-M^2)}}{1-M^2} & \text{if } \omega < \omega^c \;, \\ k^{\oplus}_{mn} = \frac{-M\omega/c + \sqrt{(\omega/c)^2 - (\eta_{mn}/R)^2(1-M^2)}}{1-M^2} & \text{if } \omega \geq \omega^c \;. \end{cases} \tag{A.10}$$

$$k^{-}_{mn} = \begin{cases} k^{\oplus}_{mn} = \frac{-M\omega/c + \sqrt{(\omega/c)^2 - (\eta_{mn}/R)^2(1-M^2)}}{1-M^2} & \text{if } \omega < \omega^c \;, \\ k^{\ominus}_{mn} = \frac{-M\omega/c - \sqrt{(\omega/c)^2 - (\eta_{mn}/R)^2(1-M^2)}}{1-M^2} & \text{if } \omega \geq \omega^c \;. \end{cases} \tag{A.11}$$

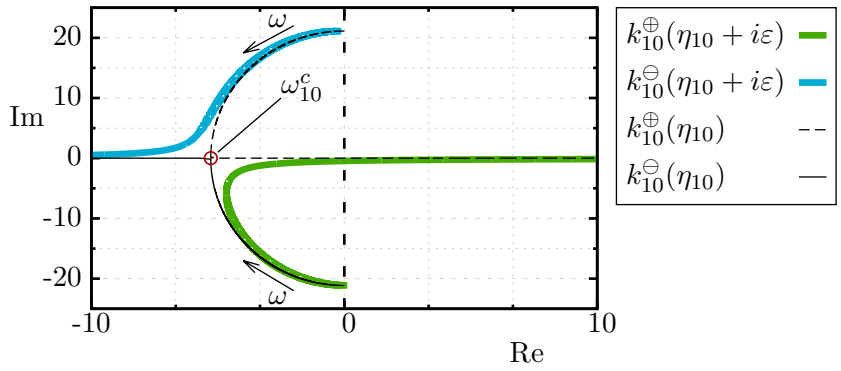

Figure A.1: Two branches of solution of dispersion relation for the hard-wall case, thin lines. Limiting case of soft-wall with complex-valued radial wave number, thick line.

This can be established by building the limiting case of a soft-wall duct with infinitesimal dissipative wall real part of the wall impedance is large and positive (purely real valued reflection coefficient $r \approx 1 - \varepsilon$ and $\varepsilon \ll 1 \;\; \rightarrow Z \approx \infty$). This leads to radial wave numbers α_{mn} close to the hard-wall values but with small positive imaginary part $\alpha_{mn} \approx \eta_{mn} + \varepsilon i$ and $\varepsilon \ll 1$. This case is also plotted in Fig. A.1. For a soft-wall duct, the two branches of the dispersion relation do not cross each other and no discontinuity is exhibited. Thus, up- and downstream traveling waves are associated to one of the branches over the whole frequency range. In the limiting case $\varepsilon \rightarrow 0$ (hard wall), the axial wave numbers of the soft-wall duct would converge towards the expressions given by Eqs. (A.10) and (A.11).

The propagation of waves at complex valued frequencies is similar. In this case, the branches of the dispersion relation do not cross with each other, either. Thus, the up- and downstream traveling waves have to be associated to one of the branches for the whole frequency range and no switch is needed. However, the interpretation of the cut-on condition is difficult, because the imaginary part of the frequency would lead to a growth or decay of the wave amplitudes. An asymptotic analysis similar to the one presented for soft-wall ducts might help in the identification. However, this case is not treated in this work. The Nyquist-plot method employed in the stability analysis evaluates the system only at purely real valued frequencies.

A.3 Relation for the mean properties across a temperature jump

For a temperature jump and assuming ideal gas properties with $p = \rho R_s T$ and $c^2 = \gamma R_s T$, mass conservation can be written for the mean properties as:

$$\rho_c u_c = \rho_h u_h \quad \rightarrow \quad \frac{\rho_c c_c}{\rho_h c_h} = \frac{M_h}{M_c} \equiv \xi \quad . \tag{A.12}$$

Similarly, the momentum conservation can be written as:

$$p_c + \rho_c u_c^2 = p_h + \rho_h u_h^2 \quad \rightarrow \quad \frac{\rho_c c_c^2}{\gamma} + \rho_c c_c^2 M_c^2 = \frac{\rho_h c_h^2}{\gamma} + \rho_c c_h^2 M_h^2 \quad . \tag{A.13}$$

Substitution of the excess temperature $\Xi = (c_h/c_c)^2 - 1 = T_h/T_c - 1$ and the mass conservation into the momentum conservation leads after some rearrangement to the following relation:

$$\Xi = \left[\frac{\xi^2 + \gamma M_h^2}{(1 + \gamma M_h^2)\,\xi}\right]^2 - 1 \quad . \tag{A.14}$$

Thus, for an excess temperature of $\Xi = 12$, and a Mach number on the hot side of $M_h = 0.25$ the ratio of acoustic impedances should be $\xi \approx 3.84$.

For vanishing mach numbers $M_h \ll 1$, the relation can be approximated as:

$$\Xi \approx \xi^2 - 1 \quad \text{or} \qquad \xi \approx \sqrt{\Xi + 1} \quad . \tag{A.15}$$

B Analytical Expression for Laminar Pulsating Flows

B.1 Flow Induced by the Oscillation of an Infinite plate

The flow over an infinite flat plate that oscillates harmonically in its plane along the x direction is a very simple example that indicates some of the important characteristics of pulsating flows. This problem was solved analytically by Stokes, and it is often referred to in literature as Stokes' second problem. Due to the symmetry of the problem no quantities vary with x and the incompressible momentum equation reduces to:

$$\frac{\partial u}{\partial t} = \nu \frac{\partial^2 u}{\partial y^2} \quad , \tag{B.1}$$

with the boundary conditions for the problem:

$$\begin{aligned} u &\to 0 && \text{as} && y \to \infty \quad , \\ u &= a_u \cos(\omega t) && \text{for} && y = 0 \quad , \end{aligned} \tag{B.2}$$

where a_u is the velocity amplitude the plate and ω the oscillating frequency. The solution is based on an harmonic approach for the fluid velocity:

$$u = \hat{u} e^{i\omega t} \quad , \tag{B.3}$$

where a complex notation is used with a complex valued amplitude $\hat{u}$. Substitution of this approach into Eq. (B.1) gives after some rearrangement:

$$\nu \frac{\partial^2 \hat{u}}{\partial y^2} = \frac{i\omega}{\nu} \quad . \tag{B.4}$$

The solution of this equation satisfying the boundary conditions of the problem is given by [125]:

$$\hat{u} = a_u e^{\sqrt{\frac{i\omega}{\nu}} y} = a_u e^{\sqrt{\frac{\omega}{2\nu}} y} e^{i\sqrt{\frac{\omega}{2\nu}} y} \quad , \tag{B.5}$$

where the following identity has been used:

$$\sqrt{i} = \left(e^{i\frac{\pi}{2}}\right)^{0.5} = \frac{1}{\sqrt{2}} + \frac{i}{\sqrt{2}} \quad . \tag{B.6}$$

Using the Stokes' length δ_s to express the amplitude decay in the y direction, the general solution can be finally written as:

$$u = a_u e^{-\frac{y}{\delta_s}} e^{i\frac{y}{\delta_s}} e^{i\omega t} \quad . \tag{B.7}$$

B.2 Pulsating flow, Lighthill approximation

Lighthill was one of the first researchers that studied the response of the boundary layer to fluctuations of small amplitude in the far field flow about a steady mean value [75], that corresponds to laminar pulsating flow. This section summarizes his solution procedure. In the two dimensional case he expresses the flow just outside the boundary layer in the following exponential form:

$$U(x,t) = \bar{U}(x)(1 + \epsilon e^{i\omega t}) \quad , \tag{B.8}$$

where the perturbations are of small order $\epsilon \ll 1$. Note that the unperturbed velocity profile $\bar{U}(x)$ depends on the geometry of the problem. Lighthill studied the pulsating flow past a flat plate (*Blasius layer*) and pulsating flow past a circular cylinder close to its stagnation point (*Hiemanz layer*). He assumes that the boundary layer velocities will perform small harmonic oscillations about a steady mean, too:

$$u(x,t) = \bar{u}(x) + \epsilon \hat{u} e^{i\omega t} \quad , \qquad v(x,t) = \bar{v}(x) + \epsilon \hat{v} e^{i\omega t} \quad , \tag{B.9}$$

however with a possible phase angle compared to the external flow oscillations, and thus, the amplitudes $\hat{u}$ and $\hat{v}$ can be complex valued quantities. Substitution in the boundary layer equations retaining only the first order ϵ terms yields:

$$\frac{\partial \hat{u}}{\partial x} + \frac{\partial \hat{v}}{\partial y} = 0 \quad , \tag{B.10}$$

$$i\omega\hat{u} + \bar{u}\frac{\partial \hat{u}}{\partial x} + \hat{u}\frac{\partial \bar{u}}{\partial x} + \bar{v}\frac{\partial \hat{u}}{\partial y} + \hat{v}\frac{\partial \bar{u}}{\partial y} = i\omega\epsilon\bar{U} + \frac{d}{dx}\left(\epsilon\bar{U}^2\right) + \nu\frac{\partial^2 \hat{u}}{\partial y^2} \quad , \tag{B.11}$$

with the boundary conditions $\hat{u} = \hat{v} = 0$ at the wall $y = 0$ and $\hat{u} \to \epsilon\bar{U}$ far away from the wall $y \to \infty$.

Lighthill solved this problem for two limiting cases defined by the ratio of boundary layer thickness to Stokes' length:

- The *high frequency approximation* is valid for flows with boundary layer thickness much larger than the Stokes' length, $\delta_s \ll \delta$. Following the theory of differential equations with large parameters, only the terms involving ω and the derivative of highest order are retained:

$$i\omega(\hat{u} - \bar{U}) = \nu\frac{\partial^2 \hat{u}}{\partial y^2} \quad . \tag{B.12}$$

  The solution of this equation is:

$$\hat{u} = \epsilon\bar{U}\left(1 - e^{-y\sqrt{\frac{i\omega}{\nu}}}\right) \quad . \tag{B.13}$$

  Applying the identity (B.6) the solution (B.13) can be split into real and imaginary parts $\hat{u} = u_r + iu_i$:

$$u_r = U_0\left[1 - e^{-y/\delta_s}\cos\left(y/\delta_s\right)\right] \quad , \quad u_i = U_0 e^{-y/\delta_s}\sin\left(y/\delta_s\right) \quad . \tag{B.14}$$

The phase lag between the boundary layer velocity and the far field velocity oscillations can be determined from the following expression:

$$\tan(\phi_u) = \frac{\sin(y)}{e^{\delta_s^2}/\delta_s - \cos(y)} \quad . \tag{B.15}$$

The bounds of the phase lag are $\pi/4$ at the wall $y \to 0$ and 0 for $y \to \infty$. This means that in the high frequency regime, the velocity fluctuations in the boundary layer advance always the fluctuations of the external flow.

- The *low frequency* approximation is valid for flows with boundary layer thickness much smaller than the Stokes' length, $\delta_s \gg \delta$. Lighthill splits the solution into a *quasi steady* contribution u_{qs}, which is in phase with the external perturbation, and an out of phase contribution u_{op}:

$$\hat{u} = u_{qs} + i\omega u_{op} \quad . \tag{B.16}$$

The quasi steady contribution represents the functional dependency of $\bar{u}$ to $\bar{U}$, which for small perturbations reads:

$$u_{qs} = \epsilon \bar{U} \frac{\partial \bar{u}}{\partial \bar{U}} \quad . \tag{B.17}$$

For several geometries like the Blasius layer (flat plate) or the Hiemanz-layer (circular cylinder), this dependency can be approximated with good accuracy with polynomial expressions on $\eta = y/\delta$ according to a Karman-Pohlhausen treatment [44]. For the flow past a flat plate, $\bar{U} = const.$ and evolution of the boundary layer flow along the plate is given by the following expressions [75]:

$$\frac{\bar{U}\delta^2}{\nu} = 34x \quad , \tag{B.18}$$

$$\frac{\bar{u}(x)}{\bar{U}} = 1 - (1-\eta)^3 (1+\eta) \quad . \tag{B.19}$$

Substitution of the previous relations into equation (B.11) yields again a partial differential equation for the out of phase contribution u_{op}. The resulting equation can be solved integrating it over the boundary layer thickness using also a polynomial approximation for u_{op} (not shown here).

The low frequency approximation for the pulsating flow past a flat plate, split again in real and imaginary parts, can be finally written as:

$$\begin{aligned} u_r = u_{qs} &= \bar{U}\left[1 - (1-\eta)^2(1-\eta-3\eta^2)\right] \quad , \\ u_i = \omega u_{op} &= 34\omega x (1-\eta)^2 \frac{\eta}{5}\left(\frac{3}{4} - \eta\right) \quad . \end{aligned} \tag{B.20}$$

The components of the skin friction can be determined from the wall normal derivative of the velocity components:

$$\begin{aligned} \tau_{w,qs} &\sim \left.\frac{\partial u_{qs}}{\partial y}\right|_{y=0} = 3\bar{U} \quad , \\ \tau_{w,op} &\sim \omega \left.\frac{\partial u_{op}}{\partial y}\right|_{y=0} = \frac{51}{10}\omega x \quad . \end{aligned} \tag{B.21}$$

The phase lag of the skin friction in this low frequency approximation can be determined from the following expression:

$$\tan(\phi_{\tau_w}) = \frac{\tau_{w,op}}{\tau_{w,qs}} = \frac{17}{10}\frac{\omega x}{\bar{U}} \quad . \tag{B.22}$$

C Computational Fluid Dynamics

C.1 Incompressible turbulent channel flow with heat transfer and constant properties

C.1.1 Very low Reynolds number

A stationary case without pulsation is computed and compared against the DNS results of Iida et al. [60]. The flow is a fully developed, incompressible turbulent channel flow at low Mach number and constant fluid properties. The flow is driven by an homogeneous momentum source term, while bottom and top walls are kept at constant but different temperatures $T_H > T_C$, see Sec. 6.2.1. Table C.1 summarizes the relevant non-dimensional parameters of the test case.

Table C.1: Turbulent channel flow with heat transfer validation case: flow parameters.

	Approach	Re_τ	Nu	Pr
Iida et al.	DNS (spectral)	150	13.4	0.71
Present simulation	LES (dyn. TKE)	150	4.5	0.71

Details about the chosen mesh parameters are given in Tab. C.2. Two grid resolutions are compared. The channel half-height h is taken as the reference length. The mesh resolution in the wall normal direction follows a stretching function in order to fully resolve the boundary layer, while in the streamwise and spanwise direction the resolution is homogeneous. The distribution of the grid points in the wall normal direction are given according to the function:

$$y_j = h\left[1 + \frac{\tanh(\beta(j/N_y - 0.5))}{\tanh(0.5\beta)}\right] \quad , \tag{C.1}$$

where y_j corresponds to the coordinate of the cell nodes.

Table C.2: Turbulent channel flow with heat transfer validation case: Grid details.

	Domain size $(L_x \times L_y \times L_z)$	Number of cells $(N_x \times N_y \times N_z)$	Stretching factor β
Mesh A	$2\pi h \times 2h \times \pi h$	$64 \times 64 \times 64$	2
Mesh B	$2\pi h \times 2h \times \pi h$	$32 \times 32 \times 32$	5

The streamwise component of the velocity is initialized with a parabolic profile. A sinusoidal perturbation is superimposed to all components of the velocity. For the temperature, a linear profile in the wall normal direction is used. Since the flow is

treated as incompressible, only pressure differences are of interest. For accuracy reasons the pressure is initialized as $P_0 = 0Pa$. The averaging procedure is started after a time frame that equals almost 300 FTT[1], during which the transition to the turbulent state takes place. The time averaging is performed for almost 150 FTT, while one sample is acquired each time steps. Furthermore, to improve the statistics, spatial averaging in the stream- and spanwise direction is performed, see Sec. 6.2.4.

The results of the comparison are plotted in Fig. C.1 to C.2 for the average velocity and temperature, Reynolds stresses and temperature fluctuations respectively. For the fine mesh A, the agreement between the LES and the DNS data is very good.

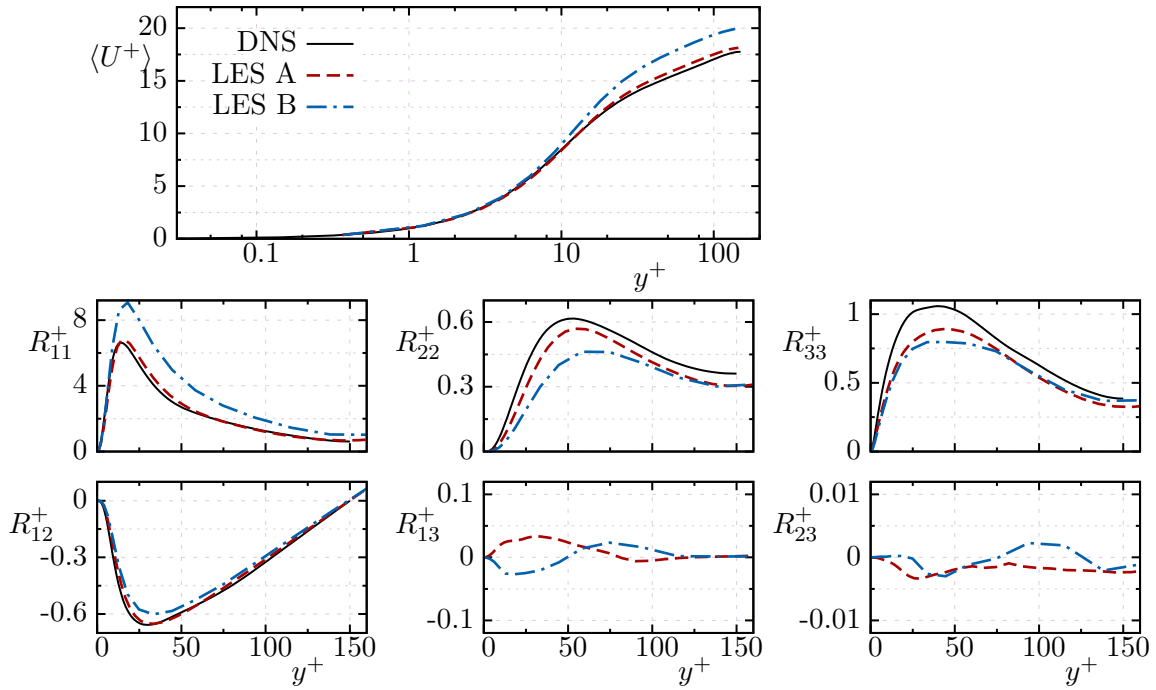

Figure C.1: Mean streamwise velocity and average Reynolds stresses $R_{ij}^+ = \langle \overline{u_i' u_j'} \rangle / u_\tau^2$ in wall units. DNS data reproduced from data basis available from [60]

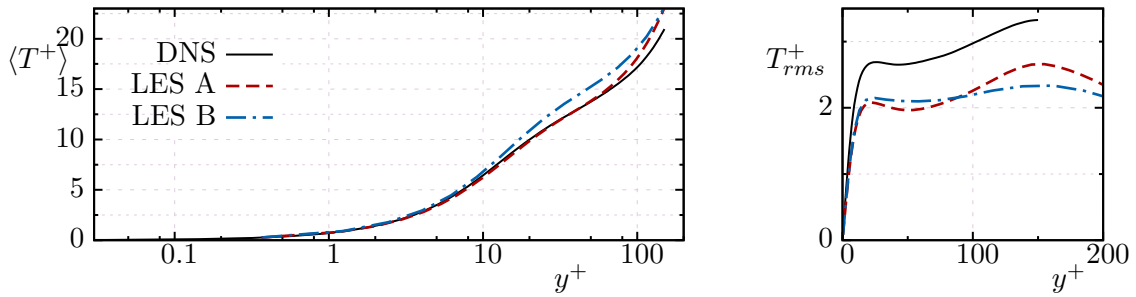

Figure C.2: Mean and fluctuations of Temperature in wall units. DNS data reproduced from data basis available from [60].

[1] Flow-through time: time it takes to cross the computational domain at the bulk velocity.

C.1.2 Moderate Reynolds number

For the validation at moderate turbulent Reynolds numbers, data from Debusschere and Rutland [26] has been used. They studied the turbulent transport of scalars in channel flow at $\mathrm{Re}_\tau = 186$.

For this validation, the same set-up as in App. C.1.1 has been used. However, the momentum source term is increased leading to a trubulent Reynolds number of $\mathrm{Re}_\tau = 180$. Only one simulation using the mesh A described in Tab. C.2 has been computed. The comparison of the results is given in Figs. C.3 to C.4.

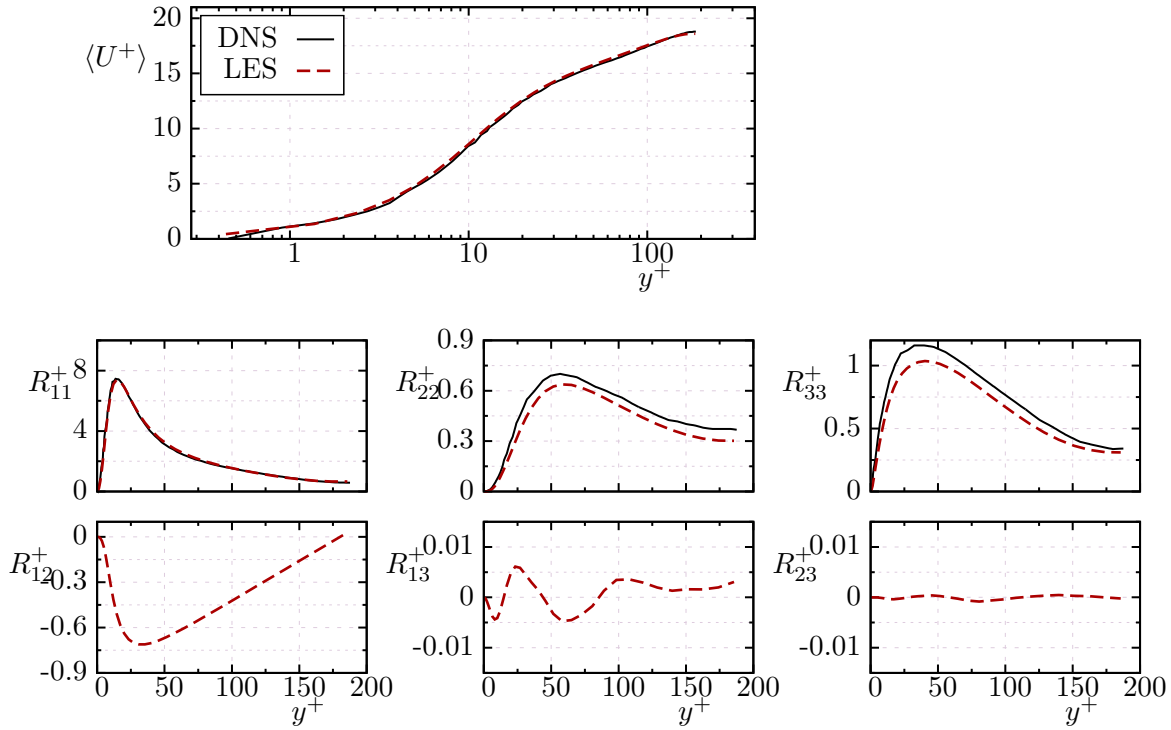

Figure C.3: Mean streamwise velocity and average Reynolds stresses $R_{ij}^+ = \langle \overline{u_i' u_j'} \rangle / u_\tau^2$ in wall units. DNS data taken from [26].

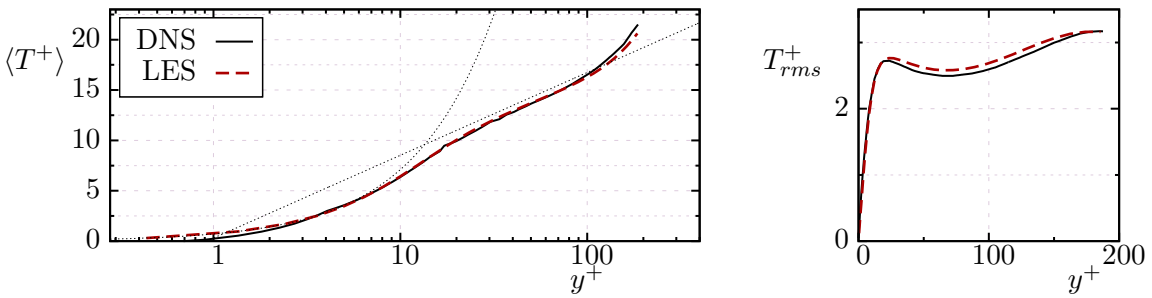

Figure C.4: Mean temperature and temperature fluctuations in wall units. DNS data taken from [26].

C.2 Weakly Compressible Turbulent Channel Flow

To validate the implementation of the dynamic One-Equation subgrid scale model for the weakly compressible case, a reference case has been computed and compared against data available from the literature. The case studied by Lessani and Papalexandris [74] is used for this validation corresponding to an open channel flow with considerable heat transfer. The flow is driven as usual by an homogeneous momentum source term. Table C.3 gives an overview of the test case parameters used in the simulations. Due to the temperature dependent properties, the turbulent Reynolds and Nusselt number differ for cold bottom and hot top wall. Reynolds and Nusselt numbers of the two studies are very similar.

Table C.3: Turbulent channel flow with heat transfer validation case: Grid details.

	T_h/T_c	$\mathrm{Re}_{\tau c}$	$\mathrm{Re}_{\tau h}$	Nu_c	Nu_h	μ/μ_{ref}	T_s/T_{ref}	Pr	Pr_t
LP	2	224.1	91.2	6.45	3.94	$\left(\frac{T}{T_{\mathrm{ref}}}\right)^{0.7}$	—	0.8	0.9
CAR	2	212.7	85.6	5.92	3.63	$\left[\frac{T_{\mathrm{ref}}-T_s}{T+T_s}\right]\left(\frac{T}{T_{\mathrm{ref}}}\right)^{1.5}$	0.368	0.71	dyn.

For variable density flows, the van Driest velocity transformation is usually employed in an attempt to collapse the velocity profiles into the classical law of the wall. Using the notation of Huang and Coleman [54], the transformation can be expressed as:

$$u^+_{\mathrm{vD}} = \int_0^{u^+} \left(\frac{\rho}{\rho_w}\right)^{1/2} du^+ \approx \frac{1}{R}\left[\arcsin\left(\frac{R(u^+ + H)}{D} - \arcsin\left(\frac{RH}{D}\right)\right)\right] \quad , \tag{C.2}$$

where the index $_w$ denotes values at the wall temperature and the following substitutions are used:

$$M_\tau = \frac{u_\tau}{\sqrt{(\gamma-1)c_p T_w}} \quad , \quad B_q = \frac{\dot{q}_w}{\rho_w c_p u_\tau T_w} \quad ,$$
$$R = M_\tau\sqrt{(\gamma-1)\frac{\mathrm{Pr}_t}{2}} \quad , \quad H = \frac{B_q}{(\gamma-1)M_\tau^2} \quad , \quad D = \sqrt{1+R^2H^2} \quad . \tag{C.3}$$

Figure C.5 shows the comparison of the present LES results against the data of Lessani and Papalexandris for the velocity profiles. The flow field is considerably different at the two walls, in accordance to the Reynolds numbers listed in Tab. C.3. On the hot side, the flow field has a very low Reynolds number and the logarithmic sublayer can not really be observed. In contrast, the cold side is turbulent clearly developing the logarithmic sublayer. The agreement between the two studies is much better on the hot side. This leads to the conclusion that the mesh used in the simulation was too coarse in order to adequately resolve the sublayer on the cold side (lower viscosity leads to higher turbulent Reynolds numbers). Nevertheless, concerning the thermal boundary layer, the agreement is very good.

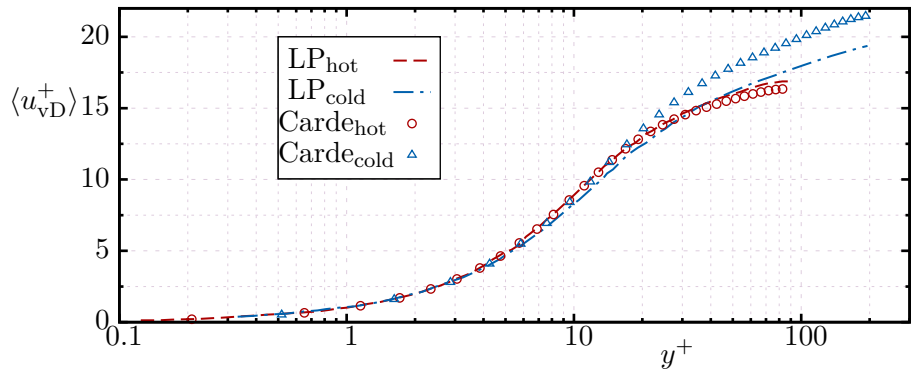

Figure C.5: Mean velocity using the van Driest transformation in wall units. LP taken from [74].

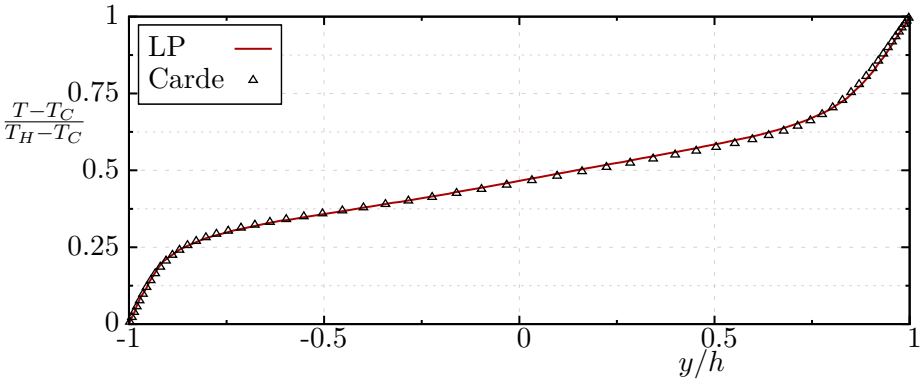

Figure C.6: Non-dimensionalized temperature across the channel height. LP taken from [74].

List of Figures

List of Tables

Supervised Theses

Im Rahmen dieser Dissertation entstanden am Lehrstuhl für Thermodynamik in den Jahren 2009 bis 2012 unter wesentlicher wissenschaftlicher, fachlicher und inhaltlicher Anleitung des Autors die im Folgenden aufgeführten studentischen Arbeiten. Ergebnisse aus diesen Arbeiten können in Teilen in das vorliegende Dokument eingeflossen sein. Der Autor dankt hiermit nochmals explizit allen ehemals betreuten Studenten für ihr Engagement bei der Unterstützung dieser wissenschaftlichen Arbeit.

Associated with this Ph.D. thesis are a number of *student theses* (Semesterarbeiten, Diplomarbeiten, Bachelor theses, or Master theses) that were supervised by the author of the present work. These theses were prepared at the Lehrstuhl für Thermodynamik in the years 2009 through 2012 under the close supervision of the present author in its full academical and professional breadth. Under certain circumstances, parts of those supervised theses may have been incorporated into the present thesis. Finally, the author would like to express his sincere gratitude to all formerly supervised students for their commitment supporting this research project.

Student	**Thesis**
Matthias Plank	*Implementierung eines CFD Codes für inkompressible Strömungen mit veränderlichen Stoffparametern in OpenFoam*, (in German), Semesterarbeit, filed in December 6th, 2010.
Thomas Emmert	*Untersuchung der Fluid-Struktur-Interaktion periodisch instationnärer Strömungen in Bezug auf Wärmeübergang* (in German), Diplomarbeit, filed in Mai 26th, 2011.
Christoph Kunzer	*Untersuchung der numerischen Eigenschaften unterschiedlichen Diskretisierungsschemata in OpenFoam* (in German), Semesterarbeit, filed in December 9th, 2011.

References

[1] Astrium. URL `cs.astrium.eads.net`. Stand 2014.

[2] The OpenFOAM Foundation. URL `www.openfoam.org`. Stand 2014.

[3] Sonderforschungsbereich Transregio 40, SFBTRR40. URL `www.sfbtr40.de`. Stand 2014.

[4] T. Acker and C.E. Mitchell. Combustion Zone-Acoustic Cavity Interactions in Rocket Combustors. *Journal of Propulsion and Power*, 10(2):235–243, 1994.

[5] J.S. Alonso and R.A. Burdisso. Eigenvalue Solution of the Convected Wave Equation in a Circular Soft Wall Duct. *Journal of Sound and Vibration*, 315:1003–1015, 2008. doi: 10.1016/j.jsv.2008.02.006.

[6] V.S. Arpaci, J.E. Dec, and J.O. Keller. Heat Transfer in Pulse Combustor Tailpipes. *Combustion Science and Technology*, 94(1-6):131–146, 1993. doi: 10.1080/00102209308935307.

[7] S. Bade, M. Wagner, C. Hirsch, T. Sattelmayer, and B. Schuermans. Design for Thermo-Acoustic Stability: Modeling of Burner And Flame Dynamics. *Journal of Engineering Gas Turbines and Power*, 135(11):111502–1–7, 2013. doi: 10.1115/GT2013-95058.

[8] H.D. Baehr and K. Stephan. *Heat and Mass Transfer*. Springer-Verlag Berlin Heidelberg, second edition, 2006. doi: ISBN-103-540-29526-7.

[9] W.A. Bell and B.T. Zinn. The Prediction of Three-Dimensional Liquid-Propellant Rocket Nozzle Admittances. Technical Report NASA CR-121129, Georgia Institute of Technology, 1973.

[10] D.W. Bogdanoff. *A Study of the Mechanisms of Heat Transfer in Oscillating Flows*. PhD thesis, Princeton University, Department of Aerospace and Mechanical Sciences, Princeton, New Jersey, October 1967.

[11] I.N. Bronstein and K.A. Semendjajew. *Taschenbuch der Mathematik*. Verlag Harry Deutsch Thun, Frankfurt am Main, 1989.

[12] A. Cárdenas Miranda and W. Polifke. Effects of Temperature Inhomogeneity on the Damping Characteristics of Quarter Wave Resonator Rings. Technical report, SFB/TRR 40, Annual Report, pages 41–54, November 2010. URL `http://www.sfbtr40.de/images/stories/annualreport2010/a3-effects.pdf`.

[13] A. Cárdenas Miranda and W. Polifke. Damping Characteristics of Resonator Rings with Application to Low Order Stability Prediction of Rocket Thrust Chambers. In *4th European Conference for Aerospace Sciences, St. Petersburg, Russia*, Juli 2011.

[14] A. Cárdenas Miranda and W. Polifke. Study of Enhanced Heat Transfer in Generic Configurations of Pulsating Flow. Technical report, SFB/TRR 40, Annual Report, pages 31–42, 2011. URL `http://www.sfbtr40.de/images/stories/annualreport2011/a3-study.pdf`.

[15] A. Cárdenas Miranda and W. Polifke. Enhanced Heat Transfer in Laminar Pulsating Flow Past a Flat Plate. In *9th International Conference on Heat Transfer, Fluid Mechanics and Thermodynamics HEFAT 2012*, pages 1112–1119. HEFAT, Juli 2012.

[16] A. Cárdenas Miranda and W. Polifke. On the Reflection, Transmission, Coupling and Damping of Non-Plane Acoustic Modes by Resonator Rings. Technical report, SFB-TRR 40, Annual Report, pages 29–40, November 2012. URL `http://www.sfbtr40.de/images/stories/annualreport2012/a3.pdf`.

[17] A. Cárdenas Miranda and W. Polifke. On the Reflection, Transmission, Coupling and Damping of Non-Plane Acoustic Modes by Resonator Rings. In *Proc. 5th European Conference for Aeronautics and Space Sciences, Munich, Germany*, 2013.

[18] A. Cárdenas Miranda and W. Polifke. Combustion Stability Analysis of Rocket Engines with Resonators Based on Nyquist Plots. *Journal of Propulsion and Power*, 30(4):962–977, July 2014. doi: 10.2514/1.B35149.

[19] M.Ö. Çarpinlioğlu and M.Y. Gündoğdu. A Critical Review on Pulsatile Pipe Flow Studies Directing Towards Future Research Topics. *Flow Measurement and Instrumentation*, 12(3):163–174, 2001. doi: 10.1016/S0955-5986(01)00020-6.

[20] X. Chai and K. Mahesh. Dynamic k-Equation Model for Large-Eddy Simulation of Compressible Flows. *Journal of Fluid Mechanics*, 699:385–413, 2012. doi: 10.1017/jfm.2012.115.

[21] T. Colonius and S.K. Lele. Computational Aeroacoustics: Progress on Nonlinear Problems of Sound Generation. *Progress in Aerospace Sciences*, 40(6):345–416, 2004. doi: 10.1016/j.paerosci.2004.09.001.

[22] B. Ćosić, T.G. Reichel, and C.O. Paschereit. Acoustic Response of a Helmholtz Resonator Exposed to Hot-Gas Penetration and High Amplitudes Oscillations. *Journal of Engineering Gas Turbines and Power*, 134(10):1–9, 2012. doi: 10.1115/1.4007024.

[23] L. Crocco. Aspects of Combustion Instability in Liquid Propellant Rocket Motors Part2: High Frequency Instabillity. *Journal of American Rocket Society*, 1:7–16, 1952.

[24] F.E.C. Culick. Combustion Instabilities in Liquid-Fueled Propulsion Systems - An Overview. In *Proc. of the 72B Specialists' Meeting of the Propulsion and*

Energetics Panel, number 450, pages 1–74, 7 Rue Ancelle 92200 Neuilly Sur Seine France, 1988. AGARD.

[25] F.E.C. Culick and . Yang. Overview of Combustion Instabilities in Liquid-Propellant Rocket Engines. Technical report, AIAA, 1995.

[26] B. Debusschere and C.J. Rutland. Turbulent Scalar Transport Mechanisms in Plane Channel and Couette Flows. *International Journal of Heat and Mass Transfer*, 47(8–9):1771–1781, 2004. doi: 10.1016/j.ijheatmasstransfer.2003.10.031.

[27] J.E. Dec and J.O. Keller. Pulse Combustor Tail-Pipe Heat-Transfer Dependence on Frequency, Amplitude, and Mean Flow Rate. *Combustion and Flame*, 77(3–4): 359–374, 1989. doi: 10.1016/0010-2180(89)90141-7.

[28] J.E. Dec and J.O. Keller. Time-Resolved Gas Temperatures in the Oscillating Turbulent Flow of a Pulse Combustor Tail Pipe. *Combustion and Flame*, 80(3-4): 358–370, 1990. doi: 10.1016/0010-2180(90)90112-5.

[29] J.E. Dec, J.O. Keller, and V.S. Arpaci. Heat transfer enhancement in the oscillating turbulent flow of a pulse combustor tail pipe. *International Journal of Heat and Mass Transfer*, 35(9):2311–2325, 1992. doi: http://dx.doi.org/10.1016/0017-9310(92)90074-3.

[30] J.D. Eldredge. On the Interaction of Higher Duct Modes with a Perforated Liner System with Bias Flow. *Journal of Fluid Mechanics*, 510:303–331, 2004. doi: 10.1017/S0022112004009504.

[31] T. Emmert. Untersuchung der Fluid-Struktur-Interaktion periodisch instationnärer Strömungen in Bezug auf Wärmeübergang. Diplomarbeit, Lehrstuhl für Thermodynamik der Technischen Universität München, Mai 2011.

[32] T. Emmert, A. Cárdenas, and W. Polifke. Low-Order Analysis of Conjugate Heat Transfer in Pulsating Flow with Fluctuating Temperature. *Journal of Physics: Conference Series*, 395(1):012040, 2012. doi: 10.1088/1742-6596/395/1/012040.

[33] S. Evesque and W. Polifke. Low-Order Acoustic Modeling for Annular Combustors: Validation and Inclusion of Modal Coupling. In *Proc. ASME Turbo Expo 2002*, number GT-2002-30064, page 11, Amsterdam, NL, June 2002. ASME.

[34] J.H. Ferziger and M. Perić. *Computational Methods for Fluid Dynamics*. Berlin Springer, third edition, 1996.

[35] K. Förner, A. Cárdenas Miranda, and W. Polifke. Mapping the Influence of AAcoustic Resonators on Rocket Engine Combustion Stability. Technical report, SFB-TRR 40, Annual Report, pages 33–45, 2013.

[36] C. Fureby. On Subgrid Scale Modeling in Large Eddy Simulations of Compressible Fluid Flow. *Physics of Fluids*, 8(5):1301–1311, 1996. doi: 10.1063/1.868900.

[37] C. Fureby, G. Tabor, H.G. Weller, and A.D. Gosman. A Comparative Study of Subgrid Scale Models in Homogeneous Isotropic Turbulence. *Physics of Fluids*, 9(5):1416–1429, May 1997. doi: 10.1063/1.869254.

[38] G. Gabard. Mode-Matching Techniques for Sound Propagation in Lined Ducts with Flow. In *Proc. 16th AIAA/CEAS Aeroacoustic Conference*, number AIAA 2010-3940, pages 1–12. AIAA, 2010.

[39] G. Gabard and R.J. Astley. A Computational Mode-Matching Approach for Sound Propagation in Three-Dimensional Ducts with Flow. *Journal of Sound and Vibration*, 315(4):1103–1124, Feb 2008. doi: http://dx.doi.org/10.1016/j.bbr.2011.03.031.

[40] G.D. Garrison, A.C. Schnell, C.D. Baldwin, and P.R. Russell. Suppression of Combustion Oscillations with Mechanical Damping Devices. Interim Report PWA FR-3299, Pratt & Whitney Aircraft, Box 2691, West Palm Beach, Florida 33402, 1969.

[41] M. Germano, U. Piomelli, P. Moin, and W.H. Cabot. A Dynamic Subgrid Scale Eddy Viscosity Model. *Physics of Fluids A Fluid Dynamics*, 3(7):1760–1765, 1991. doi: 10.1063/1.857955.

[42] J. Gikadi, T. Sattelmayer, and A. Peschiulli. Effects of the Mean Flow Field on the Thermo-Acoustic Stability of Aero-Engine Combustion Chambers. In *ASME Turbo Expo 2012*, number No. GT2012-69612, Copenhagen, DK, 2012.

[43] J. Gikadi, M. Schulze, S. Föller, J. Schwing, and T. Sattelmayer. Linearized Navier-Stokes and Euler Equations for the Determination of the Acoustic Scattering Behaviour of an Area Expansion. In *18th AIAA/CEAS Conference*, number AIAA2012-2292, Colorado Springs, June 4-6 2012.

[44] S. Goldstein. *Modern developments in fluid mechanics, Vol. I.* Oxford at the Claredon Press, 1950.

[45] M.Y. Gündoğdu and M.Ö. Çarpinlioğlu. Present State of Art on Pulsatile Flow Theory (Part 1: Laminar and Transitional Flow Regimes). *JSME International Journal. Series B, Fluids and Thermal Engineering*, 42(3):384–397, 1999.

[46] M.Y. Gündoğdu and M.Ö. Çarpinlioğlu. Present State of Art on Pulsatile Flow Theory (Part 2: Turbulent Flow Regime). *JSME Iinternational Journal. Series B, Fluids and Thermal Engineering*, 42(3):398–410, 1999.

[47] M.A. Habib, A.M. Attya, A.I. Eid, and A.Z. Aly. Convective Heat Transfer Characteristics of Laminar Pulsating Pipe Air Flow. *Heat and Mass Transfer*, 38 (3):221–232, 2002. doi: 10.1007/s002310100206.

[48] M. Habiballah, D. Lourme, and F. Pit. PHEDRE - Numerical Model for Combustion Stability Studies Applied to the Ariane Viking Engine. *Journal of Propulsion and Power*, 7(3):332–329, 1991. doi: 10.2514/3.23330.

[49] D.T. Harrje. *Liquid Propellant Rocket Combustion Instability.* NASA. SP-194.

[50] D.T. Harrje. Heat Transfer in oscillating Flow, Final Report. Technical Report 483-g, Princeton University, Department of Aerospace and Mechanical Sciences, Oct 1967.

[51] H.M. Hemida, M.N. Sabry, A. Abdel-Rahim, and H. Mansour. Theoretical analysis of heat transfer in laminar pulsating flow. *International Journal of Heat and Mass Transfer*, 45(8):1767 – 1780, 2002. doi: 10.1016/S0017-9310(01)00274-5.

[52] A.S. Hersh, B.E. Walker, and J.W. Celano. Helmholtz Resonator Impedance Model, Part 1: Nonlinear Behavior. *AIAA Journal*, 41(5):795–808, May 2003. doi: 10.2514/2.2041.

[53] K. Horiuti. Large Eddy Simulation of Turbulent Channel Flow by One-Equation Modeling. *Journal of the Physical Society of Japan*, 54(8):2855–2865, 1985. doi: 10.1143/JPSJ.54.2855.

[54] P.G. Huang and G.N. Coleman. Van Driest Transformation and Compressible Wall-Bounded Flows. *AIAA Journal*, 32(10):2110–2113, 1994. doi: 10.2514/3.12259.

[55] U. Ingard. On the Theory and Design of Acoustic Resonators. *Journal of Acoustical Society of America*, 25:10–37, 1953. doi: 10.1121/1.1907235.

[56] R.I. Issa. Solution of the Implicitly Discretised Fluid Flow Equations by Operator-Splitting. *Journal of Computational Physics*, 62(1):40–65, 1986. doi: 10.1016/0021-9991(86)90099-9.

[57] H. Jasak. *Error Analysis and Estimation for the Finite Volume Method with Applications to Fluid Flows*. PhD thesis, University of London, 1996.

[58] B.A. Kader. Temperature and Concentration Profiles in Fully Turbulent Boundary Layers. *International Journal of Heat and Mass Transfer*, 24(9):1541–1544, 1981.

[59] R. Kaess. *Thermoacoustic Stability Analysis from Open Loop Transfer Functions Based on LES*. PhD thesis, Technische Universität München, Lehrstuhl für Thermodynamik, 2010.

[60] N. Kasagi and O. Iida. Progress in Direct Numerical Simulation of Turbulent Heat Transfer. In *5th ASME/JSME Joint Thermal Engineering Conference*, San Diego, California, March 15-19 1999.

[61] R. Kathan. *Verlustmechanismen in Raketenbrennkammern*. PhD thesis, Technische Universität München, Lehrstuhl für Thermodynamik, 2013. ISBN 978-3-8439-1140-5.

[62] W.M. Kays and M.E. Crawford. *Convective Heat and Mass Transfer*. Number ISBN 0-07-033457-9 in Series in Mechanical Engineering. McGraw-Hill, second edition, 1980.

[63] J.J. Keller. Thermoacoustic Oscillations in Combustion Chambers of Gas Turbines. *AIA Journal*, 33(12):2280–2287, Dec 1995. doi: 10.2514/3.12980.

[64] J.J. Keller and E. Zauner. On the Use of Helmholtz Resonators as Sound Attenuators. *Zeitschrift für angewandte Mathematik und Physik ZAMP*, 46(3):297–327, 1995. doi: 10.1007/BF01003552.

[65] S.H. Ko. Sound Attenuation in Acoustic Lined Circular Ducts in the Presence of Uniform Flow and Shear Flow. *Journal of Sound and Vibration*, 22(2):193–210, 1972.

[66] J. Kopitz and W. Polifke. CFD-Based Application of the Nyquist Criterion to Thermo-Acoustic Instabilities. *Journal of Computational Physics*, 227(14):6754–6778, July 2008. ISSN 0021-9991. doi: 10.1016/j.jcp.2008.03.022.

[67] J. Kopitz, A. Huber, T. Sattelmayer, and W. Polifke. Thermoacoustic Stability Analysis of an Annular Combustion Chamber with Acoustic Low Order Modeling and Validation Against Experiment. In *Proc. of ASME Turbo Expo 2005 Power for Land, Sea and Air*, number GT2005-68797, page 11, Reno-Tahoe, Nevada, USA, June 6-9 2005. ASME.

[68] B.M. Kumar and R.I. Sijith. Exact Solution for One-Dimensional Acoustic Fields in Ducts with Polynomial Mean Temperature Profiles. *Journal of Vibration and Acoustics*, 120(4):965–969, 1998. doi: 10.1115/1.2893927.

[69] C. Kunzer. Untersuchung der Numerischen Eigenschaften Unnterschiedlichen Diskretisierungsschemata in OpenFOAM. Semesterarbeit, Lehrstuhl für Thermodynamik der Technischen Universität München, Dez 2011.

[70] E. Laudien, R. Pongratz, R. Pierro, and D. Preclik. Experimental Procedures Aiding the Design of Acoustic Cavities. *Progress in Astronautics and Aeronautics*, 96:377–399, 1995. doi: 10.2514/5.9781600866371.0377.0399.

[71] T.R. Law, A.P. Dowling, and R. Corral. Optimisation of Axially Segmented Liners for Aeroengine Broadband Noise. *Journal of Sound and Vibration*, 329 (21):4367–4379, 2010. doi: 10.1016/j.jsv.2010.04.029.

[72] R. Leandro, A. Huber, and W. Polifke. taX - a Low-Order Modeling Tool for Thermo- and Aero-Acoustic Instabilities. Technical report, Lehrstuhl für Thermodynamik, TU-München, 2010. URL `http://www.td.mw.tum.de/tum-td/de/forschung/infrastruktur/scientific_comp`.

[73] E.W. Lemmon, M.O. McLinden, and D.G. Friend. Thermophysical Properties of Fluid Systems. NIST Chemistry WebBook. Technical report, National Institute of Standards and Technology, 2005. URL `http://webbook.nist.gov`.

[74] B. Lessani and M.V. Papalexandris. Time-Accurate Calculation of Variable Density Flows with StrongTemperature Gradients and Combustion. *Journal of Computational Physics*, 212(1):218–246, 2006. doi: 10.1016/j.jcp.2005.07.001.

[75] M. J. Lighthill. The Response of Laminar Skin Friction and Heat Transfer to Fluctuations in the Stream Velocity. *Proceedings of the Royal Society of London. Series A. Mathematical and Physical Sciences*, 224(1156):1–23, 1954. doi: 10.1098/rspa.1954.0137.

[76] D.K. Lilly. A Proposed Modification of the Germano Subgrid Scale Closure Method. *Physics of Fluids A: Fluid Dynamics*, 4(3):633–635, 1992. doi: 10.1063/1.858280.

[77] A.V Luikov. Conjugate Convective Heat Transfer Problems. *International Journal of Heat and Mass Transfer*, 17(2):257–265, 1974. doi: 10.1016/0017-9310(74)90087-8.

[78] B. Lundgren, U. Marksten, and A. Holst. Enhanced Heat Transfer in an Oscillating Pipe Flow. In *6th ASME-JSME Themal Engineering Joint Conference*, March 16-20 2003.

[79] R. Mathie and C.N. Markides. Heat transfer Augmentation in Unsteady Conjugate Thermal Systems – Part I: Semi-Analytical 1-D Framework. *International Journal of Heat and Mass Transfer*, 56(1–2):802 –818, 2013. doi: 10.1016/j.ijheatmasstransfer.2012.08.023.

[80] J. Matthews and R.L. Walker. *Mathematical Methods of Physics*. WA Benjamin, 2nd edition, 1970.

[81] A. McAlpine, R.J. Astley, V.J.T. Hii, N.J. Baker, and A.J. Kempton. Acosutic Scattering by an Axially-Segmented Turbofan Inlet Duct Liner at Supersonic Fan Speeds. *Journal of Sound and Vibration*, 294:780–806, 2006. doi: 10.1016/j.jsv.2005.12.039.

[82] C.E. Mitchell. Stability of Combustors with Partial Length Acoustic Liners. *Combustion Science and Technology*, 6(1):61–70, 1972. doi: 10.1080/00102207208952305.

[83] P. Moin, K. Squires, W. Cabot, and S. Lee. A Dynamic Subgrid-Scale Model for Compressible Turbulence and Scalar Transport. *Physics of Fluids A*, 3(11):2746–2757, 1991. doi: 10.1063/1.858164.

[84] C.L. Morfey. Rotating Pressure Patterns in Ducts: Their Generation and Transmission. *Journal of Sound and Vibration*, 1:60–87, 1964.

[85] C.L. Morfey. Sound Transmission and Generation in Ducts with Flow. *Journal of Sound and Vibration*, 14(1):37–55, 1971.

[86] D. Morgenweck, T. Sattelmayer, F. Fassl, and R. Kaess. Influence of Scaling Rules on the Loss of Acoustic Energy. *Journal of Spacecraft and Rockets*, 48(3):498–506, 2011.

[87] M. Möser. *Engineering Acoustics an Introduction to Noise Control*. Springer-Verlag, 2004.

[88] M.L. Munjal. *Acoustics of Ducts and Mufflers*. John Wiley & Sons, 1987.

[89] M.K. Myers. On the Acoustic Boundary Condition in the Presence of Flow. *Journal of Sound and Vibration*, 71(3):429–434, 1980.

[90] U. Neunert. *Thermoakustische Stabilität einer Reisemobilheizung*. PhD thesis, Technische Universität München, Lehrstuhl für Thermodynamik, 2009.

[91] F. Nicoud, L. Benoit, C. Sensiau, and T. Poinsot. Acoustic Modes in Combustors with Complex Impedances and Multidimensional Active Flames. *AIAA Journal*, 45(2):426–441, Feb. 2007. doi: 10.2514/1.24933.

[92] F.C. Nicoud. Numerical Study of a Channel Flow with Variable Properties. Technical report, Center of Turbulent Research, 1998.

[93] C.L. Oberg. Combustion Stabilization with Acoustic Cavities. *Journal of Spacecraft and Rockets*, 8(12):1220–1225, 1971.

[94] C.L. Oberg, T.L. Wong, and W.M. Ford. Evaluation of Acoustic Cavities for Combustion Stabilization. Final Report CR-115087, NASA, July 1971.

[95] M. Oschwald and Z. Faragó. Acoustics of Rocket Combustors Equipped with Absorber Rings. In *Proc. 44th Joint Propulsion Conference*, number AIAA 2008-5112, page 10, Hartford, CT, July 2008. AIAA.

[96] M. Oschwald, Z. Faragó, G. Searby, and F. Cheuret. Resonance Frequencies and Damping of a Combustor Acoustically Coupled to an Absorber. *Journal of Propulsion and Power*, 24(3):524–533, 2008. doi: 10.2514/1.32313.

[97] R.L. Panton. *Incompressible Flow*. Number ISBN 0-471-89765-5. John Wiley & Sons, 1984.

[98] R.L. Paton and J.M. Miller. Resonant Frequencies of Cylindrical Helmholtz Resonators. *Journal Acoustical Society of America*, 57(6):1533–1535, Jnue 1975.

[99] E.H. Perry and F.E.C. Culick. Measurements of Wall Heat Transfer in the Presence of Large-Amplitude Combustion-Driven Oscillations. *Combustion Science and Technology*, 9(1-2):49–53, 1974. doi: 10.1080/00102207408960336.

[100] J. Pieringer. *Simulation selbsterregter Verbrennungsschwingungen in Raketenschubkammern in Zeitbereich*. PhD thesis, Technische Universität München, Lehrstuhl für Thermodynamik, 2008.

[101] J. Pieringer, T. Sattelmayer, and F. Fassl. Simulatioon of Combustion Instabilities in Liquid Rocket Engines with Acoustic Perturbation Equations. *Journal of Propulsion and Power*, 25(5):1020–1031, September-October 2009. doi: 10.2514/1.38782.

[102] M. Plank. Implementierung eines CFD Codes für Inkompressible Strömungen mit Veränderlichen Stoffparametern in OpenFOAM. Semesterarbeit, Lehrstuhl für Thermodynamik der Technischen Universität München, Dez 2010.

[103] T. Poinsot and D. Veynante. *Theoretical and Numerical Combustion*. Aquaprint, third edition. doi: ISBN978-2-7466-3990-4.

[104] W. Polifke. Low-Order Analysis Tools for Aero- and Thermo-Acoustic Instabilities. In C. Schram, editor, *Advances in Aero-Acoustics and Thermo-Acoustics*, number ISBN-13 978-2-87516-012-6 in VKI LS 2011-01. Von Karman Institute, Rhode-St-Genèse, BE, 2011.

[105] W. Polifke and J. Kopitz. *Wärmeübertragung: Grundlagen, analytische und numerische Methoden*. Pearson Deutschland GmbH, 2009.

[106] W. Polifke, C.O. Paschereit, and T. Sattelmayer. A Universally Applicable Stability Criterion for Complex Thermo-Acoustic Systems, August 1997.

[107] W. Polifke, C.O. Paschereit, and K. Döbbeling. Constructive and Destructive Interference of Acoustic and Entropy Waves in a Premixed Combustor with a chocked Exit. *International Journal of Acoustics and Vibration*, 6(3):135–146, 2001.

[108] S.B. Pope. *Turbulent Flows*. Number ISBN 0-521-591-25-2. Cambridge University Press, 2000.

[109] M. Poschner and M. Pfitzner. Realgas Modelling of Injection Mixing and Combustion Processes in Rocket Combustion Engines. Technical report, SFB/TRR 40, Annual Report 2009, pages 149–164, November 2009. URL `http://www.sfbtr40.de/images/stories/annualreport2009`.

[110] B.R. Ramaprian and S.W. Tu. Fully Developed Periodic Turbulent Pipe Flow. Part 2. The Detailed Structure of the Flow. *Journal of Fluid Mechanics*, 137: 59–81, 1983.

[111] F.R.S. Rayleigh. The Explanation of Certain Acoustical Phenomena. *Nature*, 18: 319–323, 1878.

[112] S.W. Rienstra. Private Communication, 2013.

[113] S.W. Rienstra. A Classification of Duct Modes Based on Surface Waves. *Wave Motion*, 37:119–135, 2003.

[114] S.W. Rienstra. Acoustic Scattering at a Hard-Soft Lining Transition in a Flow Duct. *Journal of Engineering Math*, 59:451–475, 2007. doi: 10.1007/s10665-007-9193-z.

[115] S.W. Rienstra and A. Hirschberg. An Introduction to Acoustics. Technical report, Eindhoven University of Technology, 2012.

[116] N. Riley. Steady Streaming. *Annual Review of Fluid Mechanics*, 33:43–65, Jan 2001. doi: 10.1146/annurev.fluid.33.1.43.

[117] N. Rott and R. Hartunian. *On the Heat Transfer to the Walls of a Shock Tue*. Graduate School of Aeronautical Engineering, 1955. Cornell University Report.

[118] T. Sattelmayer and W. Polifke. A Novel Method for the Computation of the Linear Stability of Combustors. *Combustion Science and Technology*, 175(3): 477–497, 2003.

[119] M. Schmid and T. Sattelmayer. Interaction of Acoustic Pressure Fluctuations with Supercritical Nitrogen Jets. In *AIAA/ASME/SAE/ASEE Joint Propulsion Conference & Exhibit*, Atlanta, Georgia, 2012. AIAA.

[120] B. Schuermans. *Modeling and Control of Thermoacoustic Instabilities*. PhD thesis, École Polythechnique Fédérale de Lausanne, 2003.

[121] A. Scotti and U. Piomelli. Numerical Simulation of Pulsating Turbulent Channel Flow. *Physics of Fluids*, 13(5):1367–1384, May 2001. doi: 10.1063/1.1359766.

[122] A. Scotti and U. Piomelli. TurbulenceModels in Pulsating Flows. *AIAA Journal*, 40(3):537–544, March 2002. doi: 10.2514/2.1679.

[123] J. Smagorinsky. General circulation experiments with the primitive equations: I. the basic experiment*. *Monthly Weather Review*, 91(3):99–164, 1963. doi: 10.1175/1520-0493.

[124] S.F. Tardu, G. Binder, and R.F.ls Blackwelder. Turbulent channel flow with large-amplitude velocity oscillations. *Journal of Fluid Mechanics*, 267:109–151, 5 1994. doi: 10.1017/S0022112094001138.

[125] D.P. Telionis. *Unsteady Viscous Flows*. Springer Series in Computational Physics. Springer Berlin Heidelberg, 1981. doi: 10.1007/978-3-642-88567-9.

[126] S. Thyageswaran. Numerical Modeling of Pulse Combustor Tail Pipe Heat Transfer. *International Journal of Heat and Mass Transfer*, 47(12-13):2637–2651, 2004. doi: 10.1016/j.ijheatmasstransfer.2003.12.020.

[127] H. Tijdeman. On the Propagation of Sound Waves in Cylindrical Tubes. *Journal of Sound and Vibration*, 39(1):1–33, 1975. doi: 10.1016/S0022-460X(75)80206-9.

[128] VDI Verlag. VDI Wärmeatlas. Springer, 2006.

[129] L. Wang and X.-Y. Lu. An Investigation of Turbulent Oscillatory Heat Transfer in Channel Fows by Large Eddy Simulation. *International Journal of Heat and Mass Transfer*, 47:2161–2172, 2004. doi: 10.1016/j.ijheatmasstransfer.2003.11.010.

[130] H.G. Weller, G. Tabor, H. Jasak, and C. Fureby. A Tensorial Approach to Computational Continuum Mechanics Using Object-Oriented Techniques. *Computers in Physics*, 12(6):620–631, Dec 1998. doi: 10.1063/1.168744.

[131] F.M. White. *Viscous Fluid Flow*. Number 0072402318 / 9780072402315. McGraw-Hill, 3 edition, 2006.

[132] B.T. Zinn and M.E. Lores. Application of the Galerkin Method in the Solution of Non-Linear Axial Combustion Instability Problems in Liquid Rockets. *Combustion Science and Technology*, 4(1):269–278, 1972.

[133] B.T. Zinn and E.A. Powell. Application of the Galerkin Method in the Solution of Combustion Instability Problems. In *Proceedings of the 19th International Astronautical Congress*, volume 3, pages 59–73, 1970.

[134] Y.B. Zudin. *Theory of Periodic Conjugate Heat Transfer*, volume 5. Springer, 2011.